2013-ENAM-0028

2013-ULg

École doctorale n° 432 :
Sciences des Métiers de l'Ingénieur

Collège de doctorat en Sciences de l'Ingénieur
Architecture – Géologie - Construction

T H È S E

en cotutelle internationale

pour obtenir le grade de Docteur en Sciences de l'Ingénieur délivré par

l'Université de Liège

et le grade de docteur délivré par

l'École Nationale Supérieure d'Arts et Métiers

Spécialité « Mécanique–Matériaux »

présentée et soutenue publiquement par

Joseph FANSI

le 2 Juillet 2013 à Liège (Belgique)

Prediction of DP steel fracture by FEM simulations using an advanced Gurson model

Directeurs de thèse : **Anne-Marie HABRAKEN** et **Tudor BALAN**

Jury:

M. Thomas Pardoen, Professeur, Université Catholique de Louvain, Belgique	Président
M. Eric Maire, Directeur de recherches CNRS, INSA-Lyon, France	Rapporteur
M. Ton Van Den Boogaard, Professeur, Université de Twente, Pays-Bas	Rapporteur
Mme. Anne-Marie Habraken, Directrice de recherches FNRS, Université de Liège, Belgique	Examinateur
M. Laurent Duchêne, Maître de conférences, Université de Liège, Belgique	Examinateur
M. Mohamed Ben Bettaieb, Maître de conférences, ENSICAEN, France	Examinateur
M. Tudor Balan, Maître de conférences HDR, Arts et Métiers ParisTech-Metz, France	Examinateur
M. Xavier Lemoine, Docteur/Ingénieur, ArcelorMittal Maizières-Lès-Metz, France	Examinateur
M. Olivier Bouaziz, Docteur/Ingénieur HDR, ArcelorMittal Maizières-Lès-Metz, France	Invité

Arts et Métiers ParisTech - Centre de Metz
Laboratoire d'Etude des Microstructures
et de Mécanique des Matériaux – LEM3

Université de Liège
Faculté de Sciences Appliquées
Département ArGEnCo, Secteur MS²F
Mécanique des Solides et des Matériaux MSM

T H È S E

Dédicace, Widmung, Dedicate

Le château de ma mère

La gloire de mon père

Marcel Pagnol , 1957

To my Cameroonian, French, and German family

To my wife

To the next generation

In memory of

Emilie Fansi and Christel Schäfer

Acknowledgments

La production de cette thèse est avant tout le fruit d'un travail d'équipe basé sur la confiance entre personnes. Pour cela je remercie Anne-Marie HABRAKEN (Université de Liège), Tudor BALAN (ENSAM-Metz) et Xavier LEMOINE (ArcelorMittal-Maizières) de m'avoir encadré et entièrement fait confiance tout au long de ces trois années de recherche. Il faut dire que confier un tel sujet de travail aussi techniquement, et administrativement complexe, et doté d'un enjeu industriel aussi important à une personne venant de l'industrie et avec peu de connaissance de l'endommagement n'a pas été une décision prise à la légère. Durant ces trois années j'ai pu m'immerger dans le monde de la mécanique des matériaux avec Anne-Marie, que je remercie grandement ainsi que toute son équipe. Je remercie Tudor qui avec son humour décapant a permis de me relaxer un peu durant les longues réunions de projet. Bien sûr, ses compétences en calculs numériques m'ont permis de comprendre un peu le fonctionnement des logiciels de simulations. Non loin de son bureau se trouvait Xavier qui partagé entre les cours d'enseignement supérieur et ses obligations chez ArcelorMittal m'a largement aidé à accomplir les innombrables formalités administratives dans l'entreprise. Bien entendu, je ne nie pas ces grandes compétences en programmation qui m'ont permis de gagner un temps inestimable pour la rédaction de livrables pour l'entreprise: l'ANRT que je remercie au passage et les deux écoles doctorales. Mes remerciements vont également à Mr BABBIT, directeur au sein du secteur Auto (ArcelorMittal à Maizières-lès-Metz) de m'avoir intégré dans l'équipe AUP² (Automotive Product Properties). Je suis également reconnaissant envers ce centre de recherche et particulièrement à Stéphane DOUCHAMPS pour m'avoir accueilli afin de réaliser les essais expérimentaux. Et, je n'oublie pas l'aide administrative d'Alain GASPAROLI.

Je souhaite également préciser que ce projet n'aurait jamais pu techniquement démarrer sans la lourde tâche de Mohamed BEN BETTAIEB qui m'a initié à la compréhension de son model de Gurson. Je le remercie d'avoir pris du temps et la patience pour m'enseigner les rudiments de l'implémentation d'un calcul numérique. Les précisions et les détails apportés à ses explications m'ont éblouit sachant le nombre de projets dont il avait la charge. Nous avons eu également de très bons moments de relaxation à chaque étape de compréhension.

C'est avec beaucoup d'honneur que je remercie Thomas PARDOEN d'avoir accepté d'être président de ce jury qui correspond pour moi à la « dream team » de l'endommagement. Je remercie aussi Eric MAIRE et Ton VAN DEN BOOGAARD d'avoir accepté d'être des rapporteurs. Je remercie également Laurent DUCHÊNE pour avoir voulu examiner mon travail et je remercie Olivier BOUAZIZ de sa présence dans ce jury qui a participé aux discussions sur l'endommagement tout au long de ces trois années consacrées à mes recherches. L'établissement du modèle GTNBF (Gurson-Tvergaard-Ben Bettaieb-Fansi) n'aurait pas pu être possible sans le remarquable travail expérimental de Caroline LANDRON sur l'endommagement des aciers Dual-Phases. Donc, merci à Caroline.

Je remercie ma famille d'Allemagne, du Cameroun et de France, mes parents (Jean Bernard, Marie-Solange), mes frères (Bob, Christopher, Clarence, Idriss, Sonny) et sœurs (Cécile-Laure, Myriam) pour les encouragements et les inoubliables réunions de famille. Danke KURT für dein Verständnis. Je dédie ce travail à mes proches qui m'ont quitté trop tôt, je pense à ma mère Emilie FANSI, mes deux grands parents et ma belle-mère Christel SCHÄFER.

Je remercie mes deux supers garçons Clarence-Félix et Simon-Maxence, dont j'ai la chance de les voir grandir au point de devenir de vrais dictionnaires Franco-allemands vivants. Aujourd'hui vous ne comprenez pas tout à fait ce que je faisais en Allemagne, en Belgique et en France durant ces trois années mais dans quelques années vous aurez la réponse en lisant ce manuscrit. Alors encore un peu de patience mes garçons. Ce travail est aussi pour que vous sachiez qu'après être devenu athlète de haut niveau, éducateur dans un centre de jeunesse, musicien, entrepreneur, ingénieur, j'étais apprenti scientifique.

En espérant n'avoir oublié personne je tiens à remercier une personne sans qui cette thèse n'aurait jamais vu le jour, c'est ma femme, la courageuse, grande de taille et de cœur, Silvia FANSI.

Etat d'esprit adopté durant la période de thèse:

Le sentiment d'isolement que j'ai parfois ressenti lorsque j'étais loin de ma famille a été un atout efficace pour me concentrer sur l'essentiel, à savoir, ma femme, mes enfants, ma famille en France et mon travail de Thèse. Ce travail dont j'ai investi beaucoup de temps et d'énergie est en fait le point de départ et la base d'une réflexion pour que dans le future mes enfants et ma famille puissent croire en des choses qu'ils veulent réaliser et de s'engager jusqu'au bout, en travaillant très dur pour cela. Je suis persuadé que l'intelligence ou le savoir n'a ni odeur, ni couleur et encore moins de limite. Il n'existe pas une intelligence mais plusieurs.
Il existe une expression qui résume cet état d'esprit et que les africains aiment fréquemment utiliser dans des situations particulièrement difficiles *"On va faire comment?"*.

He who is not courageous enough to take risks will accomplish nothing in life.

Age is whatever you think it is. You are as old as you think you are.

Hating people because of their color is wrong. And it doesn't matter which color does the hating. It's just plain wrong.

Muhammad Ali

Contents

Chapter I. **Introduction**

Contents

I.1 Context

I.1.1 Automotive history

According to French study on walk activity practiced in France since 1800 (Grübber and Nakicemovic, 1991), means of transportation such as car and bus have surged since 1900 compared to walk activity. Figure I.1 illustrates the evolution of the walk distance accomplished by French citizen per day since 1800 and compares it to other means of transportation like train, motorcycle, and plane. Y-axis describes the mean distance per day and X-axis plots the time. The graphic depicts a rapid slow down of the walk activity in benefit to car as a mean of transportation. Plane, motorcycle, train inverted a little bit the trend after world war II but not enough to last more than a decade.

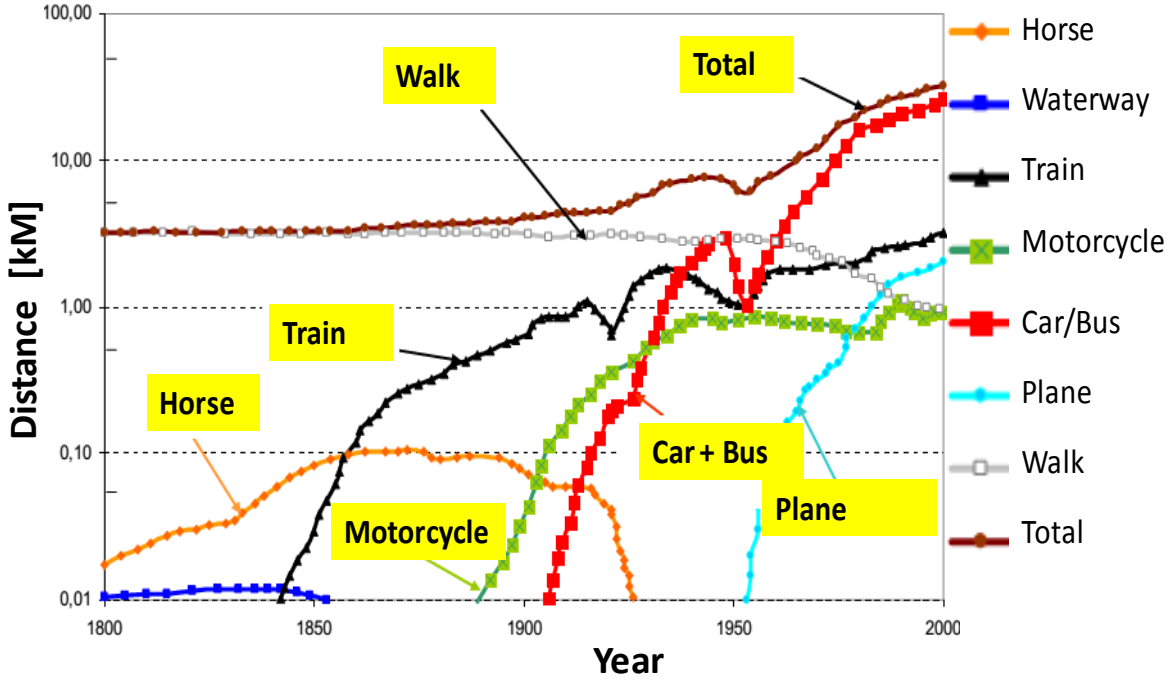

Figure I.1: Evolution of the walk distance per person and per day in France since 1800 according to Grübber and Nakicenovic translated from [PIN 2012].

The car dominance in our daily life has tremendously changed our habits and makes towns always closer. Unfortunately, the perpetual innovations in automotive industry have settled new challenge for instance, environment, climate change, fuel reduction. More recently, the economic crisis has pushed the car industry to drastically reduce the weight and to increase the car efficiency.

The car from 1936 (Figure I.2a) still has four wheels as today but the design and the efficiency are quite different compared to the modern one (Figure I.2b).

a)  b) 

Figure I.2: a) Rolls-Royce-Phantom from 1936, b) Audi R8 from 2006.

I.1.2 Production and development of new materials

Since 1980, auto manufacturers are challenged to improve safety, fuel consumption and weight reduction. Advanced High-Strength Steels (AHSS) tremendously help carmakers to meet requirements for safety, fuel efficiency, exhaust gas pollution, manufacturability, durability, environment politics and quality at a low cost [TAM 2011].
According to steelmakers such as AK Steel, ArcelorMittal Steel, Baosteel, Essar Steel Algoma Inc., Tata Steel Europe, United States Steel, voestalpine Stahl GmbH, AHSS are the actual generation of steel grade that provides extreme high-strength while maintaining a high formability.
Figure I.3 represents a graphic of the AHSS grades. In details, the Y-axis plots the elongation in percent whereas the X-axis plots the tensile strength. It shows the particular combinations of material and mechanical properties in a banana form. Most of the materials result from a controlled heating and cooling processes.
The most challenging task for engineers is to choose the material with the right combination of strength, ductility, toughness, and fatigue properties. The graphic also depicts a wide range of AHSS such as Transformation Induced Plasticity (TRIP), Ferritic-Bainitic (FB), Complex Phase (CP), Martensitic (MART), High-Strength Low-Alloy (HSLA) and the widely used Dual Phase (DP) steels. The present research is only focusing on same grades of DP steels providing various properties. DP steels can have a high elongation and low tensile strength or combine low elongation and high tensile strength. These characterisations underline the importance of ranking with special care the DP grades before using them to meet key criteria such as crash performance, stiffness and most important forming requirements.

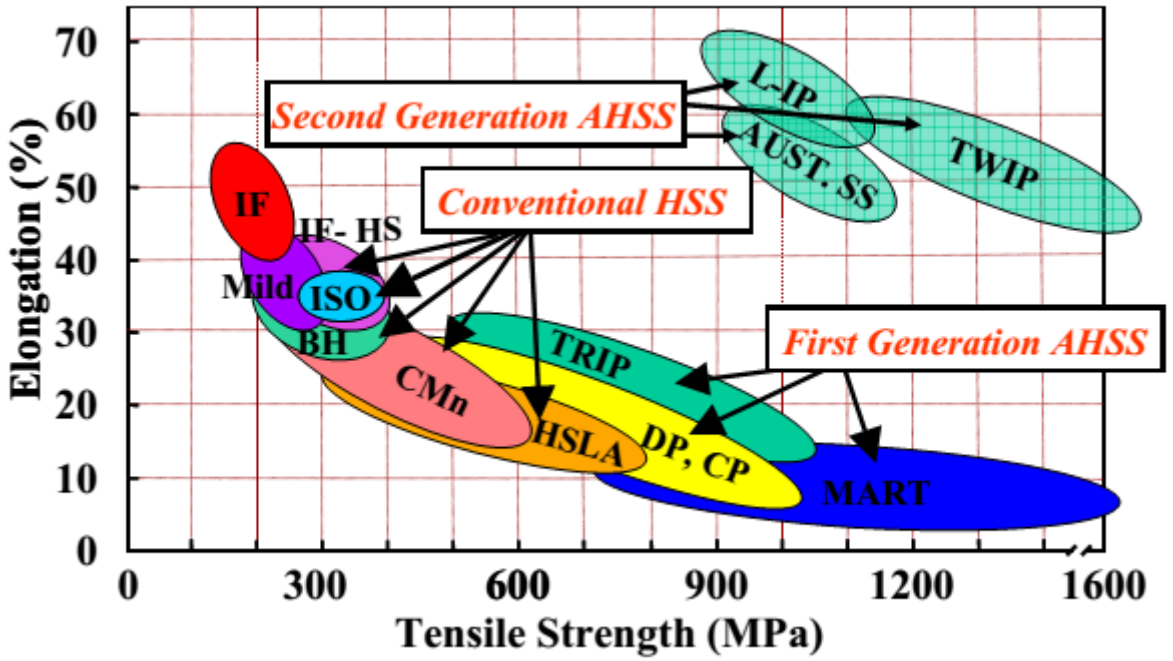

Figure I.3: Strength-Elongation curve for low strength, conventional HSS and first generation AHSS steels [WAG 2006].

According to Advanced High Strength Steel Workshop held in 2006 [WAG 2006] and more recently steel market development institute study on AHSS [TAM 2011], the future AHSS applications in automotive is rapidly growing. Steelmakers are studying them to better understand their potentialities and limitations and others are more focused on improving the technology necessary for manufacturing parts made of these steels. Nowadays, steel and car makers are combining their effort by developing multiple joints research to put the next generation of safer, cheaper, fuel efficiency and environmentally friendly vehicles on the road.

I.I.3 Dual-Phase in automotive industry

As already mentioned, the selected DP steels in the present study are the widely advanced high-strength steels used in the automotive industry. A literature survey [ZÜR 2005], [WAG 2006], [WIE 2006], [AHM 2011], [LAN 2011], [MAT 2012], [PIN 2012], [PAR 2012] confirms that, DP steels usually consist of a ferrite matrix containing a hard martensite second phase in the form of islands. Increasing the volume fraction of hard second phases generally increases the strength. DP steels are obtained by controlled cooling from the austenite phase (in hot-rolled products) or from the two-phase ferrite plus austenite phase, to transform some austenite to ferrite before a rapid cooling transforms the remaining austenite to martensite. According to [PAR 2012], roll forming, as a metal fabricating process, is used to add both strength and rigidity to manufactured DP steels. Figure I.4 illustrates the application of various DP steels in automotive industry such as bumper beam, A-frame reinforcement, roof bow, B-pillar reinforcement, rear side member, front floor cross member, floor side reinforcement, front side members and Body-in-White (BIW) structural parts.

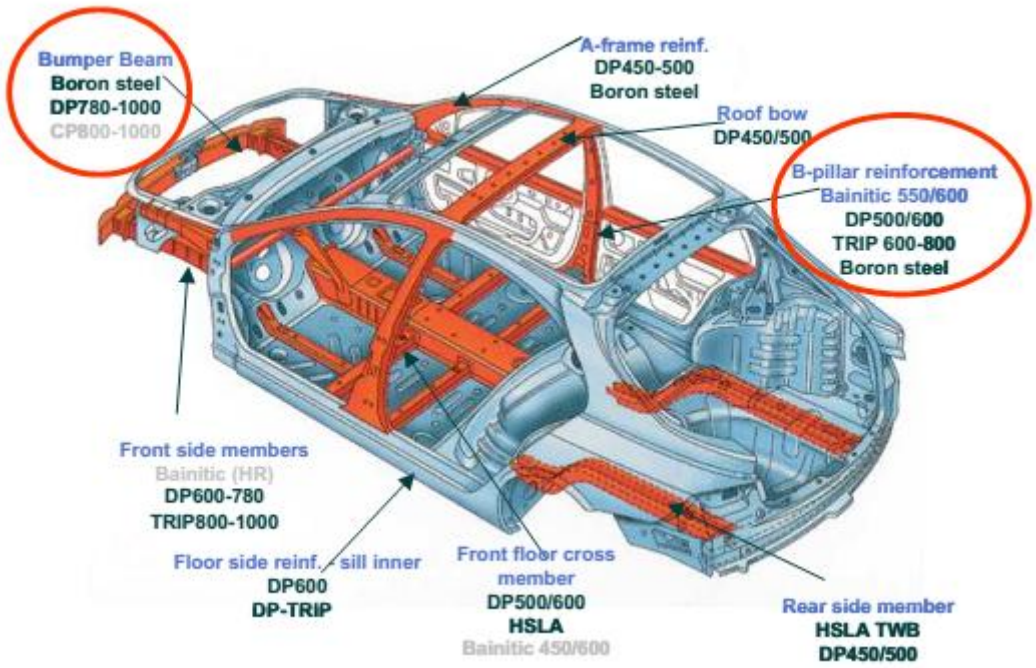

Figure I.4: Automotive industry applications of the DP steels in automotive industry [PIN 2012].

The soft ferrite phase is generally continuous, giving these steels outstanding ductility. The influence of the volume fraction and the shape of the martensite have been widely investigated by numerous authors such as Huang et al. [HUA 1989], Sarwar et al. [SAR 1996] and Bello et al. [BEL 2007]. According to these contributors, the growth of the volume fraction of martensite around 55% results in increased yield point, tensile strength and impact strength of DP steels. At higher volume fraction of martensite values a decrease of the strength properties is detected.

I.2 Objectives of the thesis

DP steels modelling has been since 1980 a huge interest for car and steel makers. The control of their mechanical properties depends on their formability characteristic which influences the manufacturing quality. Regarding the constant increasing complexity of the technology employed to reach the industrial requirements, the needs of experiment and analytical models are lead by the development of numerical simulations. This technology, born forty years ago is in constant improvement years after years thanks to powerful computers and broad research on the Finite Element method and on constitutive laws based on phenomenological or multi-scale approaches. Nowadays, the accuracy of the simulations results is gaining credibility compared to the experimental test. The numerical simulation reduces dozen of experiments, time framework and manufacturing costs. On top of that, an accurate simulation needs realistic boundary conditions, good sketch of the sample and tooling geometries and the most important a reliable material behaviour model.
Regarding the last requirement, the needs for ArcelorMittal is to predict with good accuracy the rupture in forming processes taking into account the edge effects, the residual stress, the

material and mechanical anisotropy. Therefore a study has been carried out in 2008 by a joint research composed of MS²F Argenco (Liège, Belgium) and ArcelorMittal-Maizières (Maizières-Lès-Metz, France) targeting the development of a formability criterion for deep drawing, rolling, bending etc... As a result of this research study conducted by Ben Bettaieb for 2 years, an extended Gurson-Tvergaad-Needleman (GTN) model [BEN 2010] has been proposed for ductile failure. The study included a literature review and state of the art of formability criteria [BEN 2011], the development of a 3D advanced GTN Formability criterion (damage modelling) [BEN 2012] implemented in the finite element code Lagamine [ZHU 1992]. The Gurson-Tvergaard-Needleman-Ben-Bettaieb model (GTNB) takes into account the void nucleation. It allows for the accurate modelling of the observations of damage initiation and growth in DP steels measured by high-resolution X-ray absorption tomography [BOU 2008]. The numerical implementation used an explicit-implicit algorithm. It is explicit for the porosity state variables and implicit for other variables (macroscopic plastic strain and the yield stress of the dense matrix, backstress, equivalent plastic strain). This choice, justified by the complexity of the porosity function and dependency of the other variables, requires small time steps to avoid any convergence problem during the computation.
The success of the GTNB model application on smooth specimen motivates the joint research to stretch the model out and to implement it into a commercial finite element code used by ArcelorMittal, through a three years PhD work. At the starting point of the present research, further X-ray tomography measurements have been investigated by Landron et al. [LAN 2011] on in situ tensile notched specimens made of DP steels. The experiments revealed a strong dependency between the density of voids, the back stress, and the triaxiality for these grades. Motivated by these new experimental observations and the industrial needs, the extension of the GTNB model has been developed in cooperation with four research teams (ArcelorMittal-Maizières, INSA-Lyon, ENSAM ParisTech-Metz and University of Liège) [FAN 2013].

The main goal of this work is to correlate the experimental results on notched samples and the model predictions for better understanding of the DP steel ductile fracture. To attempt this aim, the GTNB model has been adapted as "User-defined Material model subroutine" (VUMAT) in the Abaqus/explicit FE code [ABA 2011]. The model has been enriched by adding a coalescence model, a recent void nucleation and growth laws integrating the back stress variable [LAN 2011] and a fracture initiation criterion. These enhancements have been done based on high resolution X-ray tomography observations and measurements. In order to accurately correlate the finite element predictions with the experiments, a precise post-processing method has been developed taking into account identical results extraction between experiments and simulations. The numerical void volume fraction definition is the same as the one used in the test related to the number of cavities and their size in a fixed volume. Along with the attempt of integrating the back stress variable in the new nucleation law, a discussion has been opened regarding the triaxiality definition.
The second objective is to be able to rank the DP steel grades chosen in this study. Finally, the experimental validation is being further extended to other sample geometries in flat sheet steels, as well as industrial application such as cross-die drawing test.

I.3 Contents

The aim of the second chapter is to give a general presentation of the Dual-Phase (DP) steels. It will show typical DP steels microstructures, mechanical properties and formability characteristics.
The third chapter presents how the mechanical behaviour of DP steels can be predicted by plasticity, damage or fracture modelling.
The experiments carried out on in-situ tensile notched axisymmetric specimens of DP steels [LAN 2011] revealed a strong dependency between the density of voids, the back stress, and the triaxiality.
The fourth chapter summarizes the contributions brought to the damage and fracture modeling during this thesis. These contributions are based on the recent experimental results of [LAN 2011] on in-situ tensile notched axisymmetric specimens of DP steels, and the one-dimensional metallurgical models inferred therein. These contributions concern the void nucleation and void growth law, the coalescence model and an additional fracture initiation criterion, which were extended to the 3D incremental case and integrated in the proposed model (further called GTNBF).
The parameter identification of the whole set of parameters of the GTNBF model for three DP steels is described in chapter five. Chapter six deals with the finite element implementation of proposed model in the commercial code Abaqus/Explicit. The implementation follows the path previously adopted by Ben Bettaieb [BEN 2012] in the finite element code Lagamine. The proposed implementation remains compatible with the two finite element codes, with the Abaqus routine "VUMAT" being used as an interface. The developed algorithm and code is numerically validated.
The potentialities and limitations of the model are contained in Chapter seven where the material parameters sensitivity is carefully checked. In front of that, the post processing and the element size influence on the current model are carried out.
Chapter eight illustrates the industrial applications of the GTNBF model. Finally, the conclusions are summarized in chapter nine along with some potential future work.

Chapter II. **Dual-Phase steels**

Contents

The aim of the current chapter is to give a general presentation of the Dual-Phase (DP) steels. The first part presents the typical properties of DP steels: microstructures, mechanical properties and formability characteristics. The second part of the chapter focuses on the experimental damage tests realized to evaluate the void evolution in DP steels, and gives more details of the DP steels studied.

II.1 Description of DP steels

II.1.1 Microstructures

Dual Phase steels belong to the larger category of Advanced High Strength Steels (AHSS) used by automakers. They provide an outstanding combination of strength and ductility as a result of their microstructure, in which hard islands of Martensitic phase (α') are dispersed in a soft Ferritic matrix (α) as shown in Figure II.1.

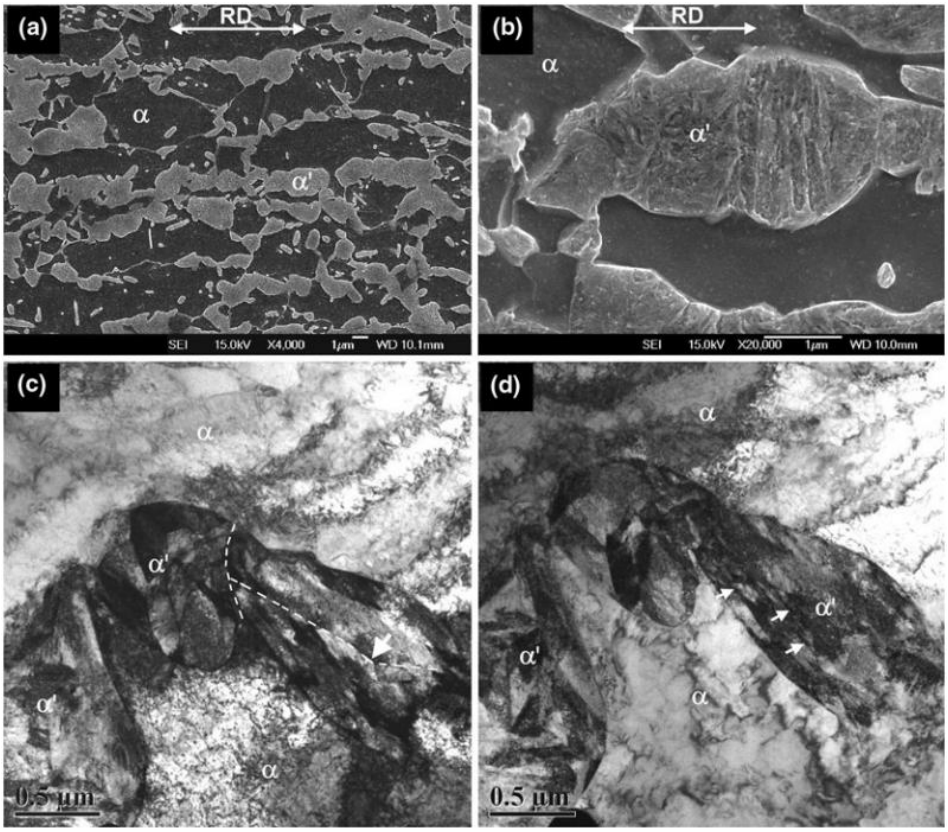

Figure II.1: SEM micrographs of a typical DP steel's microstructure showing (a) ferrite (α) - matrix along with banded islands of martensite (α'), (b) sub-structure within (α') phase, and (c) and (d) TEM bright-field images taken at two tilt angles illustrating (α') phase and α matrix [BAL 2011].

According to Landron et al. [LAN 2010-2011], Tamarelli et al. [TAM 2011], and Tsipouridis

et al. [TSI 2006], the DP steels microstructure is manufactured by intercritical heat treatment [SHA 2009] of an initial ferrite/pearlite ($\alpha + Fe_3C$) microstructure followed by an accelerated cooling as shown in Figure II.2. During the heating, the austenitic phase γ appears for a temperature $\theta > A_1$. The amount of austenite, being later the amount of martensite, is ruled by the temperature level estimated between A_1 and A_3. The final quenching allows the transformation $\gamma \rightarrow \alpha$ to take place, leading to the final microstructure of the DP steel.

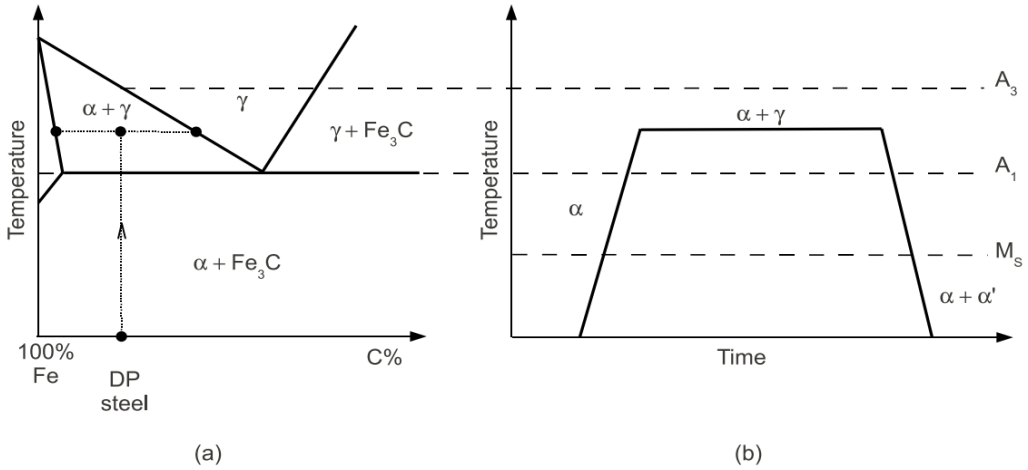

Figure II.2: Heat treatment to obtain a DP microstructure: (a) schematic Fe-C diagram, (b) applied heat treatment [LAN 2011].

Although the structure of the DP steel contains ferrite and martensite, sometime a small amount of residual austenite may appear after the heat treatment. This residual microstructure could have an effect by modifying the mechanical properties. The presence of austenite phase reduces the martensite volume fraction and affects its distribution after the heat treatment. Experimental literature [SCH 2010], [KRE 2010], [NIA 2012] describes that the variation of the martensite quantity and the microstructural features of the martensite distribution affect the macroscopic behaviour of the DP steel. Referring to Tamarelli et al. [TAM 2011] observations, the ferrite is continuous for many grades up to DP780 steel, but as volume fraction of martensite exceed 50 percent (as might be found in DP980 steel or higher strengths), the ferrite may become discontinuous.

In addition to the presence of this residual phase, the DP steels can contain negligible quantities of inclusion particles or voids generated during the production of the material (cold or hot-rolling procedures [TSI 2006]) or after the forming process of the DP steel blank.

II.1.2 Mechanical properties

The variety of microstructures and especially the volume fraction of martensite reveal a large multitude group of tensile strength levels. Table II.1 summarizes the product property requirements for various types of DP steels. It also underlines the effect of strain and bake hardening (locking dislocation by solute Carbone) [MAR 1982] [CAI 1985] [SUH 1997] [BAG 1999] [ERD 2002] [KAW 2003] [MAZ 2007] [AVR 2009].

Table II.1: Dual Phase steels and their mechanical property requirement according to ArcelorMittal standard tensile test for DP steel less than 3mm thick.

Product	Yield Strength (YS) [MPa]	Ultimate Tensile Strength (UTS) or R_m [MPa]	Total Elongation or Ag [%]	Direction
FF280DP	300-380	≥490	≥25	Transversal
DP450	280-340	450-530	≥27	Transversal
DP500	300-380	500-600	≥25	Longitudinal
DP600	330-410	600-700	≥21	Longitudinal
DP780 Y450	450-550	780-900	≥15	Longitudinal
DP780 Y500	500-600	780-900	≥13	Longitudinal
DP980 Y700	700-850	980-1100	≥8	Longitudinal
DP1180	900-1100	≥1180	≥5	Longitudinal

As mentioned in section 0, there is a strong link between the tensile strength or the elongation and the fraction of martensite contained in the material. Figure II.3 presents the variation of the mechanical properties in function of the volume fraction of martensite for the DP580 steel (Fe0.09, C1.9, Mn0.1, Si0.3, Cr0.15, Mo). The tensile strength increases gradually when the fraction of martensite rises. In contrast, the elongation decreases when increasing the fraction of martensite [ALL 2012].

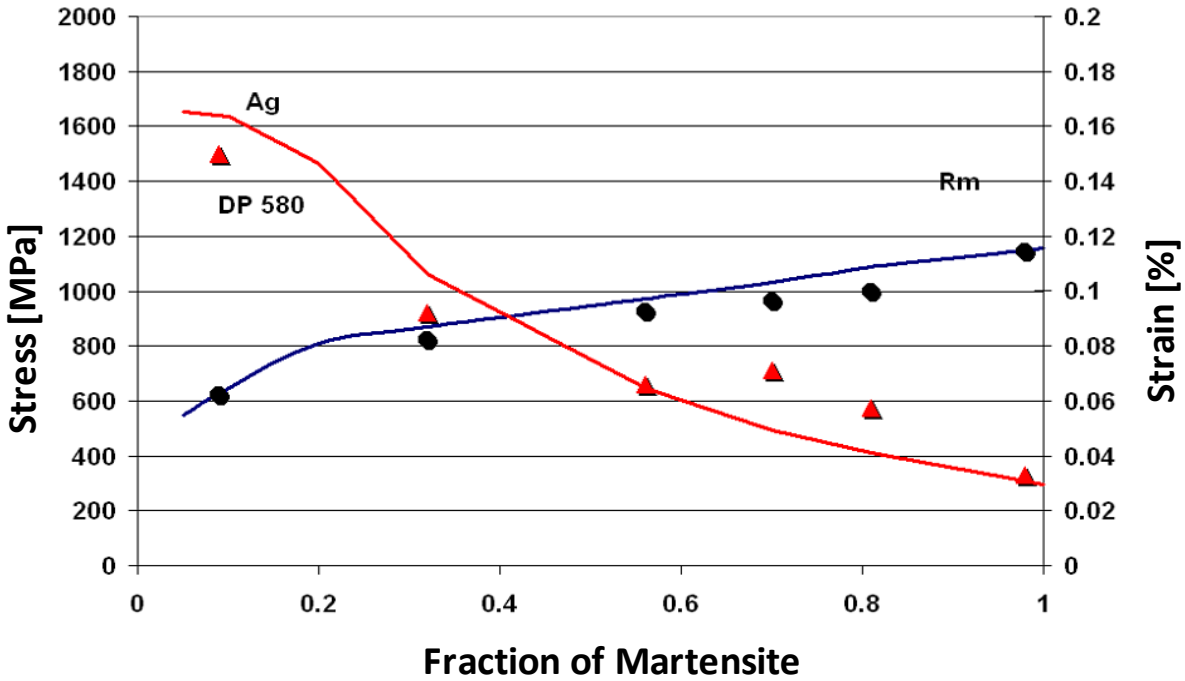

Figure II.3: Mechanical properties in function of the volume fraction of martensite. R_m is the tensile strength and Ag the elongation for DP580 (Fe0.09, C1.9, Mn0.1, Si0.3, Cr0.15, Mo) [ALL 2012].

II.I.3 Formability characteristics

The Dual-Phase steels present an excellent candidate for the car body structural components. These are often produced for safety-critical parts (see Figure II.4) which maintain passenger surviving space in crash events. The DP steels present a good balance of strength, formability, energy absorption and durability. Also the employability of this kind of steel provides the possibility of reducing the weight of the vehicle.
DP is sometimes selected for visible body parts and closures, such as doors, hoods, front and rear rails. Other well known applications include: beams and cross members; rocker, sill, and pillar reinforcements; cowl inner and outer; crush cans; shock towers, fasteners, and wheels [TAM 2011].

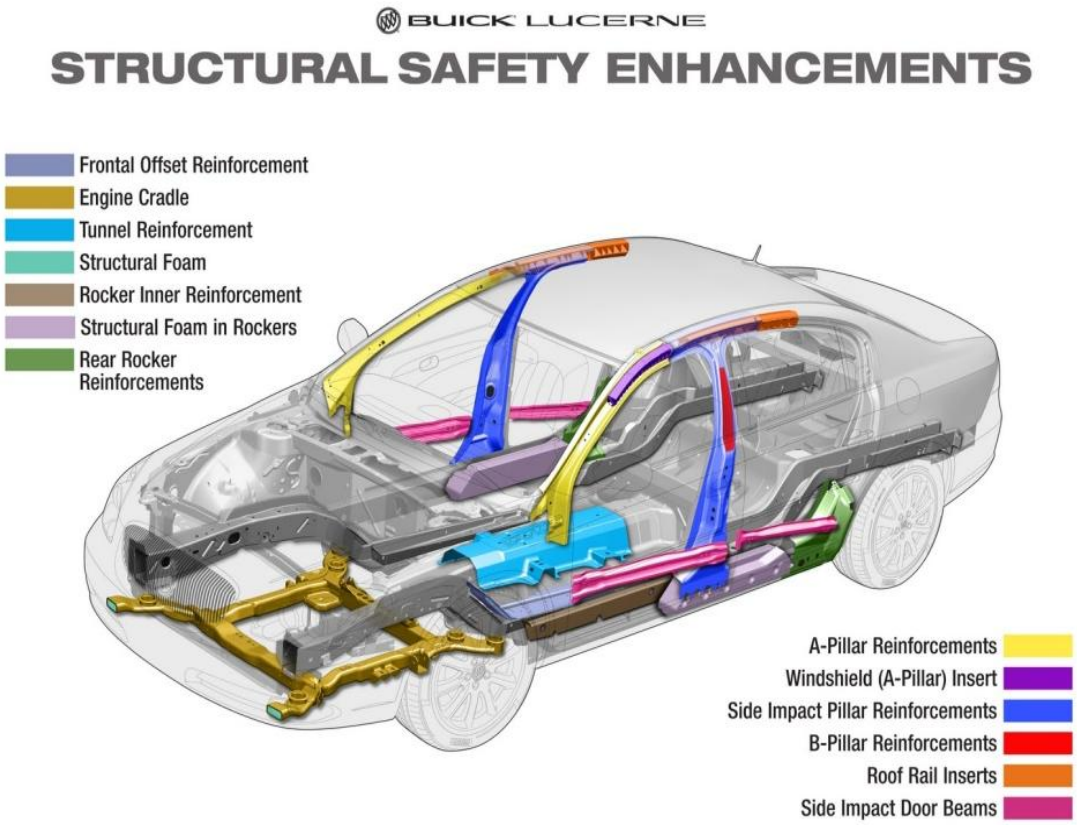

Figure II.4: DP steels used for safety-critical body parts (General Motors, [BUI 2011]).

However, the excellent structural properties of this AHSS group are limited by the fracture phenomena. Fractures are different from ordinary steel and depend strongly on the DP steel grades used. The Figure II.5 below shows a shear fracture, an edge cracking and a crack during a hole expansion test. Numerous factors can affect the outstanding DP properties such as number of forming stages, tool geometry for each stage, boundary constraints, lubrication conditions, material variability and eventually the product changes [KEE 2009].

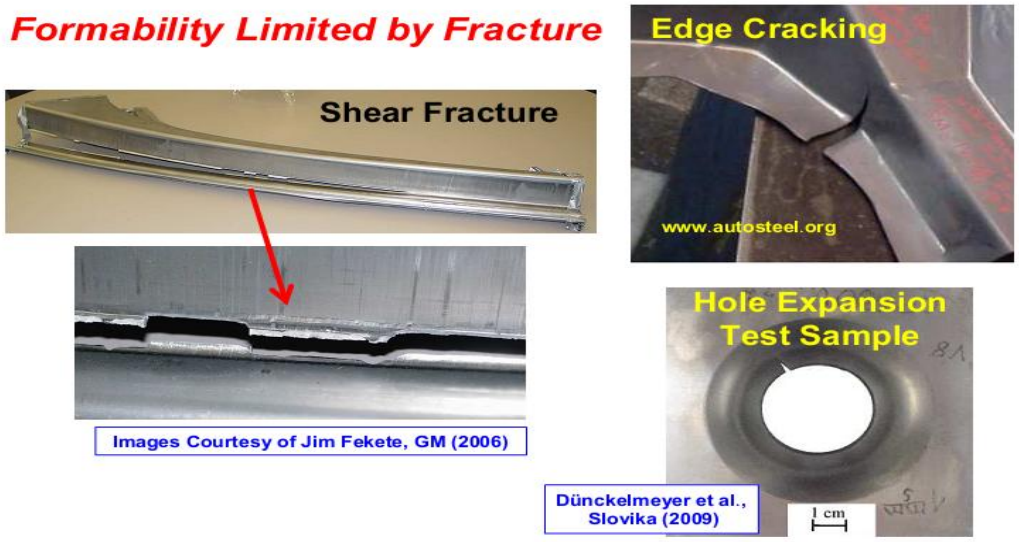

Figure II.5: Fracture type in automotive part for DP steel in different solicitations [MAT 2012].

Another crucial cause (*not studied in this document*) for the fabrication of inconsistent sheet metal part is springback i.e. the elastic strain recovery in the DP steel after the tooling is removed. Springback of sheet metal parts after forming causes deviation from the designed target shape and produces downstream quality problems and assembly difficulties as seen in Figure II.6.

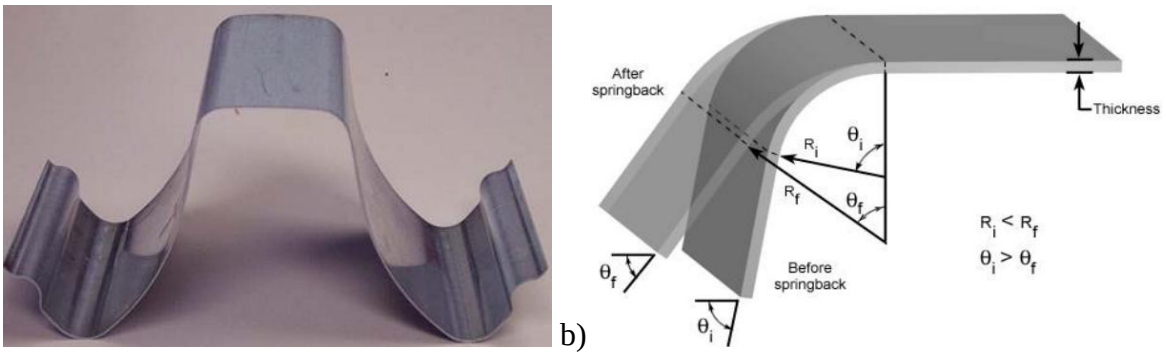

Figure II.6: a) Springback of DP600 channel draw, b) Elastic strain recovery after the tooling is removed called Springback phenomenon [WAG 2006].

Figure II.7 provides an example of the well know Forming Limits Diagrams (FLD) used to quantify formability and allows the steel and automotive makers to reduce the costs of designing tools and to shorten the time-to-market cycle. It gathers the published curves measured by different research groups (ArcelorMittal, Ramazani et al. [RAM 2012], Uthaisangsuk et al. [UTH 2008-2009].

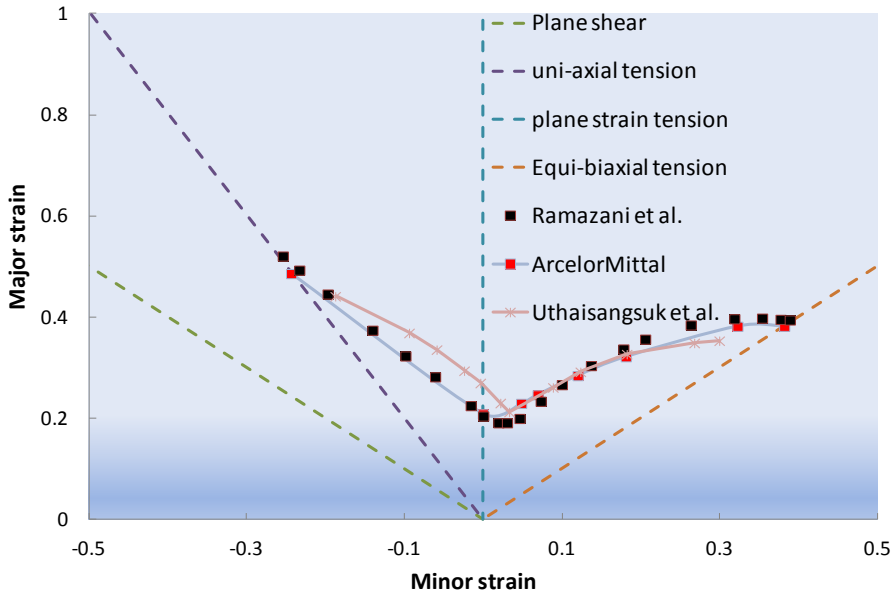

Figure II.7: Forming Limit Diagrams (FLD) with experimental points from different research team for DP600 steel.

II.2 Experimental Damage Investigation of DP steels

II.2.1 Experimental techniques to study fracture

Although the DP steel is a good compromise between strength and ductility its formability is limited by mechanical fracture. The investigation of fracture has been a challenging task for engineers and researchers since a century [MAL 1846], [HAL 1953], [RAS 1976], [RAM 1979]. Ductile and Brittle fracture of metals have been predicted with high or low accuracy in many cases [TAS 2009-2010], [XUE 2012]. Since the early fracture investigations [Rice & Tracey 1969, Gurson 1977, Tvergaad 1984], etc..., it is well known that the ductile failure has four steps; void nucleation, void growth, void coalescence and propagation of a macroscopic crack. The understanding of these stages to optimize the damage models needs an accurate quantitative damage observations and measurements.

In his thesis, Weck [WEC 2007] summarizes the different techniques available to extract quantitative and qualitative damage parameters and crucial information. Table II.2 shows direct and indirect, two-and three-dimensional methods. Some of them are destructive such as fractography, polishing, serial sectioning, while the rest are non-destructive.

The current work is focused on exploiting 3D X-ray tomography coupled with the in-situ mechanical testing approach. The data resulting from this technique consumes a lot of time of preparation, and few results are publicly available [KAD 2011], [RAM 2012]. The work of Landron et al. [LAN 2011] using this new 3D approach is the experimental physical base of the current numerical investigation.

Table II.2: Experimental techniques available to study ductile fracture [WEC 2007].

Technique	Advantages	Disadvantages
Fractography	Easy	2D No sub-surface information No deformation history Destructive
Freeze Fractography	Easy Deformation history	2D No sub-surface information Destructive Only for BCC materials
Polishing	Easy Sub-surface information Deformation history	2D Polishing artefact Destructive
3D-Fractography	3D	No sub-surface information Destructive
3D-Freeze-Fractography	3D Deformation history	Only for BCC materials No sub-surface information Destructive
Serial sectioning	3D Full 3D reconstruction Can reveal microstructure	Time consuming Polishing artefact Destructive
X-Ray tomography	3D Full 3D reconstruction High resolution Non destructive History from a same sample Can follow deformation in-situ	Expensive, time consuming on analysis
Ultrasound	3D	Averaged information
Densimetry	3D	Averaged information

II.2.2 X-ray tomography principle

The technique of X-Ray tomography started in the end of the 80's in the medical field by improving the detection of brain and breast cancer tumor. This was available by using 2D radiographies. In the middle of the 90's the X-ray tomography was adapted and found its respective place in materials science to analyze debris from plane and cars crashes for the insurance companies. Since 2000 the method has become an efficient investigation tool for various materials.

The principle of X-ray tomography used by Landron and co-workers shown in Figure II.8 is composed of X-ray beam, the sample to analyze, the camera and the projections acquisition. The object to characterize rotates about a single axis while a series of 2D X-ray absorption images is recorded. Using mathematical principles of tomography, this series of images is reconstructed to produce a 3D digital image where each voxel (volume element or 3D pixel) represents the X-ray absorption at that point.

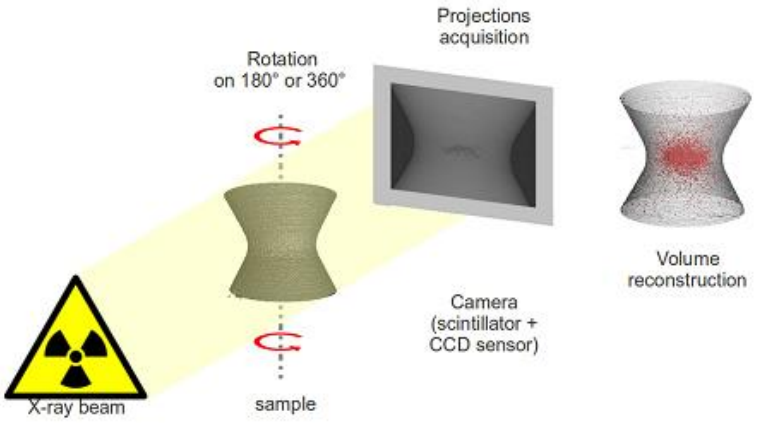

Figure II.8: X-Ray tomography principle [LAN 2011].

II.2.3 In-situ tensile tests

Due to the fact that the X-ray tomography is a non destructive test as mentioned previously, this technique has been coupled with an in-situ tensile test as seen in Figure II.9(a). One specimen is pulled for a given deformation. The specimen presented in Figure II.9(b) is unloaded. The tensile device is placed on the beam line. During imaging, the deformation is stopped but maintained constant.

Landron also performed a so called in-situ continuous test. It is the same procedure as the previous one but with no interruption of the deformation during the tensile test. This characterization requires a small scan time to have clear images of the reconstructed volume (as shown in Figure II.9(c)). The displacement speed of the tensile device is between 1µm/s and 5µm/s and the reconstructed volume is equal to 0.3×0.3×0.3mm³.

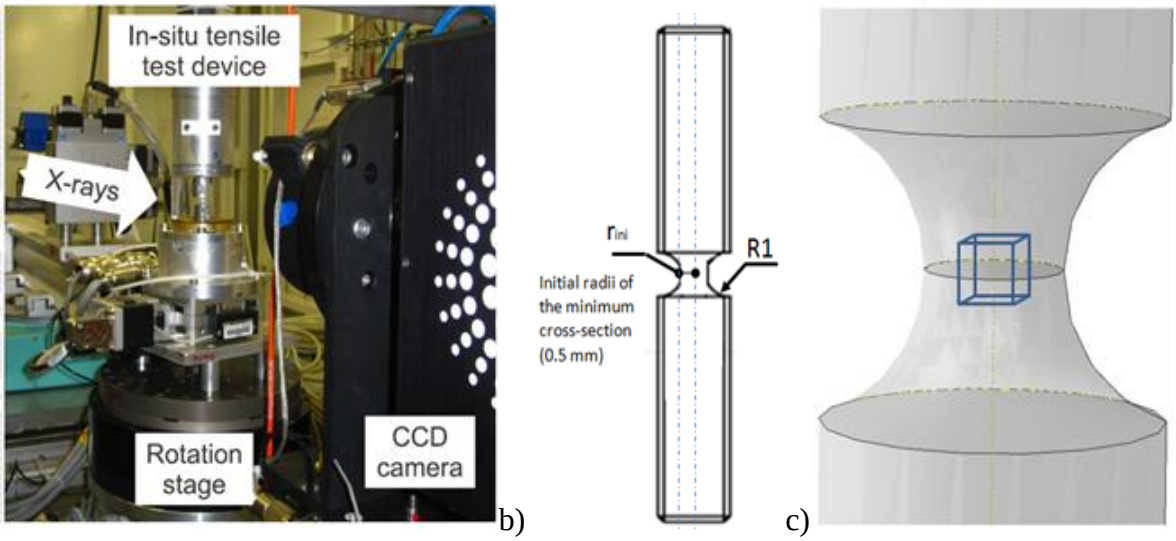

Figure II.9: Experimental test setting. (a) In-situ X-ray experimental device with 1-mm notched sample [LAN 2011], (b) the specimen design, (c) Studied spatial volume for the porosity measurement at the center of the specimen, of dimensions 0.3×0.3×0.3mm³.

II.3 Selected DP steels grades

In this study, three Dual-Phases microstructures have been chosen. All three named DPI, DPII and DPIII come from ArcelorMittal steels research and development center. The chemical composition of the selected steels is given in Table II.3.

Table II.3: Chemical composition of the DP steel selected (Wg%).

Material name	C	Mn	Si	Cr
DPI	0.08	0.8	0.23	0.68
DPII	0.076	1.439	0.351	0.204
DPIII	0.081	1.955	0.158	0.102

The micrography of the DPI microstructure is presented in the Figure II.10a. Light gray is the Ferrite phase and dark gray shows the islands of martensite. This grade contains a volume fraction of martensite equal to 11% on a rolled 2.5-mm thick sheet. The micrography of the DPII microstructure is presented in Figure II.10b. This grade contains a volume fraction of martensite equal to 5% on a rolled 1.5-mm thick sheet. The micrography of the DPIII microstructure is presented in Figure II.10c. This grade contains a volume fraction of martensite equal to 12% on a rolled 1.5-mm thick sheet.

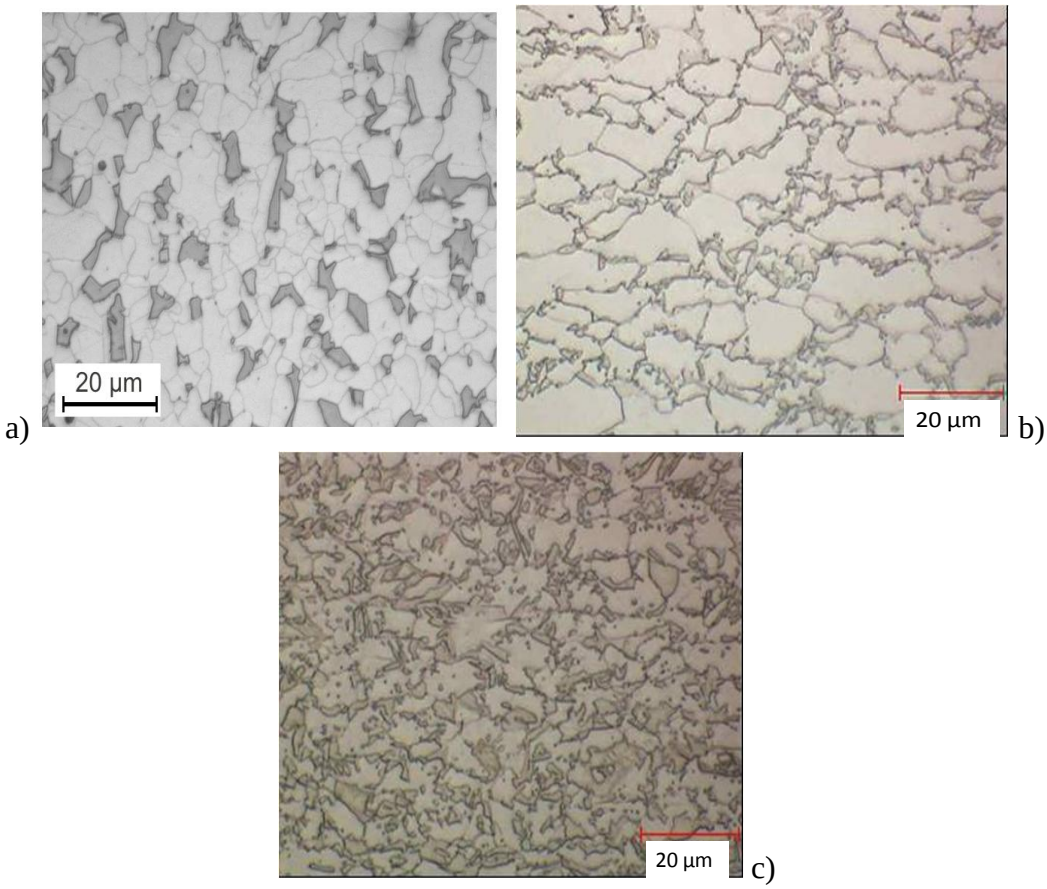

Figure II.10: Optical micrographs; light gray is ferrite matrix (α),dark gray is islands of martensite phase (α') a) DPI steel [LAN 2011], b) DPII steel and c) DPIII steel (ArcelorMittal source [ARC 2012]).

Table II.4 presents the DP steels mechanical properties used in this study. It shows the heterogeneity of this category of AHSS in terms of stress, microstructure, and formability. DP steels with the same volume fraction of martensite for instance DPI and DPII have different material behaviour only by changing the sheet thickness or the cooling process. Indeed, DP steels can be hot or cold rolled formed (HR or CR). If hot-rolled, cooling is carefully controlled to produce the Ferritic-Martensitic structure from austenite. If continuously annealed or hot-dipped, the final structure is produced from a dual phase Ferritic-Austenitic structure that is rapidly cooled to transform some of the austenite to martensite [ARC 2012]. Krebs et al. [KRE 2010] observations on DP steel accurately shows that the hot and cold rolling processing conditions generate 'banded structures' i.e., irregular, parallel and alternating bands of ferrite and martensite, which are detrimental to mechanical properties and especially for in-use properties. Already mentioned, it is known the volume fraction of martensite has an influence on the mechanical properties. Although, DPII and DPIII have the same cooling process and sheet thickness, they have different mechanical properties. The Yield stress and the ultimate tensile stress rise by increasing significantly the volume fraction of martensite (α') appearing in the structure as seen in Figure II.10.

Table II.4: Studied Dual Phase steels and their mechanical property requirement according to ArcelorMittal standard tensile test.

	Product	Thickness [mm]	YS [MPa]	UTS or Rm [MPa]	Ag (%)	A (%)	Phases (α: Ferrite, M: Martensite)
DPI	HR	2.5	380	610	16.5	25	α + M (11%)
DPII	CR	1.5	370	631	16	25	α + M (5%)
DPIII	CR	1.5	592	830	11	17	α + M (11%)

In addition to Figure II.10 and Table II.4, Figure II.11 shows the tensile stress-plastic strain curves of the three DP steels grades used in the study. One can easily understand the strong difference in term of tensile stress behavior in function of strain for various range of volume fraction of martensite. DPI and DPII have a good balance of strength, formability, energy absorption and durability while DPIII has a high strength and a weaker formability characteristic. Apart of this, the effect of the hard Martensitic islands is important but the role of the soft Ferrite in the final DP material is not negligible. Ferrite matrix is exceptionally ductile and absorbs strain around the Martensitic islands, enabling uniform elongation with high work hardening rate.

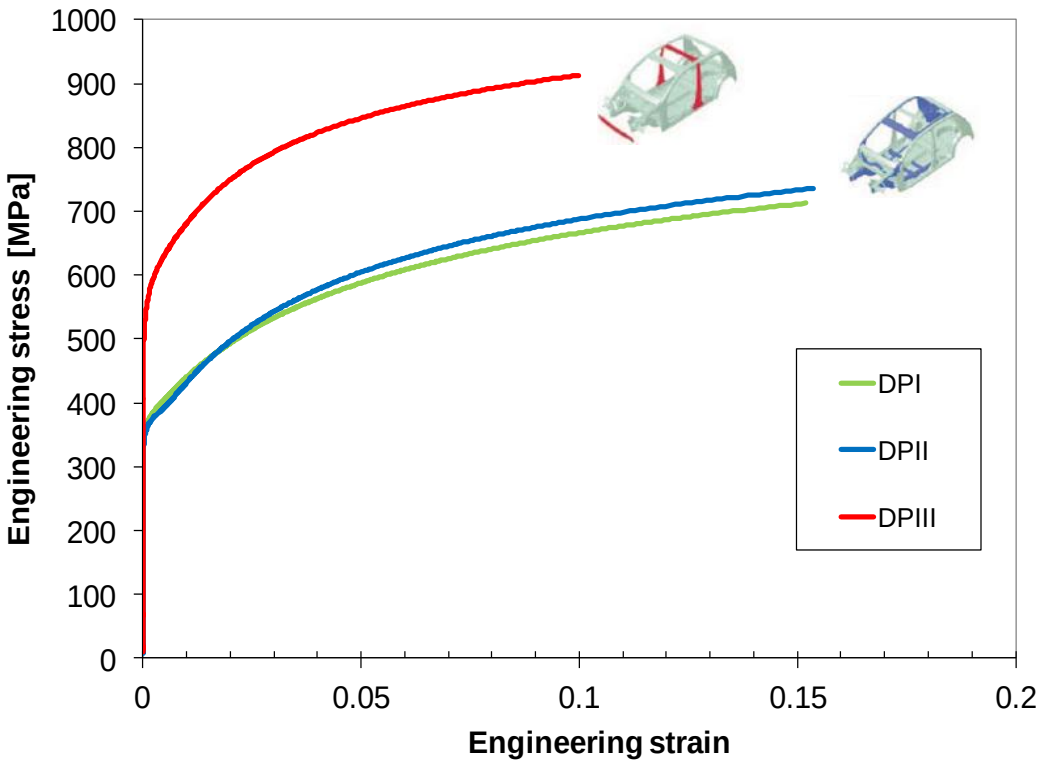

Figure II.11: Stress-strain curves for the 3 DP steel grades (ArcelorMittal data base).

The 3 studied DP steels are often used for deep drawing body-parts (DPII and DPIII), and safety-critical parts (maintaining a passenger survival space in crash event, DPIII) in automotive industry.

The current part explains the choice of the studied DP steels. At first, DPI has been retained in this numerical investigation for many raisons. First and foremost, the steel has been already used during the previous joint research gathering the X-ray tomography measurements launched by Bouaziz et al. [BOU 2008] and the numerical investigations of Ben Bettaieb et al. [BEN 2011]. In addition, the same steel composition has been employed again by Landron et al. [LAN 2011] for further X-ray tomography experiments. The present numerical study is a good opportunity to compare more easily the potentialities and limitations of Landron and Bouaziz void nucleation predictions. The second raison of choosing DPI steel is regarding the anisotropy sensitivity. Generally, the DP steel is less sensitive to the anisotropy effect than other AHSS, however it has been observed that the DPI steel flow during the deep-drawing process is also affected by the blank sheet anisotropy [PAD 2007]. According to the author, Anisotropy in blank sheets is usually the result of a large deformation during initial processing operations such a rolling, extrusion. This anisotropy prevalent in the pre-processed sheet segment influences subsequent deformation, such as deep-drawing. It dictates the shape of the yield surface and strongly affects the strain distributions obtained during sheet metal forming [MOR 2000]. The two other steels, especially DPII, have less anisotropy effect by using appropriate combination of rolling direction orientation to significantly improve the strength and the formability.

The DPII and DPIII steels have been selected because they are commonly selected as automotive applications (Crumple zone, Passenger compartment), to increase the crash

performance and protect the passenger by absorbing the low and high-speed vehicle deformation over a specific distance. Beyond the safety requirement, DPI and DPIII steels give the opportunity to compare the plasticity and the damage mechanisms provided by the hot and cold rolled forming process.

Chapter III. **State of the art**

Contents

III.1 Introduction

The previous chapter presented the DP steels as the coexistence of hard islands of Martensitic phase dispersed in a soft Ferritic matrix. This microstructure provides a good combination of strength and ductility. The mechanical behaviour until failure has been studied for more than four decades. Nowadays, the ductile failure mechanism is well known and divided in three steps before fracture: void nucleation, void growth, and void coalescence.
Chapter III describes the different proposals that the scientific community has developed to model the mechanical behavior of metals such as elasto-plastic damage constitutive laws as well as rupture criteria. Of course as often as possible, examples will be dedicated to DP steels.

Many researchers have contributed to give a proper microscopic approach. Habraken [HAB 2004] presents general features of crystal plasticity models and homogenization techniques to reach macroscopic scale while [KAD 2011], [VAJ 2012], [CHO 2013] are studying specifically DP models at microscopic or macroscopic scales. Very often macro scale is the world of phenomenological approaches which can however have roots within micro scale. The mechanical behaviour of DP steels can be modeled, based on elasto-plastic theory including both scales.

The phenomenological approach of elasto-plastic behaviour will be used within this thesis. It can mainly be defined by three different assumptions: a yield function, a hardening model and a plastic flow rule.
The first hypothesis is described by an initial yield surface defined in stress space. This function also called plastic yield criterion is a mathematical description of the initial yield surface. It can be isotropic (von Mises [MIS 1928], Tresca [TRE 1868]) or anisotropic (Hill48 [HIL 1948], Barlat [BAR 2004]).**The second hypothesis** known as hardening model describes the evolution of the shape, the size and the position of the yield surface during the deformation. It is mainly divided in two categories: isotropic and kinematic hardening. The isotropic hardening models the expansion of the yield surface with no shape distortion while the kinematic hardening also called anisotropic hardening computes the yield surface displacement in the stress space. Shape distortion is only seldom addressed with phenomenological models.
The third hypothesis called the flow rule defines the relation between the plastic strain rate tensor and the stress tensor. A plasticity model is called associative, if the yield function is considered as a plastic potential and its derivative provides the strain rate direction.

In the microscopic approach, not studied within this thesis, the global macroscopic stress and strain tensors are calculated relying on a numerical simulation of each particle or grain of the DP steels [KAD 2011], [VAJ 2012], [CHO 2013]. This approach physically describes the heterogeneity of plastic strain contained in the material. However, it requires a huge quantity of data storage and CPU time. Both approaches are complementary, the microscopic approach

allows understanding the mechanical plastic deformation and validating the phenomenological approach.

Section III.2 presents how the mechanical behaviour of DP steels can be predicted with the plasticity theory. Attention will be devoted to explain the isotropic and anisotropic yield functions as well as the hardening models. Section III.3 describes the coupled damage modeling concept where mechanical behavior is affected by the damage growth due to loading. The specific case of DP steels will be investigated. Within this section, both ductile damage mechanisms and some damage models are unveiled. Preceding the conclusion, the last section is dedicated to the fracture criteria or uncoupled damage approach applied on the DP steels.

III.2 Plasticity modeling

III.2.1 Yield functions

The Dual-Phase steel deforms elastically. During a monotonic loading it suddenly yields. In the plastic strain domain, the flow stress first increases due to hardening then eventually, it may soften due to damage. In numerous mechanical books [LEM 1988], [HOS 2005], [ROE 2006], the yield function defines the transition between elastic and plastic behaviour under complex stress states. According to Lemaitre and Chaboche [LEM 1988], the first scientific work on plasticity modeling began in 1868 with Tresca work on the maximum shear stress criterion [TRE 1868].
The goal of this section is to define the yield function with its associative normality rule. It briefly summarizes the most commonly isotropic and anisotropic yield functions that can be used to model the plastic behaviour of the DP steels.

III.2.1.1 Yield function and the associative normality rule

The yield surface or plastic yield criterion defined in the stress space as seen Figure III.1, models the elastic limit and the beginning of the plastic flow. It is written as:

$$F_p = \sigma_{eqv}\left(\underline{\underline{\sigma}}\right) - \sigma_y \quad , \quad F_p \leq 0 \tag{III.1}$$

Where $\sigma_{eqv}\left(\underline{\underline{\sigma}}\right)$ is the equivalent stress and σ_y is the material flow stress. On one hand, when $\sigma_{eqv}\left(\underline{\underline{\sigma}}\right)$ is smaller than σ_y $\left(F_p < 0\right)$, the deformation is purely elastic.
On the other hand when $\sigma_{eqv}\left(\underline{\underline{\sigma}}\right)$ is equal to σ_y $\left(F_p = 0\right)$, the border is reached and the DP steel starts to plastically deform.
At initial state and before hardening function takes place, the yield surface is written as following:

$$F_p = \sigma_{eqv}\left(\underline{\sigma}\right) - \sigma_0 = 0 \tag{III.2}$$

σ_0 is a scalar called the initial elastic limit of the material in uniaxial tensile. A general expression given by Hooke allows computing the stress tensor in elastic state:

$$\underline{\sigma} = \underline{\underline{C}}^e : \underline{\varepsilon}^e \tag{III.3}$$

Where $\underline{\sigma}$ is the macroscopic Cauchy stress tensor and $\underline{\underline{C}}^e$ is the elastic stiffness tensor (chosen isotropic and linear).

In metal forming, the elastic strain tensor contribution $\underline{\varepsilon}^e$ is a very small part compared to the total macroscopic strain tensor $\underline{\varepsilon}$. Equation ((III.4) indicates additive the decomposition of the total strain, used in non linear FE code in its strain rate form:

$$\underline{\varepsilon} = \underline{\varepsilon}^e + \underline{\varepsilon}^p \quad \text{and} \quad \dot{\underline{\varepsilon}} = \dot{\underline{\varepsilon}}^e + \dot{\underline{\varepsilon}}^p \tag{III.4}$$

Where $\underline{\varepsilon}^p$ describes the plastic strain tensor contribution.

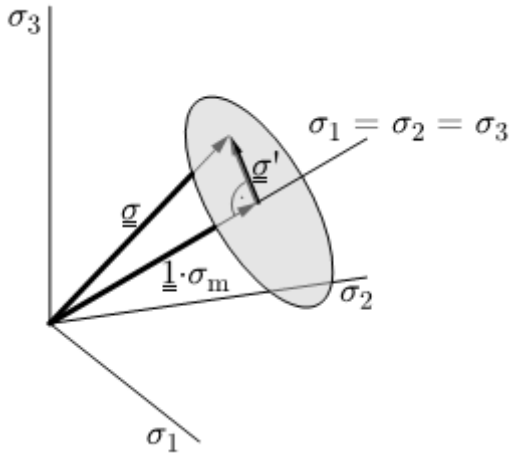

Figure III.1: Yield surface in principal deviatoric stress space [ROE 2006].

The second hypothesis of the phenomenological approach describes the normality rule which is the relation between the plastic strain rate tensor and the stress tensor. The approach is named the associated plasticity models, if the yield function is considered as plastic potential. Non associative plasticity models are characterized by other rule than Equation (III.5). It is the mostly used in the literature, and it illustrates the associative plastic flow law used within our work.

$$\dot{\underline{\varepsilon}}^p = \dot{\lambda} \frac{\partial F_p}{\partial \underline{\sigma}} \quad \begin{cases} \dot{\lambda} = 0 & \text{if} \quad F_p < 0 \\ \dot{\lambda} \geq 0 & \text{if} \quad F_p = 0 \end{cases} \tag{III.5}$$

Where $\dot{\lambda}$ is the plastic multiplier.

Figure III.2 shows that there are dozens of yield functions or plastic criteria usable for DP steels in metal forming processes, generally split in two families: the isotropic (von Mises, Tresca…) and the anisotropic (Hill, Barlat…) yield functions.

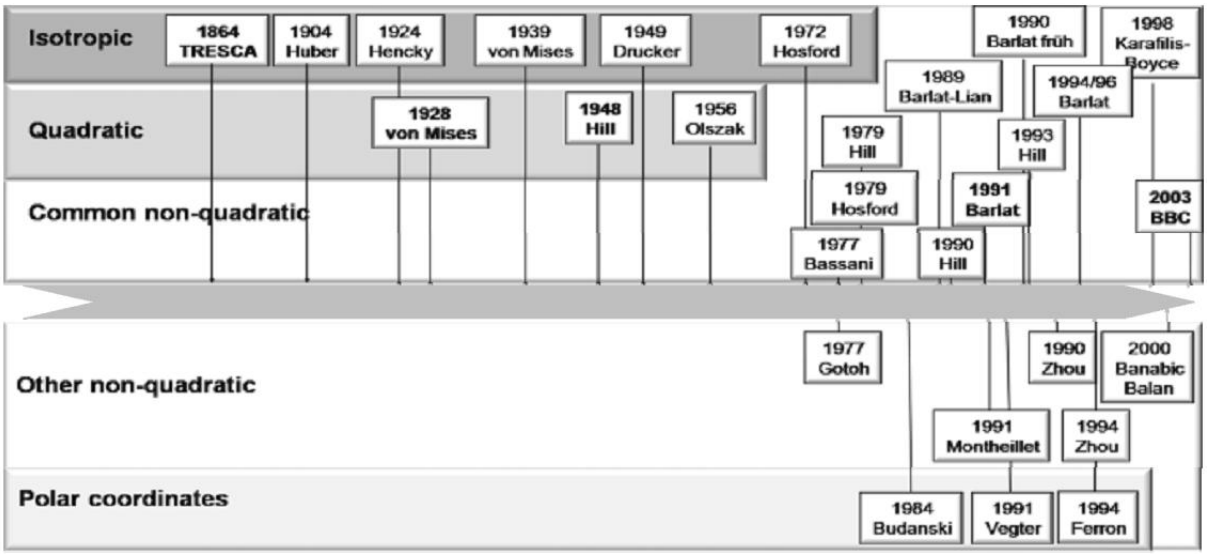

Figure III.2: Historical overview of different yield criteria [LIE 2009].

III.2.1.2 Isotropic yield functions

The isotropic yield functions must not depend on the orientation of the load. The yield function F_p is based on the deviatoric stress tensor invariants. Figure III.2 shows an overview of the most used isotropic yield criteria.

The von Mises yield criterion

The von Mises criterion [MIS 1928], known as the maximum distortion energy criterion, octahedral shear stress theory, or Maxwell-Huber-Hencky-von Mises theory, states that the plasticity is isotropic. The equation for the von Mises yield function is:

$$F_p = \sigma_{eqv}\left(\underline{\sigma}\right) - \sigma_y = \sqrt{\frac{3}{2}\left(\underline{\sigma}' : \underline{\sigma}'\right)} - \sigma_y \qquad \text{(III.6)}$$

Where $\underline{\sigma}'$ is the deviatoric stress tensor: $\underline{\sigma}' = \underline{\sigma} - \frac{1}{3} tr\left(\underline{\sigma}\right)\underline{I}$ with I second order unit tensor.

Consequently, the corresponding equivalent plastic strain rate $\dot{\varepsilon}^p_{eqv}$ can be given by the explicit expression:

$$\dot{\varepsilon}^{p}_{eqv} = \sqrt{\frac{2}{3}\left(\underline{\dot{\varepsilon}}^{p} : \underline{\dot{\varepsilon}}^{p}\right)} \tag{III.7}$$

If one couples the normality law (Equation (III.5)) and the von Mises yield function (Equation (III.6)), one can check that the plastic strain rate is a tensor normal to the yield surface in the space of stress, which is also coaxial to the Cauchy stress tensor $\underline{\sigma}$ (see Figure III.3), $\underline{n} = \underline{\dot{\varepsilon}}^{p} \Big/ \left\| \underline{\dot{\varepsilon}}^{p} \right\|$.

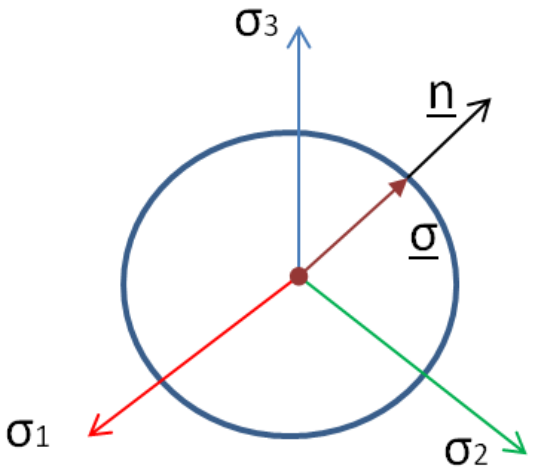

Figure III.3: Representation of associative normality law with the von Mises criterion.

The most important benefit of the von Mises law is its simplicity. Since the direction of the plastic rate is coaxial to the Cauchy stress, numerical resolution can be reduced to only one nonlinear equation (with unknown $\dot{\varepsilon}^{p}_{eqv}$). In the anisotropic case, a system of six scalar equations will have to be solved as this coaxiality property is not anymore applicable.

The number of material parameters to be included in the model is quite restrained (E Young's modulus, ν Poisson coefficient, and parameters for the isotropic hardening law). A simple uniaxial tensile test or a shear test is sufficient to identify all the parameters.

Although the von Mises criterion is very valuable for isotropic plasticity, it has notable limitations. Since the plastic anisotropy is not taken into account, the isotropic criteria have been extended by many authors, the Hill'48 [HIL 1948] criterion being the most famous one (Figure III.2).

III.2.1.3 Anisotropic yield functions

Isotropic yield functions previously described are not able to accurately predict alone the mechanical DP steels behaviour in function of the rolling direction orientation, therefore the next section presents the most commonly used anisotropic yield functions.

The HILL'48 quadratic yield criterion

Hill's criterion is the first and simplest one able to take into account the plastic anisotropy. Steel manufacturers clearly know that no matter how the quality of steel sheet is, anisotropy appears along the forming processes (deep drawing, rolling, drawing folding, bending etc...). It means that there is a strong relation between the forming direction and the plastic deformation.

The plasticity in Hill's criterion is anisotropic and incompressible. The von Mises yield function is modified so that the anisotropic phenomenon can be embodied (Equation (III.8)) while remaining simple:

$$F_p = \bar{\sigma}(\sigma) - \sigma_y = \sqrt{\frac{1}{2}\left(\underline{\sigma}' : \underline{\underline{H}} : \underline{\sigma}'\right)} - \sigma_y \tag{III.8}$$

Where $\underline{\underline{H}}$ is the fourth order Hill matrix (or anisotropic material tensor depending on the material) defined for instance as a function of Lankford coefficients r_0, r_{45}, r_{90}. These scalars are a ratio between the width and the thickness strains corresponding to the rolling direction 0°, 45° and 90°.

$$\underline{\underline{H}} = \begin{bmatrix} G+K & -K & -G & 0 & 0 & 0 \\ -K & K+F & -F & 0 & 0 & 0 \\ -G & -F & F+G & 0 & 0 & 0 \\ 0 & 0 & 0 & 2N & 0 & 0 \\ 0 & 0 & 0 & 0 & 2L & 0 \\ 0 & 0 & 0 & 0 & 0 & 2M \end{bmatrix} \tag{III.9}$$

$$F = \frac{2r_0}{r_{90}(1+r_0)}; G = \frac{2}{(1+r_0)}; K = \frac{2r_0}{(1+r_0)}; L = M = N = (F+G)(r_{45}+0.5) \tag{III.10}$$

For simple approaches, one chooses constant (average value) of Lankford coefficients and keeps a constant shape to the Hill criterion, however more complex versions could take into account true experimental observation with variable Lankford coefficients. Constant values are used during this study.
Figure III.4 clearly underlines the difference between the von Mises and Hill criterion at plane strain tension for DPIII steel anisotropic plastic material. It is also to notice that conventionally, the Hill and von Mises criteria coincide at uniaxial tension.

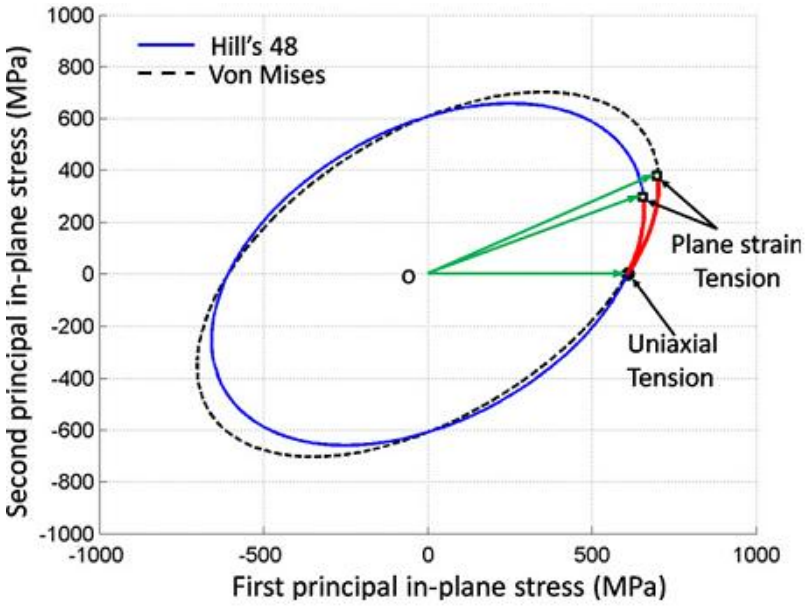

Figure III.4: Hill'48 vs. von Mises criterion for DPIII steel [LUO 2010].

Contrary to von Mises criterion the normal $\underline{n}_{Hill}$ is not any more coaxial (Figure III.5) with the Cauchy stress tensor $\underline{\sigma}$.

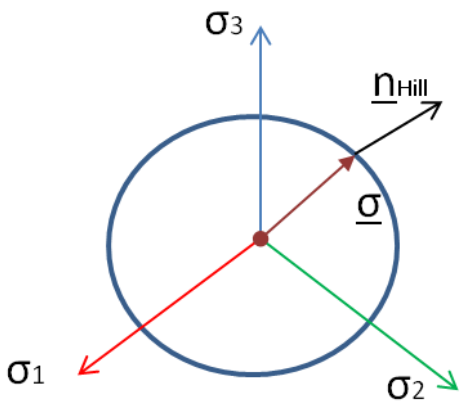

Figure III.5: Representation of associative normality law in Hill criterion.

The Hill criterion is suitable for anisotropic plastic material. It is simple to use and implement in numerous finite element codes.

Other anisotropic yield criteria

Figure III.2 shows numerous extensions of Hill anisotropic yield criterion such as Hill'79 [HIL 1979], along with non-quadratic criteria developed by Hosford [HOS 1979], Barlat et al. [BAR 1979], Hu [HU 2007]. Many other researchers proposed more accurate anisotropy predictions such as [KAR 1993], [DAR 2003], [BRO 2004], [BAN 2005], [CAZ 2006]. In those publications, the anisotropic yield function is introduced by means of a linear stress

transformation. These approaches show a simple development of convex formulations leading to stable numerical simulations.
Figure III.6 displays some anisotropic shapes of yield criteria such as Hill, Barlat compared to the von Mises isotropic yield criterion.

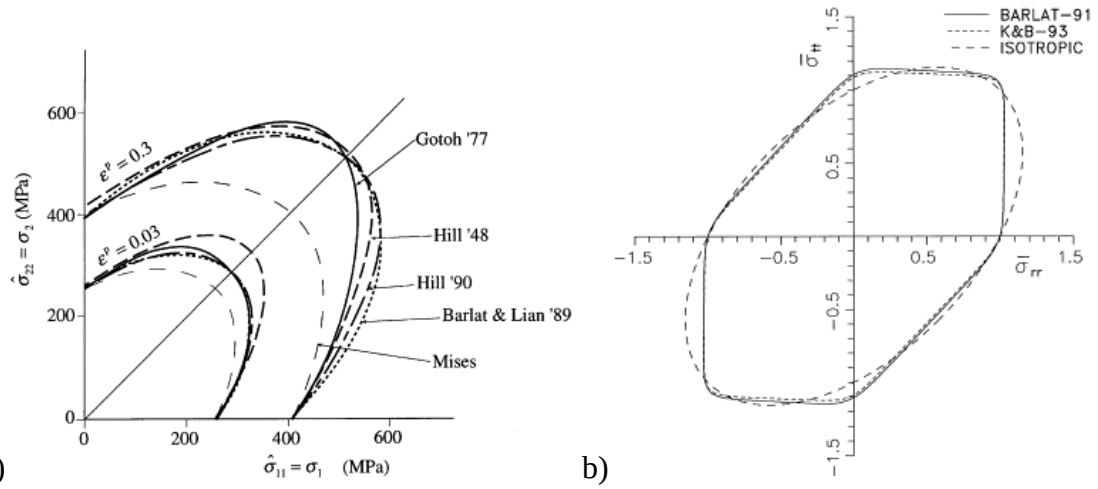

a) b)

Figure III.6: a) Comparison of shapes of yield surfaces at small and large strain levels [KUR 2000], b) Comparison of two anisotropic yield surfaces and isotropic von Mises yield surfaces, each normalized with respect to its own equivalent stress for steel [TUG 2001].

III.2.2 Hardening functions

Isotropic hardening functions

Although most DP steels present a strong Bauschinger effect, isotropic hardening functions are used because of their simplicity and good prediction in radial loading [KIM 2006] [TAS 2009-2010] [SCH 2010] [SOD 2012]. In isotropic hardening, the yield surface expands symmetrically, monotonously and proportionally with respect to the initial yield surface. It is governed by a single scalar state variable: for instance, the cumulated plastic strain. The yield criterion is written as following:

$$F_p\left(\underline{\sigma}, \sigma_y\left(\varepsilon_{eqv}^p\right)\right) = 0\,. \tag{III.11}$$

with the initial condition

$$\sigma_y\left(\varepsilon_{eqv}^p = 0\right) = R_p = \sigma_0 \tag{III.12}$$

Figure III.7 sketches the evolution of the yield surface in the stress space and in tensile - compression for the isotropic hardening modeling.

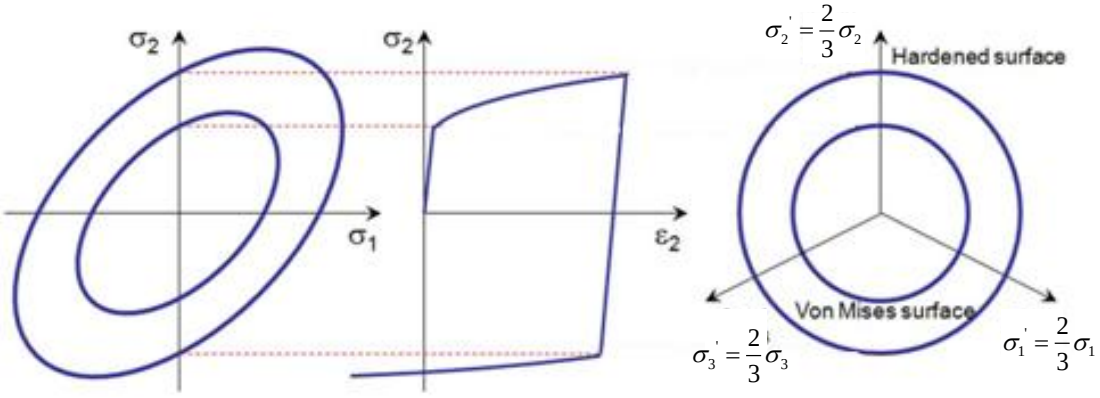

Figure III.7: Isotropic hardening model showing the expansion of the yield surface with plastic strain and resulting stress–strain curve in tension-compression.

Figure III.8: gives a historical overview of the most popular isotropic hardening laws. The oldest contribution was published by Ludwig [LUD 1909] in 1909 and was modified by Hollomon [HOL 1945] in 1945. Other developments were established by Voce [VOC 1948], Swift [SWI 1952] and Hockett and Sherby [HOC 1975].

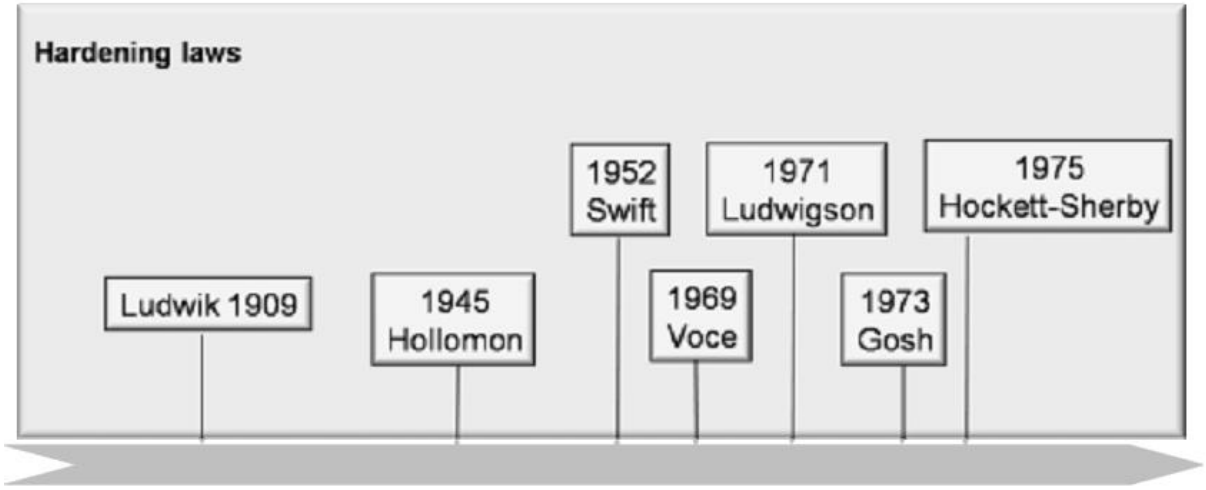

Figure III.8 :Historical overview of different isotropic hardening criterions [LIE 2009].

The most commonly used isotropic work hardening constitutive equations are briefly presented to describe the elasto-plastic behavior of DP steels. These equations are defined in one-dimension and usually applied for a large number of materials.

Ludwig law

The Ludwig isotropic hardening model is defined by:

$$\sigma = \sigma_y + K\left(\varepsilon_{eqv}^{p}\right)^{m} \tag{III.13}$$

where *K* and m are material parameters.

Hollomon law

The Hollomon isotropic hardening model defined by:

$$\sigma = K\left(\varepsilon_{eqv}^{p}\right)^{n}. \tag{III.14}$$

This relationship gives, in the case of a monotonic uniaxial loading, the material flow stress. The main parameter is the work hardening exponent n.

Swift law

The Swift isotropic hardening model defined by:

$$\sigma_y = K\left(\varepsilon_0 + \varepsilon\right)^{n} \tag{III.15}$$

where K, n, ε_0 are material parameters ε strain.

Voce law

The Voce isotropic hardening model expressed by:

$$\sigma = \sigma_0 + \sigma_{sat}(1 - e^{-b\varepsilon_{eqv}^{p}}) \tag{III.16}$$

where σ_0, b, σ_{sat} are material constant parameters.

Figure III.9 shows the comparison of classical isotropic hardening equations identified on uniaxial tensile test for a DPI-1.4-mm flat sheet steel. It can be noted that at low strain these isotropic hardening models are similar. Unfortunately, they begin to diverge with the experiment data (bulge tests) at 0.15 of strain. The limit of these simple mathematical equations is underlined at large strains. The fitting becomes more difficult and needs improvement.

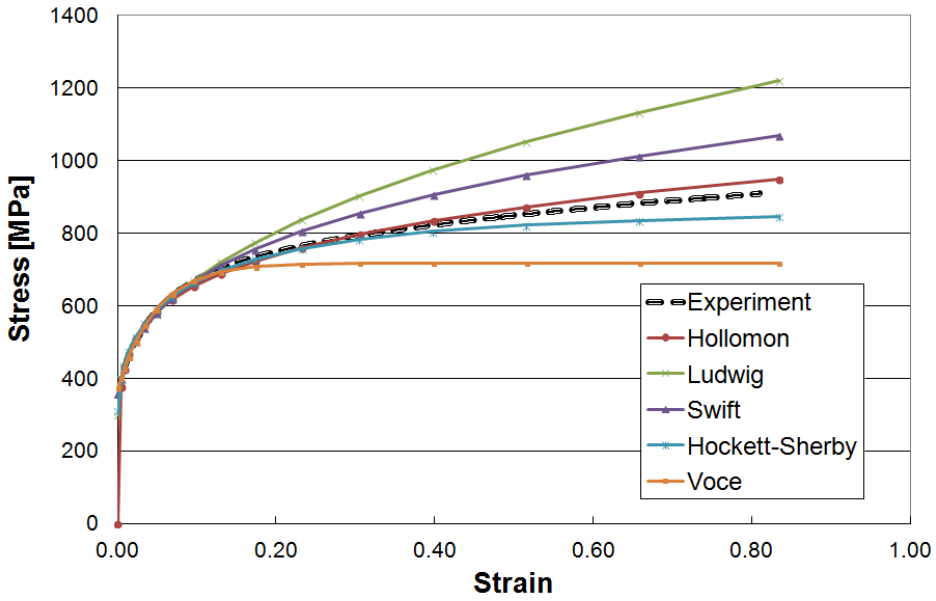

Figure III.9: Stress-strain curves of experimental uniaxial tensile test and its analytical isotropic hardening models for DPI steel (ArcelorMittal data base).

The stress gap calculated between the experiment and the isotropic hardening laws at large strain are often minimized by combining them (e.g., Voce and Swift).

Kinematic hardening models

During sheet-forming process of DP steels, non-proportional strain paths frequently occur, even during single step processes (e.g., bending-unbending over a die radius). In such circumstances, complex stress-strain behavior is observed that cannot be described by isotropic hardening models (see Figure III.10).

Many authors such as Prager [PRA ,1956,1958], Ziegler [ZIE 1959], and Chaboche et al. [LEM 1988] have contributed to the modeling of this complex transient behaviour including Bauschinger effect, permanent softening, and work-hardening stagnation. These phenomena are illustrated in Figure III.10a by a generalized tensile-compression curve and in Figure III.10b by a specific example for DP590-1.4mm flat sheet steel.

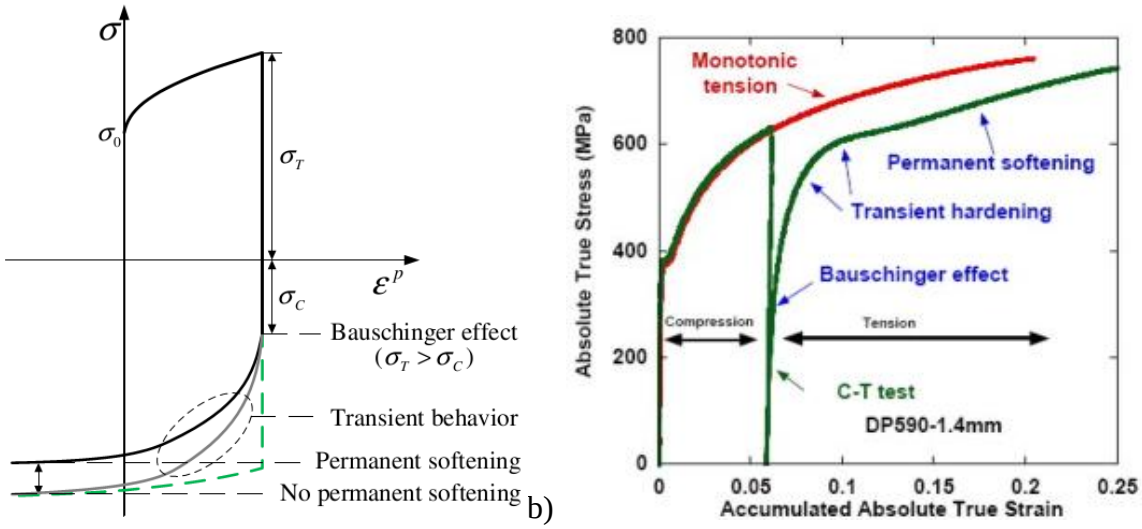

Figure III.10: a) Generalized schematic view of Bauschinger, transient and permanent softening behaviors during reverse loading [CHU 2012], b) Monotonic and reverse compression-tension (C-T) test experimental curves that illustrate the three characteristic regions of reverse hardening for a 1.4mm flat sheet DP590 steel [SUN 2013].

The Bauschinger effect is a premature re-yielding of the material during reverse loading. The transient hardening is a smooth, elastic-plastic transition with very rapid change of the work-hardening rate. The permanent softening is known as stress offset. Since the isotropic hardening with its assumptions is not able to take into consideration these effects, kinematic hardening laws have been introduced especially for unloading and cyclic loading.
There are two approaches. The first one based on the shifting of one single yield surface has been proposed by Prager and Ziegler to describe the Bauschinger effect. Armstrong-Frederick [ARM 1966] and Chaboche [CHA 1986] included another term to Prager's kinematic hardening model in order to take into account the transient behavior. The second approach is characterized by implementing multiple yield surfaces [MRO 1967].

Classical kinematic work hardening equations were used to describe the behavior of a DP steels by [TAH 2009] [MOR 2010] [KAD 2011] [VLA 2010] [MUR 2011] [CHU 2012] [VAJ 2012] [SUN 2013].

Kinematic hardening with von Mises yield surface

The kinematic hardening is associated to the usual yield surfaces it preserves their shape and size, but translates in the stress space (Figure III.11). The von Mises yield function including a kinematic hardening model can be expressed by:

$$F_p\left(\underline{\sigma},\underline{X},\sigma_y\right)=\sigma_{eqv}-\sigma_y=\sqrt{\frac{3}{2}\left[\left(\underline{\sigma}'-\underline{X}\right):\left(\underline{\sigma}'-\underline{X}\right)\right]}-\sigma_y \qquad \text{(III.17)}$$

where $\underline{X}$ is the back-stress tensor defining the shift of the center of the elastic domain. it is a tensorial hardening variable.

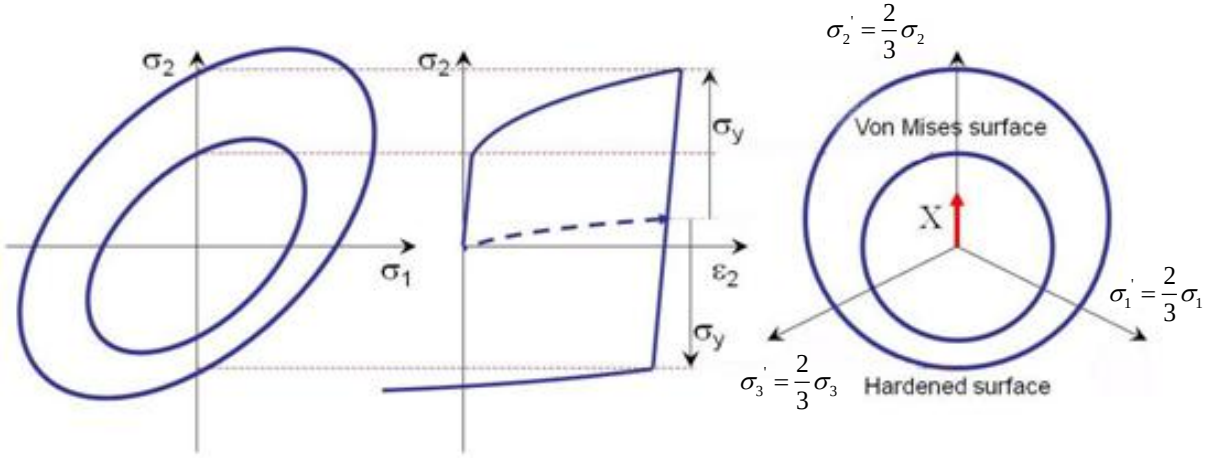

Figure III.11 : Kinematic hardening and von Mises surface representation.

Prager law

Prager proposed a kinematic hardening law governing the evolution of the back-stress tensor

$$\dot{\underline{X}} = \overline{H_k}\,\dot{\underline{\varepsilon}}^p \tag{III.18}$$

where the rate of the back-stress is proportional to the plastic strain rate. The proportionality factor $\overline{H_k}$ is directly related to the plastic modulus.

Armstrong-Frederick law

Armstrong-Frederick (1966) is a nonlinear kinematic hardening law. It improves the Prager's kinematic law by adding a term proportional to the current back-stress multiplied by the equivalent plastic strain rate. The evolution of the back-stress is expressed by

$$\dot{\underline{X}} = C_x\left(S_{sat}\,\dot{\underline{\varepsilon}}^p - \underline{X}\left(\sqrt{\frac{2}{3}\left(\dot{\underline{\varepsilon}}^p : \dot{\underline{\varepsilon}}^p\right)}\right)\right) \tag{III.19}$$

where C_x, S_{sat} are constant material parameters.

Mixed hardening functions

Recent developments relative to the elasto-plastic modeling of a DP steel show that rather than using purely isotropic or purely kinematic hardening laws, it is generally better to combine both (see Figure III.12c). It allows the yield surface to either expand or contract and simultaneously translate.

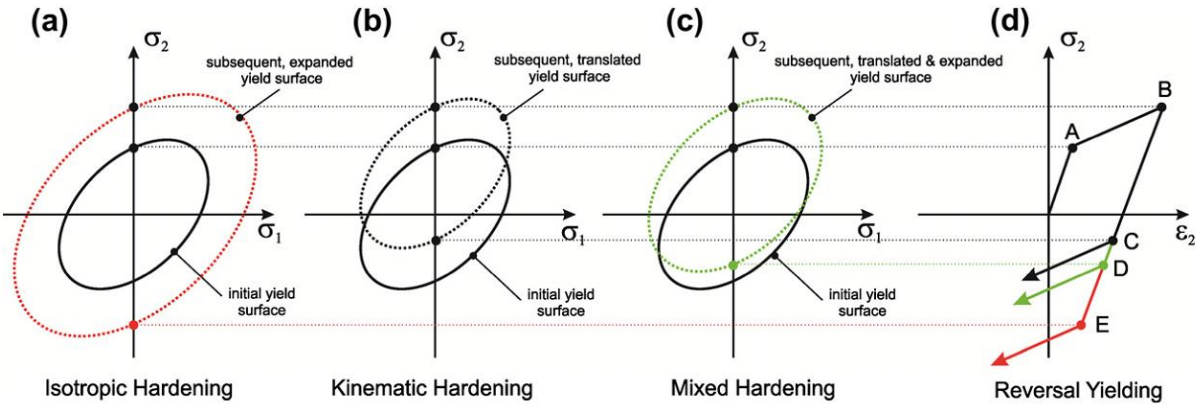

Figure III.12 : a) Isotropic hardening model showing the expansion of the yield surface with plastic strain; b) kinematic hardening model showing the translation of the yield surface with plastic strain; c) mixed isotropic–kinematic hardening model showing the expansion and translation of the yield surface with plastic strain; and d) resulting stress–strain curves showing different yield stress in compression as predicted by different plasticity models; C) kinematic hardening, D) mixed hardening, and E) isotropic hardening [MUR 2011].

III.3 Damage modeling

The previous section shows the possibility to model the DP steel behaviour with elasto-plastic models before the occurrence of large strains and fracture. In the real life, large plastic are desired in automotive applications and most of the time DP material is damaged during or after the forming process, and fracture may occur. The fracture mechanism can broadly be classified as brittle and ductile (Figure III.13). The brittle fracture appears with little or no plastic deformation which is undesirable by manufacturers. The maximum fracture strain in this mechanism is often under 5%. In opposite, the ductile fracture or ductile damage mechanism most frequently observed in metal forming occurs under large plastic strain, which is our interest.

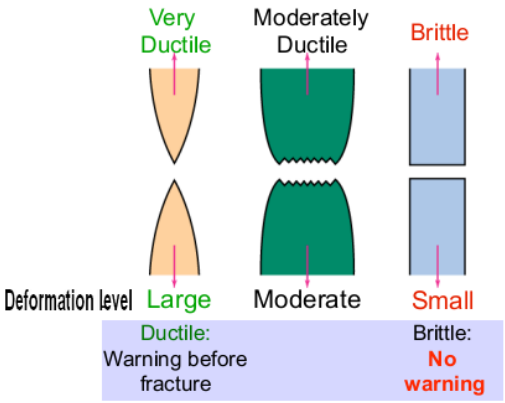

Figure III.13: Ductile and brittle failure behavior.

III.3.1 Ductile damage mechanism

Since more than three decades it is well known that damage in ductile materials is due to the presence of voids at microscopic-scale. Numerous researchers observed with the microscopy help [RIC 1969], or more recently with X-ray tomography [WEC 2007] [BOU 2008], [MAI 2008], [LAN 2010, 2011], that this damage process is divided in three specific mechanisms: nucleation, growth and coalescence of voids. Figure III.14 illustrates these stages along a tensile test of a notched plate specimen.

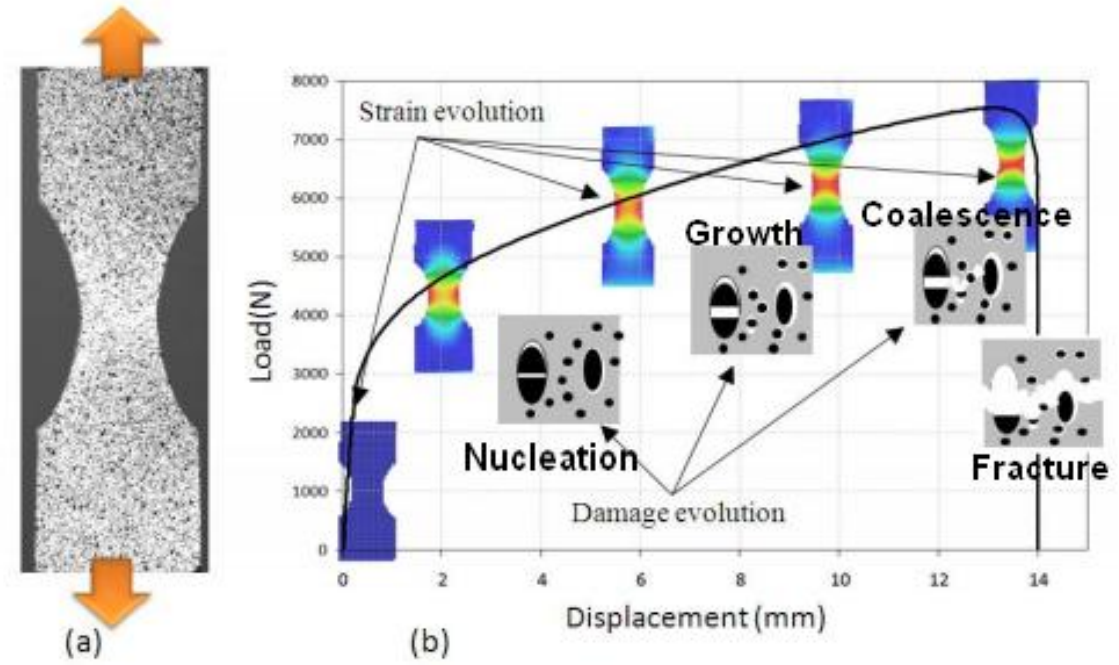

Figure III.14: a) Tensile test of notched plate specimen, b) evolution of the damage process in a ductile metal related to the macroscopic loading evolution [ABB 2010].

Ductile damage starts with micro-cavity nucleation often localized at weak material points such as grain boundaries, interface between inclusion and matrix or at brittle inclusion. Then, the voids growth and coalesce to create local cracks which propagate more or less rapidly in the specimen. More specifically, Avramovic et al. [AVR 2009] observations on DPI steel fracture revealed that voids nucleation occurs by martensite cracking, separation of adjacent martensite regions, or by decohesion at the ferrite/martensite interface. The study also added that, martensite morphology and distribution had a significant influence in the accumulation of damage. The DP steel with a more uniform distribution of martensite showed a slower rate of damage growth and a continuous void nucleation during the deformation process, which resulted in a higher void density before fracture (Figure III.15).

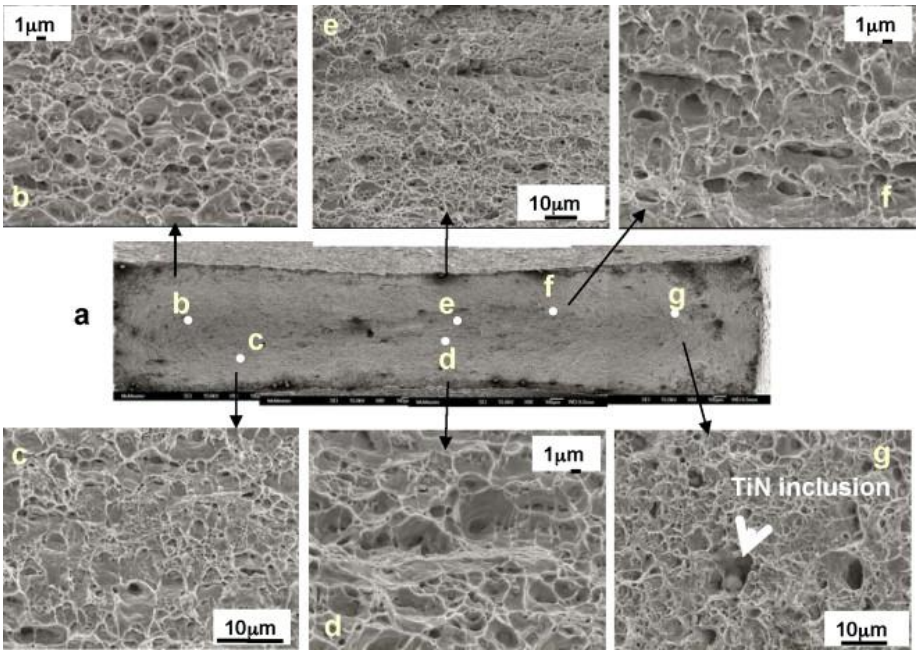

Figure III.15: SEM fractography of the DPI steel: SEM fractography of the DPI fracture surface: (a–f) ductile dimples; (e and d) different dimple size in ridges and valleys; (g) inclusions present within the dimples [AVR 2009].

The following sub-sections describe the three mechanisms defining the ductile damage. The current literature review is mainly based on Weck [WEC 2007] and Landron [LAN 2011] works picturing accurately the stand of the ductile damage mechanism research and its experimental evidences (distribution of microscopic voids, cavities or microcracks).

III.3.1.1 Void Nucleation

General characterization

The experimental evidences observed by X-ray tomography and completed by optical microscopy able to differentiate ferrite and martensite revealed that void nucleation stage can be homogeneous or heterogeneous. Homogeneous nucleation appears within grains without any relation with inclusions or a second phase in the microstructure. On the other hand, heterogeneous nucleation occurs due to heterogeneous strain close to inclusions, grain boundaries or precipitates [GOO 1979]. Most observations conclude that heterogeneous nucleation is the most encountered mode of nucleation. In this case, voids appear either by fracture of the second phase inclusion, or by decohesion at the interface or by cavitation in the matrix next to the particle. Figure III.16 illustrated the most frequent nucleation mechanisms: interface decohesion and inclusion fracture. More recently, Achouri et al. [ACH 2012] has highlighted the evolution of a cavity around a $MgO\text{-}Al_2O_3$ particle during an insitu tensile and shear tests of a HSLA sample (see Appendix (A.8).

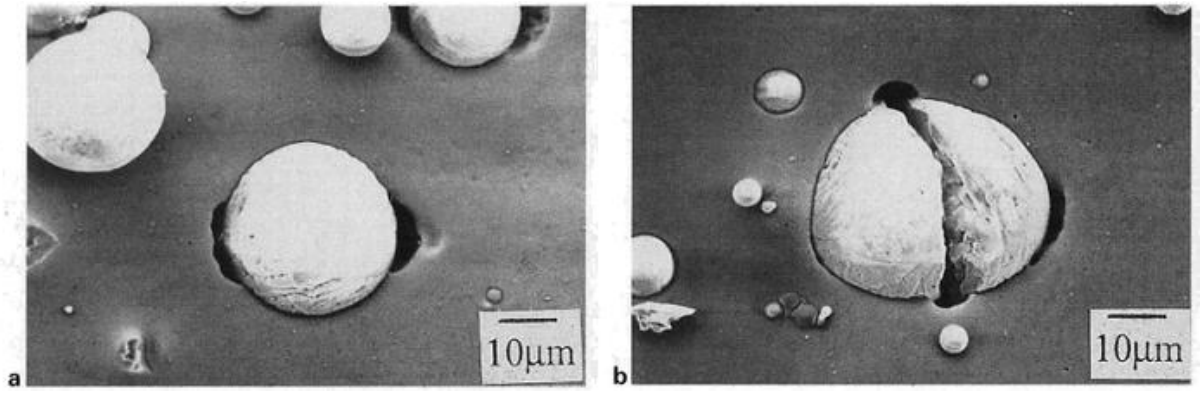

Figure III.16: Damage in an aluminum 6061 matrix reinforced with Al_2O_3 particles (a) decohesion; (b) particle fracture [KAN 1995].

Characterizations on studied DP steels

Recent works on DP steels by Maire et al. [MAI 2008], Avramovic et al. [AVR 2009], Landron et al. [LAN 2011] showed that the mechanisms of void nucleation can be observed by using optical micrographs of fractured specimens (see Figure III.17a) and quantified with in situ X-ray tomography (see Figure III.17b). The main conclusions of these contributions unveiled that the DP steels microstructure accelerates drastically the number of void nucleated compared to a single-phase steel. The mechanisms depend on the steel microstructure: if the interface strength is weak, voids occur at the martensite-ferrite interface, otherwise they appear in the martensite. According to Landron, in the DPI sample (Figure III.18a), where the Ferritic matrix is soft and the inclusions of Martensite are hard, voids mainly appear by decohesion of the interface ferrite/martensite. In the DP steel with 62% of Martensite (Figure III.18b), where the martensite is softer, cavities appear inside the martensitic phase.

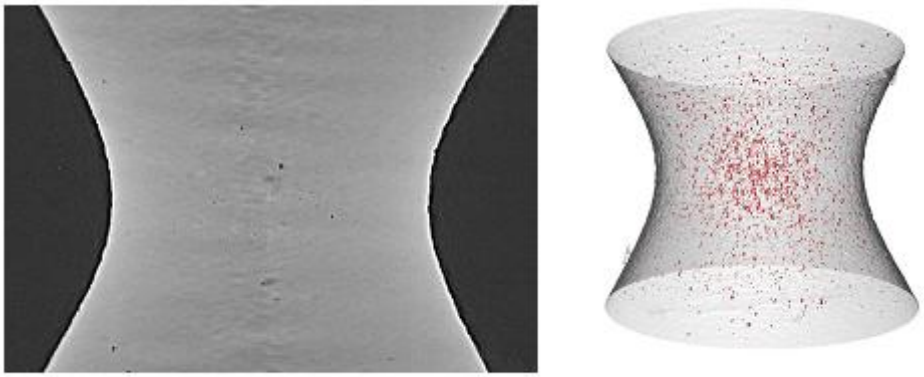

Figure III.17:Views of the same DPI steel specimen coming from the acquired tomogram: (a) 2D view of a section inside the volume, (b) 3D in situ X-ray tomography view of the entire volume [LAN 2011].

a) 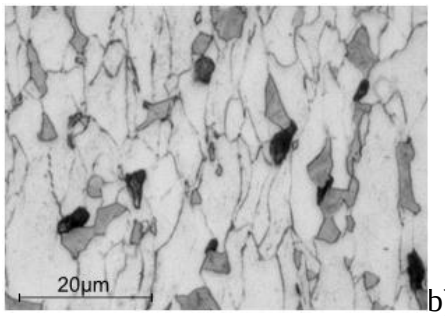

b) 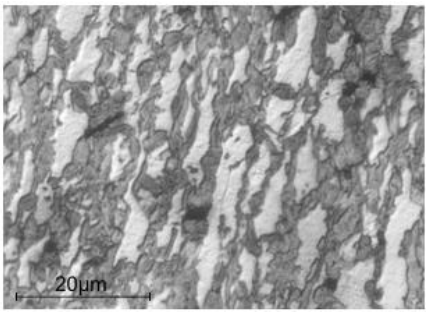

Figure III.18: Optical micrograph of a fractured sample: a) DPI steel, b) DP steel with 62% of Martensite. White is ferrite, gray martensite, black cavities.

General modeling

This part presents few void nucleation models. Literature review [ARG 1975] [BER 1981] [NEE 1987] on these modeling approaches involves models based on critical stress, strain or energy level thresholds. The energy criterion defines for instance the required energy to generate new surfaces inside the inclusion or at the inclusion-matrix interface.

Argon criterion

Argon [ARG 1975] model is an analytical model involving a critical stress condition for void nucleation by interface decohesion. It includes the contribution of the mean normal stress $\sigma_m = \frac{1}{3} tr(\underline{\sigma})$ and the equivalent stress $\sigma_{eqv}(\underline{\sigma})$ inside the material:

$$\sigma_{eqv}(\underline{\sigma}) + \sigma_m = \sigma_C \tag{III.20}$$

where σ_C is the critical stress allowed at the interface inclusion/matrix without fracture.

Beremin criterion

Beremin et al. [BER 1981] proposed a model based on Eshelby theory [ESH 1957]. In this criterion, the void nucleation occurs when the stress inside the particle reaches the critical stress σ_C for the interface decohesion or the particle fracture. The criterion is expressed as following:

$$\sigma_I^{\max} + k_s\left(\sigma_{eqv}(\underline{\sigma}) - \sigma_{eqv}(\underline{\sigma})_{matrix}\right) = \sigma_C \tag{III.21}$$

Where $\sigma_I^{\max}$ is the maximal principal stress, $\sigma_{eqv}(\underline{\sigma})_{matrix}$ is the equivalent stress inside the matrix, and k_s a stress concentration factor depending on the particle shape.

Needleman and Tvergaard criterion

Needleman and Tvergaard [NEE 1987] introduced a strain criterion to model the void nucleation evolution. It is based on the assumption that voids appear when the critical plastic strain ε_N is reached inside the material.

$$A_N = \frac{f_N}{s_N\sqrt{2\pi}} \exp\left[-0.5*\left(\frac{\bar{\varepsilon}^p_{eqv} - \varepsilon_N}{s_N}\right)^2\right] \quad \text{(III.22)}$$

Where

A_N : Number of voids nucleated.

f_N : Potential nucleated void fraction in relation, for instance, with the inclusion volume fraction.

ε_N : Equivalent means plastic strain of the matrix at incipient nucleation.

S_N : Gaussian standard deviation of the normal distribution of inclusions.

$\bar{\varepsilon}^p_{eq}$: Equivalent plastic strain in the matrix.

Modeling on studied DP steels

Bouaziz and Maire criterion

The improvement of microstructure observation method enhanced the void nucleation law from the initial Needleman and Tvergaard model. Recently, Helbert et al. [HEL 1998], Bouaziz et al. [BOU 2008] and Maire et al. [MAI 2008] with help of X-ray tomography method accurately modeled the voids nucleation stage for DP steels. In this approach, the numerical void density N (number of voids per unit volume) is related to the triaxiality *T* and to the macroscopic equivalent plastic strain ε^p_{eqv} by the following relationship:

$$N = A\left(\frac{\varepsilon^p_{eqv}}{\varepsilon_N}\right)\exp\left(\frac{\varepsilon^p_{eqv}}{\varepsilon_N}\right); \quad \varepsilon_N = \varepsilon_{N0}\exp(-T) \quad \text{(III.23)}$$

Where A is a material constant and ε_N is the critical strain value for which nucleation is supposed to start. The parameter ε_{N0} designates the value of this critical strain for pure shear loading.

Landron et al criterion

Recently, further X-ray tomography measurements have been carried out and investigated by Landron et al [LAN 2011] on in-situ tensile notched axisymmetric specimens of DP steels. The experiments revealed a strong dependency between the density of voids, the backstress,

and the triaxiality for these grades. The law proposed by Landron [LAN 2011] defines the rate of the numerical void density *N* by:

$$\frac{dN}{d\varepsilon_{eqv}^{p}} = \frac{B\ \sigma_{eqv}}{\sigma_c}\left(1+T\frac{\sigma_{eqv}}{\sigma_{eqv}-X}\right)\frac{N}{N_0} \qquad \text{(III.24)}$$

Where B and N_0 are material constants and σ_c is the critical shear stress value that the Martensite/Ferrite interface can support without breaking (see Equation (III.20)). The quantities $\sigma_{eqv}(\underline{\sigma})$ and X represent the equivalent macroscopic stress and backstress scalar, in the context of the uniaxial tensile loading that served to derive the law.

III.3.1.2 Void growth

General characterizations

After the nucleation stage, voids grow by plastic deformation and the second stage of the ductile damage process happens. This phenomenon can be easily observed compared to the previous stage. A simple low resolution optical micrograph (Figure III.19a) is necessary to localize growing voids at the surface of a specimen during the insitu tensile test. Recently Weck et al. [WEC 2007] gave more details on voids observations (quantitative and morphology) with X-ray tomography (Figure III.19b). The characterizations of this stage revealed some parameters influencing the void growth. The triaxiality induces a significant increase of the void growth. In a lower impact, the void density can introduce some differences regarding the growth kinetic. Researchers affect this difference to the interactions between cavities leading to an acceleration of the void growth. Others scientists like Pardoen [PAR 1998] demonstrated that the isotropic strain hardening decreases the void growth rate. In opposite Besson [BES 2005] concluded that the kinematic hardening increases the cavity growth.

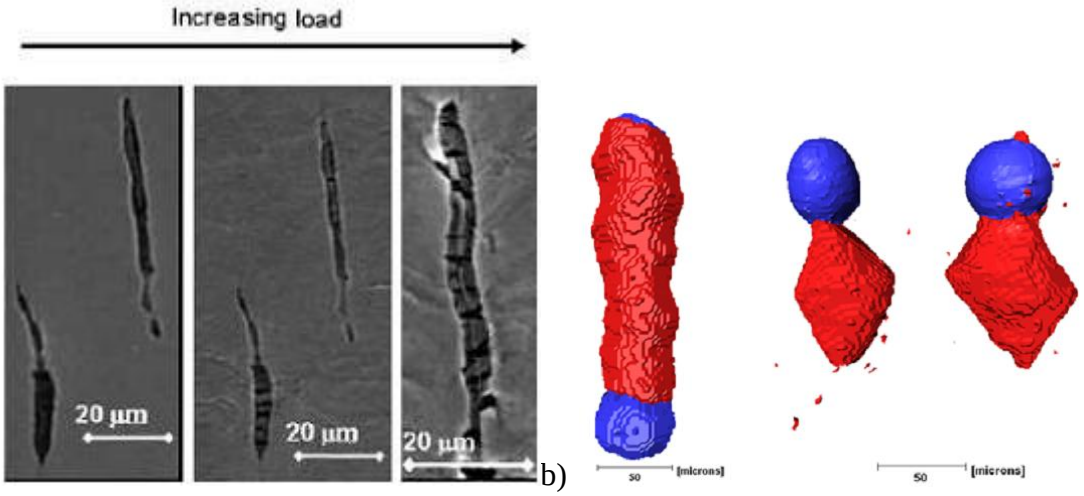

a) b)

Figure III.19: a) SEM observations during the in-situ tensile test of ductile steel [BOU 2008], b) Tomography reconstruction of voids (blue colors) nucleated at zirconia particles (red colors) [WEC 2007].

Characterizations on studied DP steels

By X-ray tomography, Maire et al. [MAI 2008] enhanced volume acquisition during in-situ tensile tests and quantified in 3D the void growth in DPI steel. It occurs that the mean radius calculated over the entire void population remained approximately constant during the tensile test (Figure III.20a) while the radius of the largest cavities was increasing (Figure III.20b).

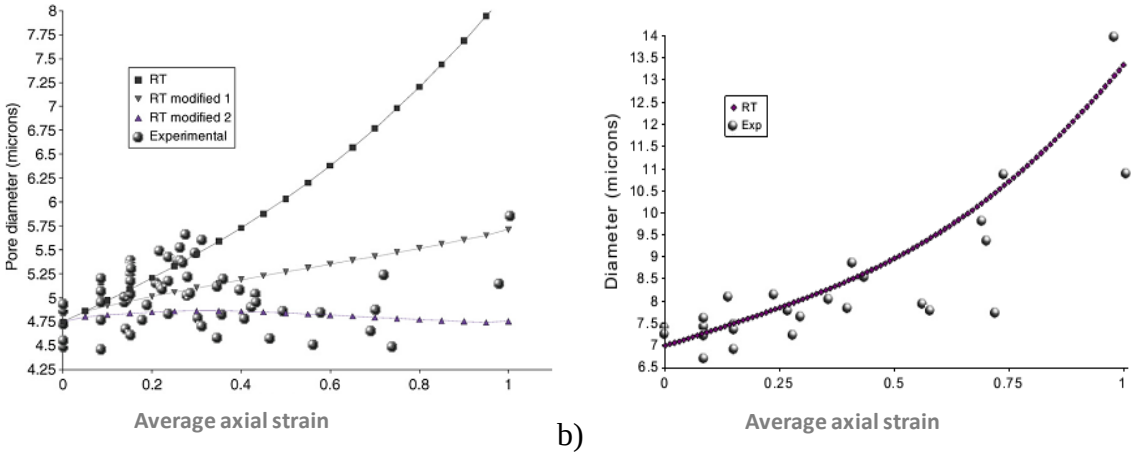

a) b)

Figure III.20: a) Evolution of the equivalent mean radius in function of strain calculated over the entire void population in DPI steels [MAI 2008], b) the equivalent diameter evolution of the largest cavities.

Landron [LAN 2011] improved the observation by using high resolution (1.59 µm) in-situ tensile test X-Ray tomography. The void growth was tracked and the shape measured at different steps of deformation (see Figure III.21). These observations show that the study of the mean diameter of the twenty largest cavities in the population gives an accurate representation of the growth of single voids. Another conclusion of this study underlines that the growth kinematics are impacted by the steel microstructure and mechanical behaviors. In particular, the higher is the yield stress in the studied DP steel, the faster is the growth of cavities.

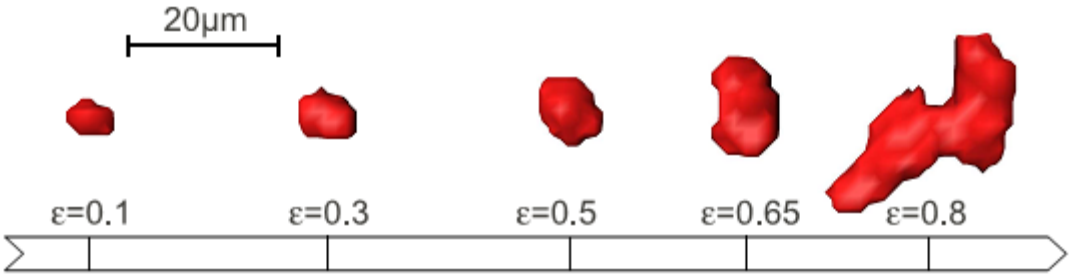

Figure III.21: 3D visualization X-Ray tomography of the same cavity at different steps of deformation in the selected DP steel (DPI smooth sample, see chapter II.3) [LAN 2011].

General modeling

Rice and Tracey

The most popular and the oldest void growth model was proposed by Rice and Tracey [RIC 1969]. It was based on a simple analytical approach for a spherical void in an infinite rigid perfectly plastic material subjected to a uniform remote strain field. The equation is restricted to a fully isotropic void growth and is expressed as below:

$$\frac{dR}{R} = 0.283 \exp\left(\frac{3}{2}T\right) d\varepsilon \tag{III.25}$$

where current R is the void radius, ε the plastic equivalent strain and T the stress triaxiality. Until today, Equation (III.25) is often used and adapted for different materials [HUA 1986] [ZHA 1994] [PAR 1998] [HUG 2003] [GRU 2012], void shapes (cylindrical, elliptical). The most famous application is in the original Gurson damage model (see section III.3.2.1).

Huang

Another significant contribution is the Huang model [HUA 1991]. He replaced the constant factor of Rice and Tracey by two new factors: a new constant and a function of the triaxiality:

$$\begin{aligned} \frac{dR}{R} &= 0.427\left(T^{0.25}\right)\exp\left(\frac{3}{2}T\right)d\varepsilon \quad \text{for } T \le 1 \\ \frac{dR}{R} &= 0.427\exp\left(\frac{3}{2}T\right)d\varepsilon \quad \text{for } T > 1 \end{aligned} \tag{III.26}$$

Modeling on studied DP steels

The growth models used for DP steels will be presented: the Bouaziz & Maire and the Landron laws.

Bouaziz and Maire law

At each deformation stage of the specimen, the growth of existing voids and the nucleation of new voids are observed. Consequently, the evolution of the mean void radius R as defined by the Rice and Tracey model [RIC 1969] is modified by Bouaziz et Maire. [BOU 2008], [MAI 2008] as expressed in Equation (III.27):

$$\frac{dR}{d\varepsilon_{eqv}^{p}} = \overbrace{0.283\exp\left(\frac{3}{2}\frac{\sigma_m}{\sigma_{eqv}}\right)R}^{Rice\ and\ Tracey} \underbrace{-\frac{1}{N}\frac{dN}{d\varepsilon_{eqv}^{p}}\left(R - R_0\left(\varepsilon_{eqv}^{p}\right)\right)}_{Bouaziz\ \&\ al} \tag{III.27}$$

The second term in Equation (III.27) is the reduction of the average radius of the cavities due to nucleation. Indeed, it is easy to check that this last equation reduces to the classic Rice and Tracey model when the nucleation rate dN is equal to zero.

The radius of the nucleated voids at various strain states is not constant. R_0 is the mean radius of cavities just after nucleation and before the beginning of the growth phase. It is dependent on the equivalent plastic strain (matrix+ void) and its expression is empirical.

$$R_0\left(\varepsilon_{eqv}^p\right) = R_0^i \exp\left(-a\varepsilon_{eqv}^p\right) \tag{III.28}$$

where:

R_0^i is the size of the cavities nucleating at the beginning of the deformation and a fixes the importance of the reduction of the size of the nucleating cavities with strain.

Landron law

The evolution of the mean void radius *R* defined by the Rice and Tracey model [RIC 1969] modified by Bouaziz [BOU 2008], Maire [MAI 2008], and Huang [HUA 1991] takes into account nucleation and different void sizes:

$$\frac{dR}{d\varepsilon_{eqv}^p} = \alpha_H \left(\frac{\sigma_m}{\sigma_{eqv}}\right)^{1/4} \exp\left(\frac{3}{2}\frac{\sigma_m}{\sigma_{eqv}}\right) R - \frac{1}{N}\frac{dN}{d\varepsilon_{eqv}^p}\left(R - R_0\right) \tag{III.29}$$

As in Bouaziz and Maire law, the second term in Eq. (III.29) is the reduction of the average radius of the cavities due to nucleation. α_H is a material constant introduced by Huang in order to fit the model to experimental values. R_0 is the initial mean radius of cavities, at nucleation, its evolution with strain is neglected unlike in Bouaziz and Maire law.

III.3.1.3 Void Coalescence

General characterizations

After the void growth follows the void coalescence stage. This mechanism occurs very quickly and is extremely difficult to observe . The first observation with micrography technique shows that the void coalescence starts when the deformation is localized within the ligament of the material between the cavities located in the most critical region of the sample. The use of the X-ray tomography coupled with micrography method gives more details about the mechanism Figure III.22 ([WEC 2007], [BEN 2000]).

Nowadays it is known that the void coalescence stage contains three modes:

- ✓ The first mode observed by Thomson [THO 1987] is called internal necking. It is shrinkage of the ligament between two voids with typical shape of a necking process.
- ✓ The second mode is shear localization [WEC 2007].

- ✓ The third mode is called necklace coalescence. The coalescence is localized in a direction parallel to the main loading axis [PAR 1998] [BEN 2000].

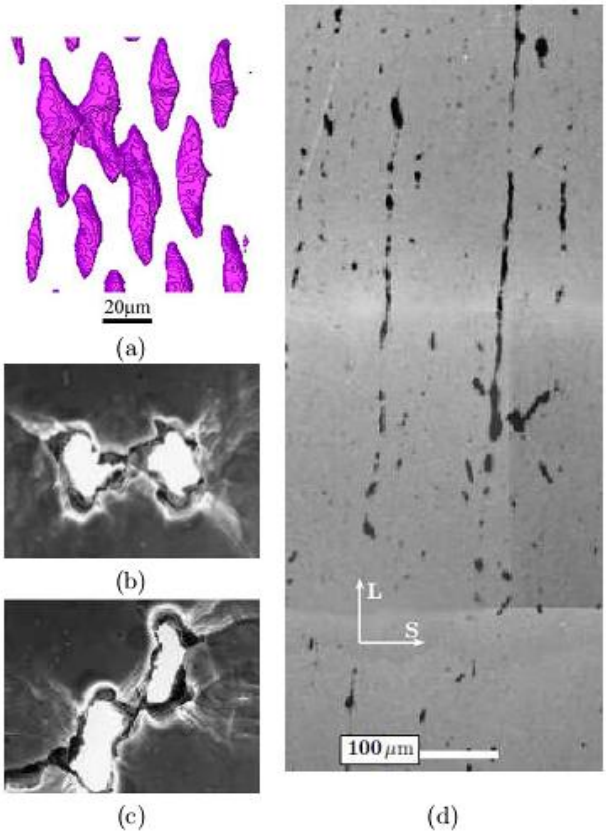

Figure III.22: Illustration of the three modes of coalescence: (a) coalescence by internal necking (X-ray tomography), (b) coalescence by internal necking (SEM observation), (c) coalescence by shear localization (SEM observation) [WEC 2007], (d) necklace coalescence (optical metallography) [BEN 2000].

Characterizations on studied DP steels

Literature dedicated to the void coalescence characterizations in DP steel grades is poor. The most notable contribution using X-ray tomography is from Landron et al. [LAN 2011]. According to her research, the void coalescence event in the DP steels (Figure III.23, Figure III.24) starts in a significant amount during an in-situ tensile test when the evolution of both the measured void density and the void equivalent diameter size is affected. In this study, it is noticed that the different modes of coalescence occurrence depend on the position of the voids coalescing. If neighboring voids were side by side, coalescence rather occurred by necking of the internal ligament. In the cases, where the angle between the voids was around 45°, coalescence resulted from shear localization. The third mode of necklace coalescence was not observed in the studied DPI steel The last observation points out that the coalescence preferentially occurs in the ferrite phase.

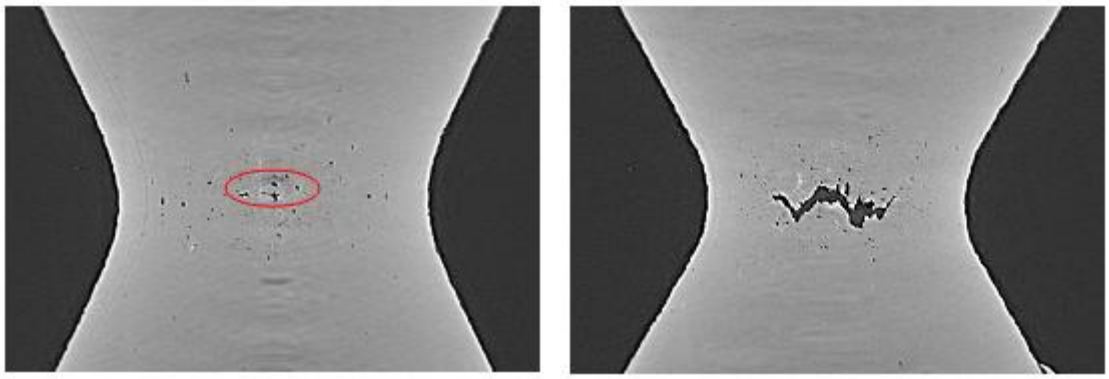

(a) (b)

Figure III.23: Observation of a longitudinal section inside the imaged specimen of DPI steel using X-ray tomography at different deformations: (a) ε= 0.69, (b) ε= 0.83 during the tensile test. [LAN 2011].

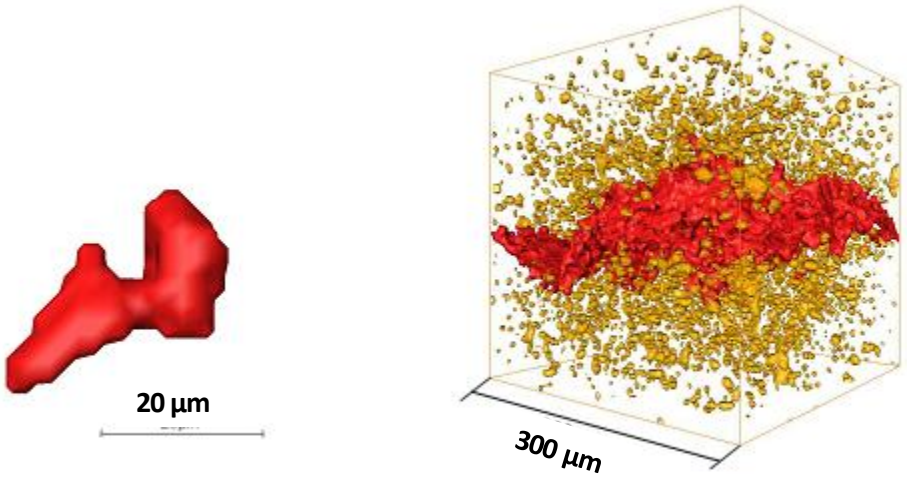

(a) (b)

Figure III.24: 3D visualization of void coalescence in a DPI steel: (a) local event of coalescence at ε= 0.69, (b) macroscopic coalescence inside the same specimen at ε= 0.83 during the tensile test (a huge cavity induced by the macroscopic coalescence appears in red) [LAN 2011].

General modeling

A review of the most popular void coalescence models has been proposed by Weck during his PhD work [WEC 2007] and is presented in Table 1.

Table 1: Historical overview of most important coalescence models [WEC 2007].

Author	Criterion	Limitations	Year
McClintock	Hole impingement	Cylindrical holes No interaction between holes No localization	1968
Brown and Embury	Void length equals intervoid spacing	For regular array of voids No hydrostatic component	1973

		No material properties	
Tvergaard and Needleman	Critical porosity and acceleration factor	Model relies on arbitrary parameters No hole geometry (average)	1984
Thomason	Plastic limit load	No micro shear localization possible Only for non-hardening materials	1990
Pardoen and Hutchinson	Plastic limit load with strain hardening	No microshear localization possible	2000
Gammage	Stress equals global work hardening rate	Local work hardening Global work hardening rate	2004

Only the models of Brown & Embury [BRO 1973] and Tvergaard &Needleman [TVE 1984] used in our applications in chapter VIII are presented hereafter.

Brown & Embury model

The model [BRO 1973] states that coalescence occurs when the length of the ligament between the voids λ_f is equal to the length of the void (see Chapter IV for more details). When the stress triaxiality is low, the length of the ligament does not vary significantly since the void grows mainly in the tensile direction. However, when the stress triaxiality is high, the voids also grow in the direction perpendicular to the tensile direction. In that case, the length of the ligament between the voids will significantly decrease as the voids are growing, leading to an earlier failure of the sample. Assuming that each void has the same radius R and is homogeneously distributed in the space during the uniaxial tensile test the model is written as:

$$\lambda_f = R\left(\sqrt{\frac{2\pi}{3f}} - \sqrt{\frac{8}{3}}\right) \tag{III.30}$$

Where: λ_f is the average inter-cavities distance and f is the void volume fraction.

Tvergaard and Needleman model

Tvergaard and Needleman [TVE 1984] used the Brown and Embury original contribution to extend the Gurson model for void growth to account for the coalescence phenomenon and final material failure. Its expression is given in the section III.3.2.2 when presenting the Gurson-Tvergaard-Needleman (GTN) model.

III.3.2 The Gurson model and its extensions

Many models for material degradation, commonly called damage, have been proposed in the past. The damage modeling is usually divided in two groups: the **phenomenological** and the **micromechanical** approaches. The phenomenological approaches initiated by Kachanov [KAC 1958] couple the elastoplasticity theory with damage in the framework of the so-called continuum damage mechanics. This approach assumes the existence of a classical true stress tensor $\underline{\sigma}$ computed from macroscopic loading and macroscopic area measurements, and an effective stress tensor $\underline{\sigma}^{effec}$ theoretically closer to the actual average microscopic stress state existing between defects. The effective stress tensor $\underline{\sigma}^{effec}$ can be related to the true stress $\underline{\sigma}$ by an effective stress operator $\underline{\underline{M}}$, depending on a damage parameter D which characterizes the state of damage of the material.

$$\underline{\sigma}^{effec} = \underline{\underline{M}}(D) : \underline{\sigma} \tag{III.31}$$

The operator $\underline{\underline{M}}(D)$ takes into account the area of the microvoids and microcracks, stress concentrations due to microcracks and the interactions between neighboring defects. The best known contribution of this type of approach is the work of Lemaitre [LEM 1992]. In his basic model, the isotropic damage depends on a scalar variable D, neglecting the microcracks orientation. He defines the effective stress by the following relation:

$$\underline{\sigma}^{effec} = \frac{1}{1-D}\underline{\sigma} \tag{III.32}$$

Cordebois et al. [COR 1983] modified the isotropic damage parameter D (Eq.(III.32)) to a second order tensor $\underline{D}$ to introduce the anisotropic damage. An elastic energy equivalence hypothesis is introduced and effective values for stress and strain tensors are defined.

The micromechanical approach chosen within this research was initially introduced by the famous Gurson model [GUR 1977], extension of von Mises plasticity model to a porous material, whose behavior depends on first stress invariant and whose equations were based on cell calculations. The sections below describe the original Gurson's contribution and its extensions. The decision to prefer a Gurson type model and not a Lemaitre type model relies on the broad literature survey performed by M. Ben Bettaieb for ArcelorMittal in 2008 [BEN 2008].

III.3.2.1 The initial Gurson model

Gurson's first assumption [GUR 1977] is that the yield function for ductile materials is modified by the presence of voids. After the porosity accumulation, the material begins to soften and loses its capability to carry loads. The initial Gurson model considers only the voids growth phase according to Rice and Tracey [RIC 1969].

Figure III.25 shows a representative volume element constituted by a spherical void inside a spherical matrix. The second hypothesis considers the matrix as a homogeneous material with

an incompressible plastic deformation. This material is assumed rigid perfectly plastic with an isotropic von Mises yield limit, and it uses an associative normal flow rule.

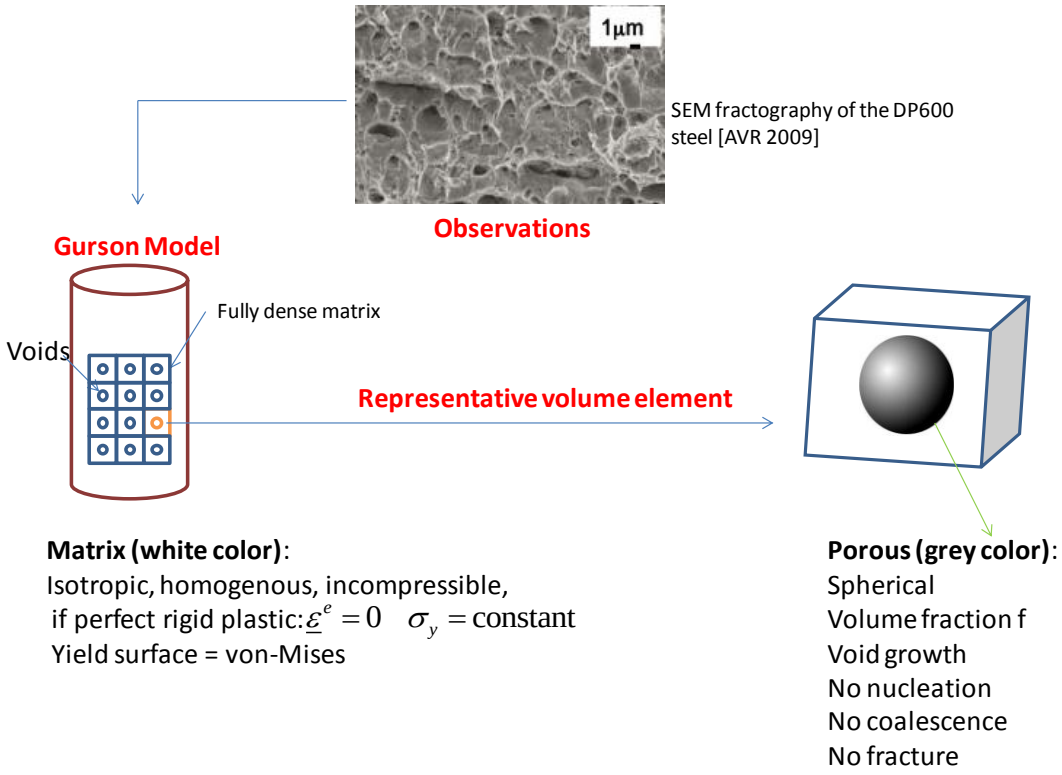

Figure III.25: Representative volume element and assumptions of Gurson model.

The originality of Gurson model is the introduction of void volume fraction or porosity f inside the yield function:

$$F_p^{Gurs}\left(\underline{\sigma}, f, \sigma_y\right) = \frac{\sigma_{eqv}^2}{\sigma_y^2} - 1 + \underbrace{\left[2f\cosh\left(\frac{3}{2}\frac{\sigma_m}{\sigma_y}\right) - f^2\right]}_{\text{Damage effect}} = 0 \qquad \text{(III.33)}$$

Where:

σ_y: yield stress of the fully dense matrix, constant and equal to σ_0 (perfect plasticity is assumed).

σ_m: macroscopic (cavity + matrix) mean stress $\frac{1}{3}tr\left(\underline{\sigma}\right)$.

σ_{eqv}: macroscopic von Mises equivalent stress (cavity + matrix).

f: Void volume fraction or porosity.

$f = \frac{V_A - V_M}{V_A}$ where V_A, V_M are respectively the elementary apparent volume of the material (matrix + void) element and the elementary volume of the matrix.

As notified earlier, Gurson model is based on von Mises criterion, consequently some equations are identical such as:

-Equation (III.4) where the total strain rate tensor (matrix + voids) $\underline{\dot{\varepsilon}}$ is divided into an elastic strain rate tensor $\underline{\dot{\varepsilon}}^e$ and a plastic strain rate tensor $\underline{\dot{\varepsilon}}^p$. Due to the rigid plastic mechanical material behaviour condition, the elastic part is ignored $\left(\underline{\dot{\varepsilon}}^e = 0\right)$.

-No expression of the isotropic hardening law is presented as a constant value is used.

$$\sigma_y = \sigma_y\left(\varepsilon^p\right) = constant \tag{III.34}$$

It is easy to check that, when there is no void $\left(f = 0\right)$ in the material, the yield function becomes identical to the von Mises one (see Equation (III.35)):

$$F_p^{Gurs}\left(\underline{\sigma}, f = 0, \sigma_y\right) = \frac{\sigma_{eqv}^2}{\sigma_y^2} - 1 = 0 \tag{III.35}$$

With the new yield function the normality rule becomes:

$$\underline{\dot{\varepsilon}}^p = \dot{\lambda}\frac{\partial F_p^{Gurs}\left(\underline{\sigma}, f, \sigma_y\right)}{\partial \underline{\sigma}} \tag{III.36}$$

where $\dot{\lambda}$ is the plastic multiplier and $F_p^{Gurs}\left(\underline{\sigma}, f, \sigma_y\right)$ is the Gurson yield function. This associative normality rule assumes that the plastic strain rate is a tensor normal to the yield surface in the stress space.

If $\dot{\lambda} = 0$ and $F_p^{Gurs}\left(\underline{\sigma}, f, \sigma_y\right) \le 0$ the behaviour is rigid.
If $\dot{\lambda} \ge 0$ and $F_p^{Gurs}\left(\underline{\sigma}, f, \sigma_y\right) = 0$ the behaviour is plastic.

The 1977 Gurson model introduced only the influence of a porosity growth in the damage effect. The growth rate equation ($\dot{f}_g$) as mentioned by many authors and for instance by Ben Bettaieb et al. [BEN 2008] comes from the apparent volume change, the mass conservation and the matrix plastic incompressibility.

$$\dot{f} = \dot{f}_g = \frac{V_A V_M}{V_A^2} = \left(1 - f\right) tr\left(\underline{\dot{\varepsilon}}^p\right) \tag{III.37}$$

The porosity modifies the usual energy equivalence and turns to a new plastic work expression:

$$\underline{\sigma} : \underline{\dot{\varepsilon}}^{p} = (1-f)\sigma_{eqv}\dot{\varepsilon}^{p}_{eqv} \qquad \text{(III.38)}$$

$$\text{If } f = 0 \rightarrow \underline{\sigma} : \underline{\dot{\varepsilon}}^{p} = \sigma_{eqv}\dot{\varepsilon}^{p}_{eqv}$$

The advantage of using the initial classic Gurson model is its ability to incorporate the damage parameter through the voids volume fraction. The model needs the same number of equations as von Mises plus the porosity growth (seven equations in total). The unknowns are $(\dot{\varepsilon}^{p}_{eqv}, f)$.

The number of material parameters increases by one compared to the von Mises criterion (f_0).

III.3.2.2 Extensions of Gurson model

The initial 1977 Gurson model has been widely used and extended. Ben Bettaieb collected the most important extended Gurson models in his literature review on damage models and rupture criteria [BEN 2008]. In this section, the main goal is to describe in details the most significant extension called GTN model, which is taken into account in the adopted modeling. The other contributions are summarized in synthetic tables (hardening functions, plastic anisotropy, visco-plasticity, void nucleation, void growth, void coalescence, shear failure provided in Appendices (A)).

Gurson-Tvergaard-Needleman model (GTN)

This Gurson model extension well known as GTN model has been proposed by Tvergaard & Needleman [TVE 1984]. It is implemented in almost all commercial finite element software and is often the base module for new extensions. GTN constitutive law completes the initial Gurson model by breaking out two of its limitations. The first one is the significant gap between numerical simulations and experimental results and the second limitation concerns the weakness of the Gurson model unable to describe the nucleation and the coalescence stages.

- ✓ -The first contribution of GTN model is the addition of the adjustment parameters q_1, q_2 and q_3 into the expression of the yield surface in order to adjust the model to experimental results and cell calculations:

$$F_p^{GTN}(\underline{\sigma}, f, \sigma_Y) = \frac{\sigma_{eq}^2}{\sigma_Y^2} + 2q_1 f \cosh\left(\frac{3q_2\sigma_m}{2\sigma_Y}\right) - 1 - q_3 f^2 = 0 \qquad \text{(III.39)}$$

These new parameters were introduced by Tvergaard [TVE 1984] and can be used to correct the effect of interaction between voids (q_1 and q_3) and void shape changes (q_2).

Often q_3 is chosen to be equal to q_1^2. Initially, Tvergaard proposed the following values of these parameters: $q_1 = 1.5$; $q_2 = 1$; $q_3 = q_1^2 = 2.25$.

- ✓ The second contribution concerns the inability of the initial Gurson model to describe the nucleation and the coalescence stages. The porosity rate is split into three parts to solve this drawback:

$$\dot{f} = \dot{f}_n + \dot{f}_g + \dot{f}_c \qquad \text{(III.40)}$$

The nucleation of new microvoids is due for instance to decohesion of matrix-inclusion or matrix-second phase interfaces, or to hard particle fracture. Considering a Gaussian inclusion distribution, an assumption is that the microvoid nucleation rate is mainly controlled by the equivalent plastic strain rate and defined by relationship proposed by Chu & Needleman [CHU 1980]:

$$\dot{f}_n = A_N \, \dot{\bar{\varepsilon}}^p_{eqv} \qquad \text{(III.41)}$$

Where

f_n : nucleated microvoid volume fraction.

A_N : number of void nucleated (seen Equation (III.22)).

$\dot{\bar{\varepsilon}}^p_{eq}$: rate of equivalent plastic strain in the matrix.

The coalescence of neighboring microvoids yields to final material failure. We used here the approach developed by Tvergaard & Needleman [TVE 1984]. This approach is based on the following experimental observation: this final stage is characterized by rapid changes in void size and shape together with significant modifications of the relative distances between the voids. So f_c is not used as an additive part of the porosity but a specific coalescence function f^* replaces the porosity f in Equation (III.39). The aim of this parameter change is to model the complete vanishing in the carrying stress capacity due to void coalescence, at a realistic void volume fraction:

$$f^* = f \quad if \;\; f < f_{cr} \quad ; \quad f^* = f_{cr} + \frac{f_u - f_{cr}}{f_F - f_{cr}}(f - f_{cr}) \quad if \;\; f > f_{cr} \qquad \text{(III.42)}$$

Where

f_u : the ultimate of value of f^* at the occurrence of ductile rupture, also related to the material parameter q_1 introduced by Tvergaard ($f_u = 1/q_1$).

f_{cr} : the critical void volume fraction at coalescence onset

f_f : the real porosity present just at final failure.

Extensions of the GTN model

One limitation of the GTN model is to consider spherical voids. In order to overcome this limitation, Gologanu et al. [GOL 1993-95] extended the GTN model by taking into account the void shape effects (this model is often called GLD). It stands for Gologanu-Leblond-Devaux. Another limitation of the GTN model is to consider the matrix isotropic in the yield function. Observations have proved that plastic anisotropy of the matrix surrounding the voids can influence the equivalent stress function and damage evolution. As a consequence the isotropic equivalent stress is often replaced by an anisotropic function adopting the Hill'48 criterion [BRU 2001]. Benzerga et al. [BEN 2001] replaced the isotropic plastic von Mises by the Hill anisotropic plastic through the identification of Lankford coefficients.

An additional significant extension is the hardening behaviour. The initial Gurson model describes a perfect plastic behavior. Leblond et al. [LEB 1995] extended in an accurate theoretical way the model to the case of a matrix with isotropic hardening. Their model introduces two new parameters in the yield function representing the plastic hardenable hollow sphere. These parameters are depending on the deviatoric and hydrostatic parts of the macroscopic plastic strain.
Mear and Hutchison [MEA 1985] as well as Ragab [RAG 2004], Ben Bettaieb [BEN 2010] extended the Gurson model to the kinematic hardening case.
Other contributions use a yield surface function of plastic strain rate and allowed the introduction of the viscoplasticity in the model for instance Nègre et al. [NEG 2003] used the Hollomon law to describe the yield stress which is a function of equivalent plastic strain.
The improvement of microstructure observation methods enhanced the development of new void nucleation laws from the initial GTN model. Recently Helbert et al. [HEL 1998] and Bouaziz et al. [BOU 2008] with help of X-ray tomography method accurately modeled the voids nucleation stage. Pardoen [PAR 2006] improved both the void growth modeling and the rupture prediction by coupling his Gurson version to the Thomason coalescence criterion [THO 1990]. Other extensions of the GTN model are presented in Appendix (A.7).
The most significant contributions concerned the coalescence stage which is considered researchers to be the beginning of the material failure. Besides, Brown & Embury [BRO 1973] criterion defining the beginning of the coalesence stage as a critical distance between the centers of neighboring voids, Thomason [THO 1990] introduced a non-hardening rigid plastic solid criterion, which contains a regular three-dimensional distribution of spherical microvoids. Nowadays, due to shear fracture, and edge cracking during sheet-forming process, the GTN model is extended to take into account the shear contribution. K. Nahshon and J.W. Hutchinson [NAH 2007] incorporated damage growth under low triaxiality straining for shear-dominated states through Lode angle for aluminium. Xue [XUE 2007] [XUE 2008] and Nielsen&Tvergaard [NIE 2010] modified the expression of the Lode angle in simple shear and small void volume fractions for DP steels.

III.4 Fracture modeling

The present section briefly introduces two types of fracture criteria (micromechanical ones and empirical ones) decoupled from any damage modeling. Again we are mainly focused on models already used for Dual-Phase steels. The micromechanical criteria are based on rigorous microscopic observations while the empirical criteria have no consistent theoretical justification.

III.4.1 Micromechanical fracture criteria

These criteria are based essentially on the study of the growth and coalescence of spherical or cylindrical cavities in porous plastic solids [ABB 2003], [WIE 2005a], [UTH 2008], [SUN 2009], [LUO 2010], [LI 2010], [UTH 2011], [VAJ 2012].

III.4.1.1 The Mc Clintock model

This criterion defined by Mc Clintock [MCC 1968] is based on the analysis of the expansion of cylindrical cavities in a plastic material under a triaxial stress state of fixed orientation. The version of Oh, Chen, Kobayashi ([KOB 1979] of the Mc Clintock model is defined by the following relation:

$$\int_0^{\varepsilon_f} \left(\frac{2}{\sqrt{3}(-n)} \sinh\left[\frac{\sqrt{3}(1-n)}{2}\frac{\sigma_3-\sigma_1}{\sigma_{eq}}\right]+\frac{\sigma_3-\sigma_1}{\sigma_{eq}}\right) d\varepsilon_{eq} = C_c \qquad \text{(III.43)}$$

where

σ_1, σ_3 : the principal stresses.

n : the exponent of the hardening law

C_c : a critical value.

This model is often applied on DP steel for comparison with the Rice & Tracey model [ABB 2003]. More recently, this criterion has been used by Lou and Li. [LUO 2010] [LI 2010] to predict the fracture of Advanced High Strength Steels (AHSS) such as DP steel with the concept of Forming Limit Curve (FLC).

III.4.1.2 The Rice & Tracey model

The Rice & Tracey model [RIC 1969] has been developed for a single spherical void located in an infinite plastic medium showing no interaction with neighboring voids. The fracture criteria form Rice & Tracey model is integrated between 0 and ε_f :

$$Ln\left(\frac{R}{R_0}\right) = \int_0^{\varepsilon_f} B \exp\left(\frac{A\sigma_m}{\sigma_{eq}}\right) d\varepsilon_{eq} = C_c \qquad \text{(III.44)}$$

Here R_0 is the initial void radius.

Rice & Tracey fracture model is more applied than Mc Clintock prediction in sheet metal forming process. Literature survey shows that Wierzbicki and co-workers [WIE 2005a], LUO

2010], [LI 2010] and others [UTH 2008], [SUN 2009], [VAJ 2012] often use this model as a reference. They usually compare this model to the modified Mohr-Coulomb fracture criterion (MMC). This approach serves to predict the initiation and propagation of cracks in industrial applications such as deep-drawing punch and cross-die drawing tests.

III.4.2 Empirical fracture criteria

According to Ben Bettaïeb [BEN 2008], the empirical ductile fracture criteria can be sorted into three classes depending on the type of function used to express the criterion: usually stress and/or strain and strain path dependent. The stress-based functions involve equivalent, mean (or hydrostatic) or shear stresses whereas the strain-based functions incorporate equivalent, mean or thickness strains. The literature on empirical fracture is quite extensive. This part based on Ben Bettaïeb work presents the most used model in forming processes.

III.4.2.1 The Cockroft & Latham model

The Cockroft & Latham model [COC 1968] was developed for the bulk forming operations and therefore is applicable only to the range of small and negative stress triaxiality. In this model, fracture occurs when the accumulated equivalent strain modified by maximum principal tensile stress reaches a critical value:

$$\int_0^{\varepsilon_f} \sigma_1 d\varepsilon_{eq} = C_c \tag{III.45}$$

This model is the most widely used empirical continuum ductile criterion and states that fracture depends on the integrated principal tensile stress. Thus, for a given material, temperature and strain rate, this criterion suggests that fracture occurs when integral of the tensile stress reaches a critical value.

III.4.2.2 The Brozzo et al. model

The Brozzo criterion [BRO 1972] improves the preceding one by including the effect of hydrostatic stress.

$$\int_0^{\varepsilon_f} \frac{2\sigma_1}{3(\sigma_1 - \sigma_m)} d\varepsilon_{eq} = C_c \tag{III.46}$$

III.4.2.3 The equivalent deformation model

Fracture is assumed to occur in a material element when the equivalent plastic strain ε_{eq}^p reaches a critical value ε_f .

$$\varepsilon_{eq}^p = \varepsilon_f \tag{III.47}$$

There is an understanding agreement that this criterion is very accurate but not valid for all possible stress states.

III.4.2.4 The FFLD model

The concept of FFLD (Fracture Forming Limit Diagram) has been developed in the metal forming industry to characterize transition from plane stress necking to transverse plane strain fracture. In the first approximation, the FFLD forms a straight line in the space of principal strains.

$$\varepsilon_{1f} + \varepsilon_{2f} = -\varepsilon_{3f} = C_c \tag{III.48}$$

where the subscript f denotes the strain magnitude at the point of fracture.

III.4.2.5 The Johnson-Cook model

Johnson & Cook postulated that the critical equivalent fracture strain (for constant strain rate and temperature) is a monotonic function of the stress triaxiality

$$\varepsilon_f = c_1 + c_2 \exp(c_3 (\sigma_m / \sigma_{eq})) \tag{III.49}$$

The Rice & Tracey and McClintock models can be considered as particular cases of the Johnson-Cook model. The constants c_1, c_2 and c_3 were determined from tensile tests with high triaxiality and in some cases from a shear test.

III.4.2.6 The Xue-Wierzbicki model

This recent model [WIE 2005a], [WIE 2005b], [XUE 2007] relies on most if not all experimental observations and is relatively easy to calibrate. Fracture is postulated to occur when the accumulated equivalent plastic strain, modified by the function of the stress triaxiality T and the deviatoric stress tensor $\underline{\sigma}'$; reaches a limiting value equal to one.

$$\int_0^{\varepsilon_{eq}} \frac{d\varepsilon_{eq}}{F(T,\xi)} = 1 \quad ; \quad \xi = \frac{27}{2}\frac{J_3}{\sigma_{eq}^3} \tag{III.50}$$

in which J_3 is the third invariant of the stress deviator and is equal to $\sigma_1'\sigma_2'\sigma_3'$ ($\sigma_1'\sigma_2'\sigma_3'$ are the principal components of $\underline{\sigma}'$).

III.4.2.7 The maximum shear stress model

There is clear evidence that ductile fracture may occur on a plane where the shear stress is maximum. For example, in upsetting test on short aluminum cylinders a spiral fracture occurs in the equatorial area of barreled specimens [DUN 2011], [KIM 2011]. It is then reasonable to postulate that fracture is governed by the condition

$$\tau_{\max} = (\tau_{\max})_f \tag{III.51}$$

Where

$$\tau_{max} = \max\left\{\frac{\sigma_1 - \sigma_2}{2}, \frac{\sigma_2 - \sigma_3}{2}, \frac{\sigma_3 - \sigma_1}{2}\right\} \quad \text{(III.52)}$$

and σ_1, σ_2 and σ_3 are the principal stresses.

III.5 Conclusions

After chapter 2 giving a general presentation of the Dual-Phase (DP) steels (microstructures, mechanical properties, and formability characteristics), the current chapter has been focused on picturing the state of the art of Dual-Phase steels behaviour modeling. DP steels mechanical constitutive laws are based on plasticity, damage theory and decoupled damage approaches rely on fracture criteria to predict rupture. Each model presents some advantages and drawbacks.

The DP steel behaviour is accurately modeled with elasto-plastic models before large strain and fracture. Recent developments in sheet-forming process with DP steels [TAH 2009], [CHU 2010], [MOR 2010], [KAD 2011], [VLA 2010], [MUR 2011], [CHU 2012], [VAJ 2012], [SUN 2013] show that rather than using a purely isotropic (Ludwig, Swift, Voce) or purely kinematic hardening laws (Prager, Ziegler, Armstrong-Frederick), mixed hardening type models enhance the stress accuracy prediction by expanding, contracting, or translating the yield surface. Kinematic or mixed hardening laws are often employed with success in automotive industry to simulate or minimize springback. These plasticity phenomena usually appear before the sheet starts to soften or damage.
The second section of this chapter focused on damage modeling of DP steels characterizes the ductile damage as the succession of three specific mechanisms: nucleation, growth and coalescence of voids. These stages occur before the material totally failed apart.

- The void nucleation stage which is most of the time heterogeneous appears either by fracture of the second phase inclusion, or by decohesion at the interface.
  Numerous void nucleation models have been proposed such as Argon [ARG 1975], Beremin et al. [BER 1981], Needleman and Tvergaard [NEE 1987] and more recently Helbert et al. [HEL 1998], Bouaziz et al. [BOU 2008], Maire et al. [MAI 2008] and Landron et al [LAN 2011] with help of X-ray tomography technique. Thanks to this new observations technique, the void nucleation models are closer to the experiment but need a lot of time to be analyzed, compared, and validated.
- The void growth stage easier to characterize takes place by plastic deformation. This mechanism is influenced by the triaxiality, the void density, the isotropic or kinematic hardening. Maire et al. [MAR 2008] enhanced volume acquisition during in-situ tensile tests and quantified in 3D the void growth in DP steels. It occurs that the mean radius calculated over the entire void population remained constant during the tensile test while the radius of the largest cavities was increasing. An advanced work with this method from Landron et al. [LAN 2011] concludes that the void growth kinematic is impacted by the steel microstructure and mechanical behaviors. In particular, the

higher the yield stress is, the faster is the cavity growth. Most of the void growth models are based on Rice and Tracey [RIC 1969] works. This model has been continuously enhanced see for instance Huang model [HUA 1991] or Bouaziz [BOU 2008] and Landron et al. [LAN 2011] for DP steels. Huang [HUA 1991] prediction permitted a good comprehension of the growth mechanism of a large family of DP steels. The author includes material parameter depending on volume fraction of martensite and completed the Rice and Tracey model with the introduction of the triaxiality to take into account the geometry of the sample. Bouaziz et al. [BOU 2008] added to the Rice and Tracey growth law the void nucleation contribution with a precise counting of the void density, function of triaxiality factor. Landron et al. [LAN 2011] enhanced the model of Bouaziz by integrating Huang prediction, the coalescence part and more important, and the backstress tensor contribution.

- The coalescence stage occurs in a short time range . It starts when the deformation is localized within the ligament of the material between the cavities located in the most critical region of the sample. This stage contains three modes: internal necking, shear localization, necklace coalescence. Landron et al.[LAN 2012] notable contribution on the comprehension of this phenomenon observed that the void coalescence in the DP steels started in a sufficient amount during an in-situ tensile test when the measured void density, the equivalent diameter and in general the void dimensions are affected. Landron checks this information to identify the coalescence start. A literature survey shows that the most used models for DP steels are Brown and Embury [BRO 1973], Tvergaard & Needleman [TVE 1984], and Thomason [THO 1990].

The micromechanical approach to damage, which is our main focus, was initially introduced by the famous Gurson model [GUR 1977] coupling deformation with damage. This model with its most popular extension well known as GTN (Gurson-Tvergaard-Needleman) has been described in details. Additional significant extensions of the GTN have been reviewed and an overview is available in Appendices (A). The GTN extensions can be separated in seven categories: hardening functions, plastic anisotropy, viscoplasticity, void nucleation, void growth, void coalescence and shear failure. In hardening function GTN extensions, the notable work of Leblond et al. [LEB 1995] commonly named GLD model introduced nonlinear kinematic hardening into the GTN-model. . Gologanu et al. [GOL 1993] took care of void shape and Pardoen [PAR 2006] extended previous approaches to handle cases of law triaxialities.

In the current study it has been noticed that generally, the DP steel is less sensitive to the anisotropy effect compared to other steels. Even though, the anisotropy influence is weak at low strain, it can have a significant effect when the material starts to damage. The damage extension of the GTN model has been widely modified.These new approaches are discussed in perspectives section in chapter IX.

Ben Bettaieb [BEN 2012] GTN extension chosen in this current study and described in the next chapter containes significant contributions for DP steels: the mixed hardening and the plastic anisotropy of the matrix, a physically based void nucleation and growth models from Bouaziz et al. [BOU 2008].

Chapter IV. **Model description**

Contents

IV.1 Introduction

The previous chapter has assumed that the ductile fracture occurs within the plastically deforming parts of most DP steels through nucleation, growth, coalescence of voids. This increase of void volume fraction softens the material until fracture takes place. The porosity evolution has been well predicted by numerous investigations [TVE 1984], [NEE 1987] using the Gurson model [GUR 1977]. This model choice presents the advantage to open doors towards many available extensions for different mechanical behaviors, for instance: anisotropic yield locus, isotropic and kinematic hardening models and viscoplastic constitutive law. It has been also adapted to ellipsoidal void shapes (see appendix (A)). The most known Gurson model extension is the one introduced by Tvergaard & Needleman usually called (GTN), see Chapter III.3.2.2.

Due to its micromechanical roots and to the explicit use of the void volume fraction as a damage state variable, the GTN model has been chosen in the current research to introduce recent results from experimental X-ray tomography measurements on DP steels. The current extended GTN damage model named GTNBF (Gurson-Tvergaard-Needleman-Ben Bettaieb-Fansi) is based on the original work of Ben Bettaieb [BEN 2011-2012]. The GTNBF model has two main contributions compared to classical GTN approach.

The first one is the original extension called GTNB (Gurson-Tvergaard-Needleman-Ben Bettaieb) developed in Lagamine FEM software of Liège University [ZHU 1992] and implemented in Abaqus-explicit during this thesis. Ben Bettaieb introduced the Hill anisotropic yield function of the matrix in the Gurson yield function, as well as a mixed hardening model (Swift law coupled with a modified Armstrong-Frederick approach). In this model, the usual GTN damage parameters (q_1, q_2, q_3) and the porosity become variables explicitly depending on triaxiality and plastic strain. Validation of the GTNB model [BEN 2012] extended to Bouaziz's void nucleation law [BOU 2008] was performed on experimental results for tensile specimens with square cross-section and very large notch radius. In the current thesis, Ben Bettaieb's GTNB model was implemented in Abaqus/Explicit.

The second contribution consists in integration in the VUMAT law of recent experimental nucleation/growth observations. Through this approach, it was possible to accurately compute the void density and the evolution of the void mean radius. The present extension, called GTNBF model was motivated by recent X-ray tomography measurements from Landron et al [LAN 2011]. The experiments carried out on in-situ tensile notched axisymmetric specimens of DP steels revealed a strong dependency between the density of voids, the backstress, and the triaxiality. In all these models Gurson's a strong assumption of spherical voids is used.

The most important part of the modeling work is to infer general three-dimensional damage evolution laws from the experimental observations on a smooth [MAI 2008] and notched [LAN 2011] tensile specimens. This goal has been reached by a close collaboration between the experimental and the numerical teams (INSA-Lyon, ArcelorMittal-Metz, and University of Liège). From a ductile damage modeling point of view, the GTNBF model is built on the Maire et Bouaziz modeling works and the experimental Landron [LAN 2011] contributions. Finally, let us remind that the GTNB model was validated only on DPI steel and for square

smooth sample whereas the GTNBF model is extended on large range of triaxiality factors and various DP steels containing from 11% to 62% of volume fraction of martensite.
Chapter 4 has two distinct objectives. The first one is to summarize the original GTNB model. Then, the second one details the new contributions (Huang void growth prediction [HUA 1991], Landron et al. nucleation law [LAN 2012], the chosen coalescence model, and an additional fracture initiation criterion) contained in the GTNBF model.

IV.2 Gurson-Tvergaard-Needleman-Ben Bettaïeb model (GTNB)

IV.2.1 Constitutive equations

The GTNB model is focused on dual phase steel behavior and introduces the Hill anisotropic yield function and a mixed hardening model of the matrix in the Gurson yield function. The hardening choice relies on a Swift law for the isotropic hardening and a modified Armstrong-Frederick law for the kinematic one. The set of constitutive equations presented hereafter uses the small strain formulation. Generally, DP steels reach large strain during the sheet forming process. Fortunately, finite element codes like Abaqus or Lagamine provide a numerical tool treatment based on coordinate reference system transformation. Abaqus/explicit gives strain components in logarithmic form and allows the material to behave in large strain formulation. More details are given in the Abaqus theory manual [ABA 2011].
The damage model consists of eight equations. The three first ones are common to any plasticity law. These equations have been already presented in chapter III.2.1.1 as Equation (III.3) Hooke's law, (III.4) additive approach of strain rates and (III.5) associative plastic flow rule when describing the plastic modeling. The other equations presented hereafter are specific to the original GTNB model.

The anisotropic yield function [BEN 2011] reads:

$$F_p = \frac{\overline{\sigma}_{eqv}^2}{\sigma_y^2} + 2q_1 f^* \cosh\left(-\frac{3q_2\overline{\sigma}_m}{\kappa\sigma_y}\right) - 1 - q_3 f^{*2} \leq 0 \qquad \text{(IV.1)}$$

Where:

- $\underline{\overline{\sigma}} = \left(\underline{\sigma} - \underline{X}\right)$ is the shifted stress tensor defined as the difference between the Cauchy stress tensor $\underline{\sigma}$ and the back stress tensor $\underline{X}$ of the macroscopic medium (matrix and void).
- $\overline{\sigma}_{eqv}$ is the anisotropic equivalent shifted stress (with respect to the quadratic Hill criterion). $\overline{\sigma}_{eqv}$ is computed by $\overline{\sigma}_{eqv} = \sqrt{\frac{1}{2}\left(\underline{\overline{\sigma}} : \underline{\underline{H}} : \underline{\overline{\sigma}}\right)}$ where $\underline{\underline{H}}$ is the Hill matrix of anisotropy coefficients defined as a function of the Lankford coefficients r_0, r_{45}, r_{90}

(see Appendix ((B.1)).

- σ_y defines the yield stress of the dense matrix, it is a scalar function of the equivalent plastic strain describing the matrix hardening.
- $\overline{\sigma}_m$ corresponds to the macroscopic mean shifted stress equal to $\frac{1}{3}tr\left(\underline{\overline{\sigma}}\right)$.
- f^* is a function of the porosity f. The coalescence event is neglected in this model. f is the void volume fraction defined as the ratio between the volume of voids V_v and the total volume $V_m + V_v$, where V_m is the matrix volume. Finally, q_1, q_2 and $q_3 = q_1^2$ are three material parameters introduced by Tvergaard and Needleman [TVE 1982]. In this case, these parameters are kept constant and take the following values: $q_1 = 1.5$ and $q_2 = 1$.
- The parameter κ is reflecting the influence of the plastic anisotropy. Derived by Benzerga and Besson [BEN 2001] from a micromechanical analysis, it is a function of the Lankford coefficients r_0, r_{45}, r_{90}. For isotropic materials, κ is equal to 2 (see Appendix ((B.2).

This damage anisotropic yield function is coupled with a mixed hardening model as described in Ben Bettaieb et al. [BEN 2011]. The isotropic hardening model is defined by the well known Swift law:

$$\sigma_y = K\left(\varepsilon_0 + \varepsilon_m^p\right)^n \tag{IV.2}$$

Where K, n and ε_0 are material parameters and ε_m^p represents the equivalent plastic strain in the dense matrix. The kinematic hardening law is described by a variant of the Armstrong-Frederick saturating model [ARM 1966], adapted to damaged materials:

$$\underline{X} = \left(1 - q_1 f^*\right)\underline{X}^*; \quad \underline{\dot{X}}^* = C_x\left(S_{sat}\underline{\dot{\varepsilon}}^p - \underline{X}^*\dot{\varepsilon}_{eqv}^p\right) \tag{IV.3}$$

Where C_x and S_{sat} are material parameters, $\underline{\dot{\varepsilon}}^p$ is the plastic strain rate in the macroscopic medium and $\dot{\varepsilon}_{eqv}^p$ is the equivalent plastic strain rate defined as:

$$\dot{\varepsilon}_{eqv}^p = \sqrt{2\left(\underline{\dot{\varepsilon}}^p : \underline{\underline{H}}^{-1} : \underline{\dot{\varepsilon}}^p\right)} \tag{IV.4}$$

Where $\underline{\underline{H}}^{-1}$ is the pseudo-inverse of Hill's anisotropy matrix (its expression is provided in the Appendix ((B.1)).). According to Arndt et al. [ARN 1997], Eq. (IV.3) respects the initial Gurson model approach when the kinematic hardening is used.

Finally, the work equivalence principle is used:

$$\overline{\underline{\sigma}} : \dot{\underline{\varepsilon}}^{p} = (1-f)\sigma_{y}\dot{\varepsilon}_{m}^{p} \quad \text{(IV.5)}$$

IV.2.2 Physically-based void nucleation and growth models

The damage law is formulated from the modeling work of Bouaziz et al. [BOU 2008] which is based on Maire [MAI 2008] measurements. This section summarizes the experimental measurements of Bouaziz and co-workers on void nucleation and its integration in the GTNB model.

IV.2.2.1 Experimental measurements by Maire et al.

The qualitative observations based on 3D X-ray tomography measurements allowed the researchers to quantitatively describe the progressive increase of the number of cavities during the plastic deformation of the studied square smooth sample made of DPI steel. This experimental information was used to develop two evolution laws: one for the nucleation phenomenon and one for the growth phase. In the latter case the classical approach from Rice & Tracey [RIC 1969] was chosen and enhanced. Bouaziz and Maire [BOU 2008] [MAI 2008] concluded that ε_{eqv}^{p} (equivalent plastic strain) and T (triaxiality) are key factors to model the void growth.

The equivalent plastic strain ε_{eqv}^{p} is calculated equal to the average axial strain defined over the entire minimal cross-section. The triaxiality T used to derive the law was also an average value over the necking section. It was determined using a modified Bridgman approximation approach [BRI 1945]. The triaxiality value was extracted by measuring the radius of curvature of the outer surface in the central section and the minimum value of this section as seen in Figure IV.1.

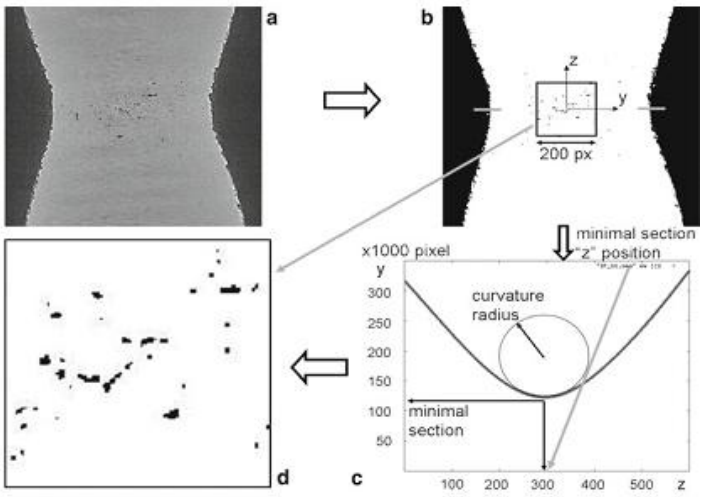

Figure IV.1: a) Grayscale slice of the DPI notched sample at the final stage of the tensile test, b) The same image filtered and binarized; the figure shows a section of the 200×200×200 voxel cubes (RVE), c) A plot of the sample shape in the y−z plane, d) A slice of the RVE, filtered and binarized, representative of the damage [BAR 2012].

IV.2.2.2 Void nucleation kinetics

The quantification of the evolution of the density and size of the voids, but also the triaxiality, and the equivalent plastic strain measured with the efficient X-ray experimental tomography technique [MAI 2006-2008], [YOU 2005] allow Bouaziz [BOU 2008] to develop few analytical relations between those quantities. The following section describes the origin of the Bouaziz &Maire damage evolution approach based on the original publication "A model for initiation and growth of damage in dual-phase steels identified by-ray micro-tomography" [BOU 2008]. Hereafter, the damage evolution ideas developed for the GTNB model are the same as the ones used in extended model (GTNBF model).

First, from the initial experimental tensile test briefly described above, Bouaziz et al. [BOU 2008] has extracted four 3D rending of cavities corresponding to the equivalent plastic strain of 0, 0.17, 0.72 and 1 as seen in Figure IV.2. The voids are presented in black color and the outer surface of the specimen in grey.

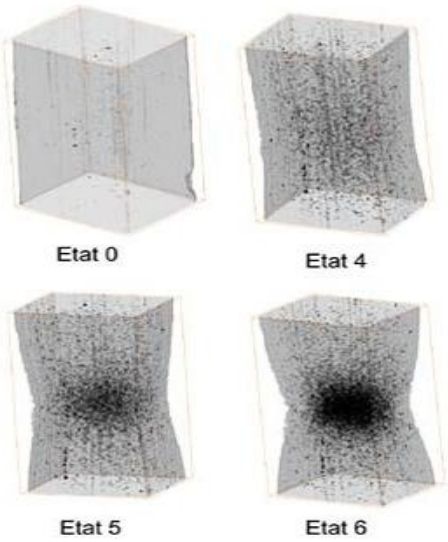

Figure IV.2: 3D rendering of cavities (black) and of the outer surface of the specimen (grey) relating necking with the increase of damage; states 0, 4, 5 6 correspond to the equivalent plastic strain of 0, 0.17, 0.72, and 1 for DPI steel [BOU 2008].

Thanks to the measurement of the values of the minimal cross-section radius ($r_{section}$) and the notch radius (r_{notch}) (chapter V, Figure V.11), the researchers estimated the equivalent plastic strain ε_{eqv}^{p} with the following expression:

$$\varepsilon_{eqv}^{p} = \frac{\ln S_0}{S} \tag{IV.6}$$

Where, S_0 and S are respectively the initial and the current surfaces of the necking section.

However within the post processing of experimental observation by metallurgist teams composed of Bouaziz and Maire, the triaxiality is assumed to be a constant value through the whole macroscopic material across the necking section. In the case of tensile tests on notched

or smooth samples, constant mean triaxiality T through the section is expressed as a modified Bridgman approximation [BRI 1945] by:

$$T = 0.33 + 0.27\left[1 - \exp\left(\varepsilon_{eqv}^{p} - n\right)^{2}\right] \qquad \text{(IV.7)}$$

With $n = 0.17$

Note that Bridgman developed his average formula for notched specimen, and here it is used as an extension even for uniaxial tests that undergo necking. However for uniaxial test before necking event, *T* should be 1/3. The triaxiality value is a key point for comparison between FE simulations and experimental observations due to is strong influence on damage evolution. The interest of FE approach is that it provides more accurate T values and takes into account any sample shape.

With the hypothesis that the necking starts at equivalent plastic strain superior to 0.17, the numerical void density N (number of nucleated voids per mm³) and their mean radius R are obtained by counting the number of voids and measuring their size in the 3D images. Due to the heterogeneity appearing and amplified when the necking becomes stronger in the specimen, an equivalent mean strain value has been taken assumed. For each measured equivalent mean strain value corresponds a void density N, a mean radius R and a triaxiality *T*. Finally, it has been possible to draw the evolution of the triaxiality (Figure IV.3a and void density (Figure IV.3b) in function of the equivalent mean strain.

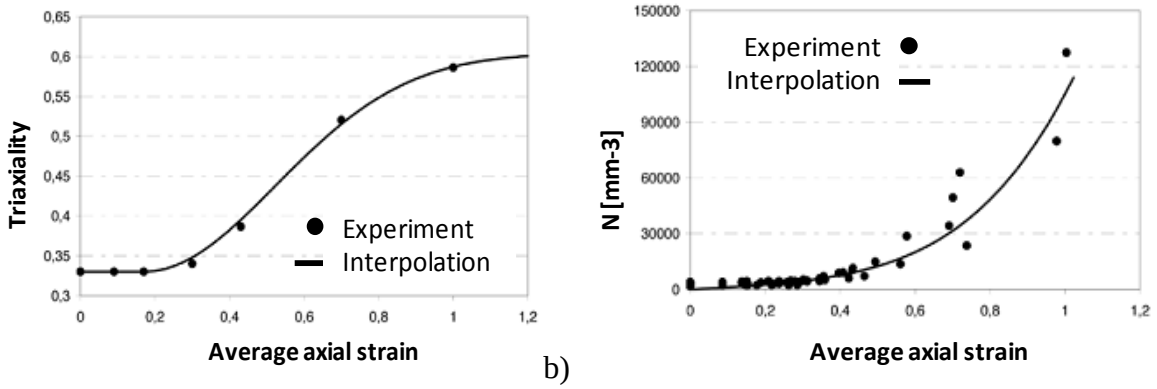

a) b)

Figure IV.3: a) Measure and interpolation of triaxiality as a function of equivalent strain for a tensile test, b) Measure and interpolation of the density of cavities as a function of equivalent strain in the center of the tensile specimen for DPI steel [BOU 2008].

The fitting of the experimental points with the analytical curves permitted to consider that the numerical void density N (number of nucleated voids per mm³) is related to T (triaxiality) and ε_{eqv}^{p} by the following relationship:

$$N = A\left(\frac{\varepsilon_{eqv}^{p}}{\varepsilon_N}\right)\exp\left(\frac{\varepsilon_{eqv}^{p}}{\varepsilon_N}\right) \qquad \varepsilon_N = \varepsilon_{N0}\exp(T) \tag{IV.8}$$

Where:

- A: Constant equal to 5000 voids/ mm³ representing the void density when the material starts to nucleate at 0.17 of equivalent plastic strain.
- ε_N: Critical value of the strain for which nucleation starts. This quantity has been identified by Leroy et al. [LER 1981]
- ε_{N0}: Critical strain when a pure shear is applied (T=0). A value of 0.8, for this critical strain in shear, provides a good fit for N evolution compared to experimental measurements.
- T: Triaxiality function.

Regarding the GTNB model, the triaxiality measured by Maire et al. [MAI 2008] is a local value computed by the FE code at each integration point as the ratio between the mean stress and the equivalent stress. These stresses are the one computed within the (matrix + void) medium, and due to the use of kinematic hardening, they are the shifted values.

IV.2.2.3 Void growth kinetics

The previous analysis on the evolution of the void density helps to model the evolution of the mean void radius R. In the same way as for the void density evolution, Bouaziz et al. [BOU 2008] established a relationship between the evolution of the mean void radius R and the measured triaxiality. It is defined by the Rice & Tracey [RIC 1969] model modified by Bouaziz et al. [BOU 2008] as expressed in Equation (IV.9):

$$\frac{dR}{d\varepsilon_{eqv}^{pl}} = \overbrace{0.238\exp\left(\frac{3}{2}\frac{\sigma_m}{\sigma_{eqv}}\right)R}^{Rice\ \&\ Tracey} \underbrace{-\frac{1}{N}\frac{dN}{d\varepsilon_{eqv}^{p}}\left(R - R_0\left(\varepsilon_{eqv}^{p}\right)\right)}_{Bouaziz\ \&\ al} \tag{IV.9}$$

The second term in Equation (IV.9) is the reduction of the average radius of the voids due to nucleation as compared to the initial Rice and Tracey model. Indeed, it is easy to check that Equation (IV.9) reduces to the classical Rice and Tracey model when the nucleation rate dN is equal to zero.

R_0 is the mean radius of nucleated cavities before the beginning of the growth phase. At each deformation stage of the specimen, the growth of existing voids and the nucleation of new voids are observed. The radius of the nucleated voids at any material point subject to a defined strain path presents some scatter before any growth stage. R_0 is the average value of these initial radii. As assumed by Equation (IV.10), this average radius is dependent on the

equivalent plastic strain (matrix+ void). The expression of R_0 is empirical and physically take into account the evolution of bigger voids.

$$R_0\left(\varepsilon_{eqv}^{p}\right) = R_0^i \exp\left(-a\varepsilon_{eqv}^{p}\right) \tag{IV.10}$$

Here, R_0^i and a are material parameters that the user identifies from experiments (see chapter VI).

The most important restriction of the present model is related to the void size observation and measurement. Indeed, the smaller void diameter observed by Maire et al. [MAI 2008] with the X-ray tomography technique is identified at 5 µm. Later, Landron et al. [LAN 2012] demonstrated that the void nucleation and growth evolutions strongly depend on the type of resolution employed to observe the ductile damage. Indeed, the work revealed that the detection of all voids (including small void size) depends on the resolution level of X-ray tomography as seen below. The volume of the smallest detectable cavities at around 10 μm^3 at low resolution leading to a diameter of 4µm under which the void cannot be detected

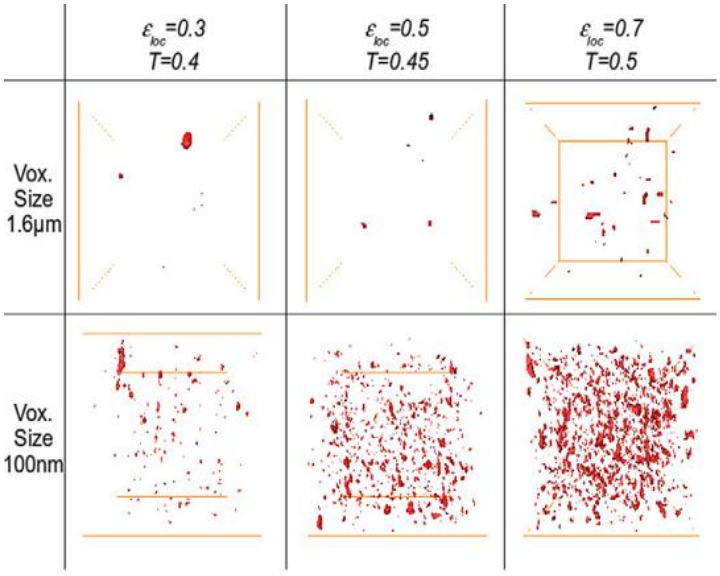

Figure IV.4: Qualitative comparison of visualized damage in central cubes (volume equal to (100 µm) ³ X-Ray tomography obtained with two different resolutions [LAN 2012] for three levels of equivalent strain and triaxiality *T* for DPI steel.

As a consequence, the resolution has an effect on the void counting and logically on the void density evolution as seen in Figure IV.5 and no effect regarding the void growth. The presence of larger voids has lead to propose an extended ductile damage model introducing the void coalescence evolution (detailed when presenting the GTNBF model).

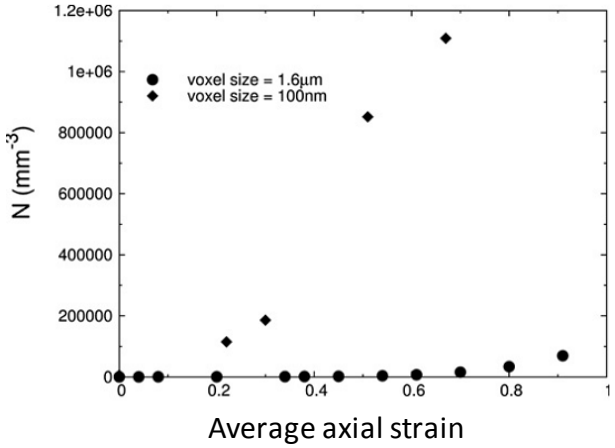

Figure IV.5: Evolution of the void density in the studied sub-volumes acquired with different voxel sizes during the tensile test for DPI steel.

IV.2.2.4 Computation of the total porosity

The current section is dedicated to the computation of the total porosity introduced in the GTNB and GTNBF models. This method has been widely published [BEN 2010-2010a-2011-2011a-2012]. The main work is to reproduce accurately the porosity evolution integrating the experimental observations of Maire et al. [MAI 2008] and the analytical void density and size evolutions proposed by Bouaziz et al. [BOU 2008].
The method consists in substituting the evolution of the real material composed of martensite and ferrite by the evolution of an equivalent virtual material as seen in Figure IV.6.

Figure IV.6 shows the evolution of a Representative Volume Element (RVE) of the real and the virtual materials between two instants t_1 and t_2. The real RVE is chosen as the minimum material volume containing the entire microstructure materializing the Dual-Phase steel. The complex evolution of the number and the size of voids in the real material are replaced by the evolution of the number of identical voids *N*, which have the same radius *R*. This mean radius applies to both voids that were already present and those who just nucleated (see Eqs. (IV.8)). The mean radius evolution is computed by (IV.9).

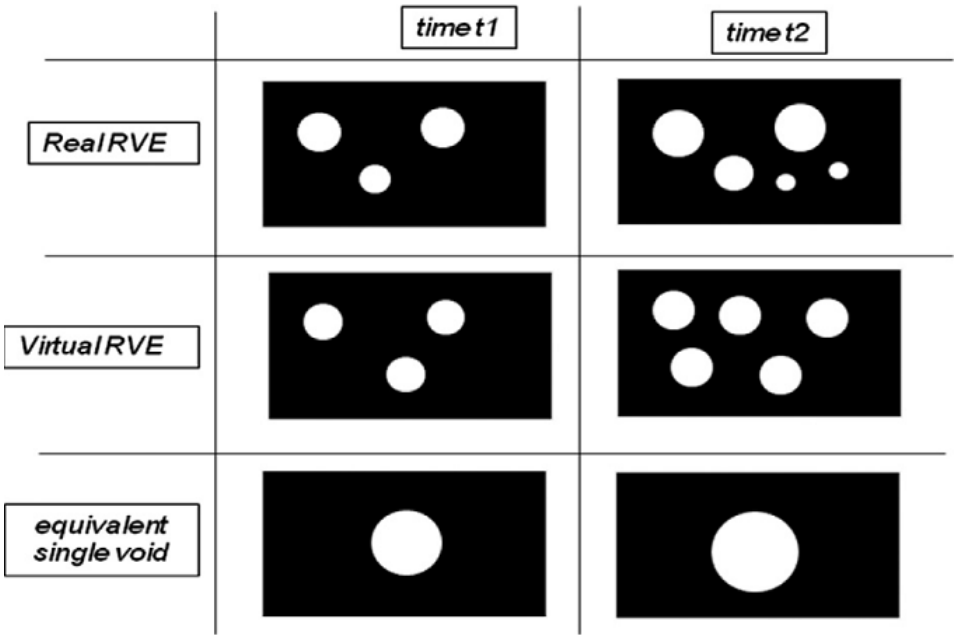

Figure IV.6: Different stages of the modeling of the porosity evolution [BEN 2012].

The void volume fraction f is defined by the following expression:

$$f = \frac{V_v}{V_m + V_v} \tag{IV.11}$$

Where

V_v is the total volume of voids, V_m the volume of the matrix.

The evolution of the porosity f constitutes a state variable depending on *N* and *R*.

Hereafter, the second part of this section illustrated how the porosity evolution is integrated in the GTNB model and its extension (GTNBF model). The method adopted in the ductile damage can be pictured with the final line representing the equivalent single void sketch at two instants t_1 and t_2 (see Figure IV.6). In this approach, the real population of voids is replacing by one single equivalent void. This void has the same volume than the sum of the volumes of the different voids defining the real population. This idea permits to integrate the homogenization model used by Bouaziz et al. [BOU 2008] and other authors [ZHA 2001] [XUE 2008]. The homogenization modeling stipulates that the increase of the void volume fraction is accumulated of the existing voids is and homogenized as one void. In other word, the volume of an equivalent single void is the same as the total volume of *N* identical voids. With this idea, the equivalent mean void radius R_{eqv} can be expressed as:

$$R_{eqv} = \sqrt[3]{N} R \tag{IV.12}$$

When replacing *N* (Equation (IV.8)) and *R* (Equation (IV.9)) in the equation (IV.12), one can easily notice that R_{eqv} depends on the triaxiality *T* and the equivalent plastic strain ε_{eqv}^{p}. It is

also to see that the nucleation evolution predicted by Bouaziz et al. is integrated in the growth of the equivalent mean void radius.
The integration of the evolution the porosity f can be found by using the plastic incompressibility of the matrix and the associated plastic normality law defining the plastic flow rule as following:

$$\underline{\dot{\varepsilon}}^{p} = \dot{\lambda}\frac{\partial F_p}{\partial \underline{\sigma}} \quad \begin{cases} \dot{\lambda} = 0 & \text{if} \quad F_p < 0 \\ \dot{\lambda} \geq 0 & \text{if} \quad F_p = 0 \end{cases} \tag{IV.13}$$

Where $\dot{\lambda}$ is the plastic multiplier. $\dot{\lambda}$ is adjusted at any given plastic strain rate $\underline{\dot{\varepsilon}}^{p}$ to ensure that the ratio $\partial F_p / \partial \underline{\sigma}$ cannot leave the yield surface during plastic deformation. F_p is the anisotropic yield function [BEN 2012] (see Eq. (IV.1)).
The porosity f can be modeled by replacing the expression of the equivalent mean radius R_{eqv} in Eq. (IV.11).

$$f = \frac{(4/3)\pi R_{eqv}^3}{V_m + (4/3)\pi R_{eqv}^3} \tag{IV.14}$$

In the initial Gurson model [GUR 1977], the void volume fraction rate for growth step remains the one defined in GTN approach and linked to the incompressibility of the matrix:

$$\dot{f}_g = (1-f)\,tr\left(\underline{\dot{\varepsilon}}^{p}\right) \tag{IV.15}$$

The Gurson's assumption imposed that V_m the volume of the matrix remains constant during the loading, which means:

$$\dot{V}_m = 0\,. \tag{IV.16}$$

The combination of Eq. (IV.11) and Eq. (IV.15) gives:

$$tr\left(\underline{\dot{\varepsilon}}^{p}\right) = \frac{\dot{V}_v}{V_m + V_v} \tag{IV.17}$$

The evolution of the total void volume is related to the evolution of the equivalent mean void radius by the relationship:

$$\dot{V}_v = 4\pi R_{eqv}^2 \dot{R}_{eqv} \quad \text{or} \quad \frac{dV_v}{V_v} = 3\frac{dR_{eqv}}{R_{eqv}}$$
$$\text{Combination with Eq (IV.17) gives } tr(d\underline{\varepsilon}^p) = 3f\frac{dR_{eqv}}{R_{eqv}} \tag{IV.18}$$

Ben Bettaieb et al. [BEN 2011] has shown that the normality law can be separated in spherical (left) or deviatoric parts:

$$tr\left(\dot{\underline{\varepsilon}}^p\right) = \dot{\lambda}\frac{\partial F_p}{\partial tr\left(\underline{\sigma}\right)} \quad ; \quad \dot{\underline{\varepsilon}}_{eqv}^p = \dot{\lambda}\frac{\partial F_p}{\partial \sigma_{eqv}} \tag{IV.19}$$

The trace of the plastic strain rate can be rewriting without $\dot{\lambda}$ as following:

$$tr\left(\dot{\underline{\varepsilon}}^p\right) = \left(\frac{\partial F_p}{\partial tr\left(\underline{\sigma}\right)}\right) / \left(\frac{\partial F_p}{\partial \sigma_{eqv}}\right)\dot{\underline{\varepsilon}}_{eqv}^p \tag{IV.20}$$

Using the yield function established in Eq. (IV.1) with the last equation and after some mathematical manipulation, one can obtain the expression below.

$$tr\left(\dot{\underline{\varepsilon}}^p\right) = \left(\frac{3fq_1q_2\sigma_y \sinh\left(\frac{3q_2\tilde{\sigma}_m}{\kappa\sigma_y}\right)}{\kappa\tilde{\sigma}_{eqv}}\right)\dot{\underline{\varepsilon}}_{eqv}^p \tag{IV.21}$$

The equality between Eq. (IV.18) and the equation (IV.21) gives:

$$\frac{dR_{eqv}}{R_{eqv}} = \left(\frac{q_1q_2\sigma_y \sinh\left(\frac{3q_2\tilde{\sigma}_m}{\kappa\sigma_y}\right)}{\kappa\tilde{\sigma}_{eqv}}\right)d\varepsilon_{eqv}^p \tag{IV.22}$$

To guarantee the plastic incompressibility of the matrix and the validity of the above evolution law Equation (IV.22), parameters q_1 and q_2 must vary. Due to the availability of this extra equation, one of the parameters q_1, q_2 and q_3 do not need any more to be postulated, but can be calculated at any time as a state variable. An explicit evolution equation is not available, but this parameter is calculated in order to verify Equation (IV.23). With the purpose to obtain a unique set of parameters $\{q_1, q_2\}$, a second assumption is adopted: q_2 is chosen as the parameter to be calculated with this approach, and the two other parameters are determined as

$$q_1 = \frac{3}{2} q_2 \; and \; q_3 = q_1^2 \tag{IV.23}$$

Using Equation (IV.22), Equation (IV.23) becomes:

$$\frac{dR_{eqv}}{R_{eqv}} = \left(\frac{3q_2^2 \sigma_y \sinh\left(\frac{3q_2 \tilde{\sigma}_m}{\kappa \sigma_y} \right)}{2\kappa \tilde{\sigma}_{eqv}} \right) d\varepsilon_{eqv}^p \tag{IV.24}$$

The parameter q_2 is now a state variable in order to take into account and reproduce the experimental results of the void nucleation Eqs. ((IV.8), (IV.9)) as well as to be consistent with the plastic incompressibility of the matrix. During this study it has been noted that the evolution of q_2 is slow and its value stays close to 1. The relationships in equation (IV.23) are kept along the loading in respect of Tvergaard and Needleman [NEE 1987].

IV.2.3 Experiments and GTNB model comparisons

While building the GTNB model, Ben Bettaieb had no full access on all damage evolution data measured by Maire et Bouaziz on the flat square specimen made of the DPI steel. Therefore, it was not possible for him to provide a complete comparison between his contribution and the experimental damage measurement. The present section has the ambition to complete the previous study [BEN 2012] in the aim to verify the GTNB model and propose some enhancements.

The study used DPI steel sample cut from a 3 mm thick sheet obtained by hot rolling and thermal treatment. The thickness of the sheet was reduced to 1 mm and a smooth specimen was obtained using an electro discharge machine (Figure IV.7a). The sample has three planes of symmetry, and for this reason only one eighth has been meshed. A tensile loading was submitted on the rolling direction coinciding with the tensile direction. Figure IV.7b shows the finite element mesh. A 3D element from Lagamine FE code contains each eight node. A refined mesh was generated near the minimum section where large strain gradients are expected, while a relatively coarse discretization was used in the rest of the specimen where a rather uniform deformation is expected.

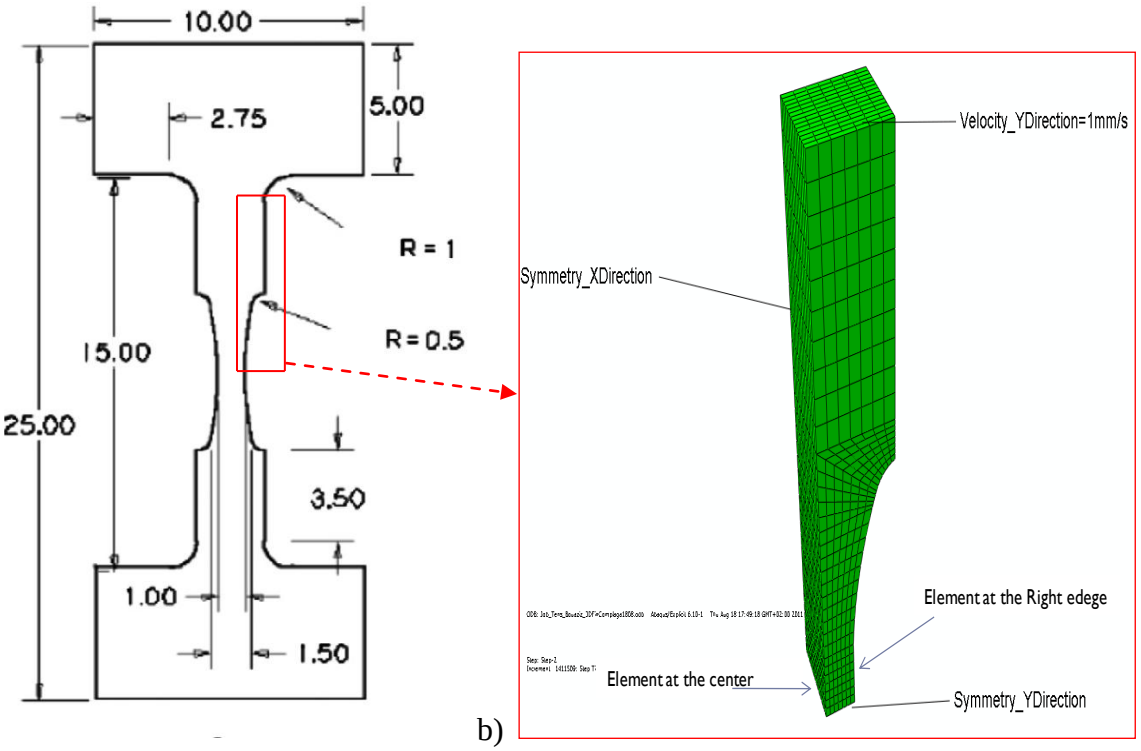

a) b)

Figure IV.7: a) Geometry of the sample (dimensions in mm), b) Mesh of the flat sheet square specimen for DPI steel 1mm thick.

The material parameters of the matrix corresponding to the DPI steel are defined in Table IV.1.

Table IV.1: Elastic, anisotropic, damage material parameters for GTNB model, corresponding to the considered DPI steel.

a) Elastic, anisotropic

Material	Elasticity		Isotropic Hardening			Kinematic Hardening		Plasticity (Lankford Coefficients)		
GTNB model	E (MPa)	ν	K (MPa)	n	ε_0	*Cx*	*Ssat* (MPa)	r_0	r_{45}	r_{90}
DPI steel	210000	0.35	891	0.245	0.02	92.04	58.02	0.85	1.04	0.94

b) Damage, parameters

Material	Initial Damage parameters				Porosity evolution			
GTNB model	f_0	q_1	q_2	q_3	ε_{n0}	A (voids/mm³)	R_0 (µm)	a
DPI steel	0.001	1.5	1	2.25	0.8	5000	2.35	0.25

A comparison between the numerical simulations and the experimental measurements is presented identical with the one performed by Ben Bettaieb [BEN 2012]. This comparison is conducted at two different scales. At a global scale, the accuracy of the assumptions used by Bouaziz et al. [BOU 2008], Maire et al. [MAI 2008] is checked and the prediction of the

evolution of a mean value of the triaxiality in the minimum cross section is compared with the experimental results (Figure IV.8a). At the local scale, the distribution of the damage over the necking section is compared to the experimental results (Figure IV.8b). Different levels of the true strain in the minimum cross section: at 0, 0.17, 0.5, 0.72, and 1. are visualized. The void density and the porosity evolution are analyzed (Figure IV.8c) at the center of the specimen where plastic strain is maximum and the surface (minimum value) see isovalues in Appendix (D.1).

The experimental triaxiality defined previously with Eq. (IV.7) is compared to the surface average of the triaxiality simulated with the GTNB model in Figure IV.8a for the same DPI steel. This comparison shows that the simulated curve is very close to the experimental curve. However, the experimental curve continuously rises at 0.17 of axial strain (critical strain when the void nucleation is activated) whereas the simulated one beginning to show some stabilities at around 0.7 of axial strain. In a global scale, the triaxiality simulation is validated with this result obtained for a square specimen.

A good agreement has been found when comparing the predicted damage state variables evolution with the experimental curve. However, some significant differences between them can be pointed out. The void density and the porosity f evolutions respectively shown in Figure IV.8b and Figure IV.8c remain uniform before the necking and suddenly becomes very heterogonous with a maximum value reached at the center of the sample (see Appendix (D.1)). This observation has been also confirmed in the study of Ben Bettaieb [BEN 2012]. Suddenly at around 0.6 of axial strain a strong increase can be observed after the necking occurs Appendix (D.1). After the necking, the damage continues to rise at a strong pace until attempting its maximum where the plastic strain and the triaxiality reach their maximum. It is noticed that after the necking apparition, the simulation fit less the experimental curve.
This analyze is particularly true for the porosity evolution in function of the axial strain. The graphic (Figure IV.8c) represents the evolution of the porosity extracted from the experiment, and the one from the GTNB model.

The comparison clearly concludes that the GTNB model alone is able to predict the nucleation and void growth evolution before the necking occurs. Unfortunately, the model is not reliable after the necking. The porosity evolution comparison confirms the importance of taking into account the coalescence modelling in the ductile damage model build by Ben Bettaieb et al. [BEN 2012], initially validated for the void nucleation and growth evolutions.

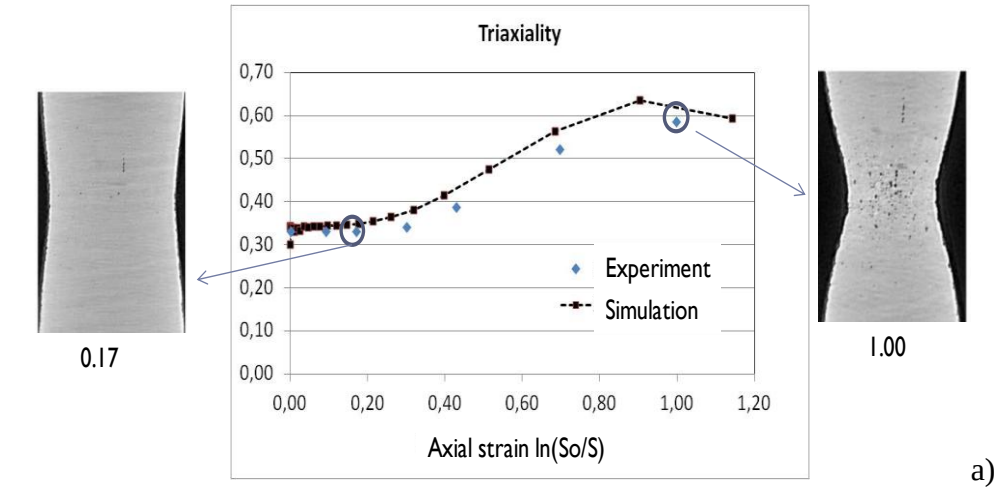

a)

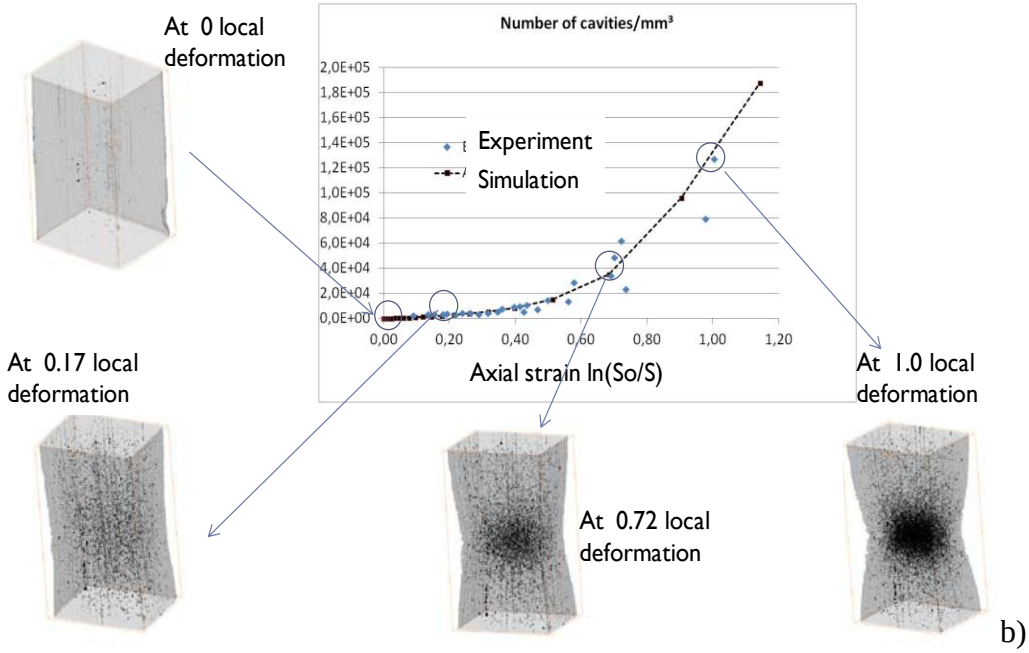

b)

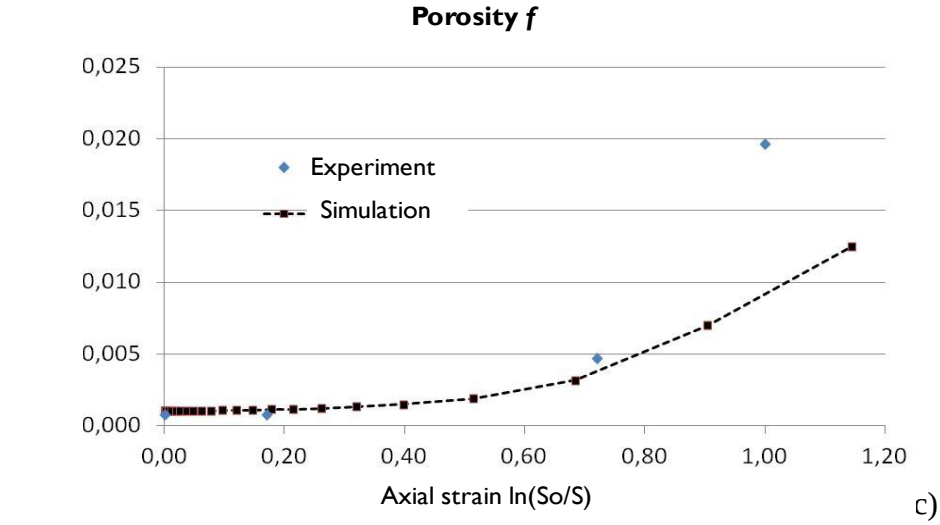

c)

Figure IV.8: Simulation and experimental results comparison of a square flat sheet loaded in tensile direction for DPI steel: a) Triaxiality, b) Void density, c) Porosity *f*.

IV.3 GTNB model extension (GTNBF)

The GTNB model has been previously described. It uses an anisotropic plastic formulation (Hill yield function) coupled with isotropic as well as kinematic hardening. It predicts well the evolution of the damage in a smooth tensile sample. The numerical predictions have shown a global agreement with the experimental results such as the evolution of average triaxiality, evolution and distribution of damage. However, the GTNB model has shown a weakness when comparing the porosity evolution with the experimental results. The model predicts well the porosity before the necking and felt to fit the curve after this event. Therefore, the introduction of the coalescence phenomenon in the GTNB model is needed to complete the ductile damage mechanisms proposed by the GTNBF model.
The GTNBF model is similar to GTNB model presented in section IV.2. However, a new nucleation function is proposed introducing the triaxiality influence extending the model to various geometries and DP steel grades. The model takes into account the kinematic hardening effect by including the backstress in the nucleation law. Indeed, a previous parameter study from Ben Bettaieb [BEN 2012] has shown that the kinematic hardening increases the plastic strain and the triaxiality and also the damage in the necking section.
This advanced physically-based model in line with the experimental X-Ray tomography measurements [LAN 2011] using high resolution is a good opportunity to complete the GTNB model by proposing a GTN coalescence model followed by a fracture initiation prediction focused on DP steels.

IV.3.1 Landron's physically-based void nucleation and growth

IV.3.1.1 Experimental measurements from Landron et al.

The experiments conducted by Landron during her PhD thesis are almost similar to the one realized previously by Maire et al. in the ID15 beam line at the European Synchrotron Radiation Facility (ESRF) in Grenoble, France [MAI 2008]. The same technique and equipment measurement are used. Indeed, Landron [LAN 2011] as well as Maire et al. quantified the ductile damage during the in situ tensile test provided by the X-ray microtomography analysis. As other authors [BUF 1999], [MAR 2000], employed this experimental method to image and quantify the microstructure of the materials. Also, in previous studies Maire & Bouaziz [BOU 2008], Ben Bettaieb et al. [BEN 2012], Fansi et al. [FAN 2013] underlined a strong inhomogeneous nucleation distribution after necking at the minimal cross-section during a uniaxial tensile test performed on DPI steel smooth specimen.
As already known, this steel contains hard martensite islands embedded in a ductile Ferritic matrix and it is particularly submitted to void nucleation mechanism. According to Steinbrenner et al. [STE 1988] and Avramovic-Cingara et al. [AVR 2009], this is due to the interface ferrite/martensite decohesion. Landron extended the work of Maire and Bouaziz (see GTNB model description) by improving the damage understanding. Motivated by modelling the three steps of the ductile damage process (void nucleation, grow and coalescence), the experiment was lead with different specimen geometries (smooth square, cylindrical and

various notched specimens) to characterize the strong effect of the triaxiality on damage. Convinced by the effect of the volume fraction of martensite on the nucleation mechanism, Landron et al. [LAN 2011] observed and quantify the void nucleation evolution on various dual-phase grades containing 0%, 11%, 62%, and 100% of hard martensite islands. Moreover, the same experimental study confirmed the influence of the resolution during the observation and the counting of the voids. Therefore, a voxel size of 1.6µm was used to compare with the bigger resolution used by Maire et al. [MAI 2008].

Several quantities were measured during the tests and used for the validation of the GTNBF model such as:

- The minimal cross-section radius ($r_{section}$) and the notch radius (r_{notch}).
- The applied force (F) device.
- The number of cavities in a fixed spatial volume located at the center of the specimen of dimensions $0.3\times0.3\times0.3mm^3$ (Fig. II.9c) in chapter II) at each step of deformation.
- The porosity *f*, the mean void radius *R* corresponding to the assumption of identical spherical voids, and the mean inter-void distance λ.

More details are given when tackling the material parameters identification in chapter V.

IV.3.1.2 Landron's void nucleation law

Qualitative observations and quantifications through tomography measurements of the void nucleation launched by Landron brought a better understanding of the nucleation mechanism for DP steels [LAN-2011-2012]. As previously mentioned, her study mainly attributes this mechanism to the decohesion of the interface ferrite-martensite. Landron and co-workers quantified and modeled the void nucleation kinetics at the ferrite-martensite interface and by fracture of martensite islands. The Argon criterion [ARG 1975] has been used. According to [LAN 2012], it is defined as a critical stress criterion: void nucleation occurs when a critical stress state necessary to generate interface decohesion is reached in the material. This stress state involves a contribution of the hydrostatic stress σ_m and the equivalent stress σ_{eqv} as following:

$$\sigma_c = \sigma_m + \sigma_{eqv} \tag{IV.25}$$

Where σ_c is the critical shear stress value that the martensite/ferrite interface can support without breaking.
Argon criterion take into account the triaxiality defined by $T = \sigma_m / \sigma_{eqv}$. With this knowledge the critical shear stress expression σ_c becomes:

$$\sigma_c = \sigma_{eqv}\left(1+T\right) \tag{IV.26}$$

In the expression above, Argon [ARG 1975] originally took the stress factor T as the macroscopic triaxiality. However, in the DP steels, the decohesion process occurs at the interface ferrite-martensite. According to Helbert et al. [HEL 1996-1998-1999], local triaxiality is higher at the interface because of the backstress X generated by the difference in mechanical behaviors of the two phases. In DP steels, the difference between the mechanical behavior of ferrite and martensite is quite high. Therefore, it would be better to use the local triaxiality at the interface $T_{decohesion}$. This microscopic stress factor can be estimated using the following expression from Helbert et al. [HEL 1998]:

$$T_{decohesion} = T\left(\frac{\sigma_{eqv}}{\sigma_{eqv} - X}\right) \tag{IV.27}$$

Where the backstress X is a scalar estimated from Allain et al. [ALL 2008] as a function of the respective hardness of martensite $HV_{martensite}$ and ferrite $HV_{ferrite}$ (see function below).

$$X_{decohesion} = 3(1-f_{martensite})\, f_{martensite}\left[HV_{martensite} - HV_{ferrite}\right] \tag{IV.28}$$

$f_{martensite}$ is the volume fraction of martensite.

The critical shear stress expression σ_c integrating the local triaxiality can be rewritten as:

$$\sigma_c = \left[1+T\left(\frac{\sigma_{eqv}}{\sigma_{eqv} - X}\right)\right]\sigma_{eqv} \tag{IV.29}$$

According to Avramovic-Cingara et al. [AVR 2009], void nucleation in DP steels occurred during the entire deformation process, i.e., each single interface probably exhibits a different value of ε_N which is the critical value of the strain for which nucleation starts (the same as Bouaziz et al law, seen section IV.2.2). After the critical strain value, interface decohesion continues progressively and constraining the evolution of the void density to be modeled as a function of strain. Landron proposed an analytical expression of the kinetics of void nucleation (predicting the evolution of the void density N) to fit the experiments based on the equivalent plastic strain and the critical shear stress of the interface decohesion.

$$\frac{dN}{d\varepsilon^p_{eqv}} = \frac{B\ \sigma}{\sigma_c}\left(1+T\frac{\sigma}{\sigma - X}\right)\frac{N}{N_0} \tag{IV.30}$$

Where B and N_0 are material constants.

Figure IV.9 depicts the comparison between the fitted curve and the experimental points obtain with smooth and notched specimens for DPI steel.

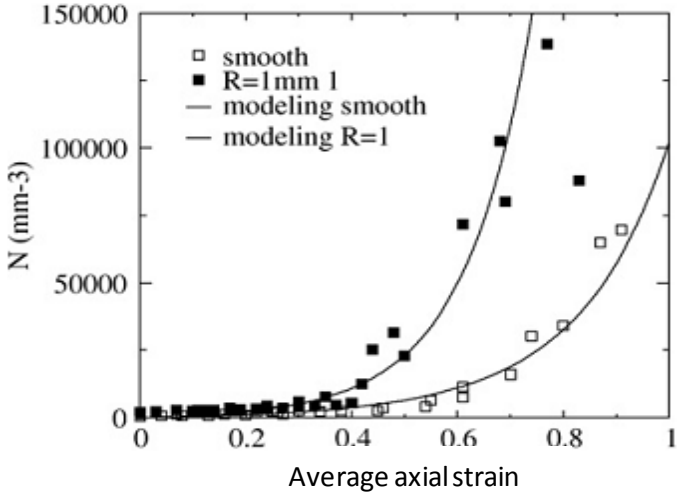

Figure IV.9: Comparison of the prediction of the nucleation model and experimental data for DPI steel [LAN 2012].

Unfortunately, the analytical expression cannot be directly integrated in the GTNB model because of the backstress dimension definition. Indeed, the GTNB model integrates the backstress as a tensor $\underline{X}$ (3-dimensions) through the kinematic hardening law from the modified Frederic Armstrong law (Eq.(IV.3)) while the Landron kinetics of void nucleation defines a backstress as a scalar X (1-dimension). The Landron expression has to be modified to be implemented in the finite element code.

IV.3.1.3 Landron's void nucleation law in GTNBF model

The present part is dedicated on finding a numerical solution to the one- dimensional backstress issue related to Landron's void nucleation expression.

The first step consists to adapt the one-dimensional void nucleation variable to those corresponding to the 3D coordinate system require by the GTNB model. Therefore, σ and $\sigma - X$ have been replaced by the quadratic Hill equivalent stress $\sigma_{eqv}\left(\underline{\sigma}\right)$ and shifted equivalent stress $\overline{\sigma}_{eqv}\left(\underline{\sigma}-\underline{X}\right)$, respectively.

The one-dimensional Landron void nucleation evolution becomes:

$$\frac{dN}{d\varepsilon_{eqv}^{p}} = \frac{B\ \sigma_{eqv\ (\underline{\sigma})}}{\sigma_c}\left(1+T\left(\frac{\sigma_{eqv\ (\underline{\sigma})}}{\overline{\sigma}_{eqv}\left(\underline{\sigma}-\underline{X}\right)}\right)\right)\frac{N}{N_0} \qquad \text{(IV.31)}$$

The expression above can be simplified by introducing a proposed triaxiality T_B. It offers a reasonable generalization to 3D of the original one-dimensional expression of the nucleation law (Eq. IV.30) under the form

$$T_B = \frac{\sigma_m}{\overline{\sigma}_{eqv}\left(\underline{\sigma} - \underline{X}\right)} = T\left(\frac{\sigma_{eqv\,(\underline{\sigma})}}{\overline{\sigma}_{eqv}\left(\underline{\sigma} - \underline{X}\right)}\right) \tag{IV.32}$$

T_B is a triaxiality definition that makes use of this particular form of the equivalent stress. This hybrid triaxiality formula neglects $\underline{X}$ effect on mean stress σ_m but takes it on equivalent stress $\overline{\sigma}_{eqv}\left(\underline{\sigma} - \underline{X}\right)$. It has been checked by extensive tests with virtual material parameters (however still with physical significance) that $\sigma_m(\underline{\sigma})$ or $\sigma_m(\underline{\sigma} - \underline{X})$ are always close as X always remains mainly deviatoric. This will be discussed in chapter VII when describing the potentialities and the limitations of the GTNBF model.

Finally, Landron et al. [LAN 2011] one-dimensional void nucleation is implemented in the GTNBF model as:

$$\frac{dN}{d\varepsilon^p_{eqv}} = \frac{B\ \sigma_{eqv\,(\underline{\sigma})}}{\sigma_c}\left(1 + T_B\right)\frac{N}{N_0} \tag{IV.33}$$

IV.3.1.4 Huang's void growth law

As already mentioned in Chapter III, Landron et al. [LAN 2011] measured with more accuracy the void growth step. The modeling of this damage part has been realized by measuring the evolution the mean diameter of the 20 largest cavities in the DP steels. Although it was observed that the void shape changed during the tensile test (initially spherical, prolate at the end), the strong assumption of no modification of shape during loading has been applied in the model. Indeed, the initial spherical void shape remains until the total fracture occurs.

The experimental contribution of Landron et al. [LAN 2011] validated at different triaxiality states the Huang correction in the classical Rice & Tracey [RIC 1969]. A significant improvement on the growth kinetic model has been seen by introducing the Huang contribution (see Figure IV.10) in the Bouaziz's kinetic law presented in section IV.2.2.3 (Eq (IV.9)).

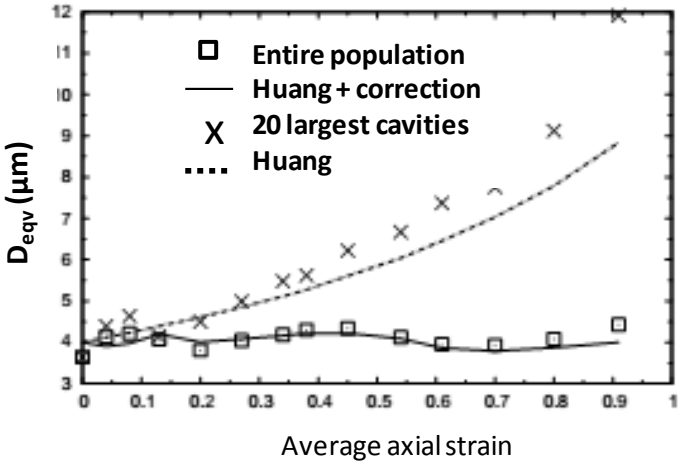

Figure IV.10: Comparison of the prediction of the Bouaziz [BOU 2008] correction applied to the Huang's model and the evolution of the mean equivalent diameter measured over the entire void population for the DPI steel [LAN 2011a].

The evolution of the mean void radius *R* is defined by the Rice and Tracey model [RIC 1969] modified by Bouaziz [BOU 2008], Maire [MAI 2008], and Huang [HUA 1991] to take into account nucleation and different void sizes:

$$\frac{dR}{d\varepsilon_{eqv}^{p}} = \underbrace{\alpha_H \left(T\right)^{1/4}}_{Huang} \overbrace{\exp\left(\frac{3}{2}T\right)R}^{Rice\ \&\ Tracey} \underbrace{-\frac{1}{N}\frac{dN}{d\varepsilon_{eqv}^{p}}\left(R - R_0\left(\varepsilon_{eqv}^{p}\right)\right)}_{Bouaziz\ \&\ al} \qquad \text{(IV.34)}$$

The second term in Eq. (IV.34) is the reduction of the average radius of the cavities due to nucleation, as compared to the initial Rice & Tracey [RIC 1969]. Indeed, it is easy to check that Eq. (IV.34) reduces to the classical Rice and Tracey model when the nucleation rate *dN* is equal to zero. In Eq. Eq. (IV.34) α_H is a material constant introduced by Huang [HUA 1991] in order to fit the model to experimental values. R_0 is the initial mean radius of cavities, at nucleation.

The Huang model will be introduced in the GTNBF model by integrating the proposed triaxiality T_B.

$$\frac{dR}{d\varepsilon_{eqv}^{p}} = \underbrace{\alpha_H \left(T_B\right)^{1/4}}_{Huang} \overbrace{\exp\left(\frac{3}{2}T_B\right)R}^{Rice\ \&\ Tracey} \underbrace{-\frac{1}{N}\frac{dN}{d\varepsilon_{eqv}^{p}}\left(R - R_0\left(\varepsilon_{eqv}^{p}\right)\right)}_{Bouaziz\ \&\ al} \qquad \text{(IV.35)}$$

IV.3.2 Void coalescence law

The proposal of Tvergaard and Needleman [TVE 1984], [NEE 1987] to take into account the coalescence phenomenon has been chosen. The yield function presented in Eq. (IV.1) is only valid for void volume fraction (Figure IV.11:) below a critical value f_c and is now modified when $f \geq f_c$ through the function $f^*(f)$ expressed by:

$$f^* \begin{cases} f \\ f_c + \dfrac{f_f^* - f_c}{f_f - f_c}(f - f_c) \\ f_f^* \end{cases} \quad \begin{cases} f < f_c \\ f_c \leq f < f_f \\ f \geq f_f \end{cases} \tag{IV.36}$$

Where

$$f_f^* = \frac{q_1 + \sqrt{q_1^2 - q_3}}{q_1} \tag{IV.37}$$

and f_f is the ultimate value of void volume fraction when the material completely fails. Initially assumed determined by experiments, this f_f^* value was indeed a hard parameter to define. Additional fracture initiation modeling performed by Abendroth et al. [ABE 2003] as well as numerical investigation of coalescence event lead these authors to an expression for f_f^* (see Eq. (37).

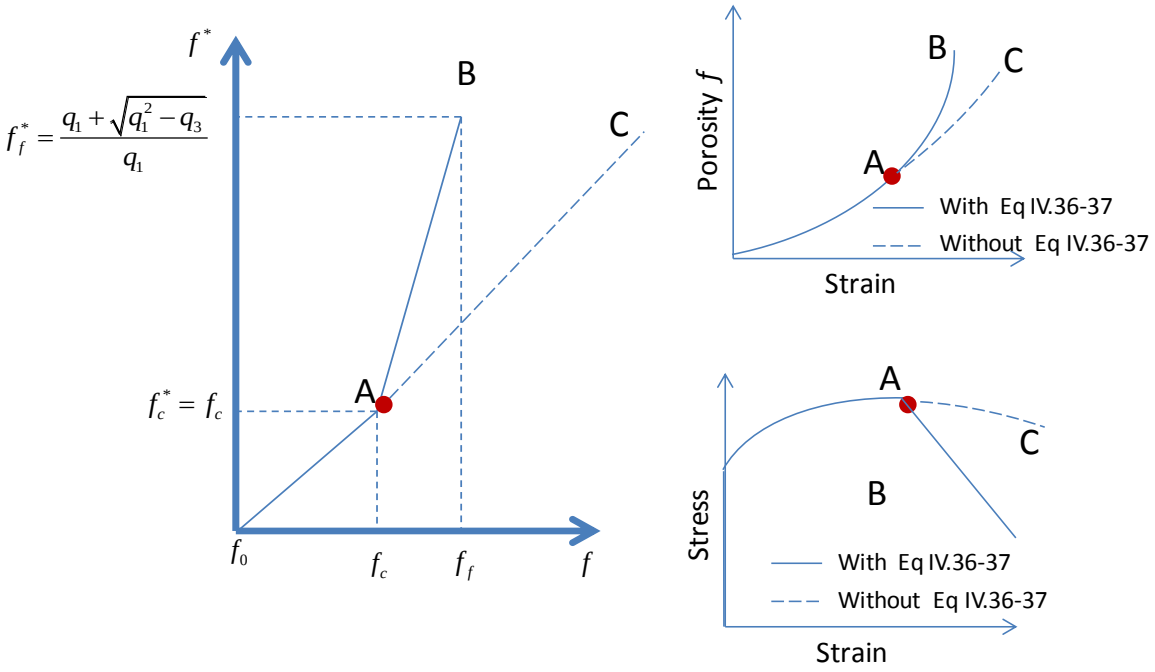

Figure IV.11: Schematic plots f^*, f (left) adopted in GTNBF model stress responses of a material point with and without Eqs.IV.36-37 (right).

This coalescence model implemented in the GTNBF model has been tested with the previous smooth square flat sheet made of DPI steel. The same simulation procedure as the one performed in section IV.2.3 has been computed with the same material parameters. The material parameters for the coalescence model are listed in Table V.3 in chapter V. The porosity evolution measured by Maire et al. [Maire 2008] in function of the axial strain is compared with the GTNB and GTNBF model results, in Figure IV.12 The simulation with the coalescence model (GTNBF model) fits better the experimental curve especially when the axial strain is above 0.7. This deformation state shows a strong necking and a high number of voids in the 3D image as seen in Figure IV.8b. This comparison confirms the importance of integrating the coalescence model in the GTNBF model.

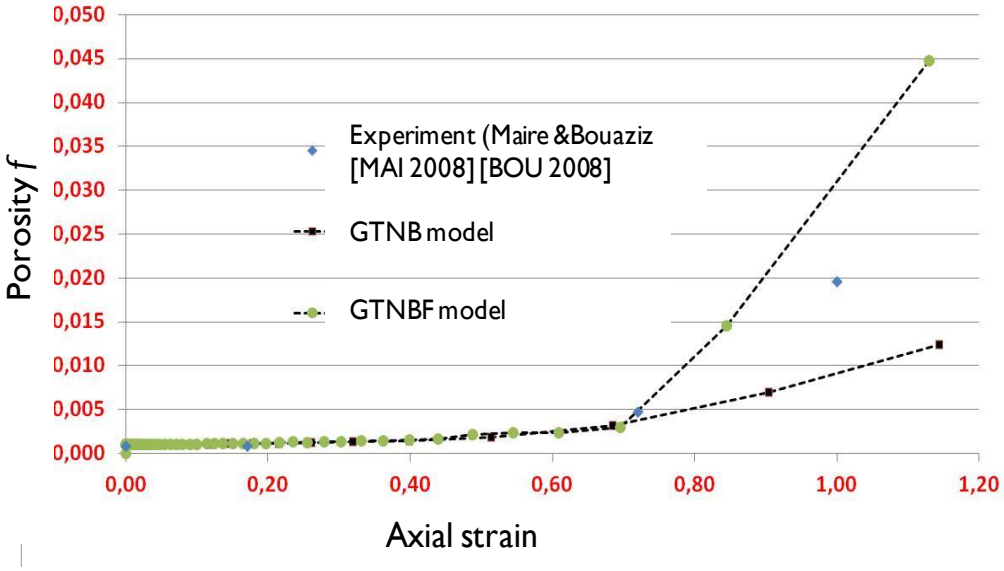

Figure IV.12: Simulation and experimental porosity *f* results comparison of a square flat sheet loaded in tensile direction for DPI steel.

IV.3.3 Fracture initiation modelling

The phenomenological void coalescence law presented in section IV.3.2 is often used for its simplicity to detect the fracture initiation in a specimen with satisfactory results [ZHA 2001], [ABE 2003], [XUE 2008], [RAM 2010]. However, the transition between the beginning of the coalescence and the complete material failure is extremely rapid and brutal and still poorly known. Once coalescence is detected within one element, its stiffness is strongly reduced trough the effect of f^*. Consequently its strain strongly increases and often its shape quickly evolves. Once a true necking is predicted the ratio of element planar edges increases, its thickness decreases and the quality of the element prediction becomes poor.
In order to illustrate this issue, let us consider the cup drawing process defined in Figure IV.13 [LI 2012]. Sheet metal forming by deep drawing is usually the most often chosen manufacturing process used in steel industries. During this process, a constant blank-holder force of about 333kN is applied on the blank sheet (300 x 300 mm²), while the punch (diameter of 75mm) travels downward and draws the 1.5mm thick blank into the die cavity

(type D792, clearance 4.2). A Coulomb friction coefficient value of 0.13 has been introduced in the finite element model to characterize the lubricant named as Quaker 6130 which was applied to all the contact surfaces. In the present study a square punch cross-section has been designed. Corresponding die and blank-holder were employed to match the punch geometry.

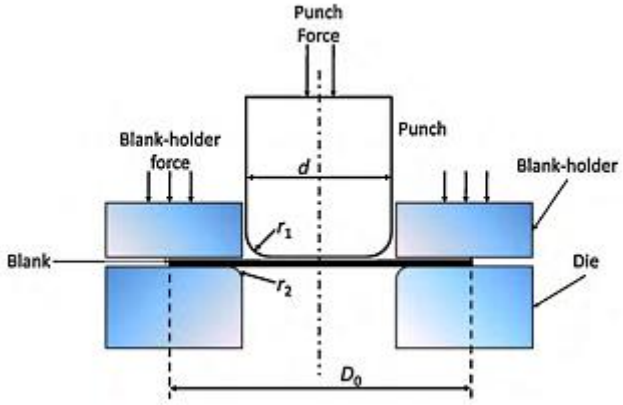

Figure IV.13: Schematic of a Deep drawing forming process [LI 2010]

The material is the DPIII steel, the material parameters are given in Table.V.2. For this problem, the condition $f = f_f$ is simultaneously reached for an entire range of elements located at the punch radius.

Figure IV.14: b shows that the elements impacted by the coalescence stage introduced in the GTN model are distorted just after reaching the ultimate volume fraction value f_f. The sudden rise of the void volume fraction makes difficult an accurate detection of the exact location of fracture initiation area.

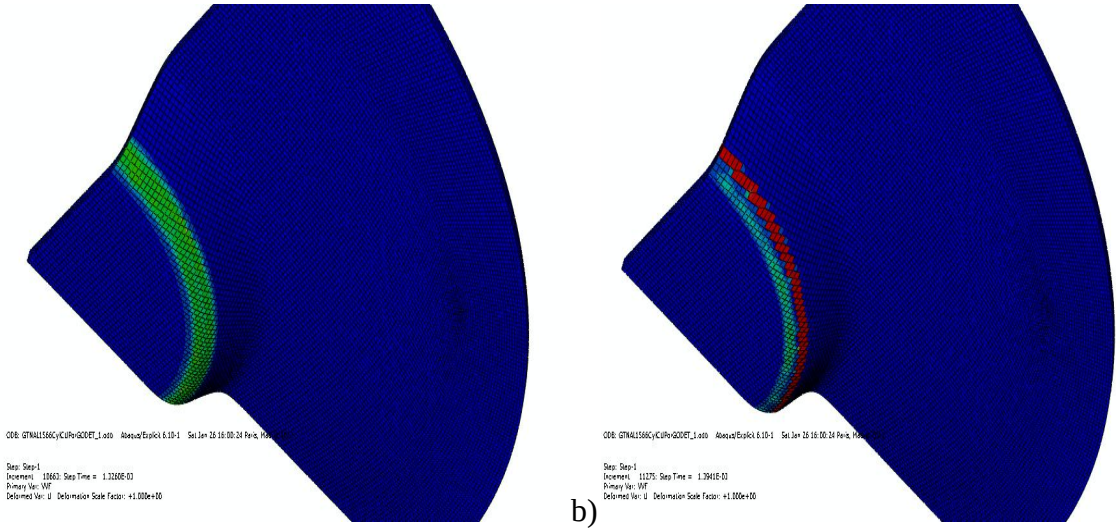

a) b)

Figure IV.14: Visualization of elements impacted by the coalescence stage during the simulation of a cup drawing with a GTN model: a) at $f < f_f$; b) at $f = f_f$ (within the red elements).

One contribution of GTNBF model is to bring some physic within Tvergaard & Needleman proposal [TVE 1984] by coupling it with microscopic observation to improve the accuracy of

the fracture initiation area. An additional fracture initiation model has been included in the GTNBF by integrating the measurement of the mean distance between two cavities (λ) provided by Landron [LAN 2012]. Figure IV.15 illustrates the two and the three-dimensional distributions of voids. This representation assumes that voids are spherical and homogeneously distributed.

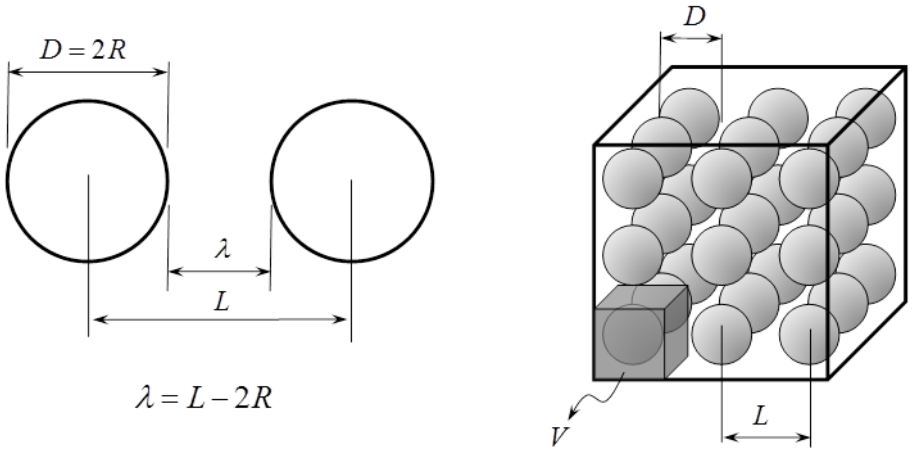

Figure IV.15: Spherical voids distributed in two-dimensions (left) and three-dimension (right) space.

Based on the hypothesis of uniform distribution of identical spherical voids in a three-dimensional domain, the inter-void distance λ can be expressed through the geometrical relation [LAN2011].

$$\lambda = \frac{1}{N^{1/3}} - 2R \tag{IV.38}$$

Where:

- N quantifies the numerical void density (number of voids per mm³) related to L (center to center average inter-cavities distance) by $V = 1/N = L^3$.
- R represents the mean void radius of the voids within the studied spatial volume.

The in-situ porosity measurements of Landron [LAN 2011a] (better described in Chapter VI) are performed within a fixed spatial domain located at the center of the specimen, of a volume of $0.3\times0.3\times0.3\text{mm}^3$. Landron [LAN 2011a] measured the whole void size population during the tensile loading of a notched specimen and found out that the mean radius of cavities can be assumed constant and equal to R_0 (see Figure IV.16).

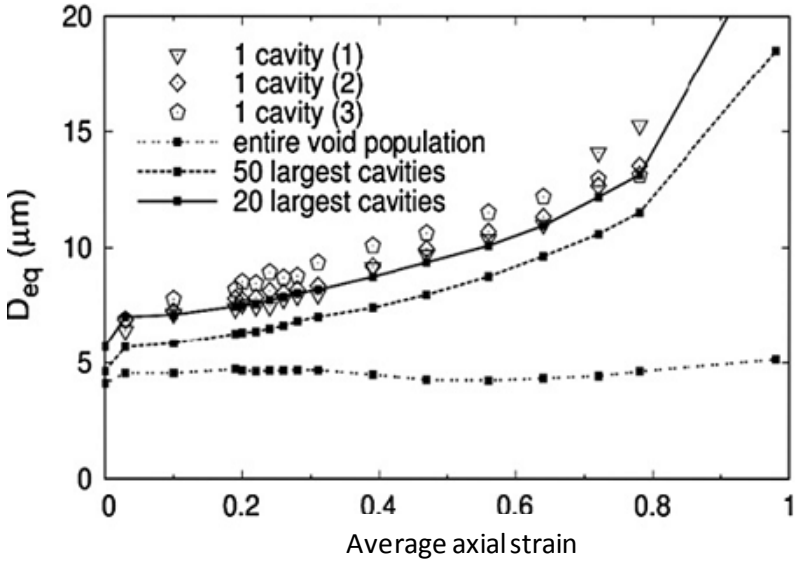

Figure IV.16: Evolution of the mean void diameter for the entire cavity population, the 50 and the 20 largest cavities (DP steel) [LAN 2012].

The porosity f can be defined by the numerical void density N, and the mean radius of the voids:

$$f = \frac{V_{voids}}{V} = \left(4/3\right) N \pi R^3 \tag{IV.39}$$

The experimental determination of the average inter-cavities distance value (λ) before fracture helps to define the fracture initiation criterion for DP steel as a post processing state variable. When the distance between two cavities is equal or less than a threshold λ_f Eq. (IV.38) the material is assumed cracked during the uniaxial test.

$$\lambda \leq \lambda_f \tag{IV.40}$$

λ_f is the ultimate average inter-cavities distance before the material completely fails.

The strong interest of this criterion is that it provides a physical way to determine void volume fraction when the material fails (f_f, see Eq (IV.36)) which is too often identified by numerical ways such as inverse modeling.

$$f_f = \frac{4\pi}{3}\left(\frac{R}{\lambda_f + 2R}\right)^3 \tag{IV.41}$$

The important contribution is here the physical meaning of f_f. Usually value of f_f is phenomenological and a precise material parameter identification campaign has to be launch for each DP steel. It is not the case for the GTNBF model. Indeed thanks to Landron

measurement of the average inter-cavities distance operated on various DP steels, a single value of λ_f as been identify for all DP studied steels. Figure IV.17 depicts the evolution of λ in fonction of the axial strain for varoius volume fraction of martensite. The distance inter-cavities decreases differently from a material to another. The ultimate average inter-cavities distance has been chosen at about 20 µm for all studied DP steels.

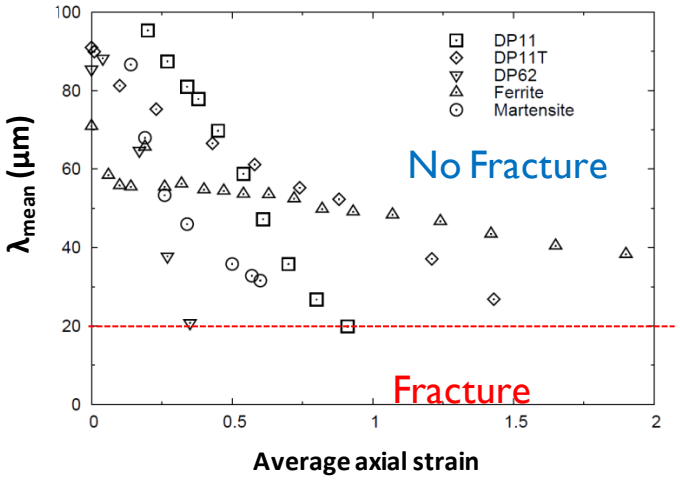

Figure IV.17: Evolution of λ_{mean} with the deformation for the studied steels [LAN 2011].

This equation of the ultimate porosity value is different from the one using the classical metallurgical method based on Rostoker et al. [ROS 1965], Brown & Embury, [BRO 1973] [WEC 2007a] in their planar section approach and written as:

$$f_f = \frac{3\pi}{2}\left(\frac{R_0}{\lambda_f}\right)^2 \qquad \text{(IV.42)}$$

Where R_0 is the mean radius of voids and measured in a plan (2D).

Because Landron measured [LAN 2011] with accuracy λ_f in 3D and for various DP steels, our choice is focused on Eq (IV.41) and integrated in the GTNBF model. The f_f value is calculated in chapter V for the studied DP steels.

IV.3.4 Flowcharts of the extended GTN models

In order to summarize the proposed model and its past evolutions, this section gives an overview of the GTN, GTNB, and GTNBF models. The flowchart components, captured below, only focused on the constitutive equations. The computational and the numerical integration of the constitutive models will be discussed in chapter VI when describing the finite element model implementation.

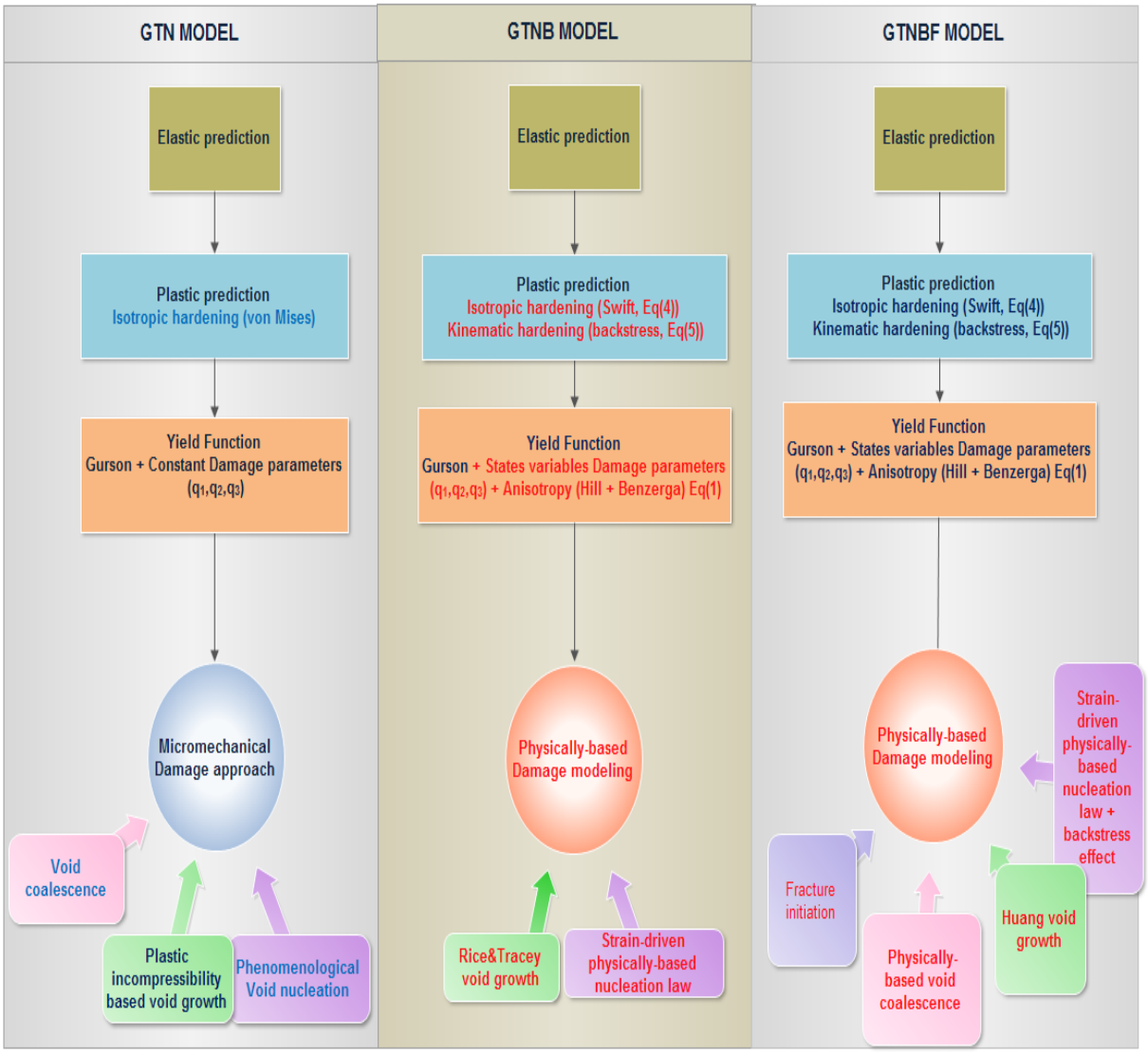

Figure IV.18: Flowcharts of GTN, GTNB, and GTNBF models (with new contributions in red color), Equation numbers referees to current chapter.

For future reference during the next chapters, the full GTNBF model is summarized hereafter, based on the developments introduced during the last two chapters. The model is composed of the set of equations presented in the table below.

Table IV.2: The GTNBF model set of equations.

N°	Equation name	Equation
(1)	The strain decomposition	$\underline{\varepsilon} = \underline{\varepsilon}^e + \underline{\varepsilon}^p$
(2)	The elasticity law	$\underline{\sigma} = \underline{\underline{C}}^e : \underline{\varepsilon}^e$
(3)	The anisotropic yield function	$F_p = \dfrac{\overline{\sigma}_{eqv}^2}{\sigma_y^2} + 2q_1 f^* \cosh\left(-\dfrac{3q_2\overline{\sigma}_m}{\kappa\sigma_y}\right) - 1 - q_3 f^{*2} \le 0$
(4)	The plastic flow rule	$\dot{\underline{\varepsilon}}^p = \dot{\lambda}\dfrac{\partial F_p}{\partial \underline{\sigma}} \quad \begin{cases} \dot{\lambda} = 0 & \text{if } F_p < 0 \\ \dot{\lambda} \ge 0 & \text{if } F_p = 0 \end{cases}$
(5)	The isotropic hardening (Swift) law	$\sigma_y = K\left(\varepsilon_0 + \varepsilon_m^p\right)^n$
(6)	The kinematic hardening (modified Fredericks-Armstrong) law	$\underline{X} = \left(1 - q_1 f^*\right)\underline{X}^*; \quad \dot{\underline{X}}^* = C_x\left(S_{sat}\dot{\underline{\varepsilon}}^p - \underline{X}^*\dot{\varepsilon}_{eqv}^p\right)$
(7)	The macroscopic equivalent plastic strain rate	$\dot{\varepsilon}_{eqv}^p = \sqrt{2\left(\dot{\underline{\varepsilon}}^p : \underline{\underline{H}}^{-1} : \dot{\underline{\varepsilon}}^p\right)}$
(8)	The work equivalence principle	$\overline{\underline{\sigma}} : \dot{\underline{\varepsilon}}^p = \left(1 - f\right)\sigma_y \dot{\varepsilon}_m^p$
(9)	Fansi et al. proposed triaxiality	$T_B = \dfrac{\sigma_m}{\overline{\sigma}_{eqv}\left(\underline{\sigma} - \underline{X}\right)} = T\left(\dfrac{\sigma_{eqv\,(\underline{\sigma})}}{\overline{\sigma}_{eqv}\left(\underline{\sigma} - \underline{X}\right)}\right)$
(10)	Landron et al. void nucleation law	$\dfrac{dN}{d\varepsilon_{eqv}^p} = \dfrac{B\,\sigma_{eqv\,(\underline{\sigma})}}{\sigma_c}\left(1 + T_B\right)\dfrac{N}{N_0}$
(11)	Huang void growth law	$\dfrac{dR}{d\varepsilon_{eqv}^p} = \underbrace{\alpha_H\left(T_B\right)^{1/4}}_{Huang}\overbrace{\exp\left(\dfrac{3}{2}T_B\right)}^{Rice\ \&\ Tracey}R - \underbrace{\dfrac{1}{N}\dfrac{dN}{d\varepsilon_{eqv}^p}\left(R - R_0\left(\varepsilon_{eqv}^p\right)\right)}_{Bouaziz\ \&\ al}$
(12)	Tvergaard & Needleman void coalescence law	$f^* \begin{cases} f \\ f_c + \dfrac{f_f^* - f_c}{f_f - f_c}\left(f - f_c\right) \\ f_f^* \end{cases} \quad \begin{cases} f < f_c \\ f_c \le f < f_f \\ f \ge f_f \end{cases}$
(13)	Physically-based fracture initiation criterion	$f_f = \dfrac{4\pi}{3}\left(\dfrac{R}{\lambda_f + 2R}\right)^3$

IV.4 Conclusions

This chapter presents extensions of the GTNB model to the GTNBF one. This enhancement is based on damage data often difficult to find in literature. The new damage formulation is physically-based on in-situ high resolution X-ray tomography technique (Landron et al. [LAN 2008]). A better description of the three ductile damage stages (nucleation, growth, coalescence) adapted to DP steel has guided all the developments of the GTNBF model.

- The first contribution of this model is a new kinetic law of void nucleation to compute the void density evolution. This model based on Bouaziz and Maire works [BOU 2008] integrates the backstress tensor and the triaxiality factor. The question of the form of the triaxiality factor has been investigated by proposing other definitions (described in section IV.3.2).
- The second improvement concerns the growth model. The experimental contribution of Landron et al. [LAN 2011a] validates at different triaxiality states, the Huang correction [HUA 1991] in the classical Rice & Tracey [RIC 1969]. After modifying the classical model Landron introduced it in the previous Bouaziz's kinetic law used in the GTNB model. The evolution of the mean void radius *R* is defined by the Rice and Tracey model [RIC 1969] modified by Bouaziz [BOU 2008], Maire [MAI 2008], and Huang [HUA 1991] to take into account different void sizes in the DP steel.
- The third enhancement is the coalescence stage. The coalescence event has been precisely observed and quantified by Landron. Accurate information was provided by the use of a high resolution observation technique and some statistical corrections for the measurement of the void radius. The modeling of this phenomenon used the GTN proposal of Tvergaard & Needleman [TVE 1984] added with an experimental identification of f_c and f_f respectively critical and ultimate porosity values. This contribution is further explained in chapter V (material parameters identification).

Chapter V. **Material parameters identification**

Contents

For the purpose of properly evaluating the contributions of the GTNBF model, this chapter is dedicated to the identification of the material parameters required before running the finite element simulation.
The first section presents the constituting the elastic-plastic parameters obtained with ArcelorMittal experimental procedures.
The second section is dedicated to the damage parameters which have been found in the literature review or by the previous work of Ben Bettaieb ([BEN 2011], [BOU 2008], [MAI 2008]).
Then, this section ends by describing the large part of the damage and fracture parameters identification specific to the GTNBF model. The experiments used for the identifications have been realized and presented by Landron during her PhD thesis [LAN 2011a].
The damage parameters related to the void nucleation, growth and coalescence stages have been carefully discussed and compared to the previous Bouaziz & Maire damage modeling. This step was necessary to separate the mechanical, metallurgical and physical contributions. Next step of the work was focused on finding mathematical relations between the damage parameters to reduce their number before numerically integrating them in Abaqus-explicit code.
Finally, the parameters have been compared when available to those found in the literature review on the studied DP steels. The research cooperation with the research team from INSA Lyon (Landron and Maire) has been fructified by the publication of a paper illustrating the numerical integration of damage quantities from 3D X-ray tomography testing in the advanced GTN model for DP steels [FAN 2013].

V.1 Elastic-plastic parameters

V.1.1 Elastic parameters

The elastic parameters defined by the Young's modulus (E) and the Poisson's (ν) coefficient have been deduced from tensile test curves (stress-strain) with a mechanical or laser extensometer (Figure V.1a) and by resonance method (Figure V.1b). The second measurement technique using a piezoelectric ceramic is the most accurate and reproductive method. The specimen is excited to obtain a vibration corresponding to its own resonant frequency which is proportional to the Young's modulus (E) [GEO 2003].

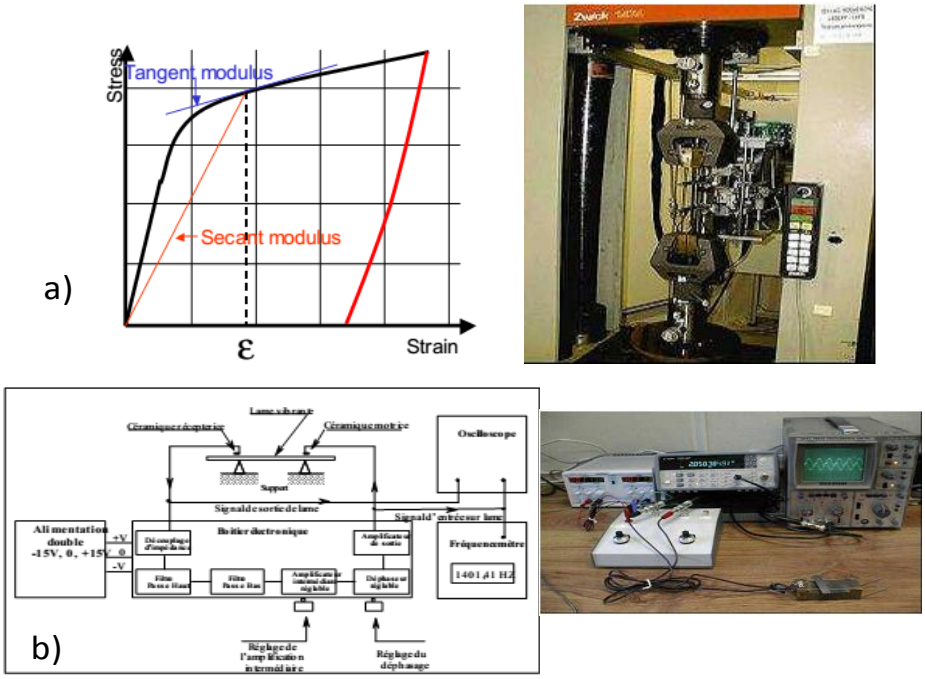

Figure V.1: Determination the Young modulus means of, a) Tensile tests (for a given strain, one can define a tangent and a secant modulus during loading or during unloading), b) Resonance method using a piezoelectric ceramic [GEO 2003].

Several assumptions have been taken when using the elastic parameters in the damage models (GTN, GTNB, and GTNBF). The first hypothesis is to consider that these values are identical for the studied DP steels [PAD 2008], and the second is to admit that they remain constant during the simulation.
Considering the GTNBF model conditions, the Young's modulus (E) and the Poisson's (ν) coefficient have been measured respectively at 210 GPa and 0.35 for the studied DP steels.

V.1.2 Anisotropic plastic parameters

Steel manufacturers usually see two phenomena, characteristics of the anisotropic plastic after the combination of the cold rolled steel sheets and the water cooling (see Figure V.2):

- The surface is hardened, leading to a greater stiffness and resistance in the thickness direction.
- The microstructure is reoriented in the rolling direction.

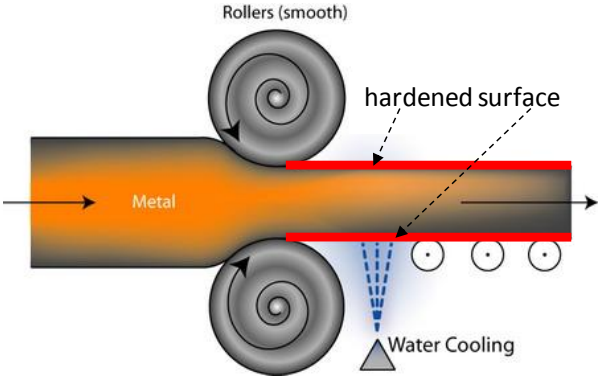

Figure V.2: Hardened surface area during the cold rolled steel sheet (adapted [LOV 2000]).

Nowadays these phenomena are well known by steel manufacturers and researchers [LOV 200], [CAL 2010], [PER 2010], [KAD 2011] who require not an isotropic yield surface such as von Mises coupled with damage modeling (initial Gurson model) but a coupling with a more complex yield surfaces to take into account the microstructure and the texture evolution in DP steels during the sheet-forming process. Most finite element software propose isotropic or anisotropic plastic yield surface such as Hill'48 but rarely couples them to a damage model. Recently, Ragab et al. [RAG 2002], Brunet et al. [BRU 2001], Benzerga et al. [BEN 2001], Monchiet et al. [MON 2006] demonstrated the importance of introducing the plastic anisotropy like Hill'48 in the Gurson model. Considering these contributions, the present part gives some details about the identification of the plastic anisotropic parameters used in the GTNB and GTNBF models.

As already presented in the chapter IV, the anisotropy is introduced in the advanced GTN models by the quadratic Hill'48 matrix $\underline{\underline{H}}$ and the Benzerga & Besson [BEN 2001] parameter κ reflecting the influence of the plastic anisotropy. Both are defined as a function of the Lankford coefficients r_0, r_{45}, r_{90} [LAN 1950] (Chapter IV; Appendix(B.1). From a pragmatic point of view, a simple quantification of these three coefficients corresponding to the rolling direction (0°, 45° and 90°) allowed to estimate:

- The anisotropic equivalent shifted stress (Chapter IV; Eq(IV .1) and Appendix(B.2).
- The equivalent plastic strain in the dense matrix using the pseudo-inverse of Hill's anisotropy matrix $\underline{\underline{H}}^{-1}$ (Appendix(B.1)).
- The anisotropic yield function [BEN 2011].

The Lankford coefficients have been obtained by performing tensile tests for each of the three studied AHSS materials (DP I, DP II and DP III). It is necessary to prepare at least three samples at each of the three orientations (0°, 45° and 90° with respect to the rolling direction, see Figure V.3).

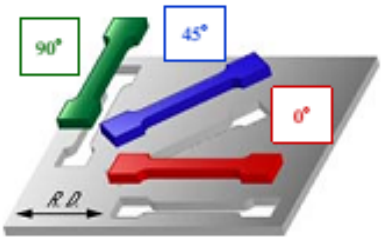

Figure V.3: Tensile specimens corresponding to the rolling direction 0°, 45° and 90° [YOS 2012].

The scalar coefficients r_0, r_{45}, r_{90} representing the normal plastic anisotropy is a ratio between the width and the thickness strains. For each DP steels, the strain ratio ($r_{rolling\ direction}$) in each direction is calculated (see Figure V.4 and Equation (V.1)).

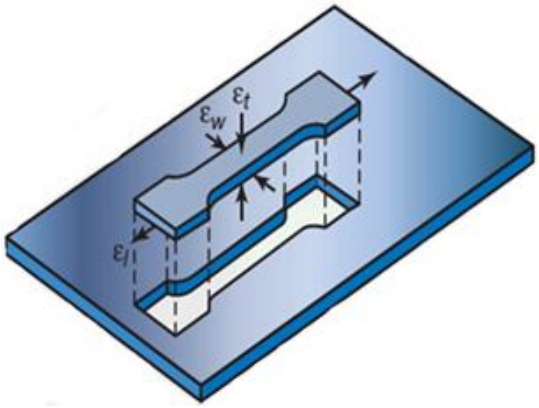

Figure V.4: Definition of the normal anisotropy, r, in terms of width and thickness strains in a tensile-test specimen cut from a rolled steel sheet (adapted [KAL 2008]).

$$r_{0°,45°or90°} = \frac{\varepsilon_w}{\varepsilon_t} \tag{V.1}$$

The ratio $r_{0°,45°or90°}$ is calculated with the width strain ε_w and the thickness strain ε_t.

V.1.3 Isotropic hardening parameters

The most used and easy to implement is the standard uniaxial tensile test. The same test is often performed with local measurement by digital image correlation (DIC) method (Aramis (see chapter VIII), Vialux,...). Figure V.5 compares the predicted and the experimental stress-strain curve for the standard tensile test in the rolling direction at small strain for DPI steel.
The isotropic hardening parameters identification must be done in a larger strain than those obtained in Figure V.5.
Thereby, more complex loading tests are conducted by steelmakers for instance; stacked compression test, bulge test, biaxial tensile test, or uniaxial tensile test prerolled flat sheet.

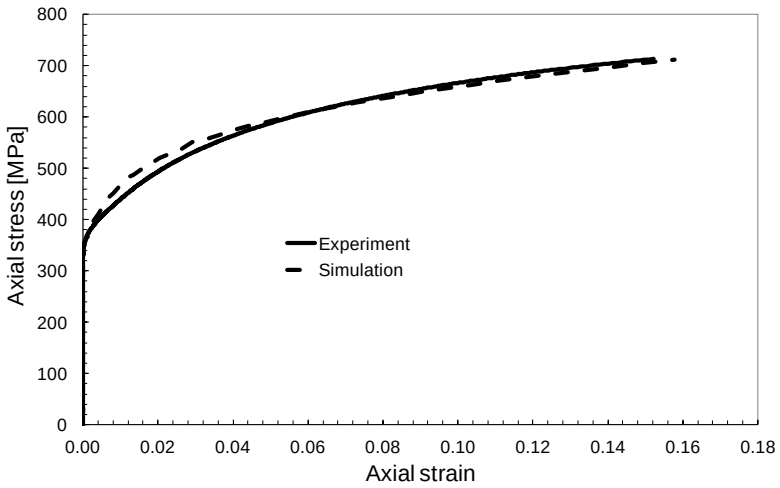

Figure V.5: Axial stress-strain curves comparison between the GTNBF model prediction and the experiment on a uniaxial tensile test for DPI.

At large plastic strains, the selection of an appropriate hardening model is a key factor for accurate sheet-forming FE simulations. ArcelorMittal [LEM 2011] pragmatically used a combination of two classical isotropic hardening models named as the S–V model (see equation (V.2)) standing for the saturating Voce model and the Swift power law [OLI 2005].

$$\sigma = (1+\alpha)\underbrace{K(\varepsilon+\varepsilon_0)^n}_{Swift} + \alpha\underbrace{\left(\sigma_0+\sigma_{sat}\left(1-\exp\left(-C_R\varepsilon\right)\right)\right)}_{Voce} \quad \text{(V.2)}$$

Where K, n, ε_0, and $\sigma_0, \sigma_{sat}, C_R$ are material parameters for the Swift and Voce models. α is a numerical parameter to better fit the model to the experimental curve.
The model parameters are identified with respect to standard tensile tests, and compared to experiments that allowed much larger plastic strain levels (i.e., uniaxial tensile test with local strain measurement, simple shear test, hydraulic bulge test, stack compression test, uniaxial tensile test after flat rolling pre-strain).

Unfortunately, regarding the PhD time framework limitation, the classical isotropic hardening Swift power law has been chosen. In that case, a monotonic shear test has been performed to identify the Swift isotropic hardening parameters (K, n, ε_0) without kinematic hardening contribution, over a wider strain range as compared to the standard tensile test.
Hereafter, Figure V.6 compares the extended curves after uniform elongation for several isotropic hardening models at larger strain for DPI steel.

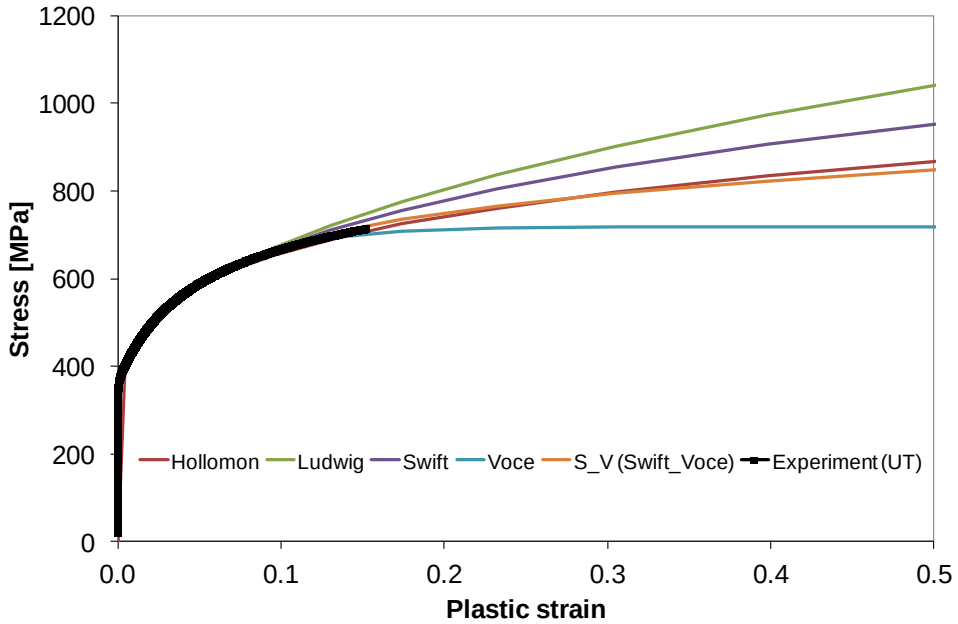

Figure V.6: Prediction/experience comparison of extend curves after uniform elongation defining the choice of isotropic hardening model for DPI steel.

The main goal of conducting a monotonic shear test is to compare and fit the Stress-Strain curve to the one obtained with the uniaxial tensile test. It uses a parameter resulting from least squares method. This method respects two constraints:

- The best approximation of the experimental true deformation curve is between [0.002:ε_{AG}] or [ε_{AE} : ε_{AG}] IF $\varepsilon_{AG} > 0.002$. This boundary is established to be near the curve on a large interval.
- The Swift law passes through the point {$\varepsilon_{RP0.2}$: $\sigma_{RP0.2}$} or { ε_{AE} : σ_{RE}}. This interval is settled to better describe the beginning of the curve.

The method permits to define the Swift parameters for the GTN model and another one for the GTNBF model where a mixed hardening law (isotropic and kinematic hardening) is used.

V.1.4 Kinematic hardening parameters

As seen in previous chapters, the Dual-Phase steel shows significant Bauschinger effect. It is characterized by a transient stage (early yielding strength and work hardening stagnation) and a permanent softening (stress offset). It is necessary to introduce a kinematic hardening law in addition to the Swift isotropic hardening law. The identification of the variant of the Armstrong-Frederick saturating model [ARM 1966] (backstress tensor function $\underline{X}$), adapted to damaged materials requires strain path reversals.

The material parameters to determine are C_x and S_{sat}. Because a simple uniaxial tensile test is not able to predict the Bauschinger effect, numerous mechanical tests have been proposed [LEM 2008] for instance; tension–compression, simple and reversible shear or bending-unbending tests (see Figure V.7). Our choice has been focused on the reverse shear test served for the identification of these parameters.

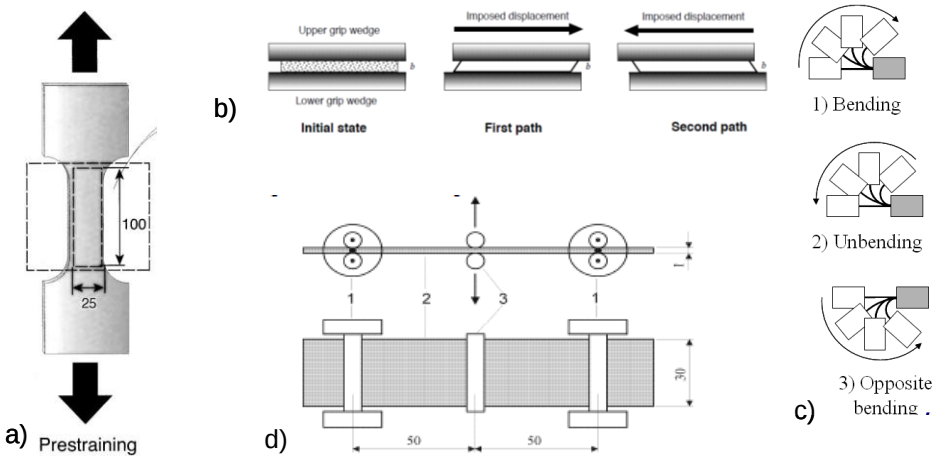

Figure V.7: Reversible tests: (a) tension-compression or compression-tension, (b) reversible shear test, (c) pure bending-unbending, (d) 3pts bending-unbending [LEM 2011].

The simple and the reversible shear are described as conformed to ArcelorMittal procedure [LEM 2011].

Reversible shear test

A simple shear test (Figure V.7b) is performed by imposing a horizontal displacement of the piston. The gap between grip wedges must remain constant. Since the active area of the simple shear specimen is very small, they use a high-resolution optical technique to determine

the shear strain γ in the middle part of the specimen, in order to increase the accuracy. The shear stress is deduced by the shearing force (F) divided by the length (l) and by the thickness (t). This value of the shear stress is the average shear stress along the specimen. The average shear stress is adopted as current value of the shear stress in the stress-strain correlations, with an error that is less than or comparable with the experimental one. A reverse test is obtained by imposing a displacement in one direction and then imposing a displacement in the opposite direction.
The shear test allows reaching large strain level but it is generally limited by the buckling for thin sheet. The monotonous path of shear test reaches equivalent tensile strain values of 0.3 or 0.5 depending on the thickness and the material. For a question of measurement accuracy, it is not possible to perform a small strain (< 0.04).
Figure V.8 shows the stress-plastic strain curves after the reverse shear test for the DPIII steel. The comparison between the experimental curve and the Armstrong-Frederick saturating model (1X- 1backstress) is in good agreement. However a good prediction at the elbow is not sufficient and the predicted curve needs a modification by the isotropic hardening parameters.

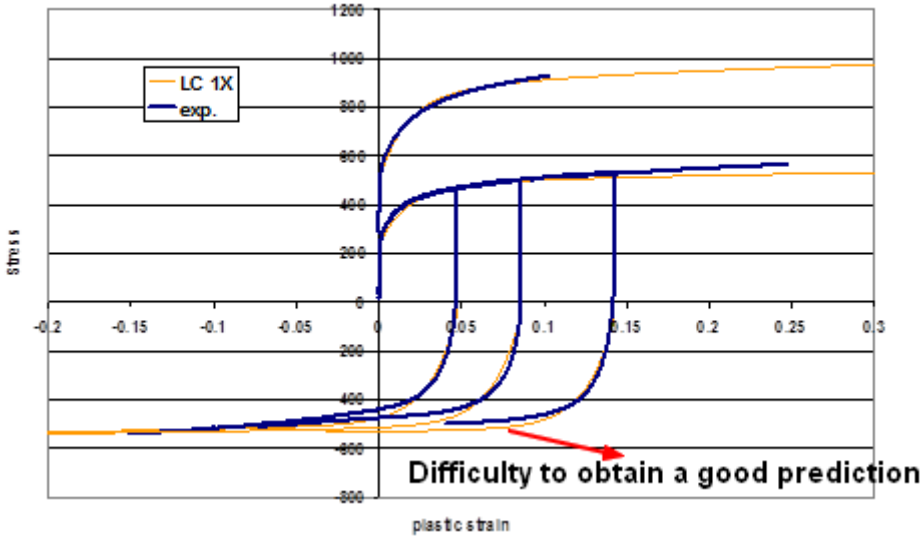

Figure V.8: Comparison of predicted flow curves for reverse shear test (SH +/-) with kinematic hardening and experimental test results for DPIII steel.

V.2 Damage and fracture parameters

V.2.1 GTN model

The GTN model presented in Chapter III was integrated in the finite element software Abaqus/Explicit. However, nine parameters (q_1, q_2, q_3, f_0, f_c, f_f, ε_N, S_N, f_N) are needed to complete the damage contribution. These have been found for all studied DP steels in a literature survey. The values q_1 =1.5, q_2 =1.0, and q_3=2.25 were recommended in Tvergaard & Needleman [TVE 1984] and Needleman & Tvergaard [NEE 1987] investigations. These values are unchanged in this study. The initial void volume fraction f_0, standard deviation (S_N), mean equivalent plastic strain (ε_N), volume fraction of secondary voids (f_N), critical void volume fraction (f_c) and the final void volume fraction (f_f) values are extracted from the

contributions of Nielsen et al. [NIE 2008] for the DPI, Ramazani et al. [RAM 2012] regarding the DPII, and Mishra et al. [MIS 2011] for the DPIII steel.

V.2.2 GTNB model

The GTNB model developed by Ben Bettaieb et al. [BEN 2011] and described in Chapter IV integrates the damage modeling physical-based on in-situ tensile test using X-ray tomography measurements method. For the first time, the porosity evolution was predicted with a micromechanical model extracted from 3D experimental tests [BOU 2008] [MAI 2008]. As already mentioned, the GTNB model requires damage parameters representing the nucleation and the growth stages quantified during the contribution works of Bouaziz et al. [BOU 2008] and Maire et al. [MAI 2008] on a square smooth specimen made of DPI steel.
The void nucleation kinetic is characterized by the numerical void density N (number of voids per unit volume) related to the triaxiality T and to the macroscopic equivalent plastic strain ε_{eqv}^{p}. There are two parameters to introduce in the finite element simulation: A (5000 voids/ mm³) is a material constant and ε_{N0} (0.8 at T equal to 0) designates the value of this critical strain for pure shear loading.

The void growth stage is defined by the evolution of the mean void radius R related to the triaxiality T and the macroscopic equivalent plastic strain. It is a Rice & Tracey [RIC 1969] model modified by Bouaziz et al [BOU 2008]. Two material parameters have to be identified: R_0^i (2.1µm) the size of the cavities nucleating at the beginning of the deformation and a (0.25) fixing the importance of the reduction of the size of the nucleating cavities with strain.

These values have been obtained by fitting the void nucleation empirical model to the evolution of the equivalent mean diameter with the experimental points (see Figure V.9). These parameters values used in the Ben Bettaieb et al. damage model will be used again as a reference when comparing GTNB and GTNBF models.

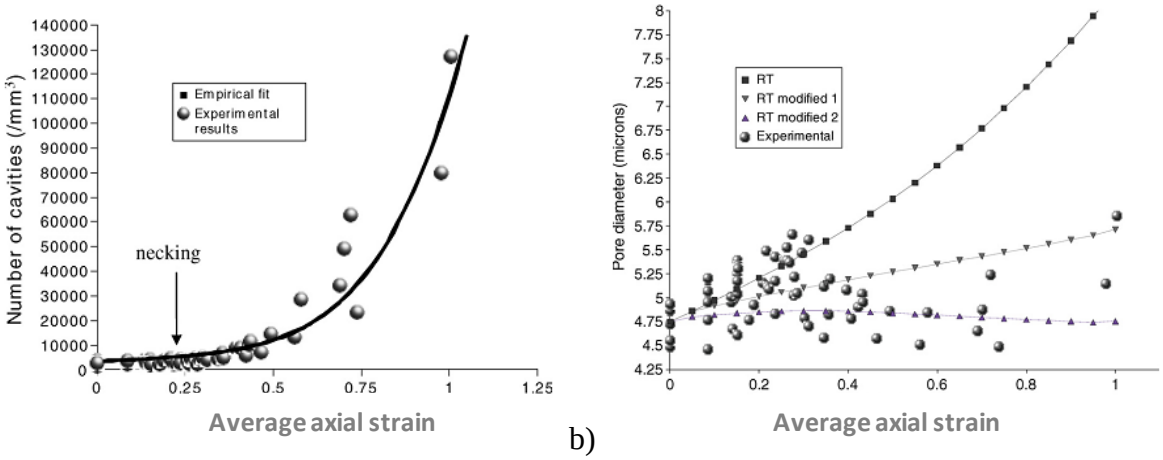

a) b)

Figure V.9: a) Measurement of the number density of cavities N as a function of the average axial strain, b) Evolution with the strain of the equivalent mean radius calculated over the entire void population in DPI steel [MAI 2008].

V.2.3 GTNBF model

The most innovative contribution of the GTNBF model [FAN 2013] concerned the damage modeling (Chapter IV.3). This part is designed on the Landron et al. new experimental investigations [LAN 2011]. During her PhD time framework, Landron identified and completed with more accuracy the void nucleation, the void growth, the void coalescence and the fracture stages for DP steels. Each stage has been quantified by using a non destructive X-ray tomography device (ID15A beamline, see chapter II.2.2) coupled with an in-situ tensile test. The damage parameters have been identified in a volume reconstruction equal to $0.3\times0.3\times0.3mm^3$ (see chapter II.2.3). Smooth and notched axisymmetric specimens (r_{notch} equal to 1mm or 2.5mm) have been machined in the steel sheet. In the case of thin sheets, flat square smooth specimens were machined (the same used by Bouaziz, Maire, and Bareggi damage quantification [BOU 2008], [MAI 2008], [BAR 2012]). The shapes of these specimens are shown in Figure V.10.

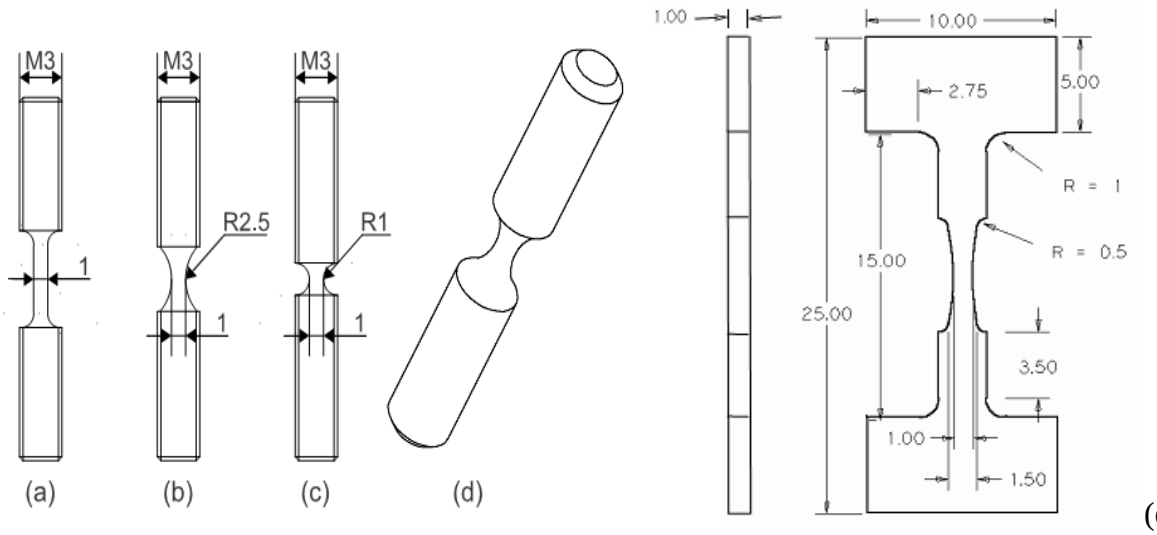

Figure V.10: (a), (b), (c), (d), smooth and notched axisymmetric specimens. This design requires a thickness of the sheet of 3mm at least [LAN 2011], (e) Smooth square specimen used for thin sheets [BOU 2008], [MAI 2008], [LAN 2011], [BAR 2012].

The measurements have been operated with DP steels containing different percentages of volume fraction of martensite (from 0% for Ferrite steel to 100% for Martensite steel).

V.2.3.1 Local deformation and triaxiality measurements

Before identifying the damage parameters, a local deformation and the triaxiality at each deformation step have been estimated focusing on the central cross-section of the specimen. It used the classical post-processing techniques initiated by Bridgman [BRI 1945] for the analysis of tensile test on notched specimens. The total tensile load provided by a load cell is divided by the smallest cross-section area and is reported as the corresponding average axial stress. The number and average radius of the voids are measured in a spatial volume located at the center of the specimen, i.e., at the intersection of the symmetry axis with the plane of the

weakest cross-section. The location of this particular material point is automatically updated during the test. In the mean time, the current radius of this minimal cross-section is recorded as well as the local profile of the neck from which the local neck radius is determined [LAN 2011a]. Due to the small dimensions of the sample and of the testing machine, the grip displacement cannot be reliably used as the driving parameter for the numerical simulation and the comparison to the experiments. Accordingly, the previously enumerated quantities were extracted from the numerical simulation in a manner similar to the experimental treatment, in order to allow a consistent confrontation of the numerical and experimental results (details in chapter VII).

The values of the minimal cross-section radius ($r_{section}$) and the notch radius (r_{notch}) (Figure V.11) are extracted from the outer shape of the specimen. These parameters are necessary to calculate the axial stress, the Bridgman approximation for the triaxiality [BRI 1945] and the axial strain at each loading step. It is important to underline the difficulty to measure the minimal cross-section radius ($r_{section}$) and the notch radius (r_{notch}) after onset of necking. Indeed, at the beginning of the tensile loading the stress state is homogeneous and uniaxial in the specimen. However, when the necking appears, the uniaxial stress state changes to triaxial stress reducing instantaneously the cross-section radius. The minimal cross-section radius cannot be easily located. In the case of round specimen which is our case, the region at the minimal cross-section tends to reduce more than the region just above and below the minimal cross section. According to Choung et al. [CHO 2008], the region above and below the minimal cross-section constrains free reduction of region at the minimal cross section, and a triaxial stress state of hydrostatic stress develops at the region of minimum cross section. This hydrostatic stress does not affect plastic straining because no shear stress is involved in the necked region but contributes to increase the average true stress σ_{axial} for plastic flow.

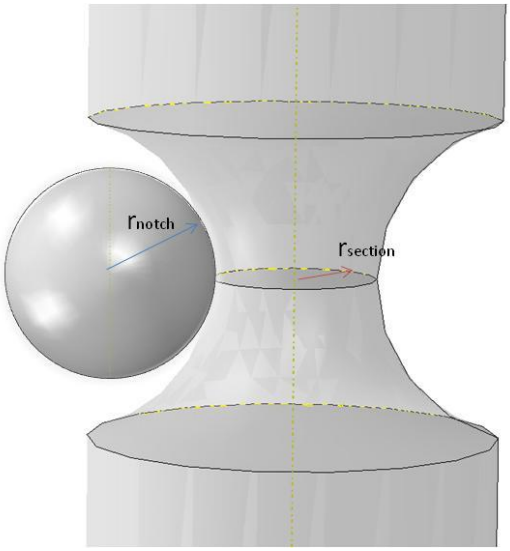

Figure V.11: The geometry parameters required for axial stress and triaxiality computation (using Bridgman's method).

The average stress calculation uses the measurement of the minimal cross-section radius of the specimen ($r_{section}$) and the measured force (F) given by the sensor during the tensile test:

$$\sigma_{axial} = \frac{F}{\pi r_{section}^2} \tag{V.3}$$

The Bridgman formula for the triaxiality T was rewritten in terms of the measured $r_{section}$ and r_{notch} [BRI 1945], [LAN 2011a]. Its expression is:

$$T = \frac{1}{3} + \sqrt{2}\ln\left(1 + \frac{r_{section}}{2r_{notch}}\right) \tag{V.4}$$

The average axial strain is defined as an average value over the entire minimal cross-section:

$$\varepsilon_{axial} = \ln\frac{r_{ini}^2}{r_{section}^2} \tag{V.5}$$

With r_{ini} and $r_{section}$ are the initial and the current radii of the minimum cross-section, respectively (see Figure V.11). Specific post processing of the FE results was applied in order to use the same definitions of triaxiality, axial stress and strain during the entire test for consistent comparisons.

V.2.3.2 Void nucleation

The quantification of void nucleation during the tensile test has been possible by counting the number of cavities N in a fixed spatial volume located at the center of the specimen of dimensions $0.3\times0.3\times0.3\text{mm}^3$ at each step of deformation for each percentage of volume fraction of Martensite (see Appendix (C)):

$$N = \frac{\text{Number of cavities}}{0.027\text{mm}^3} \tag{V.6}$$

Figure V.12 shows the evolution of the number of cavities in the studied volume (left) and the importance of taking into account the triaxiality effect on the void nucleation for a the DPI steel (right).

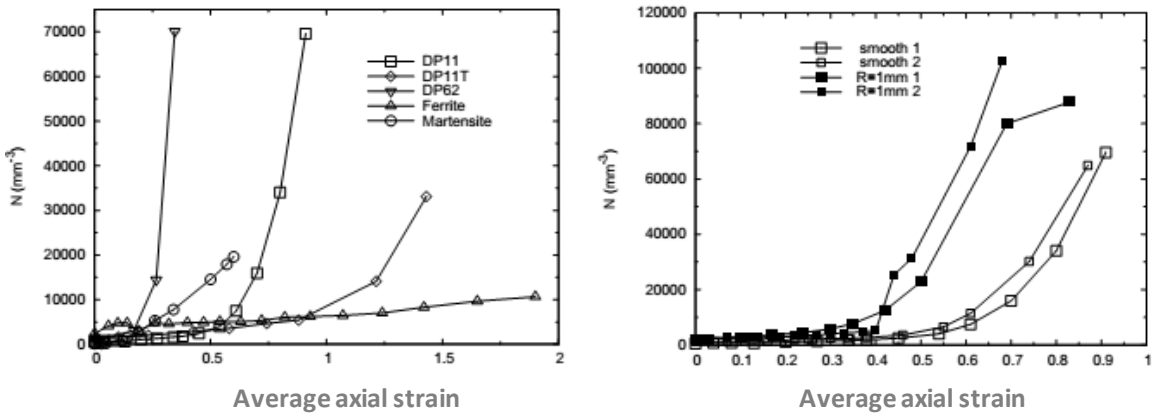

Figure V.12: a) Experimental evolutions of the void density in function of average axial strain for each percentage of volume fraction of Martensite in DP steels, b) for different geometries [LAN 2011a].

According to Landron et al. [LAN 2012] cavities with a volume bigger than 8 µm³ were detected with the use of a voxel size resolution of 1.6 µm. Fortunately, smaller cavities size detection can be improved with higher resolution (voxel size of 100 nm).

Consequently, the quantification of the void nucleation and the observations of their mechanisms (decohesion of the Ferrite/Martensite interface, and the fracture of Martensite islands) conducted to a new void nucleation law base on the Argon's decohesion criterion [ARG 1975] with the Helbert et al triaxiality expression [HEL 1998]. The expression of the void kinetic decohesion is presented in chapter IV 3.1. The integration of this equation in the GTNBF model required the identification of three material parameters: the material constants B, N_0 and the critical shear stress value that the Martensite/Ferrite interface can support without breaking σ_c.

The material constants (B, N_0) are obtained by fitting Eq. (IV.30) to the experimentally measured evolution of the number of cavities for smooth and notched samples (Figure V.13c). As already mentioned, Landron et al. [LAN 2012] have noticed a strong influence of the X-ray diffraction resolution on the number and average radius of the measured voids, and accordingly on the corresponding material parameters B (4500 voids/ mm³) and N_0 (1300 voids/mm³). However, the ratio (B/N_0) appears to be almost insensitive to the resolution of the experimental equipment or to the sample geometry used for the experiment. Accordingly, in the GTNBF model this ratio is considered as a single material parameter equal to 3.46 for all of the simulations.

The average value of the critical shear stress σ_c (Equal to 1100MPa for DPI, Figure V.13b) has been obtained by calculating the value of the stress at the Martensite/Ferrite interface at the experimentally observed nucleation strain (ε_N) for a smooth specimen (ε_N=0.17) and notched specimen (ε_N=0.02) [LAN 2010]. The nucleation strain represents the moment when the void density started to increase Figure V.13a.

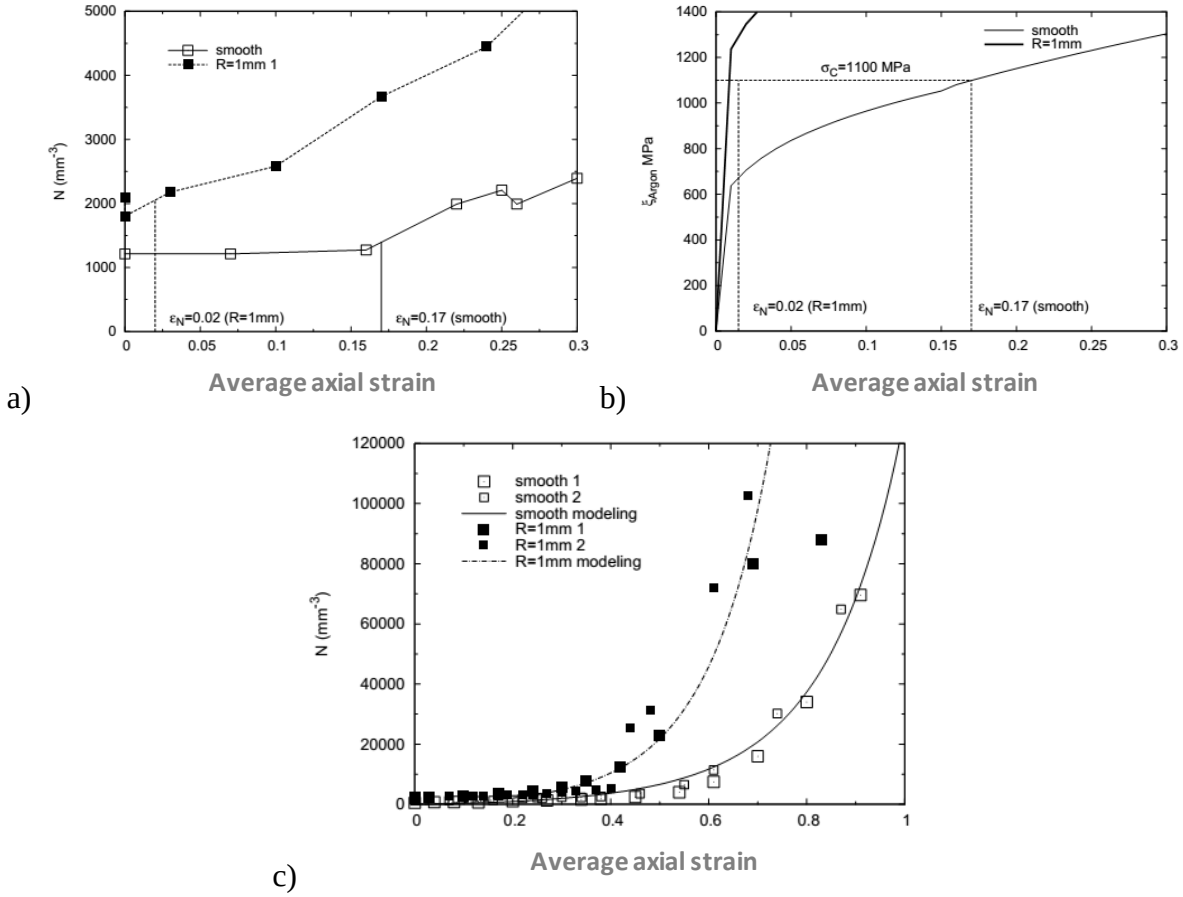

Figure V.13: a) Focus on the low strain region of the evolution on the void density in the DPI steel samples, b) Estimation of σ_c using the modified expression of Argon, c) Comparison of the prediction of the nucleation model using Argon decohesion criterion and experimental data [LAN 2011a].

V.2.3.3 Void growth

The evolution of the void growth has been quantified by measuring the equivalent diameter of the 20 largest cavities (see Figure V.14a). As already mentioned in chapter IV, the track of these cavities is sufficient to represent the entire population. During the measurement the cavities are assumed spherical and remain in this shape at each deformation step, this strong assumption has been settled to facilitate the quantification process. In reality the evolution of the cavities shape depends on the tensile ($D_{tension}$) and the transversal (D_{trans}) directions. Figure V.14b representing the evolution of the ratio W ($D_{tension}$/ D_{trans}) shows that the cavities become more and more elongated or elliptic with a weak triaxiality influence Figure V.14c. The void growth evolution quantification underlines the strong impact of the DP steel microstructure. The increase of the percentage of the volume fraction of Martensite in the material increases the diameter of the cavities (see Figure V.14a).

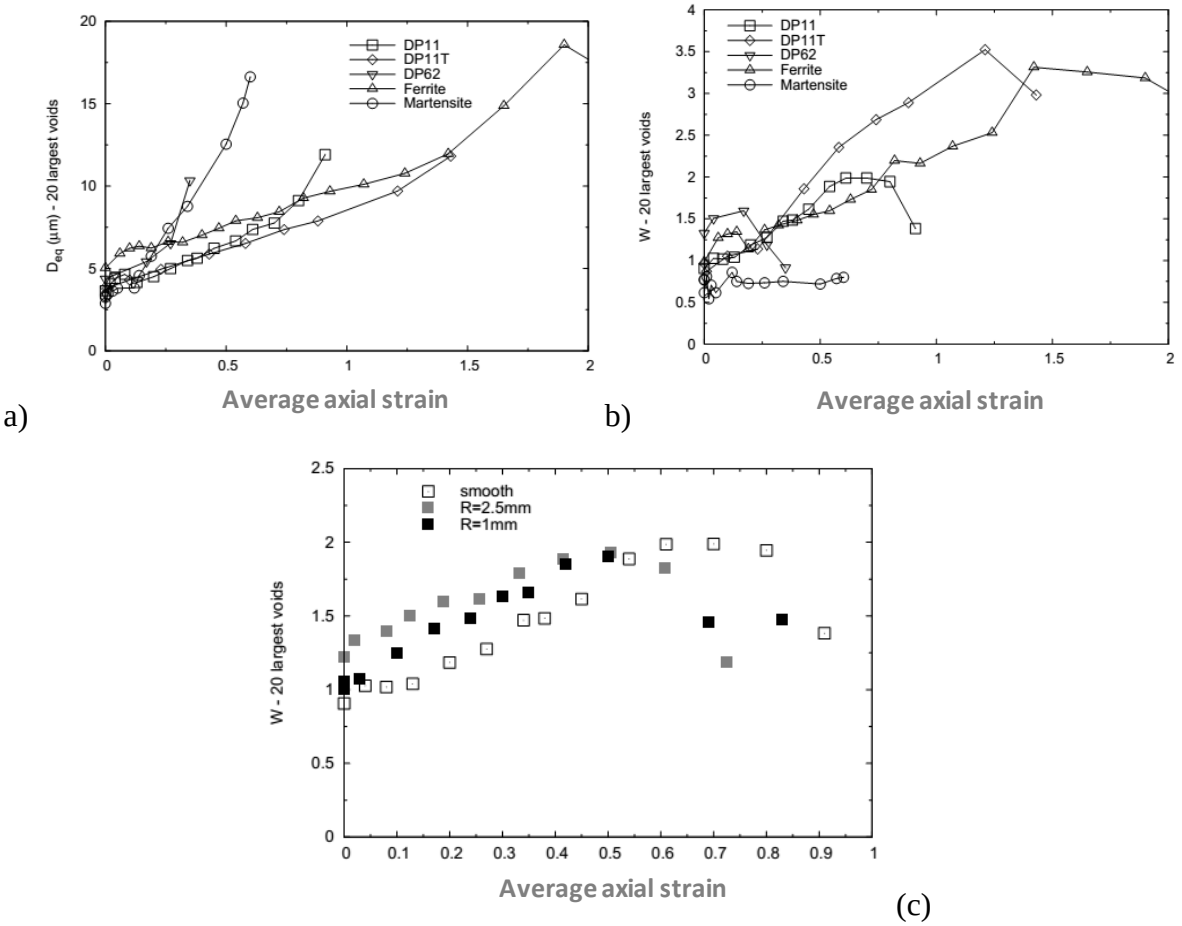

Figure V.14: a) Evolution of the average equivalent void diameter over the 20 largest cavities and b) The evolution of the void aspect in the studied steels, c) Triaxiality effect on the void shape (W) in DPI steel [LAN 2011a].

The observations and the quantification of the cavities diameter in the studied volume allowed Landron et al. to enrich the void growth evolution initially proposed by Bouaziz et Maire. [BOU 2008], [MAI 2008]. The spherical void growth modeling modified the previous one by adding the Huang contribution [HUA 1991] (see Eq.(IV.35).

This expression added another material parameter to be identified: α_H the material constant introduced by Huang. By fitting the experimental void diameter evolution with the proposed model, Landron [LAN 2011a] realized that a single value can be estimated independently of the triaxiality effect. The Huang material constant α_H has been identified chosen equal to 0.55 with respect to the DPI steel.

It is noticed that this parameter evolves with the percentage of volume fraction of Martensite. Indeed, the values of α_H given in Table V.1 increases when the percentage of volume fraction of Martensite increases.

Table V.1: Values of α_H parameter required to fit the model on the experimental void growth curve for different percentages of volume fraction of Martensite adapted from [LAN 2011a].

Steel	volume fraction of Martensite %	α_H
Ferrite	0	0.22
DPI or DP11	11	0.55
DP62	62	1.2
Martensite	100	1.6

Due to the fact that the studied DP steels (DPI, DPII, DPIII) are in the same range of percentage of Martensite in the structure, the α_H parameter is considered the same in the GTNBF model.

V.2.3.4 Void Coalescence

The coalescence model used in the GTNBF model is the same as the GTN model developed by Tvergaard and Needleman [TVE 1984], [NEE 1987] (see chapter IV.3.3). The coalescence model requires the identification of six parameters (q_1, q_2, q_3, f_0, f_c, f_f). The initial values of the Tvergaard-Needleman damage parameters (q_1, q_2, q_3) were kept unchanged from the previous estimation (section V.2.1). The originality of the present model is the accurate introduction of the initial void volume fraction f_0, the critical void volume fraction f_c and the final void volume fraction f_f based on physical measurements with X-ray tomography conducted by Landron [LAN 2011a].
The initial void volume fraction f_0 has been extracted at the beginning of the measurement process. A constant value equal to 2×10^{-5} has been measured for a smooth specimen and 1.2×10^{-4} for a notched specimen independently of the studied DP steels.

The critical void volume fraction f_c has been qualitatively and quantitatively identified by measuring the void volume fraction evolution in a notched specimen. The X-ray tomography observations have been detected at the beginning of the coalescence phenomenon at around 0.5 strain deformation leading to a critical void volume fraction of 10^{-3} for the studied DP steels.
The final void volume fraction f_f have been identified by calculating the evolution of an average inter-cavities distance λ (Eq.IV.38) available until the fracture in the studied sub-volume $0.3\times0.3\times0.3mm^3$. In a pragmatic way, a step deformation before the coalescence begins (indicated by the measurement of the void density N Figure V.15a), Landron has measured the equivalent diameter D_{eq} of the 20 largest cavities (Figure V.15b). The experiment has been operated on a notched specimen because the voids nucleated are more represented and evolved faster. The experimental determination of the average inter-cavities distance value Figure V.15c before fracture helps to define the fracture initiation criterion for DP steel as a post processing state variable. When the distance between two cavities is equal or less than λ_f Eq. (V.7) the material is assumed cracked during the uniaxial test.

$$\lambda \leq \lambda_f \tag{V.7}$$

λ_f is the ultimate average inter-cavities distance before the material completely fails. Figure V.15c shows a value of 0.02mm for three DP steels and 0.04mm for the single-phase steels (Ferrite and Martensite).

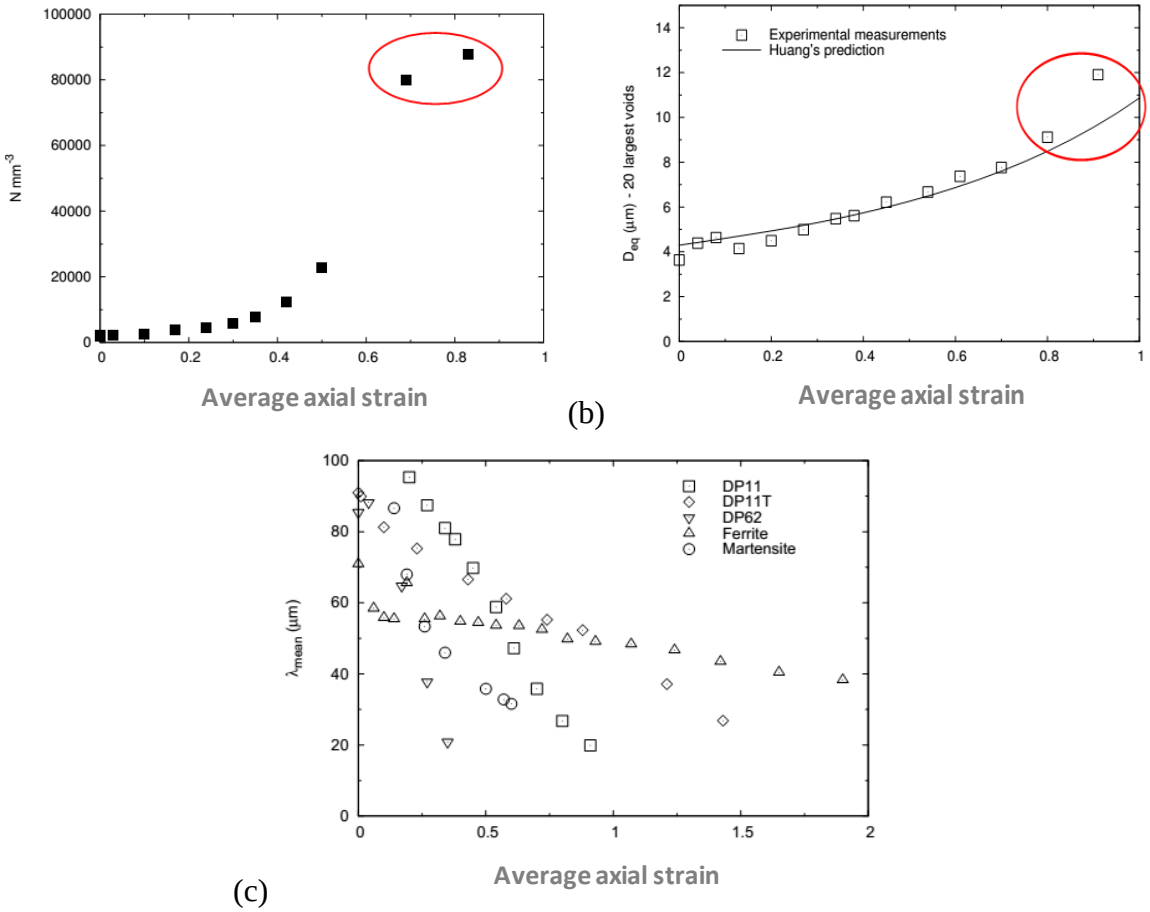

Figure V.15: a) Effect of void coalescence on the measurement of the void density, and (b) The equivalent diameter of the 20 largest cavities in DPI steel: c) Evolution of λ with the deformation for the studied steels [LAN 2011a].

The ultimate average inter-cavities distance λ_f found at 0.02mm for (DPI steel) corresponds to an equivalent diameter D_{eq} of 0.0172mm (20 largest cavities). With these values and the reminded Equation (V.8), it is possible to evaluate the ultimate value of void volume fraction when the material fails. After calculation, f_f is estimated at 0.052.

$$f_f = \frac{4\pi}{3}\left(\frac{R_{20Largest}}{\lambda_f + 2R_{20Largest}}\right)^3 \tag{V.8}$$

Conclusions

In this chapter, the parameters necessary to identify the GTN, GTNBF models have been presented. First of all, the elastic parameters the Young's modulus (E) and the Poisson's (v) coefficient have been deduced from a tensile test curve (stress-strain).

The identification of the anisotropic plastic parameters introduced in the advanced GTN models with the quadratic Hill matrix $\underline{\underline{H}}$ and the Benzerga & Besson [BEN 2001] parameter κ have been possible by measuring the Lankford coefficients r_0, r_{45}, r_{90} from the tensile tests for each of the three studied AHSS materials (DPI, DPII and DPIII). The Swift law modeling the isotropic hardening is characterized by performing a monotonic shear test. This mechanical test allows the identification of following parameters K, n, ε_0. The reverse shear test has been used to predict the Bauschinger effect by defining the material parameters C_x and S_{sat} constituting the Armstrong-Frederick kinematic hardening law [ARM 1966] for the GTNBF model. The elastic-plastic parameters identification follows the in house ArcelorMittal procedure using the least squares method. The author is aware that recent identification methods have been developed permitting better fitting. The elastic-plastic anisotropic parameters can be identified by using inverse method coupled with uniaxial tensile test performed with local measurement by digital image correlation (DIC) method [DEB 2009]. Instead of coupling with a uniaxial tensile test, other researchers used more complex loading such as biaxial tensile test [COR 2006-2007] [YOS 2012], bulge test [NAS 2010], or indentation test [NAK 2007], [CHU 2009].

The damage parameters have been differently identified. The nine parameters (q_1, q_2, q_3, f_0, f_c, f_f, ε_N, S_N, f_N) to enter in the GTN model has been found from the literature review: Tvergaard & Needleman [TVE 1984], Needleman & Tvergaard [NEE 1987] for q_1, q_2, q_3. The other parameters come from Nielsen et al. [NIE 2008] for the DPI, Ramazani et al. [RAM 2012] regarding the DPII, and Mishra et al. [MIS 2011] for the DPIII steel.

The origin of the GTNB damage parameters is a legacy of Ben Bettaieb et al. [BEN 2011], Bouaziz et al. [BOU 2008] and Maire et al. [MAI 2008] joint research on DPI steel.

The most innovative contribution of the GTNBF model concerned the damage modeling. This introduction has been possible thanks to Landron et al. new 3D experimental investigations [LAN 2011]. The void nucleation, void growth, void coalescence and fracture stages have been quantified by using a non destructive X-ray tomography device on flat square smooth and notched axisymmetric specimens for various DP steels.

Table V.2 summarizes the material data for the GTN model for all DP steels studied. The Table V.3 collects the material parameters used to model the GTNBF model. It is noticed that the damage part for the two advanced GTN models will be applied for all DP steels used in the next chapters.

Table V.2: **Material parameters for GTN model**, corresponding to the considered DP steels.

a) Elastic-plastic

Materials	Elasticity		Isotropic hardening			initial q-values and damage			
	E(GPa)	v	K^{GTN} (MPa)	n^{GTN}	$\varepsilon_0{}^{GTN}$	f_0	q_1	q_2	q_3
DPI	210	0.35	1111	0.224	0.0065	1×10^{-5}	1.5	1	2.25
DPII	210	0.35	985	0.17	0.003	8×10^{-4}	1.5	1	2.25
DPIII	210	0.35	1125	0.09	0.001	2×10^{-5}	1.5	1	2.25

b) Damage and fracture initiation

Materials	Fracture coalescence		GTN nucleation law		
	f_c	f_f	ε_N	S_N	f_N
DPI	0.08	0.15	0.35	0.11	0.02
DPII	0.028	0.09	0.2	0.1	0.02
DPIII	6.81×10^{-4}	0.0316	1125	0.09	0.001

Table V.3: Elastic, anisotropic, damage **material parameters for GTNBF** model, corresponding to the considered DP steels.

a) Elastic, anisotropic

Materials	Thickness	Elasticity		Anisotropy (*Lankford coefficients*)		
	(mm)	E (GPa)	v	r_0	r_{45}	r_{90}
DPI	2.5	210	0.35	0.85	1.04	0.94
DPII	1.4	210	0.35	0.915	0.816	1.079
DPIII	1.5	210	0.35	0.94	1.04	1.2

b) Plasticity

Materials	Isotropic hardening			Kinematic hardening	
	K^{GTNBF} (MPa)	n^{GTNBF}	$\varepsilon_0{}^{GTNBF}$	C_x	S_{sat} (MPa)
DPI	891	0.245	0.02	92.04	58.02
DPII	862.95	0.194	0.006	31.44	112.98
DPIII	741.05	0.1017	0.02	62.32	209.28

c) Damage and fracture initiation for DPI, DPII, DPIII

Nucleation and growth parameters							
R_0 (mm)	α_H	B (mm^{-3})	σ_c(MPa)	N_0 (mm^{-3})	A (mm^{-3})	ε_{N0}	a
0.0021	0.55	4500	1100	1300	5000	0.8	0.25

Coalescence parameters Eq. and initial q-values					
f_0	f_c	f_f	q_1(t=0)	q_2 (t=0)	q_3(t=0)
2×10^{-5}	10^{-3}	0.052	1.5	1	2.25

Fracture parameters for DP steels	
λ_F	N_F (mm^{-3})
0.02	80000

Remark: The ratio $B/N_0 = 3.46$ is independent on X-ray resolution, B and N_0 are measured for a resolution of 1.6µm.

Chapter VI. **Implementation of the GTNBF constitutive model**

Contents

VI.1 Introduction

The GTNBF model implementation follows the approach developed by Ben Bettaieb for the implementation of the GTNB model in the implicit Lagamine FE code [ZHU 1992-1995]. A detailed description of the GTNB model implementation has been published in [BEN 2011-2012]. The complete set of equations is solved by an iterative Newton–Raphson method [BEN 2011] [FAN 2012-2013]. In this chapter, details on the constitutive model (GTNBF) implementation in Abaqus/Explicit through a VUMAT user subroutine (**V**ectorized **U**ser **MAT**erial routine) are given. Validations are provided to check the work efficiency.

VI.2 The implementation of the GTNBF model in Abaqus/Explicit

The present section describes the numerical integration of the GTNBF elastic-plastic damage model. This advanced GTN model modified with new physically-based damage equations has been implemented in Abaqus/Explicit via a FORTRAN subroutine VUMAT (Vectorized **U**ser **MAT**erial) [HIB 2010],[FOR 1956],[ADA 1992],[SAN 2001]. This well known commercial Finite element software already integrates a number of ductile damage laws such as: the GTN model (see Chapter IV) [TVE 1987], the Johnson-Cook ductile damage model [JOH 1983-1985] coupled with a phenomenological Chaboche hardening law [CHA 1983].

As previously mentioned, the GTNBF model is a legacy of the initial GTNB model developed within the in-house finite element (FE) code LAGAMINE, developed at the University of Liège over a period of 20 years [ZHU 1992-1995]. Its main advantage is its ability to directly add in a flexible manner new features (constitutive laws, finite elements, remeshing procedure…).
The GTNBF model has been implemented by using an explicit–implicit algorithm (see section VI.2) based on the well known Aravas algorithm [ARA 1987]. The algorithm is explicit with respect to the porosity and implicit with respect to all other state variables such as the stress, backstress, macroscopic plastic strain and yield stress of the dense matrix. Ben Bettaieb [BEN 2011-2012] justified this choice by the complexity of the form of the porosity function and its strong dependency on the different variables. As a drawback, he also noticed that the explicit–implicit algorithm imposes small time steps (or the use of sub intervals) in order to preserve the accuracy.

It is worth noting that when adopting this algorithm in a dynamic explicit code like Abaqus/Explicit, the need for relatively small time steps is no longer a drawback since the time step is already strongly limited by the stability of the overall energy balance algorithm. On the other hand, this approach provides a larger flexibility in changing the damage evolution laws (nucleation, growth, coalescence) since the core algorithm is only marginally affected. Thus this approach is justified in a context of model development, especially as the industrial partner is likely to continuously alter and improve the damage evolution law in the future.

The original algorithm is presented in detail in [BEN 2011-2012] for the GTNB model. This section is focusing on the procedure needed to implement the GTNBF model within Abaqus/Explicit through a VUMAT interface. This procedure is composed of two steps:

- The implementation of the core of the GTNBF model integrating the new damage contributions in a generic form, based on the original Lagamine implementation
- The Lagamine-Abaqus interfacing via a VUMAT subroutine.

VI.2.1 The GTNBF model implementation in Lagamine framework

The number of the equations summarized in Table IV.2 can be reduced by the following steps:

- The isotropic hardening and kinematic hardening plastic laws called mixed hardening have the same unknown $\dot{\varepsilon}^{p}_{eqv}$ and can be reduced to one equation.
- The proposed triaxiality T_B is directly integrated in the Landron's void nucleation equation and the Huang void growth law.
- The physically-based fracture initiation criterion f_f is integrated in the Tvergaard & Needleman void coalescence function f^* which is included in the anisotropic yield function.

After straightforward equation rearrangement, the set of equations presented in Table IV.2 (see Chapter IV) can be reduced to the equations shown in Table VI.1, which are the basis for the numerical implementation.

Table VI.1: The GTNBF model equations to implement.

Equation name	**Equation**
Strain decomposition	$\underline{\varepsilon} = \underline{\varepsilon}^e + \underline{\varepsilon}^p$
Elasticity law	$\underline{\sigma} = \underline{\underline{C}}^e : \underline{\varepsilon}^e$
A anisotropic yield function	$F_p = \frac{\overline{\sigma}_{eqv}^2}{\sigma_y^2} + 2q_1 f^* \cosh\left(-\frac{3q_2\overline{\sigma}_m}{\kappa\sigma_y}\right) - 1 - q_3 f^{*2} \le 0$
Plastic flow rule	$\dot{\underline{\varepsilon}}^p = \dot{\lambda}\frac{\partial F_p}{\partial \underline{\sigma}} \quad \begin{cases} \dot{\lambda} = 0 & \text{if } F_p < 0 \\ \dot{\lambda} \ge 0 & \text{if } F_p = 0 \end{cases}$
Isotropic hardening	$\sigma_y = K\left(\varepsilon_0 + \varepsilon_{eqv}^p\right)^n$
Kinematic hardening	$\underline{X} = \left(1 - q_1 f^*\right)\underline{X}^*; \quad \dot{\underline{X}}^* = C_x\left(S_{sat}\dot{\underline{\varepsilon}}^p - \underline{X}^*\dot{\varepsilon}_{eqv}^p\right)$
Work equivalence principle	$\overline{\underline{\sigma}} : \dot{\underline{\varepsilon}}^p = (1-f)\sigma_y\dot{\varepsilon}_m^p$
Landron et al. void nucleation law	$\frac{dN}{d\varepsilon_{eqv}^p} = \frac{B\,\sigma_{eqv\,(\sigma)}}{\sigma_c}\left(1+T_B\right)\frac{N}{N_0}$
Huang void growth law	$\frac{dR}{d\varepsilon_{eqv}^p} = \underbrace{\alpha_H\left(T_B\right)^{1/4}}_{Huang}\overbrace{\exp\left(\frac{3}{2}T_B\right)R}^{Rice\ \&\ Tracey} \underbrace{-\frac{1}{N}\frac{dN}{d\varepsilon_{eqv}^p}\left(R - R_0\left(\varepsilon_{eqv}^p\right)\right)}_{Bouaziz\ \&\ al}$

Even if based on the GTNB model [BEN 2011-2012], the GTNBF model has several new features that have to be incorporated on the algorithm. f^* Function of the porosity f, used in the anisotropic yield function to take coalescence into account. The Landron's void nucleation model integrating the backstress tensor $\underline{X}$ through a chosen triaxiality function T_B, the Huang's void growth model, and a post-processing allowing to estimate the fracture initiation f_f based on R (mean void radius) and λ_f (ultimate average inter-cavities distance).

The unknowns of the problem can be reduced to $\dot{\varepsilon}_{eqv}^p$ (equivalent plastic strain rate), σ_y (yield stress of the dense matrix), and the component of the normal tensor $\underline{n}$ (n_1, n_2, n_3, n_4, n_5). In our case, the normal $\underline{n}$ is no more coaxial to the Cauchy stress tensor $\underline{\sigma}$ due to the form of the yield function modified by the introduction of the plastic anisotropy through Hill criterion [HIL 1948].

The resolution of this system of equations has been widely published by Ben Bettaieb [BEN 2010-2010a-2011-2011a-2012] and the goal of this current section is to remind the numerical integration principles in Lagamine [ZHU 1992-1995] framework and adapts them to Abaqus-explicit.
A preliminary task to the implementation of the new developments has been to convert the original code from Fortran77 to Fortran95, which was required for the available Abaqus/Explicit platform. This time consuming (and sometimes error prone) task has been advantageously used to rework the structure of the code in order to emphasize modular "box" zones (for example; box1 (elasticity), box2 (plasticity), box3 (damage) etc...) and to make each equation more flexible, quick readable and easy to modify. Obsolete FORTRAN features were deleted and replaced with the FORTRAN 95standard.

Incremental formulation

According to Aravas [ARA 1987], Zhang [ZHA 1995], Zengtao et al. [ZEN 2005], in non linear finite element method, the integration of the constitutive equations is incrementally carried out in each integration point of the mesh and at each time step $I_\Delta = [t,\ t+\Delta t]$. Over I_Δ, the increment of the total strain $\Delta\underline{\varepsilon}$ is assumed to be known. According to Ben Bettaieb [BEN 2011], the objective of the proposed integration scheme is to compute the evolution of the different variables $(\underline{\varepsilon}^e, \underline{\varepsilon}^p, \underline{\sigma}, \underline{X}, f^*(f), \sigma_y, q_2)$ during I_Δ and especially their value at $t+\Delta t$. These variables must satisfy the constitutive equations illustrated in Table VI.1 and their initial conditions at time *t*.

Following Ben Bettaieb's approach, a hybrid explicit-implicit algorithm is used to integrate the constitutive equations of the GTNBF model. Indeed, the hybrid algorithm is explicit with respect to $f^*(f)$ and implicit with respect to the other variables $\underline{\varepsilon}^e, \underline{\varepsilon}^p, \underline{\sigma}, \underline{X}, \sigma_y, q_2$.The implicit part of the algorithm is based on Aravas' algorithm [ARA 1987], which was extended to mixed hardening and plastic anisotropy [BEN 2012]. The constitutive equations are written in an incremental form:

The strain decomposition equation becomes:

$$\Delta\underline{\varepsilon} = \Delta\underline{\varepsilon}^e + \Delta\underline{\varepsilon}^p \tag{VI.1}$$

The increment of the plastic strain $\Delta\underline{\varepsilon}^p$ can be decomposed in the following form:

$$\Delta\underline{\varepsilon}^p = \frac{1}{3}\Delta\varepsilon_p \underline{I} + \Delta\varepsilon_q \underline{n} \tag{VI.2}$$

Where $\underline{I}$ and $\underline{n}$ are respectively the identity second order tensor and a deviatoric second order tensor normal to the Hill criterion, defining the direction of the plastic strain rate (normalized tensor):

$$\left\|\underline{n}\right\|_{Hill} = \sqrt{2\,(\underline{n} : \underline{\underline{H}}^{-1} : \underline{n})} = 1 \tag{VI.3}$$

$\Delta\varepsilon_p$ and $\Delta\varepsilon_q$ are defined by the following relations:

$$\Delta\varepsilon_p = tr(\Delta\underline{\varepsilon}^p) \quad ; \quad \Delta\varepsilon_q = \Delta\varepsilon^p_{eqa} = \sqrt{2\,(\Delta\underline{\varepsilon}^p : \underline{\underline{H}}^{-1} : \Delta\underline{\varepsilon}^p)} \tag{VI.4}$$

The stress tensor at the end of the time increment is defined by the following relationship:

$$\underline{\sigma} = \underline{\sigma}^{Tr} - \underline{\underline{C}}^e : \Delta\underline{\varepsilon}^p \tag{VI.5}$$

Where $\underline{\sigma}^{Tr}$ is the trial stress:

$$\underline{\sigma}^{Tr} = \underline{\sigma}^t + \underline{\underline{C}}^e : \Delta\underline{\varepsilon} \tag{VI.6}$$

The plastic flow rule is written in its incremental form:

$$\Delta\underline{\varepsilon}^p = \Delta\lambda \frac{\partial F_p}{\partial \underline{\sigma}} \tag{VI.7}$$

This can be written in index form:

$$\frac{\Delta\varepsilon^p_{xx}}{\left(\frac{\partial F_p}{\partial\sigma_{xx}}\right)} = \frac{\Delta\varepsilon^p_{yy}}{\left(\frac{\partial F_p}{\partial\sigma_{yy}}\right)} = \frac{\Delta\varepsilon^p_{zz}}{\left(\frac{\partial F_p}{\partial\sigma_{zz}}\right)} = \frac{\Delta\varepsilon^p_{xy}}{\left(\frac{\partial F_p}{\partial\sigma_{xy}}\right)} = \frac{\Delta\varepsilon^p_{xz}}{\left(\frac{\partial F_p}{\partial\sigma_{xz}}\right)} = \frac{\Delta\varepsilon^p_{yz}}{\left(\frac{\partial F_p}{\partial\sigma_{yz}}\right)} = \Delta\lambda \tag{VI.8}$$

The elimination of $\Delta\lambda$ in Eq. (VI.8) leads to:

$$\begin{gathered}
\Delta\varepsilon^p_{xx}\left(\frac{\partial F_p}{\partial\sigma_{yy}}\right) - \Delta\varepsilon^p_{yy}\left(\frac{\partial F_p}{\partial\sigma_{xx}}\right) = 0 \quad ; \quad \Delta\varepsilon^p_{xx}\left(\frac{\partial F_p}{\partial\sigma_{zz}}\right) - \Delta\varepsilon^p_{zz}\left(\frac{\partial F_p}{\partial\sigma_{xx}}\right) = 0 \\
\Delta\varepsilon^p_{xx}\left(\frac{\partial F_p}{\partial\sigma_{xy}}\right) - \Delta\varepsilon^p_{xy}\left(\frac{\partial F_p}{\partial\sigma_{xx}}\right) = 0 \quad ; \quad \Delta\varepsilon^p_{xx}\left(\frac{\partial F_p}{\partial\sigma_{xz}}\right) - \Delta\varepsilon^p_{xz}\left(\frac{\partial F_p}{\partial\sigma_{xx}}\right) = 0 \\
\Delta\varepsilon^p_{xx}\left(\frac{\partial F_p}{\partial\sigma_{yz}}\right) - \Delta\varepsilon^p_{yz}\left(\frac{\partial F_p}{\partial\sigma_{xx}}\right) = 0
\end{gathered} \tag{VI.9}$$

The integration of the kinematic hardening over I_Δ leads to:

$$\underline{X} = (1 - q_1^t f^t)\left(\frac{\underline{X}^{*t} + C_x s_{sat}\,\Delta\underline{\varepsilon}^p}{1 + C_x\,\Delta\varepsilon_q}\right) \tag{VI.10}$$

Analyzing Eqs. (VI.5) and (VI.10), F_p is a function of $\Delta\varepsilon^p_{ij}$, q_2^t, f^t and σ_y:

$$F_p(\underline{\sigma}, \underline{X}, f^t, q_2^t, \sigma_y) = F_p(\Delta\varepsilon_{ij}^p, f^t, q_2^t, \sigma_y) = 0 \quad (i, j = 1,2,3) \tag{VI.11}$$

Eventually, the isotropic hardening equation and the work equivalence rule lead to the following relationship:

$$\sigma_y = K(\varepsilon_0 + \varepsilon_{eqv}^p)^n = \frac{\overline{\underline{\sigma}} : \Delta\underline{\varepsilon}^p}{(1-f^t)\Delta\varepsilon_m^p} \tag{VI.12}$$

The problem of the implicit integration of the constitutive equations reduces to the solution of Eqs. (VI.9), (VI.11) and (VI.12) (7 independent scalar equations). A careful examination of these equations shows that this problem can be reduced to the determination of the unknowns: $\Delta\varepsilon_{ij}^p$ and $\Delta\varepsilon_m^p$ (7 scalar unknowns).

Newton-Raphson resolution method

Table VI.2 summarizes the variables and parameters identified in Chapter V) of the condensed form of the model.

Although the plastic strain rate direction tensor $\underline{n}$ is defined by 6 components $\underline{n} = f(n_1, n_2, n_3, n_4, n_5, n_6)$, because of its unit norm, the expression of $\underline{n}$ can be reduced to 5 independent components . In addition, the familiar incompressibility equation ($n_1 + n_2 + n_3 = 0$) allowed to express easily the component $n_3 = -n_1 - n_2$. Finally, the deviatoric second order tensor takes the following form:

$$\underline{n} = \begin{pmatrix} n_1 & n_4 & n_5 \\ n_4 & n_2 & n_6 = f(n_1, n_2, n_4, n_5) \\ n_5 & n_6 = f(n_1, n_2, n_4, n_5) & -n_1 - n_2 \end{pmatrix} \tag{VI.13}$$

Table VI.2 : The GTNBF model set of variables and parameters.

Variables	Parameters
$\Delta\varepsilon_p$; $\Delta\varepsilon_q$; $\underline{n}$ (n_1, n_2, n_3, n_4, n_5):	Elasticity coefficients: E, ν Isotropic (K, n, ε_0), kinematic hardening (C_x, S_{Sat}),Lankford coefficients r_0, r_{45}, r_{90} Initial damage f_0, q_1, q_2, and q_3, Coalescence law f_c, f_f Voids growth and nucleation laws $R_0, \alpha_H, B, \sigma_c, \varepsilon_{N0}, N_0$. Fracture initiation parameter λ_f.

Finally, the set of seven equations is solved iteratively by using the Newton-Raphson method for a system of equations. The set of equations is written in the generic form:

$$\underline{F}(\underline{x}) = 0 \tag{VI.14}$$

With F the vector of unknowns illustrate in Table VI.2:

$$\underline{x} = \{\Delta\varepsilon_p, \Delta\varepsilon_q, n_1, n_2, n_3, n_4, n_5\} \tag{VI.15}$$

The application of the Newton-Raphson method to (VI.14) leads to:

$$\underline{F}_{nr} + \sum_{l=1}^{7} \frac{\partial \underline{F}^{nr}}{\partial x_l} dx_l = 0 \quad ; \quad nr = 1,....,7 \tag{VI.16}$$

The last equation can be written in a matrix form:

$$\underline{F} = -\underline{\underline{J}}\, d\underline{x} \tag{VI.17}$$

With $\underline{\underline{J}}$ the Jacobian matrix, whose components are defined by:

$$\underline{\underline{J}}_{nr,l} = \frac{\partial \underline{F}^{nr}}{\partial x_l} \quad (k,l = 1,...,7) \tag{VI.18}$$

Eq. (VI.17) is solved to compute $d\underline{x}$ and the value of $\underline{F}$ is then updated:

$$\underline{x} \leftarrow \underline{x} + d\underline{x} \tag{VI.19}$$

This iterative procedure is continued until the convergence condition $Max\left|dF_k\right| < 10^{-6}$ ($k = 1,...,7$) is fulfilled.

The constitutive tangent matrix for implicit code (based on the Jacobian matrix and different terms due to the large strain context) is computed by using the perturbation technique. More details on the computational tangent matrix have been published by Ben Bettaieb et al. [BEN 2010] and Miehe et al. [MIE 1995]. This technique is based on a forward difference approximation, which reduces the computation of the tangent moduli to multiple stress integrations. In the current explicit implementation, the matrix was not checked.

The algorithm of the Newton-Raphson method (VI.2.1) applied to the GTNBF model is divided in two subroutines. The first subroutine named “Newton Raphson” is dedicated to the Newton-Raphson iterative resolution. Its algorithm is sketched in Figure VI.1. The second routine one called “user function”, serve to calculate the residual $\underline{F}$ and its derivatives, and to check the convergence, including some explicit updates at the last (converged) iteration. It also computes the constitutive tangent matrix. Its algorithm is shown in Figure VI.2.

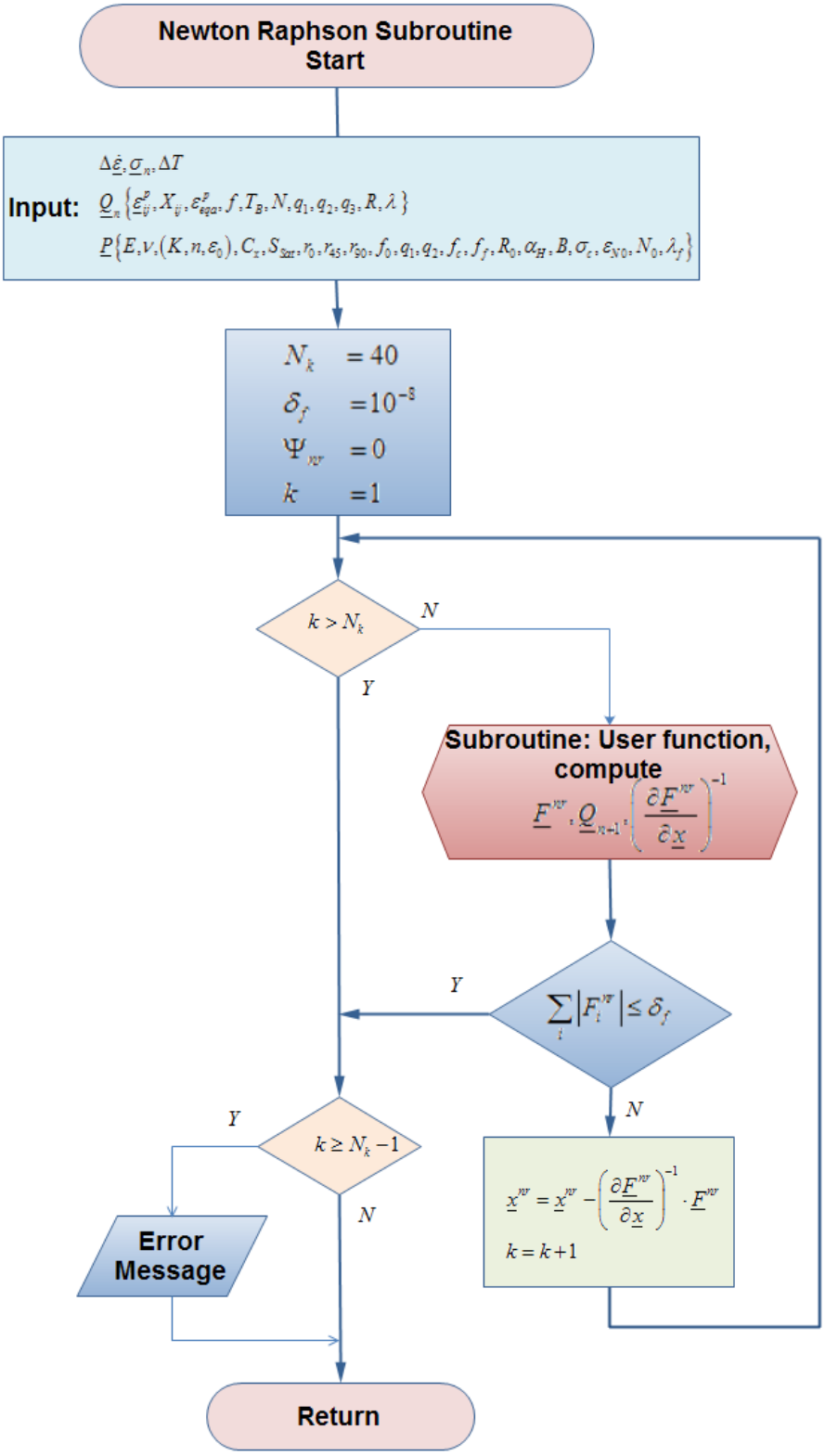

Figure VI.1: Flowchart of the Newton-Raphson subroutine algorithm.

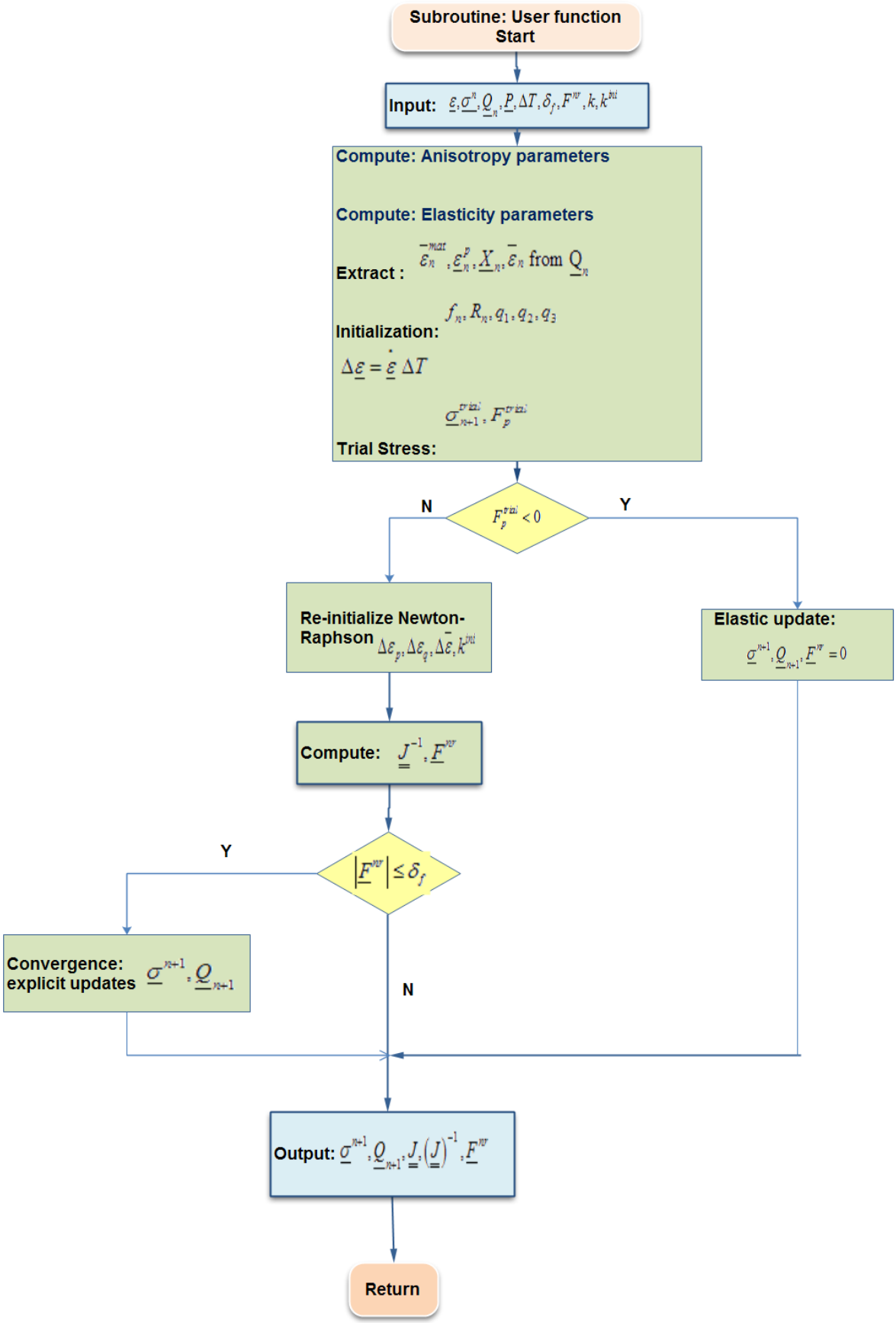

Figure VI.2: Flowchart of "user function" subroutine (algorithm for stress integration, inversion of the Jacobian matrix and state variables update).

Nomenclature of the flowcharts in Figure VI.2 and Figure VI.3:

$\underline{\dot{\varepsilon}}$: Strain rate at the current step.

$\underline{\varepsilon}_n^p$: Plastic strain tensor (matrix + void) at the beginning of the step (increment *n*).

$\underline{\bar{\varepsilon}}_n$: Total strain tensor (matrix + void) at the beginning of the step (increment *n*).

ε_0 : Material parameter for the Swift law (increment *n*)

$\Delta\varepsilon_n^m$: Incremental matrix equivalent strain at the beginning of the step (increment *n*).

$\Delta\varepsilon^m$: Increment of the equivalent strain of the dense matrix at the end of the step.

$\Delta\varepsilon_p$: $\Delta\varepsilon_p = tr\left(\Delta\underline{\varepsilon}^p\right);\ \Delta\underline{\varepsilon}^p = \frac{1}{3}\Delta\varepsilon_p\,\underline{I} + \Delta\varepsilon_q\,\underline{n}$

$\Delta\varepsilon_q$: $\Delta\varepsilon_q = \Delta\varepsilon_{eqv}^p = \sqrt{2\left(\Delta\underline{\varepsilon}^p : \underline{\underline{H}} : \Delta\underline{\varepsilon}^p\right)}$

$\Delta\varepsilon$: Total strain increment.

$\underline{\sigma}^n$: Initial stress tensor.

$\underline{Q}_n$: State variables at the beginning of the step.

$\underline{P}$: Vector of material parameters.

Δt : Time step.

N_k : Maximum number of iterations allowed.

δ_f : Error acceptance or tolerance for Newton-Raphson.

$\underline{x}^{nr}$: Vector of variables (set of 7 unknowns).

$\underline{F}^{nr}$: Residual vector (set of 7 equations).

$\underline{\underline{J}}^{-1}$: Inverse of Jacobian matrix [BEN 2011], see Appendix (B.3).

f_0 : Initial void volume fraction parameter.

R_0 : Initial equivalent void radius.

q_1, q_2, q_3 : Damage parameters.

$\underline{\sigma}_{n+1}^{trial}$: Trial stress $\underline{\sigma}_{n+1}^{trial} = \underline{\sigma}^{tr} - \underline{\underline{C}}^{el} : \Delta\underline{\varepsilon}^p ; \underline{\sigma}^{tr} = \underline{\sigma}^{t} + \underline{\underline{C}}^{el} : \Delta\underline{\varepsilon}$.

F_p^{trial} : Trial GTNBF yield locus value.

T_B : Triaxiality according to equation N°11 in Table IV.2, Chapter IV.

λ_f : Inter-cavities distance

VI.2.2 The Lagamine/Abaqus-Explicit interfacing via VUMAT

The flowchart of Figure VI.3 describes the interfacing between Lagamine and Abaqus-Explicit codes via a VUMAT.

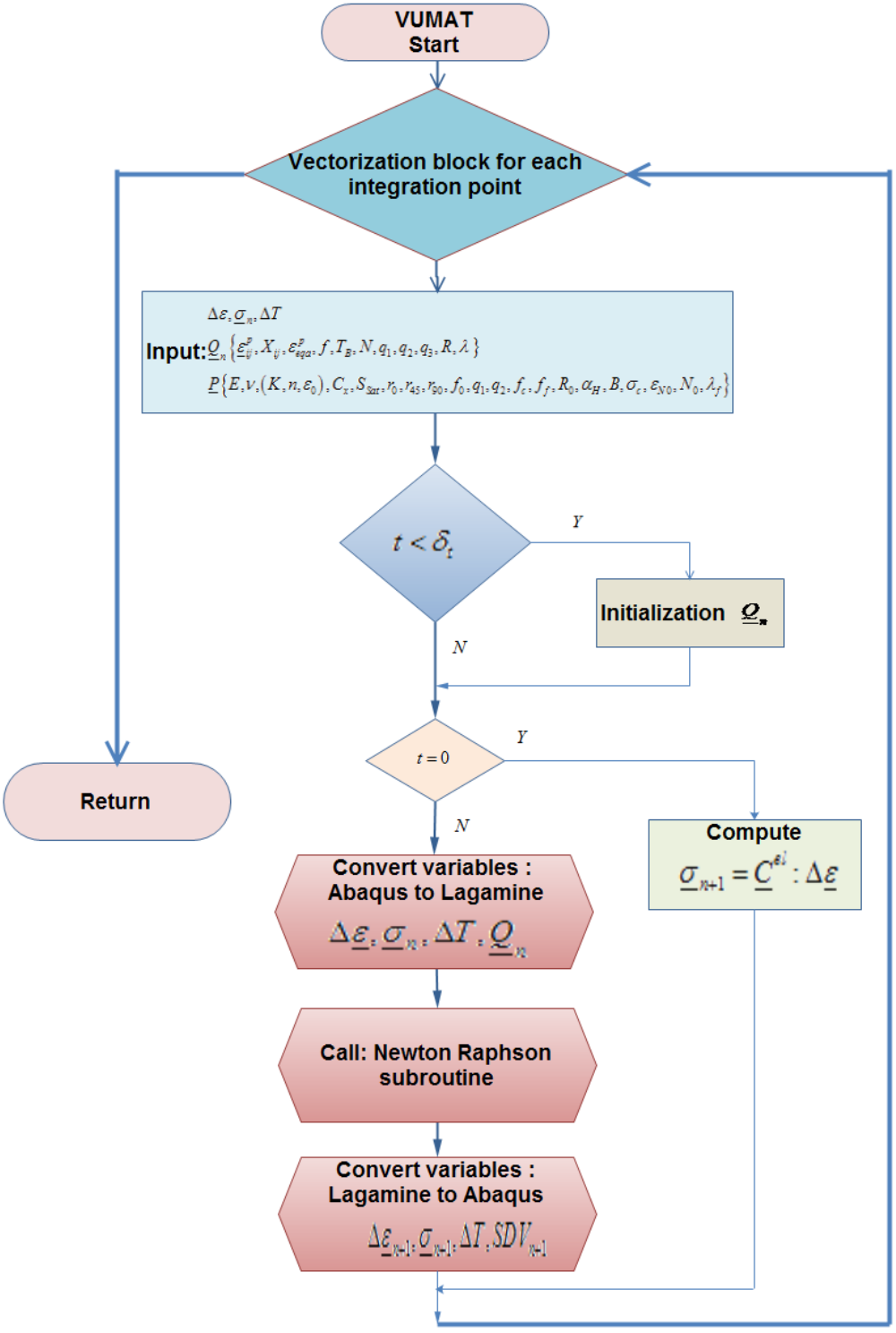

Figure VI.3: Flowchart of VUMAT to link Lagamine material routine and Abaqus/explicit (SDV designates the output variables).

VI.3 VUMAT programming validations

VI.3.1 Introduction

The VUMAT programming has been validated by comparing the stress-strain, void volume fraction-strain, and void density-strain responses from Lagamine and Abaqus-Explicit FE codes. The validation has been applied on three different geometries: single element, flat sheet and cylindrical notched specimen. The VUMAT has been built with a modular structure to allow the place for several void nucleation evolution laws (in our case (Bouaziz [BOU 2008] and Landron [LAN 2011 laws), coalescence modeling, and other isotropic hardening laws such as Voce or Swift-Voce (see chapter III).

The validation tests to check the Abaqus implementation compared with Lagamine one were performed with the set of material parameters of Ben Bettaieb [BEN 2012] corresponding to a DPI (see Table V.3). In order to compare Abaqus-VUMAT predictions and Lagamine predictions consistently, the validation is restricted here to the GTNB model, which was originally available in Lagamine at the beginning of the thesis [BEN 2012] in a well validated status.

VI.3.2 Validation on single element

Uniaxial tensile test

A cube with 8 elements has been modeled to simulate a uniaxial tensile test in Abaqus/explicit and Lagamine (implicit code). The side of the cubic domain dimension at the initial time is 1mm. The symmetry boundary conditions usual for a tensile test simulation are applied and a tensile velocity is introduced in the X direction as illustrated Figure VI.4. The element chosen for Abaqus is C3D8R [HIB 2010] and the counterpart for Lagamine is BLZ3D [ZHU 1992].

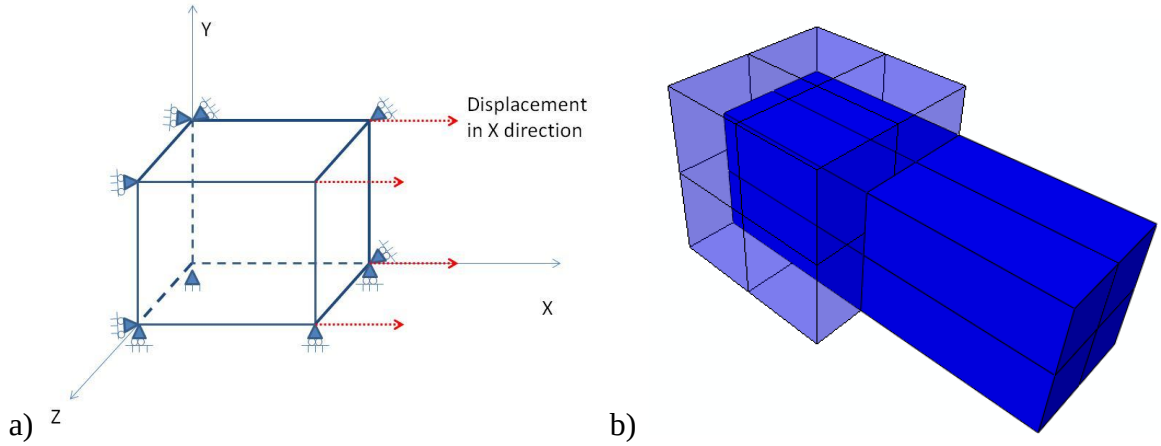

Figure VI.4: a) Uniaxial tensile test on 1-mm cube, b) The same cube after loading, performed simulations with Lagamine and Abaqus/explicit FE codes.

The comparison between Lagamine and Abaqus/explicit simulations underscores a very good similarity in terms of stress, porosity, number of voids (Figure VI.5), up to very large strains

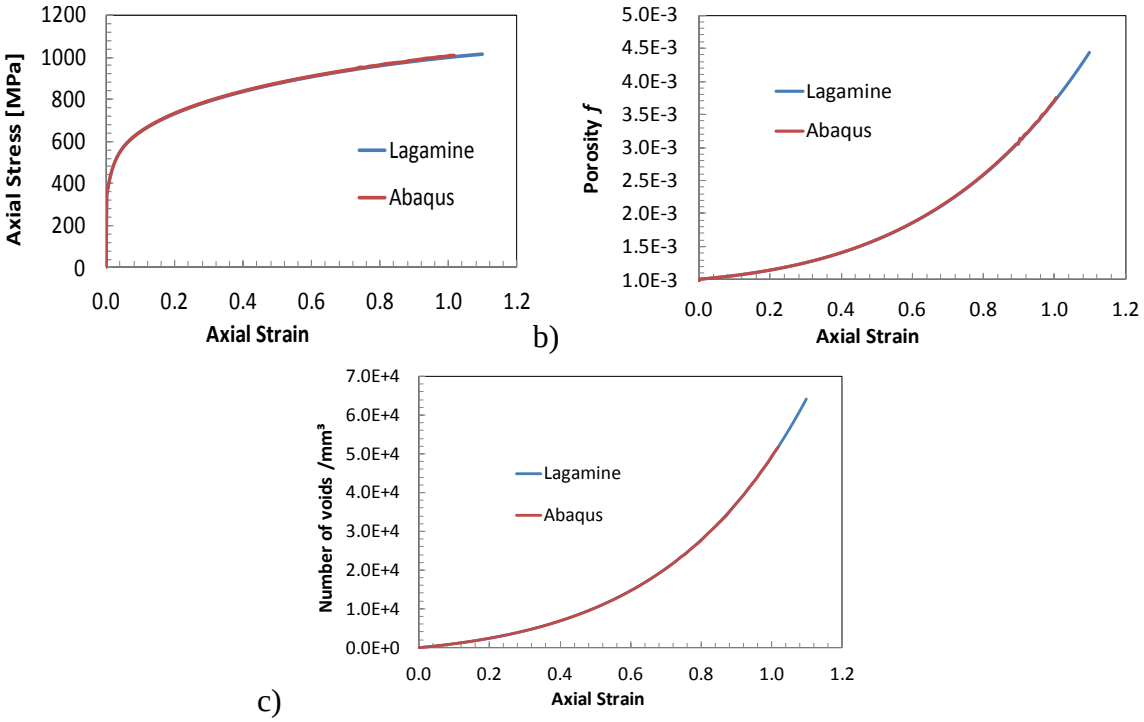

Figure VI.5: a) Stress-strain curves in tensile direction, b) Porosity-strain curves, c) Number of voids-strain curves comparison between Lagamine and Abaqus-Explicit.

Simple shear test

The same cube used in both FE codes has been adapted to perform a simple shear test simulation. Figure VI.6 presents the boundary conditions and the velocity applied on the 1-mm cubic domain.

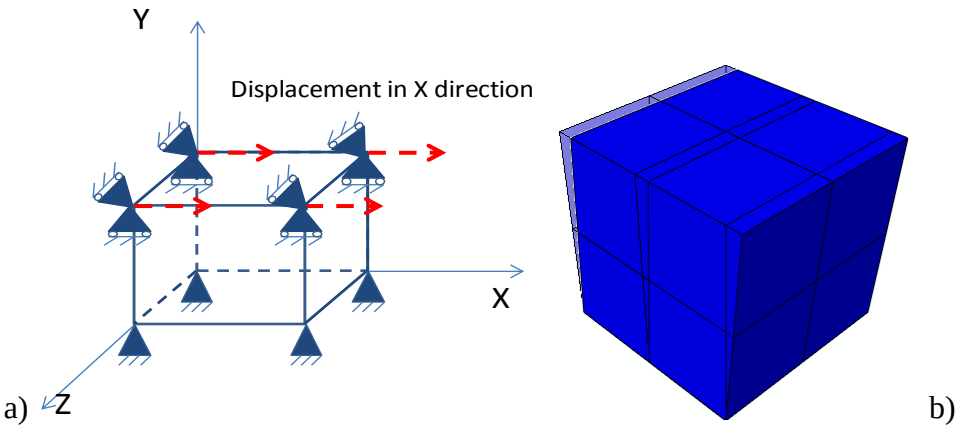

Figure VI.6: a) Simple shear test on 1-mm cube, b) The same cube after loading performed with Lagamine and Abaqus/explicit FE codes.

Figure VI.8 shows a very good agreement between Lagamine and Abaqus/explicit simulations in terms of stress, porosity, number of voids. The quantitative comparison with the uniaxial tensile simulation underscores the very small amount of voids created during the shear loading (Figure VI.8c). The evolution of the porosity f (only growth and nucleation are considered here) is significantly lower than during the uniaxial tensile loading. The influence of the loading will be studied later when dealing with the sensitivity study of the GTNBF model (chapter VII).

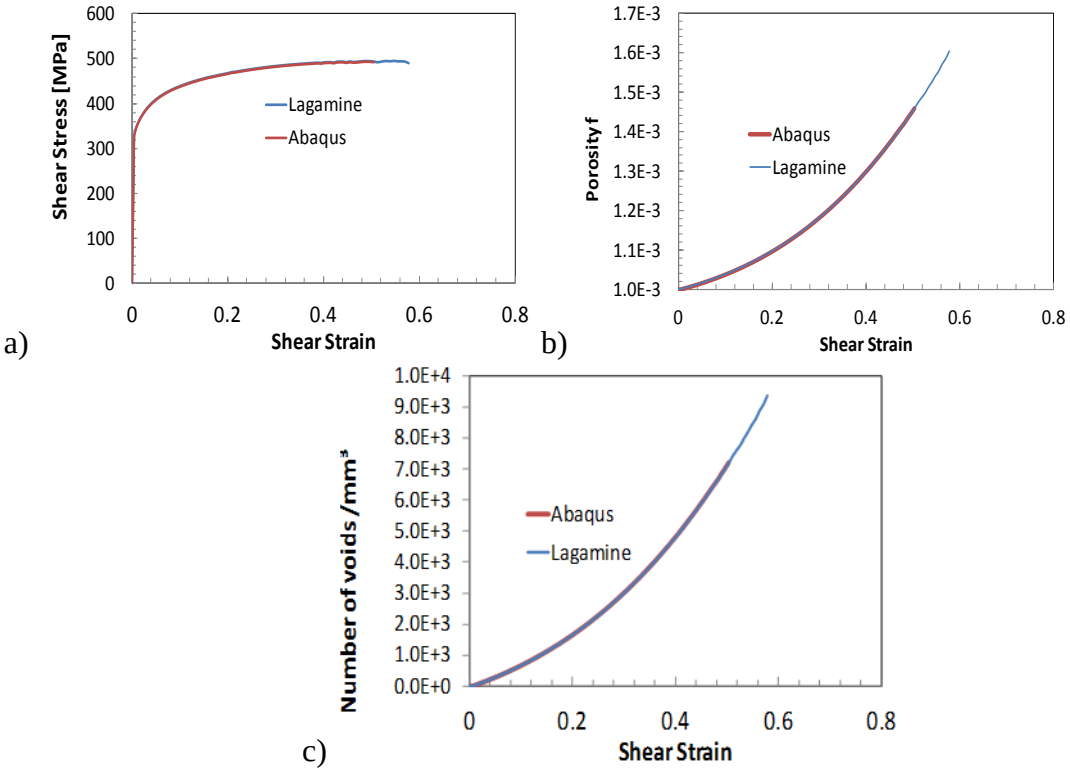

Figure VI.7: a) Shear stress-strain curves, b) Porosity-strain curves and c) Number of voids–strain curves comparison between Lagamine and Abaqus-explicit.

VI.4 Conclusions

The GTNBF model has been implemented by designing a FORTRAN program called VUMAT which connects the material routine specific to the Lagamine code to Abaqus-Explicit.

Before implementing the set of discrete equations, the first step of the work has been focused on translating the previous GTNB model built with Fortran 77 to FORTRAN 95. The second step of this work was to reduce the initial number of parameters. It has been possible to find a relation between the initial porosity parameter f_0 and the initial void density N_{ini}.

$$N_{ini} = \frac{1}{\frac{4}{3}\pi R_0^3}\left(\frac{f_0}{1-f_0}\right) \tag{VI.19}$$

Where f_0 is the initial porosity and R_0 initial void size radius in mm.

During the programming of the VUMAT, a modular structure has been configured allowing the user to modify a part of the model without altering the rest of the program.

Finally, using the original GTNB model, this VUMAT interface has been validated by comparing the stress and the damage responses obtained by Abaqus-Explicit and Lagamine codes. These comparisons have been applied on a cube with 8 elements loaded in uniaxial tensile or in simple shear direction. The stress and the damage state variables results from both FE codes are in good agreement.

Chapter VII. **Potentialities and limitations of the GTNBF model**

Contents

VII.1 Introduction

The GTNBF damage model contains innovative contributions such as a complete modeling of the ductile damage stages (growth, nucleation, coalescence, failure) inspired from previous works based on accurate tomography measurements (chapter IV).
The main goals of the current chapter are to evaluate the GTNBF model potentialities and limitations and to validate its predictions compared to experimental results. The method employed to reach this objective consists in establishing a sensitivity study of different parameters identified in chapter V and on top of that estimating their influence on the damage state variables, e.g., void volume fraction, and density of voids.

After this brief introduction, material parameters sensitivity will be performed with the characterized and identified, anisotropic and damage laws. After this step, the element size influence on the current model is carried out. Then, the second part of this work is centered on the numerical GTNBF model responses during a tensile test compared to the experimental counterpart extracted from X-ray tomography measurements [LAN 2010-2012]. The comparison includes the exact extraction of the numerical stress and triaxiality variables, followed by the evaluation of the physically-based damage modeling proposed by Bouaziz [BOU 2008] and Landron [LAN 2011]. Prior to concluding, the chapter gives more details on the backstress influence by comparing diverse triaxiality definitions in the aim to justify the choice taken for the GTNBF model.

VII.2 Sensitivity study

VII.2.1 Material parameters influence on the GTNBF predictions

VII.2.1.1 Anisotropy

In the theoretical section of this document (chapter IV), it has been shown that the GTN yield function is modified by introducing the effect of the plastic anisotropy of the matrix (see Eq.IV.1). As already shown, the anisotropy enters the model at two levels: through the Hill matrix $\underline{\underline{H}}$ of anisotropy coefficients in the equivalent shifted stress $\bar{\sigma}_{eqv}$ and by means of the parameter κ introduced by Benzerga and Besson [BEN 2001]. These anisotropy parameters are defined in terms of the Lankford coefficients r_0, r_{45}, r_{90}. The major goal of this sensitivity investigation is to quantitatively analyze the effect of the plastic anisotropy on the damage prediction. To reach this objective, four different combinations of Lankford coefficients have been proposed. The set of simulations include a series of single element simulations in uniaxial, and simple shear tests (see Figs.VI.4 to VI.7 in section VI.3) allowing studying relative effect of loading case, as well as a case of refined mesh describing a cylindrical radius notched specimen loaded in tensile direction. The initial material parameters for the GTNBF

model correspond to the DPI steel (see Table V.3). Table VII.1 compiles the three combinations of Lankford coefficients that were investigated. The first two sets of coefficients correspond to the experimental values measured for DPI and IF steel [BEN 2010]. In order to investigate only the effect of the anisotropy coefficients, all the other parameters were artificially kept identical to the values determined for DPI (see Table V.3). The third case, where the Lankford coefficients are equal to 1, defines the isotropic Mises-GTNBF model. Accordingly, the parameter κ becomes equal to 2.

Table VII.1: Lankford coefficients applied on the cylindrical notched specimen loaded on tensile direction, corresponding to the GTNBF model for DPI steel.

Lankford cases and κ	r_0	r_{45}	r_{90}	R	κ
Case 1 (DPI, as reference material)	0.85	1.04	0.94	0.97	2.012
Case 2 (IF steel)	1.98	2.56	1.67	2.19	1.746
Case 3 (Isotropic; Mises-GTNBF)	1	1	1	1	2

The normal anisotropy coefficient R is obtained from the equation:

$$R = \frac{r_0 + 2r_{45} + r_{90}}{4} \tag{VII.1}$$

Single element simulations

- Uniaxial tensile test

The three Lankford cases have been first applied on a single element loaded in uniaxial tensile direction. The details of the modeling have been presented in chapter VI.3.2.
As expected, the axial stress and the triaxiality, the total porosity and the void density could be affected as damage is linked to strain distribution. However, reasonable physical values are investigated do not induce any effect. More precisely, Figure VII.1(a-d) shows that all Lankford cases evolution curves are close to each other at initial porosity equal to $f_0 = 1.2\times10^{-4}$. These observations seems to corroborate well with the results of Zhiying et al. [ZHI 2009] in a similar study on the GTN damage model based on Hill'48 anisotropic yield criterion for aluminum alloy. It is to underline that for the cube dimension the initial porosity f_0 is far too low to have a strong influence on the stress and damage variables. A higher initial porosity value has to be defined.

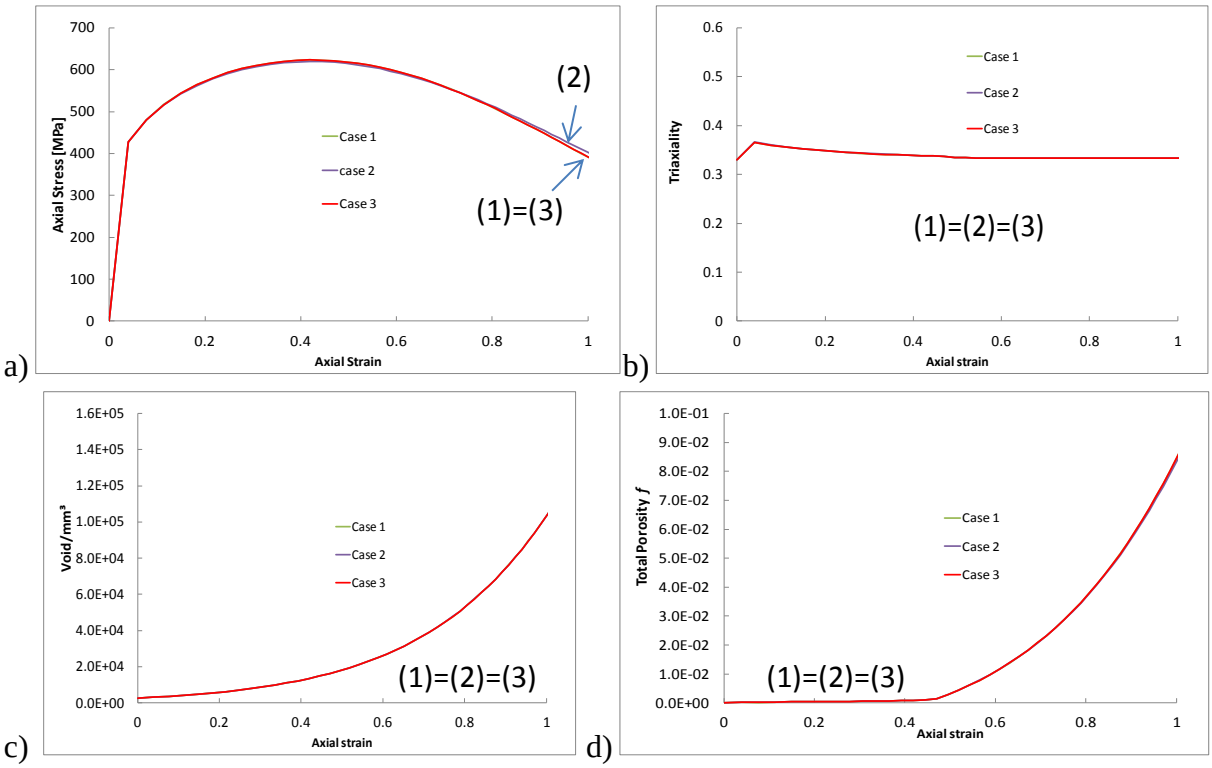

Figure VII.1: Anisotropy influence during the uniaxial tensile test; a) tensile stress-strain curves, triaxiality-strain curves, c) Void density-strain curves, d) Total porosity-strain curves. at $f_0 = 1.2\times10^{-4}$.

Hereafter, the same simulation test with a higher initial porosity value 10^{-3} shows light different results. Indeed, the case 2 curve representing the strongest Lankford coefficients has lower nucleation evolution than the von Mises isotropic hardening case (case 3). The studied DPI steel curve is exactly equal to case 3 curves. The light slow down of the void nucleation evolution for case 2 reaching quasi the end of the loading (around 0.6 of axial strain) corresponds to the tiny increase of the axial stress evolution. The change is so small that it is too soon to conclude on a plausible root cause. However, the initial porosity value f_0 has an impact on the global porosity evolution.

Moreover, the value $f_0 = 10^{-3}$ chosen is exactly the critical value f_c measured by Landron et al. corresponding to the coalescence start. This explains the rapid growth porosity evolution quasi at the beginning of the loading until a porosity value of 2.10^{-2}. After this value, the material rapidly enters in the coalescence stage; one can see that the plastic anisotropy effect seems to be negligible on porosity due to void coalescence. In fact, the void coalescence law introduced in the current damage model is similar to the GTN model assuming that the void remains spherical until failure occurs. The present phenomenological coalescence law does not integrate the macroscopic plastic strain rate necessary to have a void shape evolution such as Thomason [THO 1985], GLD [GOU 1993], Pardoen [PAR 1998-2000-2006] or Scheyvaerts [SCH 2008].

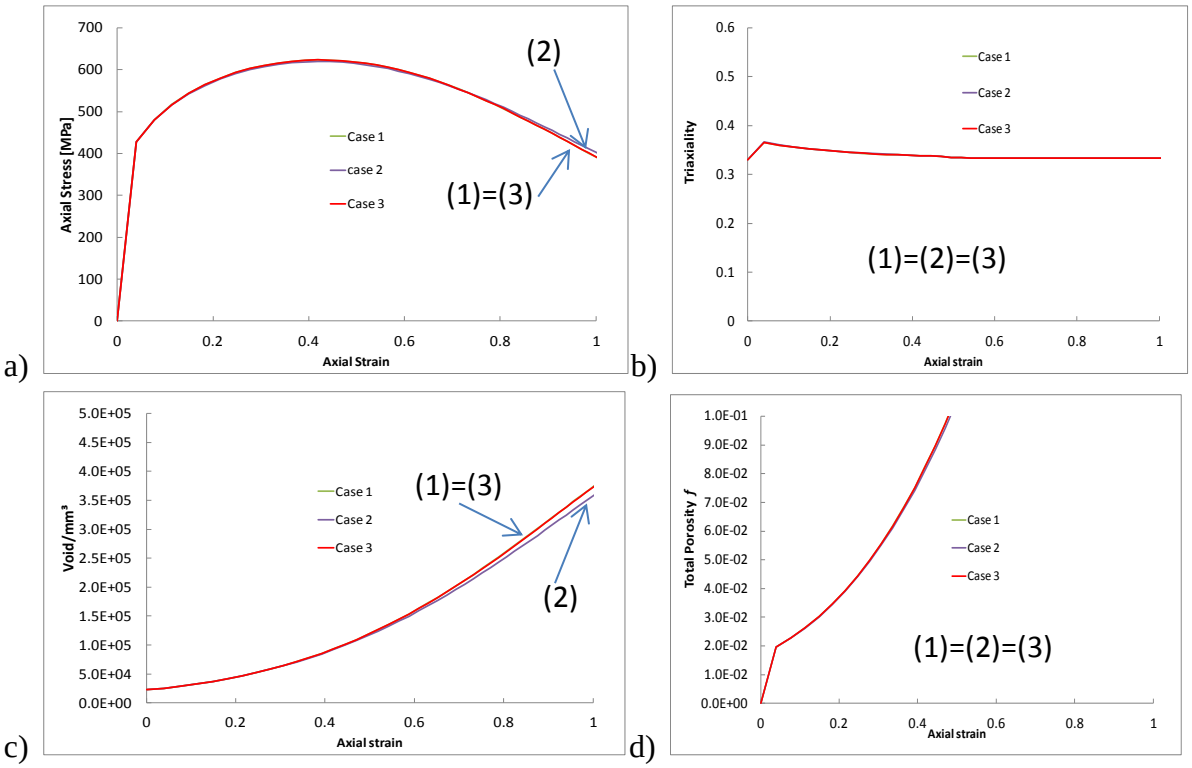

Figure VII.2: Anisotropy influence during the uniaxial tensile test; a) tensile stress-strain curves, triaxiality-strain curves, c) void density-strain curves, d) total porosity-strain curves. at $f_0 = 10^{-3}$.

- Simple shear test

The single element simple shear simulations were first performed with an initial porosity value at 1.2×10^{-4}. Unfortunately, the only variables to analyze were the stress state and the void density. The three cases were perfectly superimposed. There were no data for the triaxiality, and the total void porosity evolution as the damage model do not take pure shear effect into account. However, it has been decided to increase the initial porosity value as the same level as the previous uniaxial tensile test ($f_0 = 10^{-3}$) as simple shear test is not pure shear tests and some effect could be seen.

The results are plotted in Figure VII.3 and Figure VII.4. A significant influence of the Lankford coefficients has been detected when analyzing the nominal shear stress-strain curves evolution (Figure VII.3) and the damage state variables evolution illustrated in Figure VII.4.

Hereafter, the simple shear test results show that the dominant stress component (Figure VII.3a) in the unit cell is the nominal shear stress with a weaker axial stress component (Figure VII.3b). The increase of the nominal shear stress is gradual, and the curves do not exhibit any drop in flow stress expect for the case 3 defining the Mises-GTNBF model. Furthermore, the nominal shear stress-strain curve depicts the same evolution regarding the case 1 and 3. The most important plastic anisotropy influence appears when the Lankford coefficients are high (case 2). It is to notice that the nominal shear stress value with case 2 is strongly weaker compare to the other cases. The raison of the nominal shear stress decrease is

based on the rapid increase of the axial stress value for the case 2 compared to the other cases. The stress evolution comparison shows that the introduction of stronger Lankford coefficients rapidly changes the stress components and the shear work hardening rate. The figures reveal that the simple shear test simulation is a combination of a pure shear and a tensile loading amplified at high plastic anisotropy level.

a) 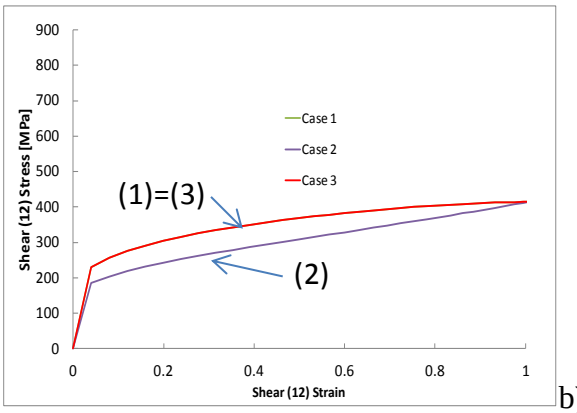

b) 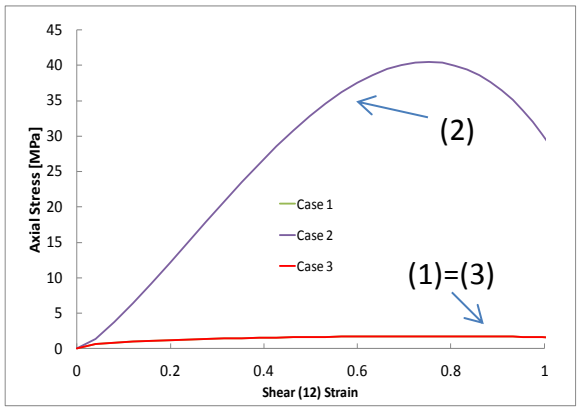

Figure VII.3: Anisotropy influence during the simple shear test; a) shear stress-strain curves, b) axial stress-strain curves at $f_0 = 10^{-3}$.

The strain-path effect on damage evolution can be seen on the graphics describing the damage evolution state variables such as void nucleation and porosity. The rapid change of work hardening rate has an important impact on the damage evolution as seen in the void nucleation-shear strain curves (Figure VII.4a). The decrease of the kinematic hardening evolution through the increase of the plastic anisotropy rate decelerates the number of void nucleation in the material (case 2). A stronger influence is highlighted when analyzing the total porosity evolution. The material cube constrained in simple shear direction and modeled with case 2 show no porosity evolution while the other cases increase very fast. The contributions of the porosity due to void nucleation, growth and coalescence underscore the same results.

a) 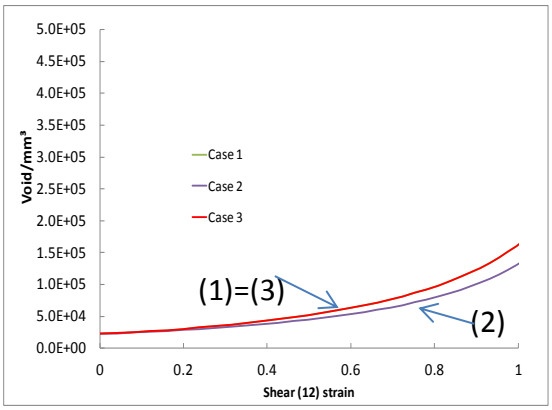

b) 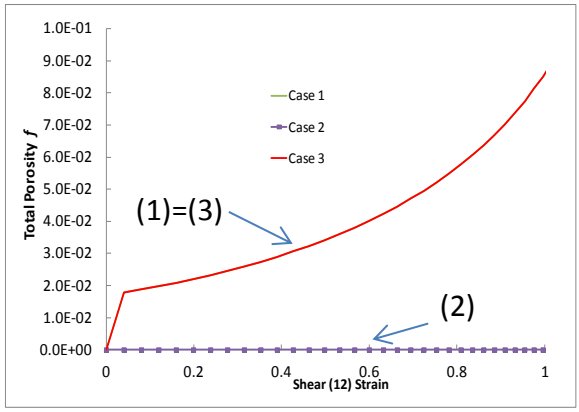

Figure VII.4: Anisotropy influences during the simple shear test; a) void density-strain curves, b) total void porosity *f*-strain curves at $f_0 = 10^{-3}$.

As already mentioned in chapter IV, the current damage model is not able to predict the porosity evolution in pure shear loading due to the plastic incompressibility of the matrix assumption. The current model as well as the GTN model assumes that the relation for the growth of a single void $\dot{f}_g$ in elastoplastic matrix depends on the macroscopic plastic strain rate trace $tr\left(\underline{\dot{\varepsilon}^p}\right)$. The plastic incompressibility of the matrix imposes that the matrix volume evolution remains constant during the loading. The shear strain components are normally not taken into account with this assumption. Therefore, the porosity due to shear loading cannot be sketched in before the coalescence occurs ($f^* < f_c$).

Both graphs underline the importance of taking into account the plastic anisotropy in the Gurson yield function. Case 3 describes a lower evolution than the isotropic plasticity (Lankford with r=1) in terms of shear stress and density of voids as function of shear strain.

Cylindrical notched specimen tensile test

Tensile loading applied on cylindrical notched specimen is a common test to estimate the ductility of materials. Therefore, the three Lankford cases (Table VII.1) have been compared using the following simulation procedure.
The axisymmetric 1-mm notched specimen is already presented in the chapter V.2.3 (see geometry in Figure V.10c). A three-dimension simulation has been realized in Abaqus-Explicit and Lagamine by using 3800 elements and 4633 nodes. The boundary conditions, the meshing and the velocity are illustrated in Figure VII.5. A refined mesh is generated near the center of the specimen where large strain gradients are expected, while a relatively coarse discretization is used in the rest of the specimen where a rather uniform deformation is expected. The damage material parameters are visible in table V.3.

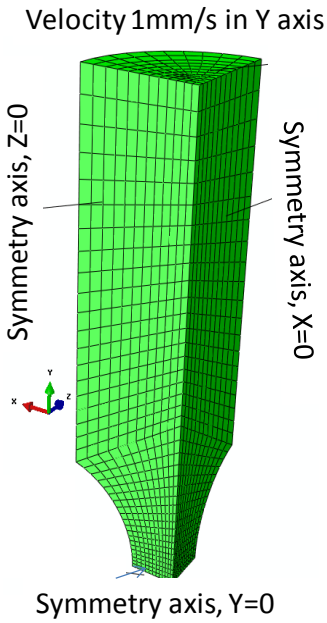

Figure VII.5: Finite element model of the tensile test on the notched 3D sample. Boundary conditions and velocity field applied.

Compared to the single element tensile test (Figure VII.1a), the axial stress for all Lankford cases is higher, and the specimen fails at lower axial strains than under axial strain tensile condition. For this kind of anisotropic plastic material (Lankford from DPI (case 1) and IF (case 2) steels), the axial tensile stress component (Figure VII.6a) is higher than the value calculated by the von Mises isotropic plastic model (Lankford equal to 1), which means the plastic anisotropic behavior has an important effect on the results.
On top of that, comparison with the single element (Figure VII.6b) reveals a higher triaxiality value and the strong effect of the plastic anisotropy parameters accelerating the ductile damage mechanisms. These observations are in line with the definition of the triaxiality. The anisotropy parameters are defined in terms of the Lankford coefficients r_0, r_{45}, r_{90} which are ratio between the width and the thickness strains of a flat sheet. In the present tensile simulation test, the major strain is the axial direction represented by r_0. Consequently, the triaxiality increases due to the dominance of the axial stress. Moreover, the proposed triaxiality T_B (see Eq.IV.32) based on Landron damage model [LAN 2012] introduces the backstress tensor through the kinematic hardening law. It means that the backstress contributes to increase the stress state and the triaxiality. This observation has been confirmed by Ben Bettaieb et al. [BEN 2012] during the sensitivity study of the kinematic hardening parameters C_x and S_{sat} introduced in the GTNB model.

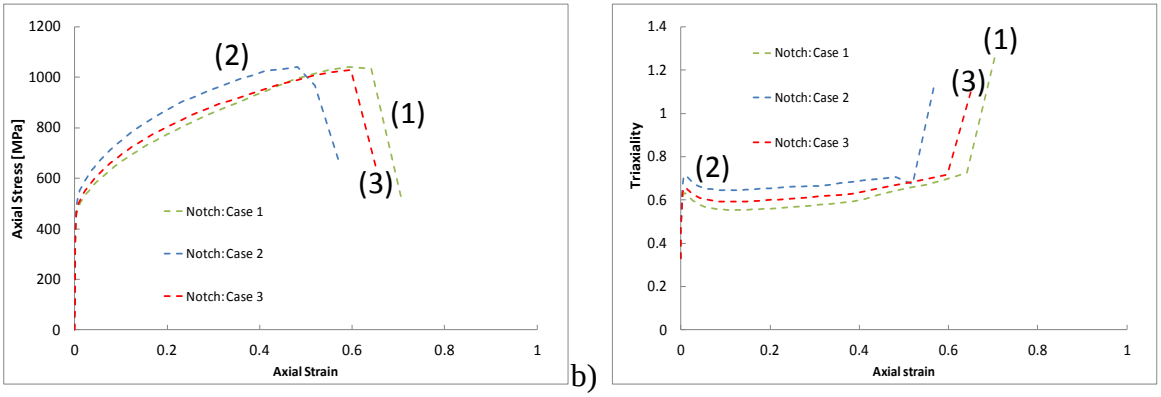

Figure VII.6: Anisotropy influence during the cylindrical notched specimen test; a) Tensile stress-strain curves, b) Triaxiality-strain curves $f_0 = 1.2\times10^{-4}$.

The introduction of the anisotropic behavior in the GTNBF model defines the stress triaxiality level in the material. The triaxiality factor will have also a strong effect on the porosity, and the void density regarding Landron et al. nucleation law (see Eq IV.33).

a) 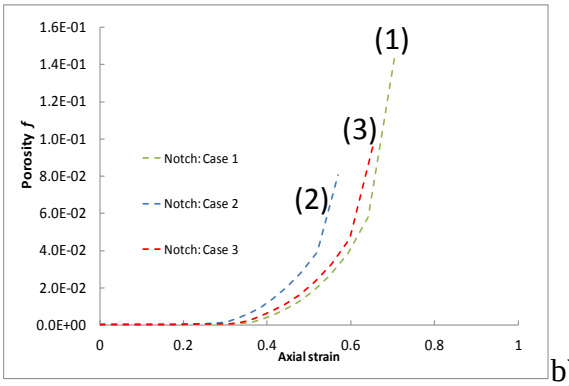

b) 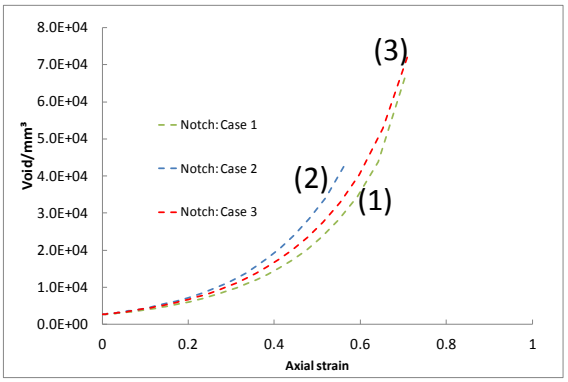

Figure VII.7: Anisotropy influence during the cylindrical notched specimen test; a) porosity-axial strain, b) void density-axial strain for $f_0 = 1.2\times10^{-4}$.

VII.2.1.2 Damage and fracture initiation

- Damage law influence

The present section studies the influence of the damage contributions in the GTNBF model. Before giving more details, a general numerical impact of the damage laws (porosity and nucleation) has been quantified with the previous geometries (single element loaded in uniaxial tensile and shear directions, tensile cylindrical notched specimen). For each geometry, two sets of material data have been simulated. One is associated to the actual DPI steel with the complete damage contribution (simply called GTNBF) and the other one is a virtual material generated with the data set of DPI without damage law (called hereafter GTNBF-no damage). The GTNBF-no damage model is obtained by setting to zero the initial porosity f_0 and the material constant B from Landron's nucleation law taken at zero (see Table V.3 chapter V).

Figure VII.8a represents the axial stress-strain curves responses of the single element loaded in tensile direction. It underscores the significant impact of the damage laws. Indeed, the GTNBF model with damage contributions drops sharply after 60% of axial strain. The notched tensile test to estimate the ductility of materials (see Figure VII.8b) highlights the importance of taking into account the cavities evolution in the modeling. In opposition to the single element test, the stress extracted at the center of the specimen softens at around 50% of strain before fracture brutally occurs.

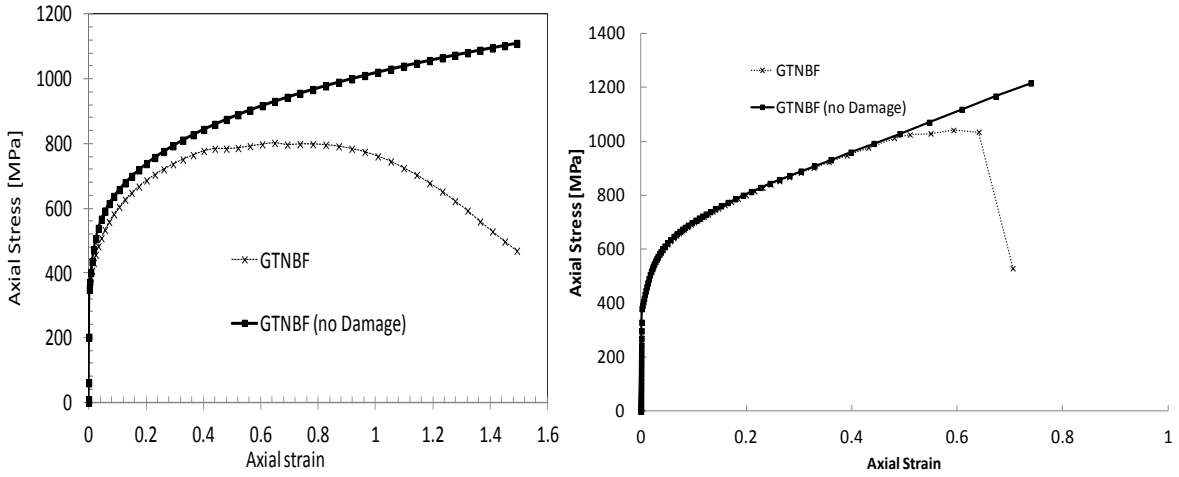

a)

Figure VII.8: Influence of the damage contribution introduced in the GTNBF model for DPI steels a) axial stress-Strain curves in uniaxial tensile test, b) axial stress-Strain curves during the cylindrical notched specimen test.

Knowing that the insertion of the damage modeling has a remarkable influence on the DP steel behaviour, a sensitivity study has been performed in the aim to accurately estimate the potentiality of the GTNBF model. A series of simulations have been operated with a single element constrained in uniaxial tensile direction. The calculations have been focused on two most important damage parameters; the initial porosity f_0 measured by Landron [LAN 2011] and the final void volume fraction f_f (see Eq IV.41) physically-based on the ultimate average inter-cavities distance measurement (λ_f , Eq V.7).

- Sensitivity to f_0

The 8-nodes single element tensile simulations were performed with the GTNBF model and with four different values of the initial porosity f_0. All the other parameters correspond to the DPI steel, (see Table V.3). It is noteworthy to know that the GTNBF model includes a relationship between the initial porosity and the initial void density. Consequently, the GTNBF model allows the user to introduce only one initial damage parameter which is the initial porosity f_0. The model automatically calculates the corresponding initial void density N_{ini} (void/mm³) with the following expression:

$$N_{ini} = \frac{1}{\frac{4}{3}\pi R_0^3}\left(\frac{f_0}{1-f_0}\right) \qquad \text{(IV.2)}$$

Where f_0 is the initial porosity and R_0 the initial void size radius in mm.

The values of f_0 for the sensitivity analysis have been carefully chosen. The first value (f_0 equal to 0) represents the case where the material has no cavity. It simulates the material without damage. The second and the third values (f_0 equal to 2. 10^{-5} and 2. 10^{-4}) have been

measured by Landron on different DP steels and the last one (f_0 equal to 2. 10^{-3}) has no physical meaning, it is integrated to evaluate the limit of the damage model. It is important to keep in mind that the critical porosity value f_c characterizing the coalescence apparition has been evaluated and keep unchanged to Landron [LAN 2011] estimation at 10^{-3}. Therefore, this value will be kept constant for all DP steels to facilitate a better understanding. It is well known that this value should be modified depending on the DP steels, and the residual stresses after forming process. Nowadays, discussions with specialists concerned of the matter have taken place to know how to clearly identify this value. According to Landron [LAN 2011], an accurate measurement is often limited by the optical low resolution used to detect the exact apparition of the coalescence. However, further works launched in the direction of enhancing the X-ray tomography method are investigated such as the 3D reconstructed image quality [BOI 2010] [MAI 2012].

The initial porosity parameter strongly influences the stress evolution. As shown in Figure VII.9, the axial stress sharply drops when the initial void volume fraction increases in the material. The graphic also underlines the importance of precisely measuring the initial porosity contained in a DP steel before deforming the material.

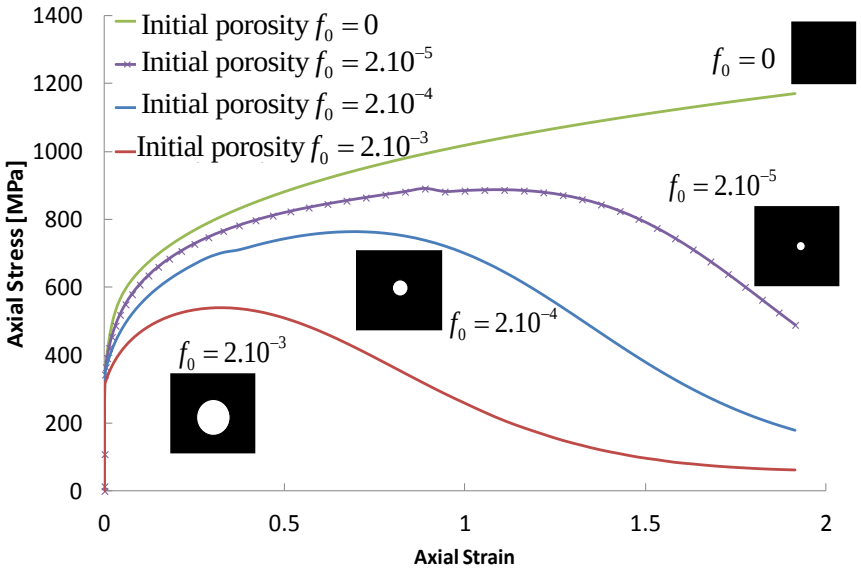

Figure VII.9: Influence of the initial porosity f_0 parameter introduced in the GTNBF model for DPI steel; axial stress-strain curves after a uniaxial tensile test.

The influence of this parameter has been detected when extracting the porosity and the void density evolutions in function of axial strain (Figure VII.10). Both damage variables surge when the initial porosity f_0 rises in the DP steel. The analysis of the initial porosity effect on the ductile damage mechanism underscores the importance of characterizing this parameter before performing a sheet metal forming simulation. The initial porosity f_0 value will particularly influence the evolution of the nucleated void and void growth predictions (see IV.3.1 especially Eqs.IV.31, IV.35). This parameter is a key point to ensure the good quality of the finished industrial product; meaning, no visible failure or necking the DP steel.

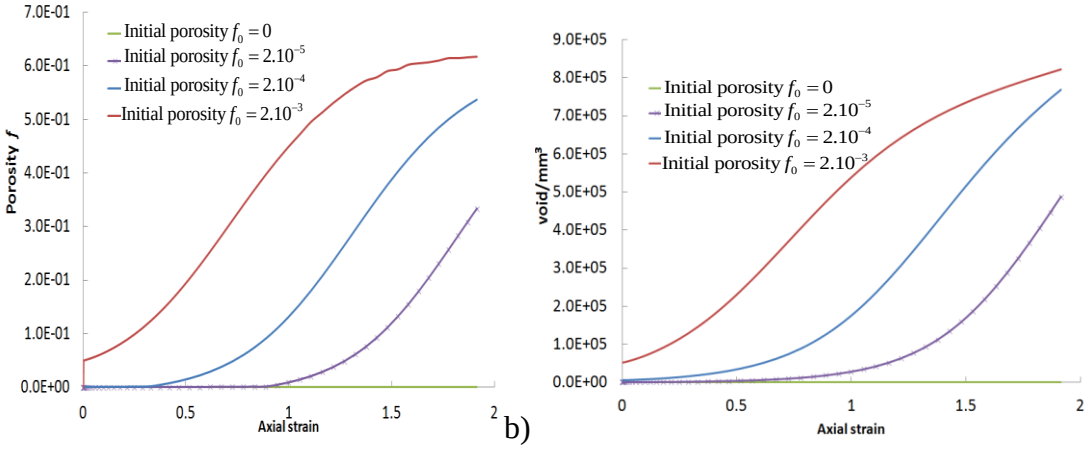

a) b)

Figure VII.10: Influence of the initial porosity f_0 parameter introduced in the GTNBF model; a) total porosity *f*-strain curves, b) void density-strain curves for DPI steel.

- Sensitivity to f_f

The previous simulations have been repeated to evaluate the influence of the final void volume fraction f_f (expression in Eq. IV.41), using this time, and the measured value of initial porosity (f_0 equal to 2. 10^{-5}). The effect of five different f_f values has been compared. The smallest value (0.005) has been chosen near the critical porosity value f_c in the aim to see if any impact is observed when coalescence event is shortened. The highest value (0.15) corresponds to a value usually found in the literature and firstly proposed by Tvergaard & Needleman [TVE 1984]. The void volume fraction equal to 0.05 corresponds to the value calculated from the equation V.8 linked to the measurement of the ultimate average inter-cavities distance. Finally, the other values have been arbitrary chosen.

In Figure VII.11, the predictions generated with these five f_f values are compared in a graphic showing the axial stress evolution during the uniaxial tensile loading. It shows that the GTNBF model is quite sensitive to a small value modification and that of course the fracture initiation occurs earlier when the final void volume fraction decreases.
When inspecting carefully the equation introducing the final void volume fraction f_f, it seems clear that this physically-based damage parameter is impacting only the final part of the axial stress-strain curves evolution. More precisely, equation IV.41 is used in coalescence modeling to predict the slope of softening at failure. If this value is chosen very small $f_f = 0.005$, the material will fail smoothly. In opposite, a great value will predict a rapid and brutal fracture $f_f = 0.15$.

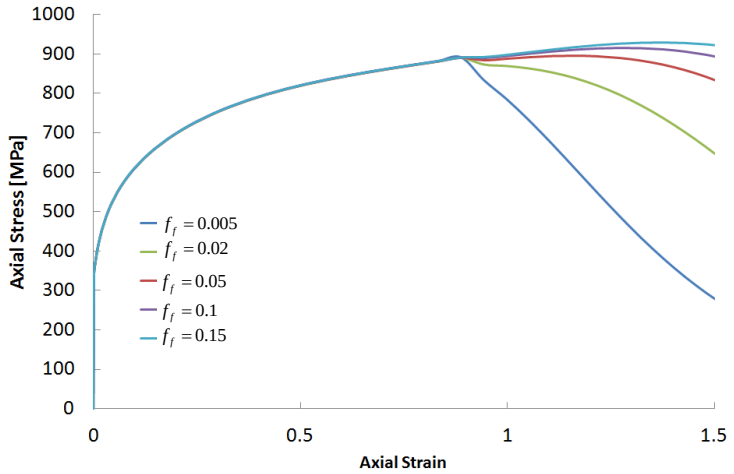

Figure VII.11: Influence of the final void volume fraction f_f parameter introduced in the GTNBF model; axial stress-strain curves after a uniaxial tensile test for DPI steel.

The curve comparison also shows that f_f strongly influences the porosity evolution during coalescence (Fig. VII.12a). However, of course, the impact is very light regarding the part of porosity evolution due to the nucleation stage (see Figure VII.12b), and inexistent for the void growth evolution, that can be understood by analysis the coalescence model equations (see Eq.IV.36). The final void volume fraction f_f appears in the ductile damage modeling when $f_c \leq f < f_f$ or $f > f_f$, symbolizing respectively the coalescence and the fracture stages.

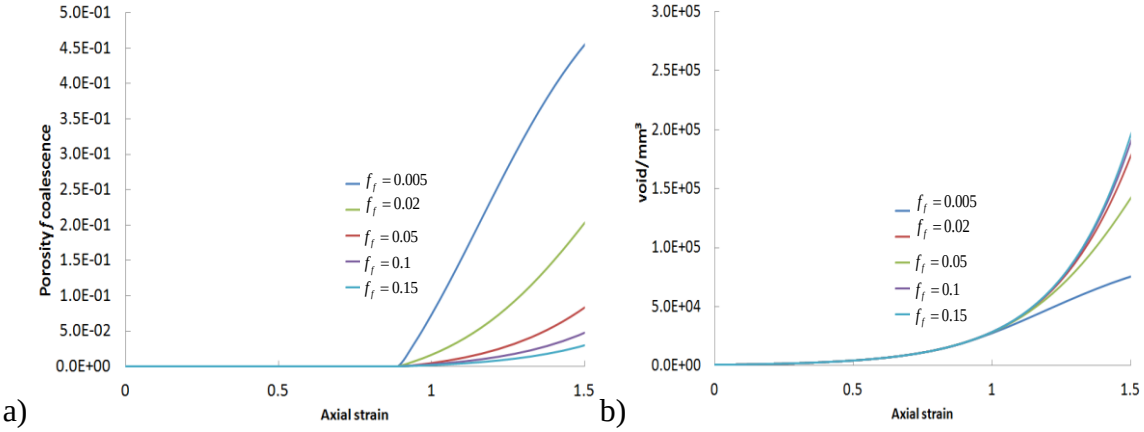

a) b)

Figure VII. 12: Influence of the final void volume fraction f_f parameter introduced in the GTNBF model; a) growth porosity *f*-strain curves, b) void density-strain curves, c) coalescence for DPI steel.

VII.2.2 Element size influence on GTNBF model

The in situ tensile test presented in chapter VII.2.2.1 has been simulated using axisymetric elements with GTNBF model. The mesh generated was constrained by the specific post-processing procedures developed in order to extract from the simulation, the physical quantities obtained from the in situ test. The need for accurate average values across the weakest cross-section, within a fixed space volume at the root zone of the sample (Figure.II.3b), and at the central zone of the neck, imposed a refined mesh at this location. Thus an adapted mesh design has been built up as shown in Figure.VII.13b. A very fine element size of 10µm×10µm (called adapted mesh) is adopted in the neighborhood of the central point of the sample. Thanks to this choice, a large number of integration points were available in the sub-volume of interest, providing accurate average values. A relatively small element size is maintained across the entire cross-section corresponding to the symmetry plane of the sample, as well as at the central part of the neck. The nodes of the three most central elements of the boundary in the neck region were used to determine the notch radius [BRI 1945], r_{notch} (see Figure.VII.13a). Homogeneous velocity boundary conditions were applied on the top surface, along with usual symmetry boundary conditions in axial and width directions. The finite element type chosen in Abaqus/explicit [HIB 2011] software is a reduced integration linear axisymetric element with four nodes and one integration point (CAX4R).

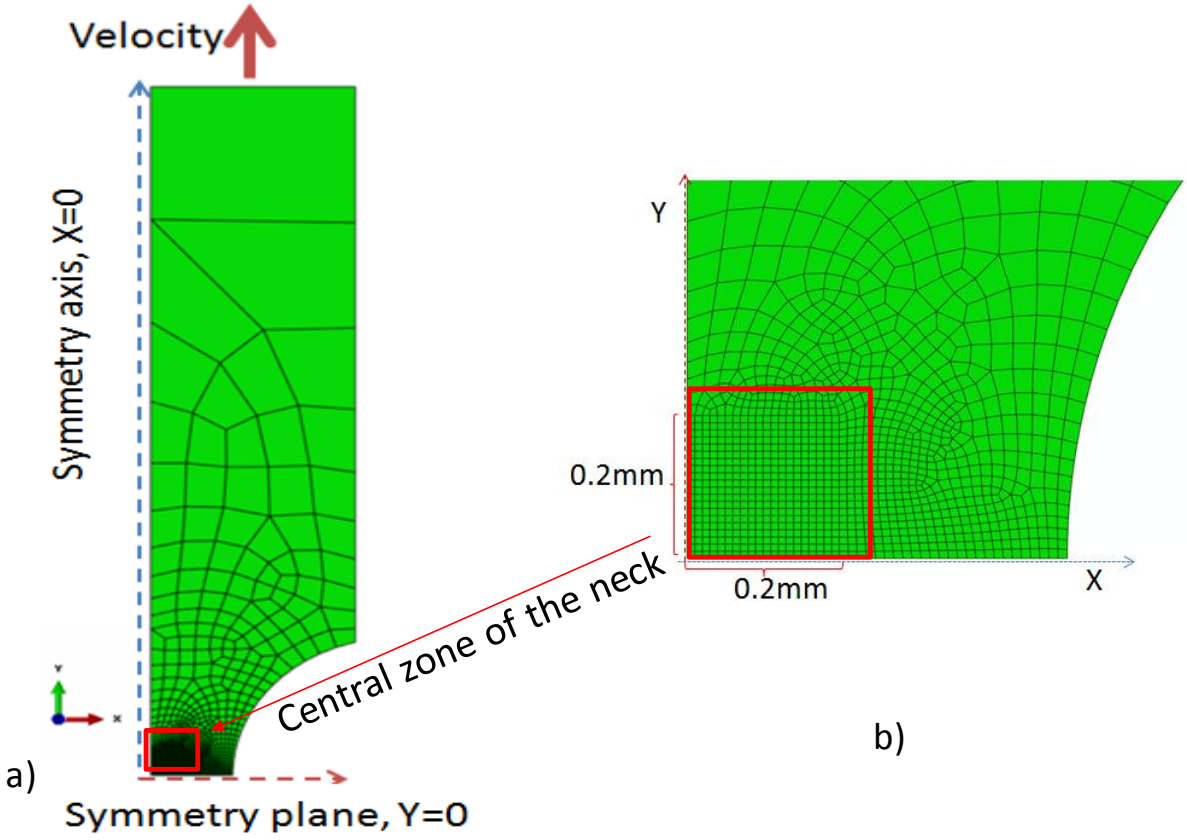

Figure VII.13: Adapted finite element model of the tensile test on the notched axisymmetric sample. (a) Boundary conditions and velocity field applied, (b) Mesh design zoomed on the sub-volume measurement area.

Figure VII.14a shows the isovalues of axial strain, triaxiality (T), stress component, numerical density of voids per mm³ (N), porosity (f) and mean void radius (R). These isovalues are shown at the moment when the maximum plastic strain is close to unity in the minimal cross-section. The fracture initiation (critical distance between two cavities λ_f) shown in Figure VII.14b is maximum at the center of the necking section due to the high concentration of the plastic deformation and the triaxiality.

a)

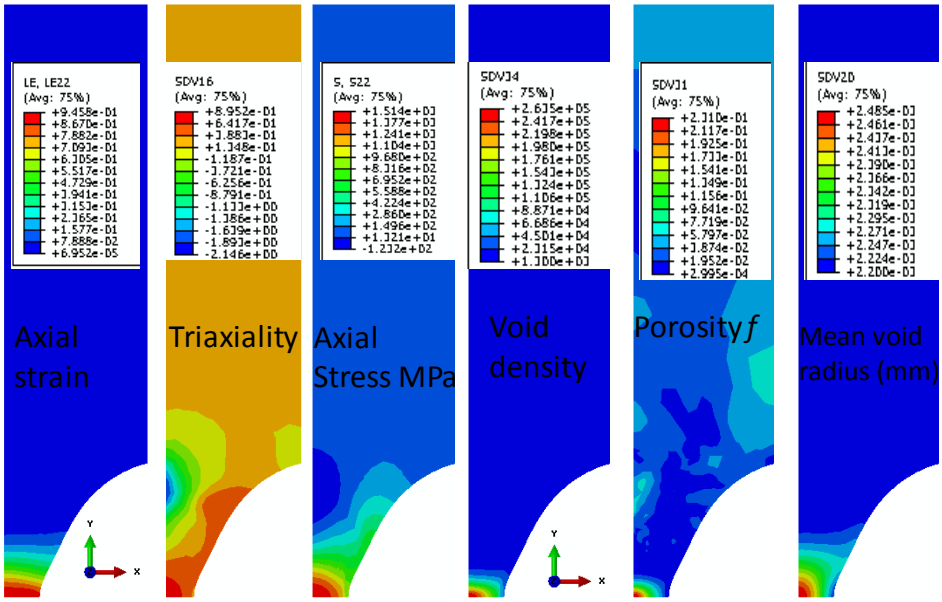

b)

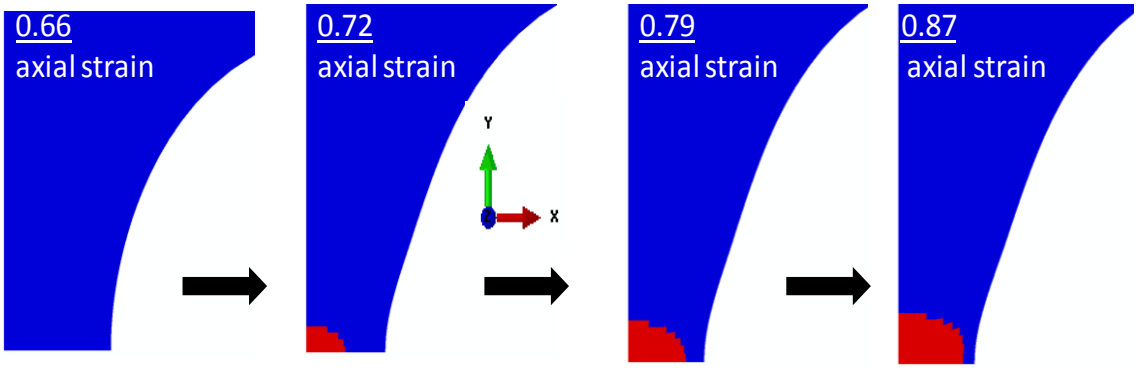

Figure VII.14: a) Simulation results isovalues when maximum plastic strain is near unity: axial strain, triaxiality, axial stress, numerical void density, porosity and mean void radius, b) Kinetic of the fracture initiation criterion (critical distance between two cavities λ_f , reached in red element).

VII.2.2.1 Post processing of FE values

Figure VII.14 underlines a strong heterogeneity in the cross-sections of the sample. In order to compare the experimental results with the numerical predictions at different levels of the axial strain in the minimum cross-section, average values of specific scalar fields of interest were extracted from the heterogeneous field distributions. The weighted average method [LIN 1996] was used to extract such average values over the central sub-volume and over the cross-section (see fig VII.15a). Due to the choice of axisymetric element configuration the central sub-volume is cylindrical rather than hexahedral, with its half-height and radius equal to 0.15 mm-see Figure VII.15 (or a cylinder of 0.3 mm radius and a height of 0.3 mm).
The loss of accuracy due to this approximation can be considered negligible as the experimental measurements [LAN 2011a] show that the void density is sufficiently homogeneous within the measurement domain. Thus, its exact shape and dimensions would not influence the result.

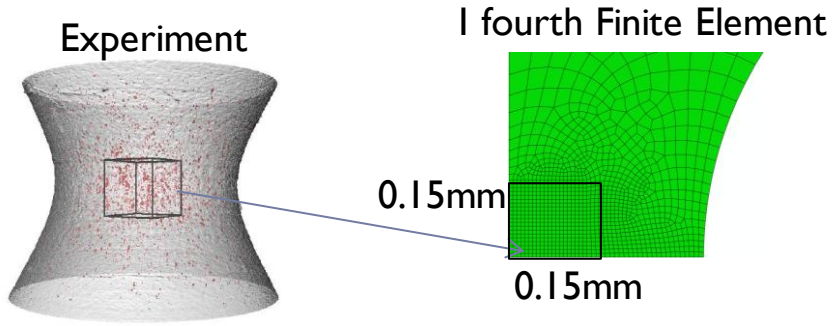

Figure VII.15: Areas of the damage values extraction over the central sub-volume and over the cross-section; a) 3D experimental view, b) The axisymetric element view.

The average values of *f*, *N*, *R* and in general for any scalar field α are calculated with this expression:

$$\alpha_{av} = \frac{\sum_{i=1}^{n_{element}} S_i \alpha_i}{\sum_{i=1}^{n_{element}} S_i} \qquad \text{(VII.3)}$$

Where α_i is the value of the scalar field α in the finite element i in the domain. S_i represents either the area of the cross-section that corresponds to the finite element i, or for the volume average calculations, S_i designates the element volume. Surface averages are performed for the calculations of the axial stress and strain values, while volume averages are used for the porosity-related quantities. It is noteworthy to tell that the set of finite elements that contribute to the volume average is evolving in time, since the average is computed over a fixed spatial domain – not a material domain.
The area of the necking section is calculated by measuring the radius of the minimal cross-section ($r_{section}$) during the test. In order to compare the triaxiality to the experiments, Bridgman Eq. V.4 is also applied to the numerical results even if we know it is just an approximation, an identical T measure is mandatory. For this purpose, the notch radius r_{notch} from FE results is required at different strain levels. The three nodes closest to the symmetry

plane on the notch radius are chosen and used to fit a circle whose center (a, b=0) is retrieved by the circle equation (Eq.(VII.4)),

$$r_{notch} = \sqrt{(x-a)^2 + (y-b)^2} \tag{VII.4}$$

Where r_{notch} (in plane X-Y) evolves during the tensile test, and (x,y) are the coordinates of the three nodes (see Figure VII.15b).

Using $r_{section}$ and r_{notch}, the average values (σ_{axial} ,T, ε_{axial}) can be computed in a similar way as in the experimental results by relations Eqs. (V.3)- (V.4)-(V.5).

VII.2.2.2 Element size influence

In order to verify the mesh convergence for the simulations of the notched tensile test, six meshes with different element sizes (see Fig.VII.16) and the previous "adapted" mesh (see Figs.VII.12-15b) have been used. The mesh sensitivity has been conducted by comparing the distribution and the evolution of the local axial strain, porosity (f), density of voids (N), and mean void radius (R).

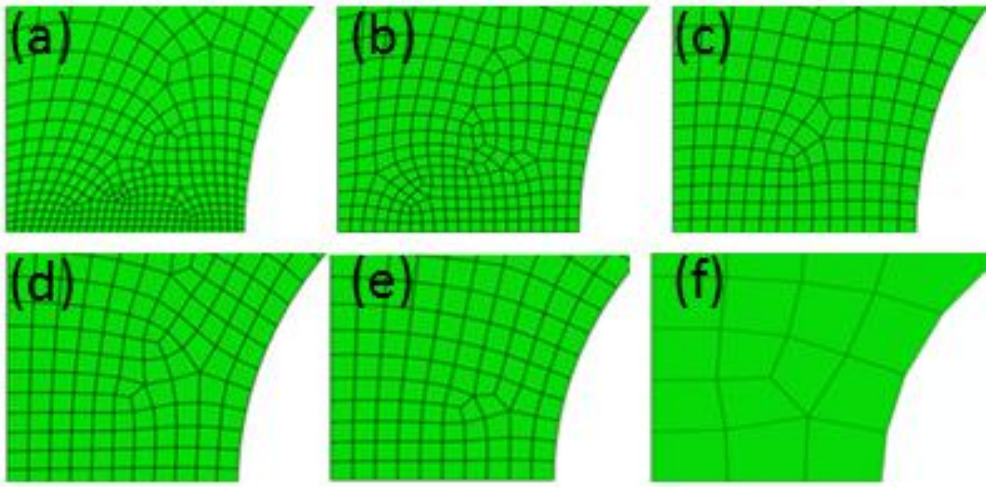

Figure VII.16: Element sizes used during the mesh sensitivity analysis on notched tensile simulations: (a) 15µm, (b) 25 µm, (c) 35 µm, (d) 45 µm, (e) 50 µm, (f) 167 µm.

Figure VII.16 shows the distribution of the axial strain and of the void radius as a function of the normalized distance from the center. Note that the center within the smallest necking section at the symmetry axis is defined by $x/r_{section}$ =0 and the notched side by $x/r_{section}$ =1. Figure VII.18 shows the distribution of the porosity at two different loading steps. Except for the coarsest mesh (Figure VII.16f), almost no mesh sensitivity has been detected during the test simulations. The local axial strain distribution (Figure VII.17a) is quite homogeneous along the cross-section for all deformation steps. A small heterogeneity of the mean void radius is observed (Figure VII.17b), with the maximum value located close to the vertical symmetry axis. One can note that the maximum is not exactly located at the center of the specimen but at about 1/10 from the center, probably due to Abaqus numerical treatment of the cylindrical symmetry.

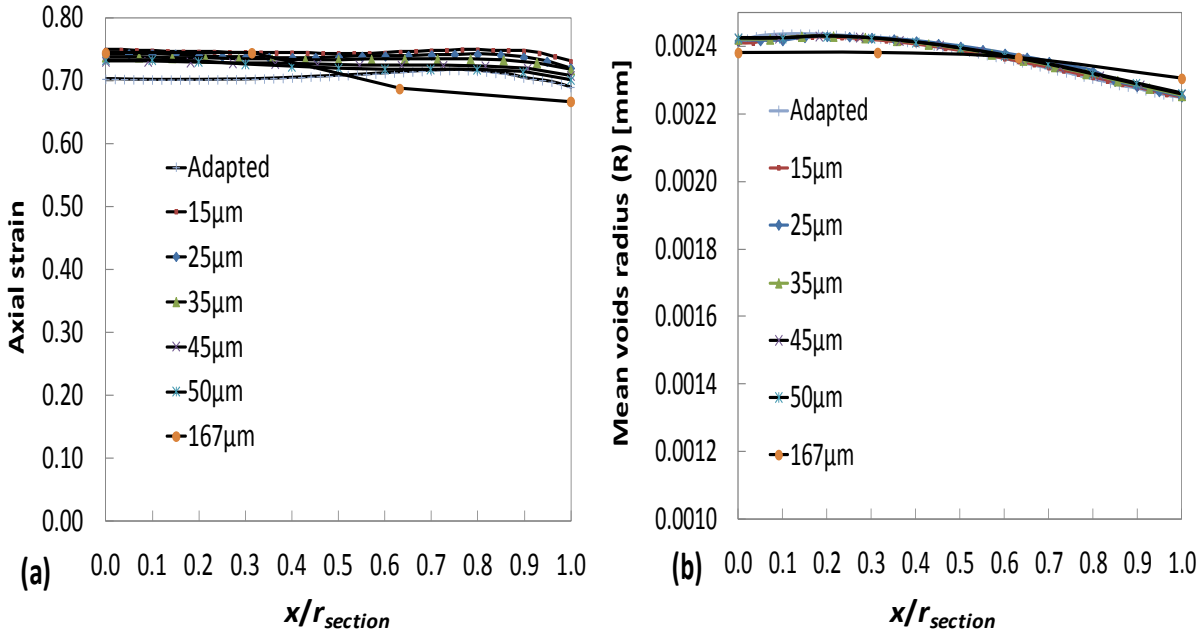

Figure VII.17: Element mesh size influence and field heterogeneity at an average axial strain of 0.75: (a) on local axial strain (ε_{axial}), (b) on mean void radius (R).

The analyses of the porosity (f) in Figure VII.18 and the density of voids (N) in Figure VII.19 point out mesh sensitivity after 0.5 of axial strain. This strain level corresponds to the beginning of coalescence according to Landron et al. [LAN 2010-2012]. The graphics at 0.75 of strain show that the values of f or N decrease when the mesh size increases as the element size prevents the simulation to compute accurate stress and strain field gradient. The distribution heterogeneity increases with the strain. The maximum value is located close to the center ($x/r_{section}$ =0) for low axial strain, but moves at around 0.1 of relative radius ($x/r_{section}$) when the axial strain reaches 0.75.

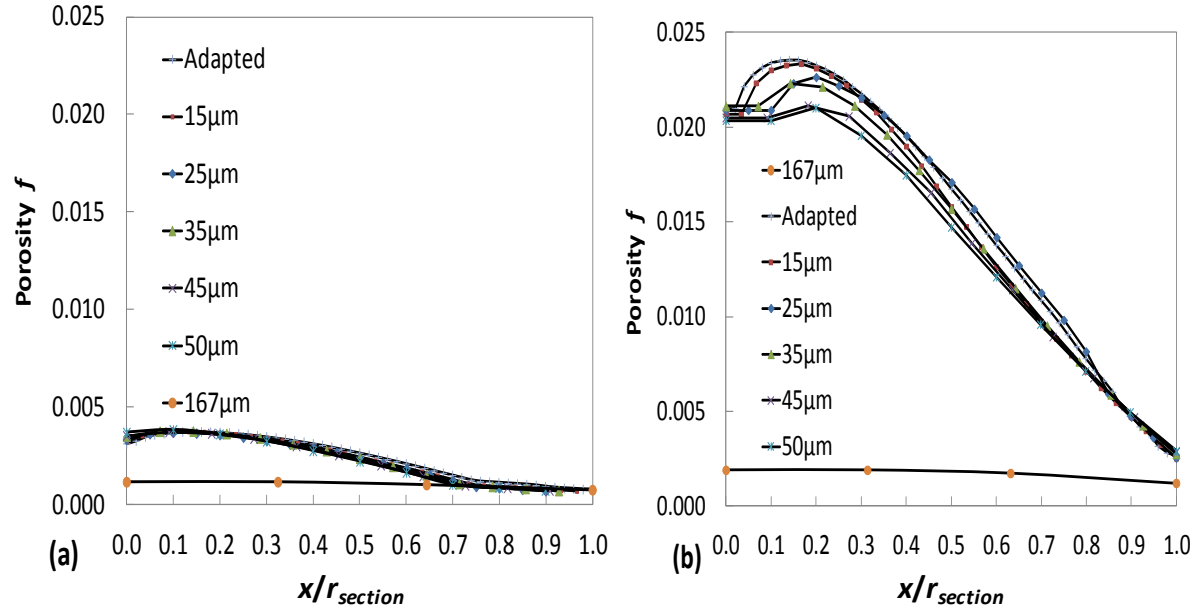

Figure VII.18: Element mesh size influence and heterogeneity distribution of the total porosity (f): (a) at an average axial strain of 0.5, (b) at an average axial strain of 0.75.

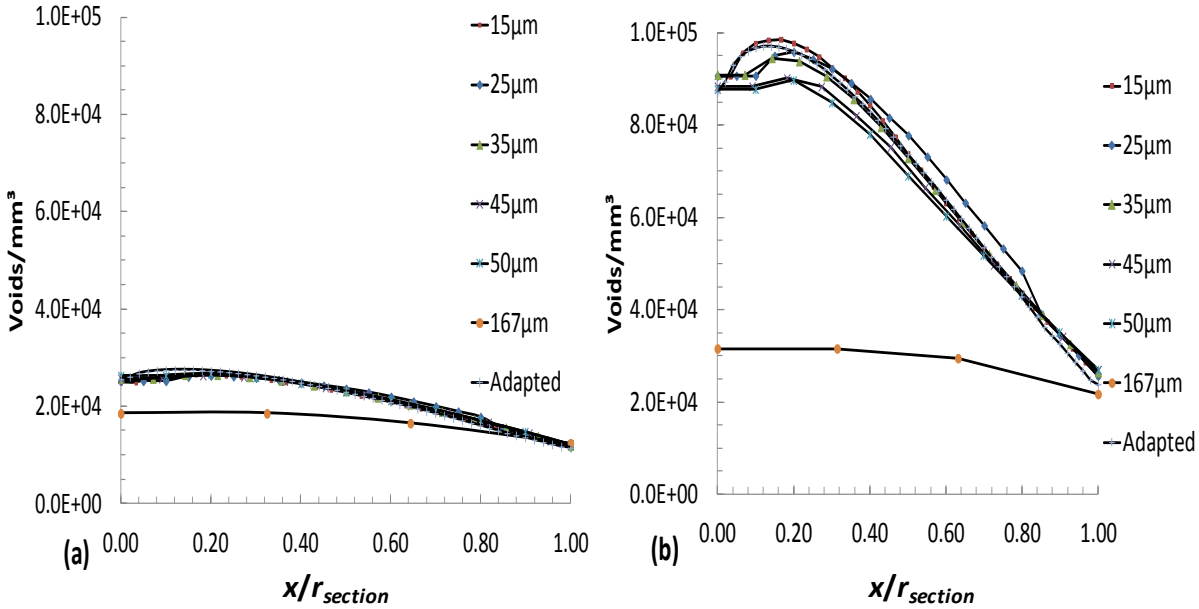

Figure VII.19: Element mesh size influence and heterogeneity distribution of the density of voids (*N*) (a) at an average axial strain of 0.5, (b) at an average axial strain of 0.75.

A strong heterogeneity of the distribution of the damage variables (porosity *f*, density of voids *N*) through the sample cross-section is observed. The element size has no influence on the axial strain and the equivalent void radius distributions, except for the 167-µm element size which is clearly too coarse to provide accurate results. The damage state variables such as the porosity (*f*) and the density of voids seem more mesh sensitive.
In the current study, the element size choice has been restricted by the experimental conditions to fine mesh density: "adapted mesh", which verifies by far these numerical considerations.

VII.3 GTNBF model validation on a notched tensile test

The present section is dedicated to the comparison between the measurements performed by the high resolution X-ray absorption tomography method [LAN 2011] and the FE predictions. The calculations are extracted from the in situ tensile test of the 1-mm notched specimen presented in section VII.2.2. The mesh used corresponds to the adapted one containing a very fine element size of 10µm×10µm available in the sub-volume (Figure.II.3b). This study has been realized with the material parameters corresponding to the GTNBF model for DPI steel (see Table V.3). Following this brief introduction, the comparison will be divided into four parts. The first one is focused on the stress and triaxiality FE responses. Then, the innovative contributions from Landron et al. [LAN 2012] to the experimental and numerical evaluations of the nucleation and the growth will be compared with the Bouaziz et al. [BOU 2008] model both laws being available in GTNBF model. The last part presents the influence of the back stress introduced through a proposed triaxiality definition T_B (see Eq.IV.32).

VII.3.1 Stress-strain curve and triaxiality evolution

Figure.VII.20 presents the comparison between the experimental and numerical average stress values. The blue curve is the experimental response from the in-situ tensile test, and the red curves are the numerical results. The dashed curve shows the stress value computed with Eq.(V.3) in a similar way as in the experimental results.The red solid curve is the stress response using the weighted average method in Eq.(VII.1). The comparison underlines that the numerical stress values lie below those obtained by the experiment. The experimental points seem to fluctuate slightly before 0.3 axial strain. The reduced size of the sample and possible geometrical inaccuracies due to its particular shape, along with the use of a miniature in-situ machine probably contributed to this effect – besides the stress heterogeneity within the notched specimen. The two numerical averaging methods show a little stress difference, except for the final stages where the differences become very large. This observation shows the importance of taking into account weighted average method in the sub-volume quantification and to consider a sufficiently large number of elements for the average calculation.

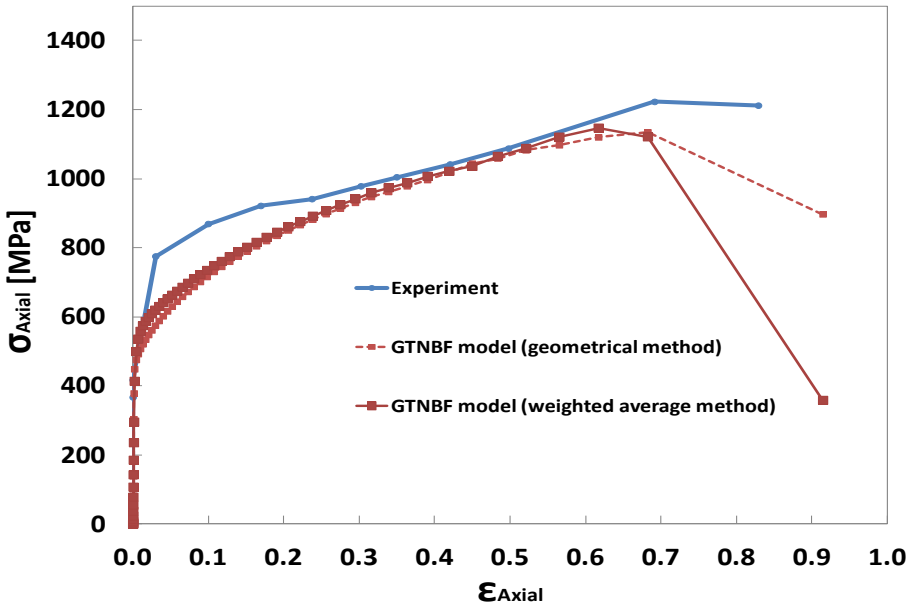

Figure VII.20: Axial stress-strain curves comparison between the GTNBF model prediction and the experiment.

Figure VII.21a compares the evolution of r_{notch} obtained by measurement and by the simulation. The experimental and numerical notch radii are in good agreement, a maximum of 11% discrepancy can be detected when the axial strain reaches 50%. This difference could be due to the material behavior model, but also to the approximate description of the notch radius based only on three nodes within the simulation. It is also important to remind that the experimental values are averaged over several tested specimens, where differences of the same order were observed between the different experiments [LAN 2011]. The radius tolerance of the specimen during the cutting process cannot be reproduced in the axisymetric (2D) simulation and some discrepancies happened within real r_{notch}.

The gap between the experimental and the simulation results is linked with the differences in the r_{notch} measurements and predictions as the values of $r_{section}$ overlap (Figure VII.21b). The evolution of the triaxiality approximated with Bridgman's formula (Eq. V.4) is shown in Figure VII.21c.

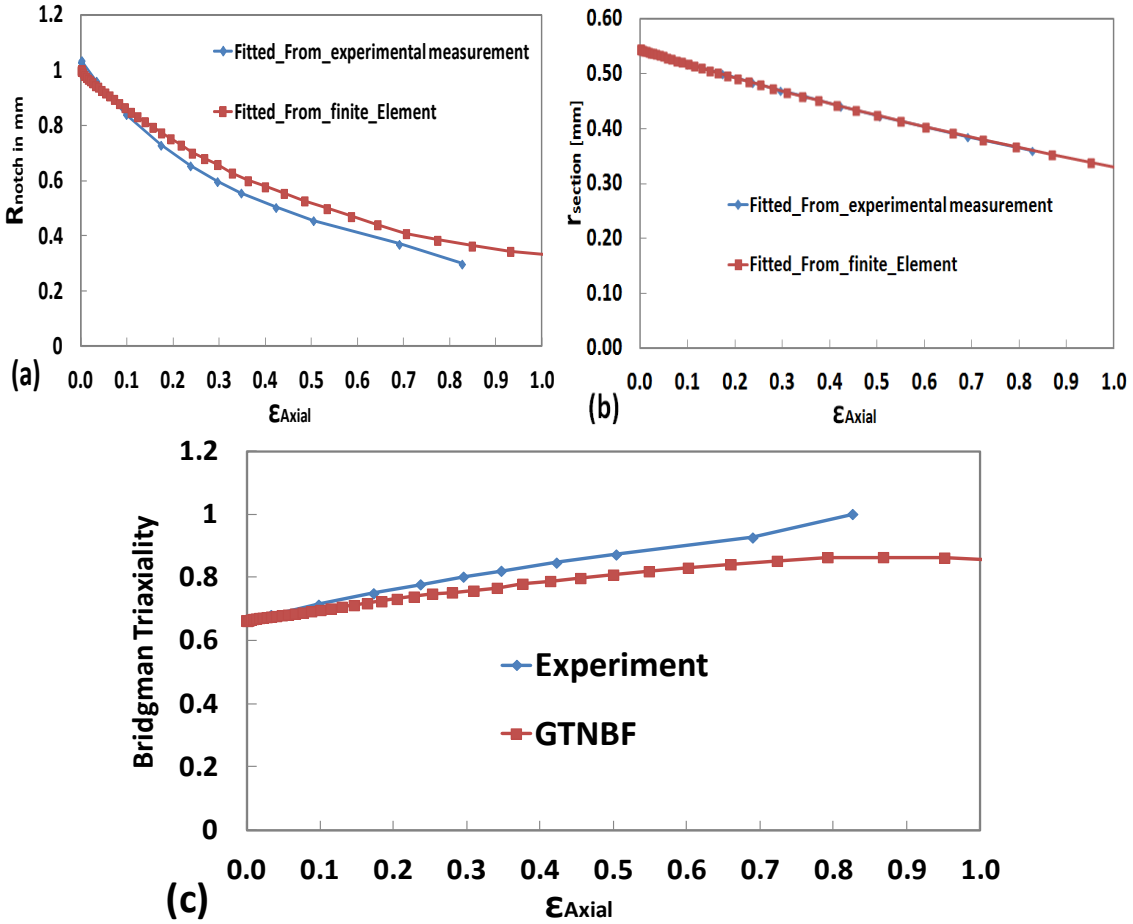

Figure VII. 21 : Comparison of r_{notch} (a) and $r_{section}$, (b) evolution obtained from measurement and finite element simulation during the notch tensile loading, (c) Triaxiality comparison, according to Bridgman's approximation, between the current GTNBF model prediction and the test.

VII.3.2 Nucleation laws comparison

Figure VII.22 shows the evolution of the numerical and experimental density of voids- with the axial strain – which plays the role of the loading parameter for all the comparisons. Simulations are performed with both nucleation equations presented in section IV.2.2.3, *i.e.* Eq. IV.8 (Bouaziz et al. [BOU 2008]) and section IV.3.1.2, *i.e.* Eq. IV.30 (Landron et al. [LAN 2011]). The two predictions lay relatively close to each other, and both approximate well the experimental curve. It is noteworthy that the parameter identification for Bouaziz et al [BOU 2008]. Law was performed using smooth tensile samples [BOU 2008], while both smooth and notched samples were used for the parameter identification of Landron et al. law [LAN 2012]. Consequently, further work would be required to investigate the respective accuracy of the two nucleation equations. After an axial strain of approximately 0.5, the number of voids drastically increases, since the coalescence phenomenon catalyzes the nucleation of new generations of small voids. When coalescence takes place and leads to micro-cracks,

interconnecting the larger voids, the assumption of spherical voids becomes more and more inadequate – as indicated by the sample's micrograph at 0.83 of axial strain in Figure VII.22. Nonetheless, the experimental numerical density of voids is measured up to such very large strain values and can be used for the validation of the models.

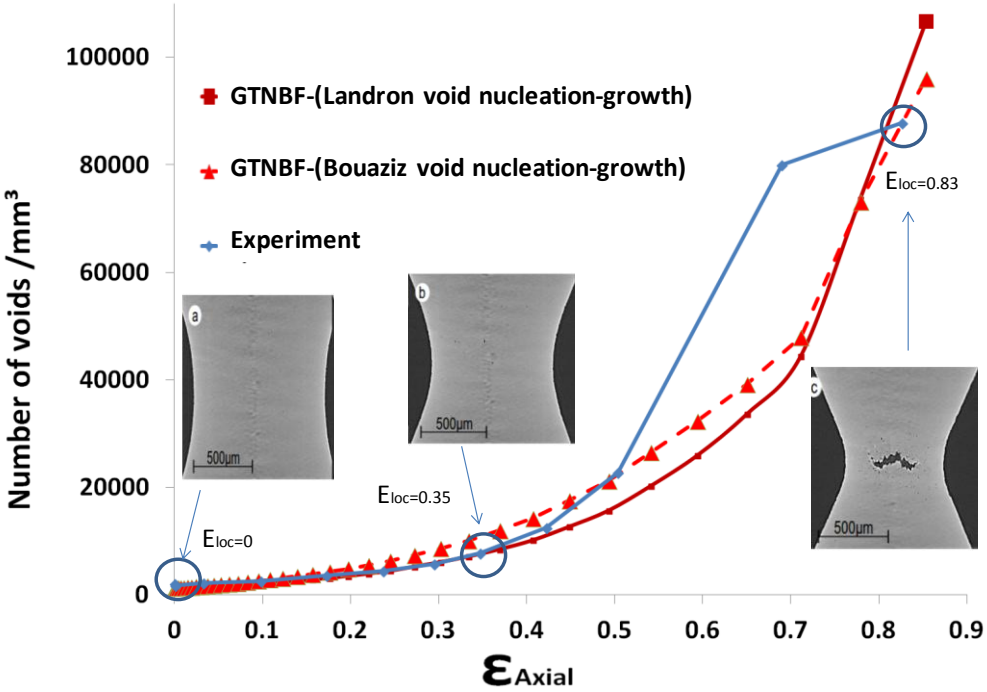

Figure VII.22: Comparisons between predictions of simulation with Landron, and Bouaziz, nucleation laws introduced in the GTNBF model and the test measurement X-Ray tomography observations [LAN 2012]. The number of voids per unit volume is calculated using the weighted average method (Eq.VII.1).

VII.3.3 Growth laws comparison

The mean void radius is calculated with Eq.IV.9 (Bouaziz et al. [BOU 2008], see section IV.2.2.3). Given that the second term in this equation is related to nucleation, the two predictions of the mean void radius are not identical, as shown in Figure VII.23. The prediction using Landron et al. law [LAN 2011] gives slightly higher mean void radius values. Note that with respect to all of the other variables related to damage, the mean void radius remains almost constant during the whole test for both nucleation laws, which is in agreement with the experimental observations. When coalescence develops at larger strains, the experimental void radius increases. The calculated ones evolve with the same very small growth rate. This is consistent with the phenomenological description of the coalescence in the present model, and indicates that the physical meaning of the quantity R is lost during the coalescence step. This observation corroborates the fact that the approximation of spherical voids of identical size becomes more and more questionable as coalescence appears.

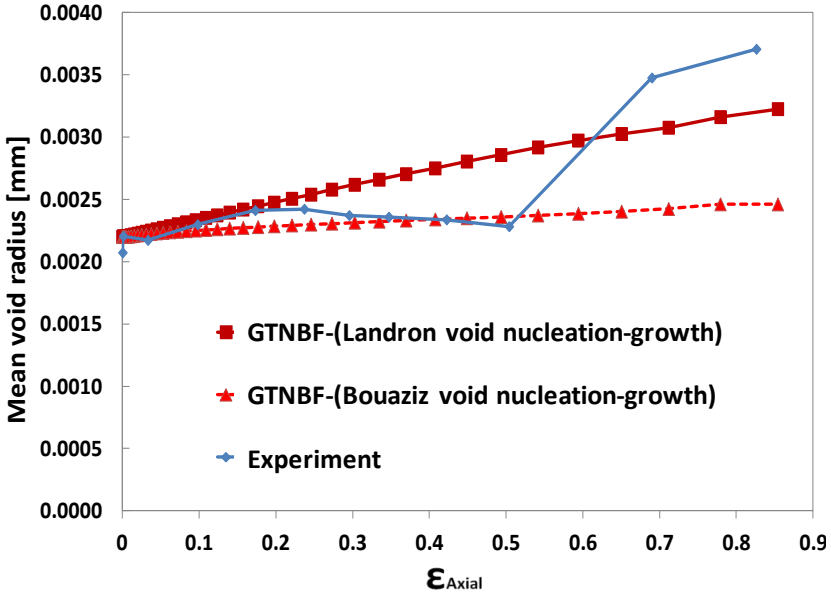

Figure VII.23: Comparison of the evolution of the mean void radius measured or predicted by Landron et al. [LAN 2011], and Bouaziz et al. [BOU 2008] growth laws, during the notched tensile test.

Eventually, the combined effect of the numerical void density and of the mean void radius provides the prediction of the void volume fraction shown in Figure VII.24. The void volume fraction evolves from its initial value of 2.10^{-4}, up to values of 2.10^{-3} and more. The two predictions have similar accuracies although with different trends. Both seem able to correctly describe the experiments. The parameter identification has a non-negligible influence on the final predictions, and future investigations will be devoted to better understand its effect.

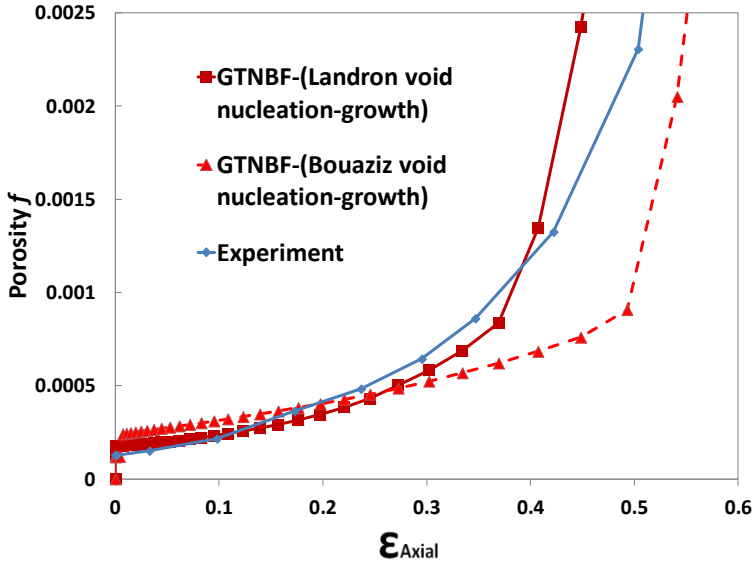

Figure VII.24: Comparison of the evolution of the porosity measured or predicted by Landron et al. [LAN 2012], and Bouaziz et al. [BOU 2008] growth laws, during the notched tensile test.

VII.3.4 GTN Abaqus-explicit and GTNBF models responses

Until this section, it is known that the GTNBF model which takes into account a more accurate void nucleation, growth and coalescence until failure than previous GTNB model, has been well validated with the cylindrical notch radius specimen used by Landron et al. [LAN 2012]. It has been observed that the extended model is also sensitive to the plastic anisotropy parameters, and the strong effect of the triaxiality. The kinematic hardening influence has been particularly highlighted numerically by Ben Bettaieb [BEN 2012] when investigating the contribution of the void nucleation law from Bouaziz et al. [BOU 2008]. Since Bouaziz and Maire experimental contributions, many authors have confirmed the strong effect of the triaxiality [ZHI 2009] [LI 2010] [LAN 2011] [BAR 2012] [REC 2012] on the ductile damage mechanisms. Researchers agree that one cannot generalize the analysis of one DP steel grade to all DP grades. Indeed, the previous sensitivity on various volume fraction of martensite has shown the importance of the microstructure, the shape of the hard martensite islands, and the void shape on the damage evolution [LAN 2011a]. The previous part has contributed to point out the importance of identifying very carefully the initial damage parameters introduced during the sheet-metal forming such as the initial porosity f_0. The fracture initiation characterized by the coalescence stage has to be well predicted to avoid necking and unwanted failure in the final products. The sensitivity of failure prediction has been underlined by studying the effect of the final void volume fraction f_f variation.

Numerous FE codes such as Abaqus, Lagamine, and ANSYS integrate predefined ductile damage laws. The most used by numerous researchers and steelmakers is the well known GTN model [TVE 1984]. Therefore, the main goal in this section is to compare the GTNBF model predictions to the ones computed by GTN model (Abaqus-explicit). To reach that goal, a comparison has been performed with the same finite element procedure using the notched sample made of DPI steel (see VII.2.2). The material properties for the GTNBF model are the same as previously and those for the GTN model have been identified by ArcelorMittal [OUS 2012] and can be found in Table V.2.
The axial stress and the porosity evolutions in function of the axial strain obtained with the damage models are compared. The axial stress-strain evolution simulated with the GTN model [TVE 1984] or GTNBF model [FAN 2013] is in good agreement compared to the experiment. However, a significant difference is noticed between the two models. Indeed, the axial stress-strain curve from the GTN model increase continuously below the GTNBF model prediction and the fracture shortly occurs later after the GTNB extended model. This first comparison in terms of axial stress highlights that both ductile damage models predict well the DPI material behaviour using on one hand the phenomenological approach developed in the GTN model thirty years ago and on the other hand the physically-based approach. The GTN model initiated by Gurson [GUR 1977] and later improved by Tvergaard & Needleman [TVE 1984] integrates an isotropic hardening law while the GTNBF model has a modified Armstrong-Fredericks mixed hardening law. The GTNBF model extended to elasto-plastic permits to take into account the plastic anisotropy influence of the matrix through the Hill matrix $\underline{\underline{H}}$ and the backstress tensor $\underline{X}$.

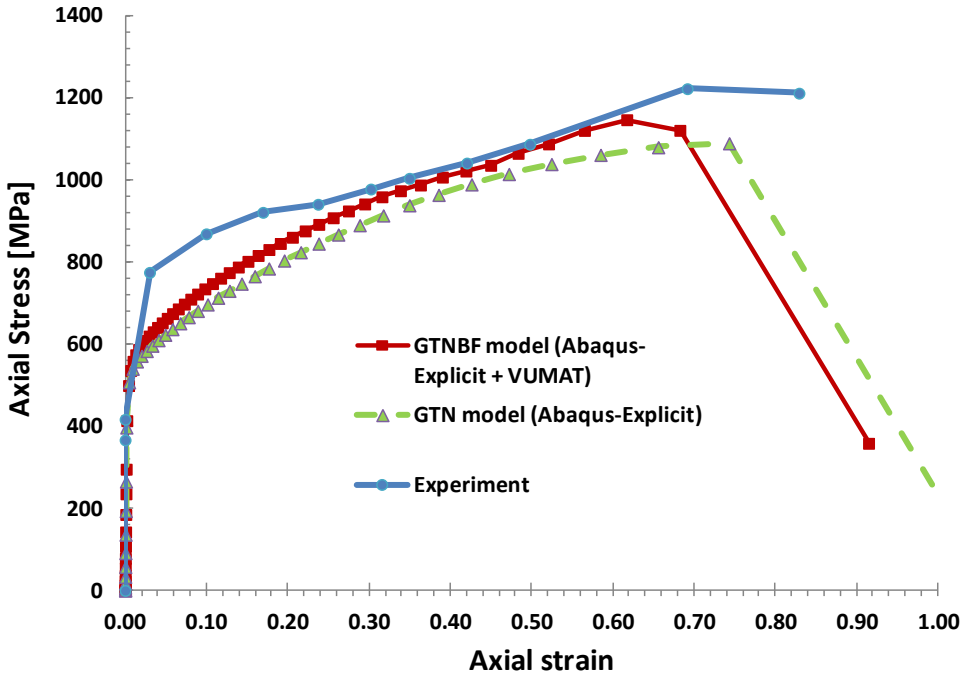

Figure VII.25: Experimental, GTN and GTNBF models axial stress-strain comparison after a tensile test with a 1 mm notch radius specimens made of DPI steel.

The stress gap between the two simulations increases rapidly when reaching large plastic strain in the material. Unfortunately, the elasto-plastic difference between both models cannot be used has the only reason explaining the stress softening predicted by GTNBF model and the brutal simulation stop characterizing the model fracture in GTN model. Therefore, the porosity predictions computed by both ductile damage models have been compared to the experimental measurement. Figure VII.26 depicts the porosity evolution of the GTN and GTNBF models.

Although, the GTN model integrates the three steps of the ductile damage mechanisms (void nucleation, growth and coalescence) before fracture apparition, it seems obvious that the GTN porosity evolution is not well predicted compared to the experiment and the validated GTNBF model. More precisely, the porosity evolution curve from GTN model fit very well the experimental curve until 0.2 of axial strain with a porosity value inferior to 0.001 (*fc*). Meaning, that the only porosity contribution is coming from void growth. Indeed, the coalescence model stipulates that if $f < f_c$ then $f^* = f$ (see Eq.IV.36). Then, the porosity curve evolution surges after the porosity reaches the critical value (*fc*). Before this point the porosity contribution is due to void nucleation and growth evolutions after coalescence is added.

It has been explained in chapters III and IV that the GTN model includes a phenomenological void nucleation while the GTNBF model thanks to the accurate 3D X-ray tomography measurements [LAN 2011] integrates a physically-based nucleation model validated with the present tensile test. All damage parameters from the GTNBF model have been identified based on this method. The identification of the six damage parameters: initial void volume fraction (f_0), standard deviation (S_N), mean equivalent plastic strain (ε_N), volume fraction of secondary voids (f_N), critical void volume fraction (f_c) and final void volume fraction (f_f) is mandatory to apply the GTN model for fracture analysis. Methods are available to best fit the

phenomenological damage predictions to the experimental results by adapted those six parameters. For instance, the nonlinear least squares fitting method of parameters, resulting from minimization of a finite element simulation (FEM) results and on the experimental specimen response (usually a tensile test) [BRO 1995]. The GTN model damage parameters (in the current study) have been identified by using inverse method [DEB 2009] [MOH 2010-2012] [LOU 2010-2012] [NIA 2012] (see conclusion, chapter VIII) and a literature survey (especially for f_f). It is noteworthy to notice that the GTN model damage parameters presented in Table V.3 correspond to the best stress-strain curve of tensile test fitting. If one tries to fit the porosity-strain curve from GTN model to the experimental curve, it will produce a stronger stress-strain evolution decrease. With this manipulation, the fracture will appeared far more later underestimating the fracture initiation in the material.

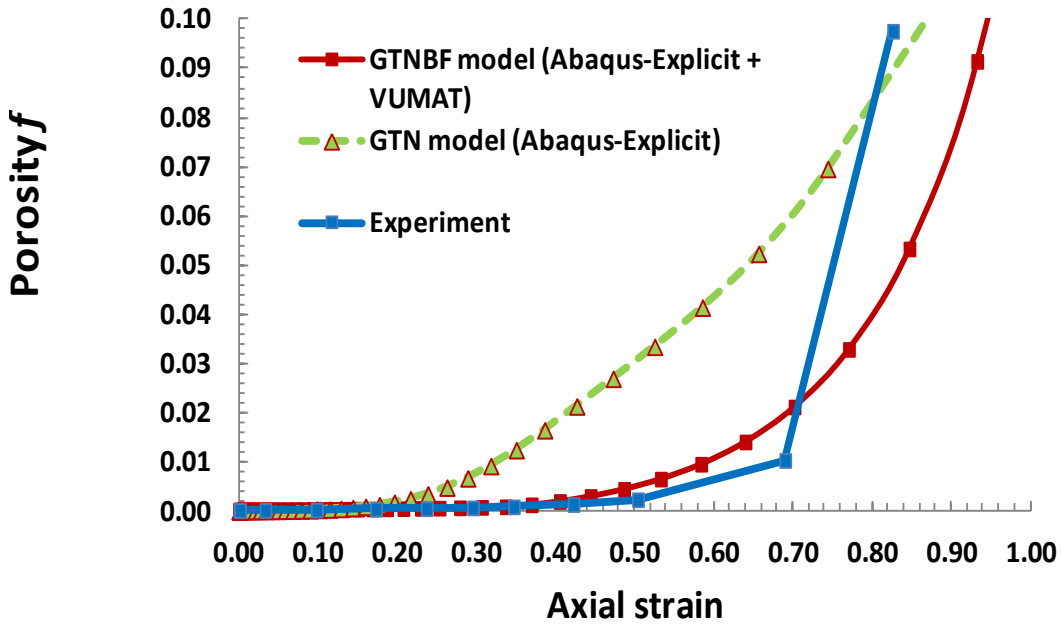

Figure VII.26: Experimental, GTN and GTNBF models porosity-strain comparison after a tensile test with a 1 mm notch radius specimens made of DPI steel.

More recently Ramazani et al. utilized a Response Surface Methodology (RSM) on similar DPI steel based on a statistical approach to calculate quantitatively the effects of different input parameters, for more details see [RAM 2012]. The parameters found with the last cited identification method have been used to simulate again the GTN model responses with no significant improvement on the porosity curve evolution.

Since the sensitivity study performed on the initial porosity f_0 and the final void volume fraction $f_{f,}$ it is known that the coalescence stage affects the fracture initiation common to both models. This statement and the GTN and the GTNBF models comparison, let us suggest that the main damage modeling difference is focus on the approach method used to predict the void nucleation evolution. The phenomenological GTN model is based on initial voids of substance grow and secondary voids nucleate while forming proceeds; when the void volume fraction reaches a critical value, fracture occurs (coalescence model). In this model, the damage variable f is the porosity, and the evaluation of voids is characterized by the growth of

existing voids and the strain-controlled nucleation of new voids. This approach differs when suing the GTNBF model in term of voids strain-controlled nucleation mechanism. It has been described as a micromechanical approach based on the interface ferrite-martensite decohesion [ARG 1975] [LAN 2011] (see section IV.3.1.2, chapter IV).

VII.3.5 Backstress definition

Chapter IV section 3.1.3 has shown that the classic triaxiality expression T_1 has been modified to integrate the backstress tensor in the nucleation and growth laws proposed by Landron et al.[LAN 2011] and Huang [HUA 1991]. Indeed, as reminded hereafter in Equations (case 1 to case 4 in Table VII.2), there are four possibilities to define the triaxiality when backstress is present. In the GTNBF model, the classic triaxiality has been transformed to the triaxiality T_4 .

Table VII.2: Triaxiality cases applied for the kinematic hardening influence.

Triaxiality cases	T_n
Case (1) (Classic)	$T_1 = \frac{\sigma_m}{\sigma_{eqv}(\underline{\sigma})}$
Case (2)	$T_2 = \frac{\overline{\sigma}_m(\underline{\sigma}-\underline{X})}{\sigma_{eqv}(\underline{\sigma})}$
Case (3)	$T_3 = \frac{\overline{\sigma}_m(\underline{\sigma}-\underline{X})}{\overline{\sigma}_{eqv}(\underline{\sigma}-\underline{X})}$
Case (4) (chosen in GTNBF model)	$T_4 = \frac{\sigma_m}{\overline{\sigma}_{eqv}(\underline{\sigma}-\underline{X})}$

$\overline{\sigma}_{eqv}(\underline{\sigma}-\underline{X})$ is the anisotropic equivalent shifted stress (with respect to the quadratic Hill criterion).

$\overline{\sigma}_m(\underline{\sigma}-\underline{X})$ corresponds to the macroscopic mean shifted stress equal to $\frac{1}{3}tr\left(\overline{\underline{\sigma}}\right)$.

The present chapter has shown a good agreement for all the numerical comparisons to the experimental results. Although this study is satisfactory, the current section has the objective to check our triaxiality choice by testing the prediction sensitivity to three other triaxiality definitions (T_1, T_2, T_3). The following methodology is adopted: in a first step we focus on the backstress influence injected in the classic mean stress and the second one is dedicated to the influence of the backstress introduced in the traditional equivalent stress.

VII.3.5.1 Mean stress response to backstress definition

The numerical impact of the backstress tensor has been quantified with the previous two geometries (single element, cylindrical notched specimen) loaded in uniaxial tensile and shear directions (see chapter VI). For each geometry, four GTNBF models have been built up with the DPI steel material property. These four GTNBF models correspond to the triaxiality definitions as seen above T_1, T_2, T_3, T_4, and referred by number: case (1) to case (4) in all figures.

- Uniaxial tensile test

The uniaxial tensile test imposes certain stress components to be equal to zero: $\sigma_2 = \sigma_3 = 0$; $\sigma_{12} = \sigma_{31} = \sigma_{23} = 0$. Only the axial stress component is different from zero, in the present simulation $\sigma_1 \neq 0$. With these conditions Table VII.2 becomes Table VII.3.
During the simulation no triaxiality difference has been noted between case (1) and case (2) with a triaxiality value equal to $1/3$. This means that the $\bar{\sigma}_m(\underline{\sigma} - \underline{X}) \approx \sigma_m$ and the backstress tensor $\underline{X}$ has no influence on damage variables (porosity and voids density evolutions) for both cases. The most important cases to analyze are case (3) and case (4).

Table VII.3: Triaxiality cases for uniaxial tensile test.

Triaxiality cases	T_n
Case (1) (Classic)	$T_1 = \frac{1}{3}$
Case (2)	$T_2 = \frac{1}{3}\left(\frac{\bar{\sigma}_m(\underline{\sigma} - \underline{X})}{\sigma_m}\right)$
Case (3)	$T_3 = \frac{\bar{\sigma}_m(\underline{\sigma} - \underline{X})}{\bar{\sigma}_{eqv}(\underline{\sigma} - \underline{X})}$
Case (4) (chosen in GTNBF model)	$T_4 = \frac{1}{3}\left(\frac{\sigma_{eqv}(\underline{\sigma})}{\bar{\sigma}_{eqv}(\underline{\sigma} - \underline{X})}\right)$

The uniaxial tensile test results of the single element with 8 nodes and one integration point are presented for case (3) and case (4) in Figure VII.26.
Figure VI.26a shows the same axial stress-strain curve evolution for all triaxiality cases. The same graphic adds the backstress-strain curve evolution for the studied cases. It appears that the backstress reaches is maximum value (60 MPa) at small strain and decreases continuously until zero. This maximum value compared to the axial stress one (900 MPa) is too weak to affect the triaxiality cases.
The uniaxial tensile test illustrates that triaxiality is constant and equal to $1/3$ during the loading except for the beginning of the curve (fig.VII.27b) where a peak is observed. At the calculation start, the VUMAT takes an initial backstress guess value internally calculated in

the program to ensure the first convergence. This backstress guess value is set slightly higher than the equivalent stress value guess. It results that the simulation does not start at $1/3$. Furthermore, the guess backstress value at initial time strongly depends on the increment time.

A part from this, the triaxiality comparison between case (3) and case (4) shows a perfect agreement. Knowing that triaxiality strongly participates on the damage modeling, the graphics underline that the kinematic hardening ($\underline{X}$) has no influence on the porosity, and density of voids.

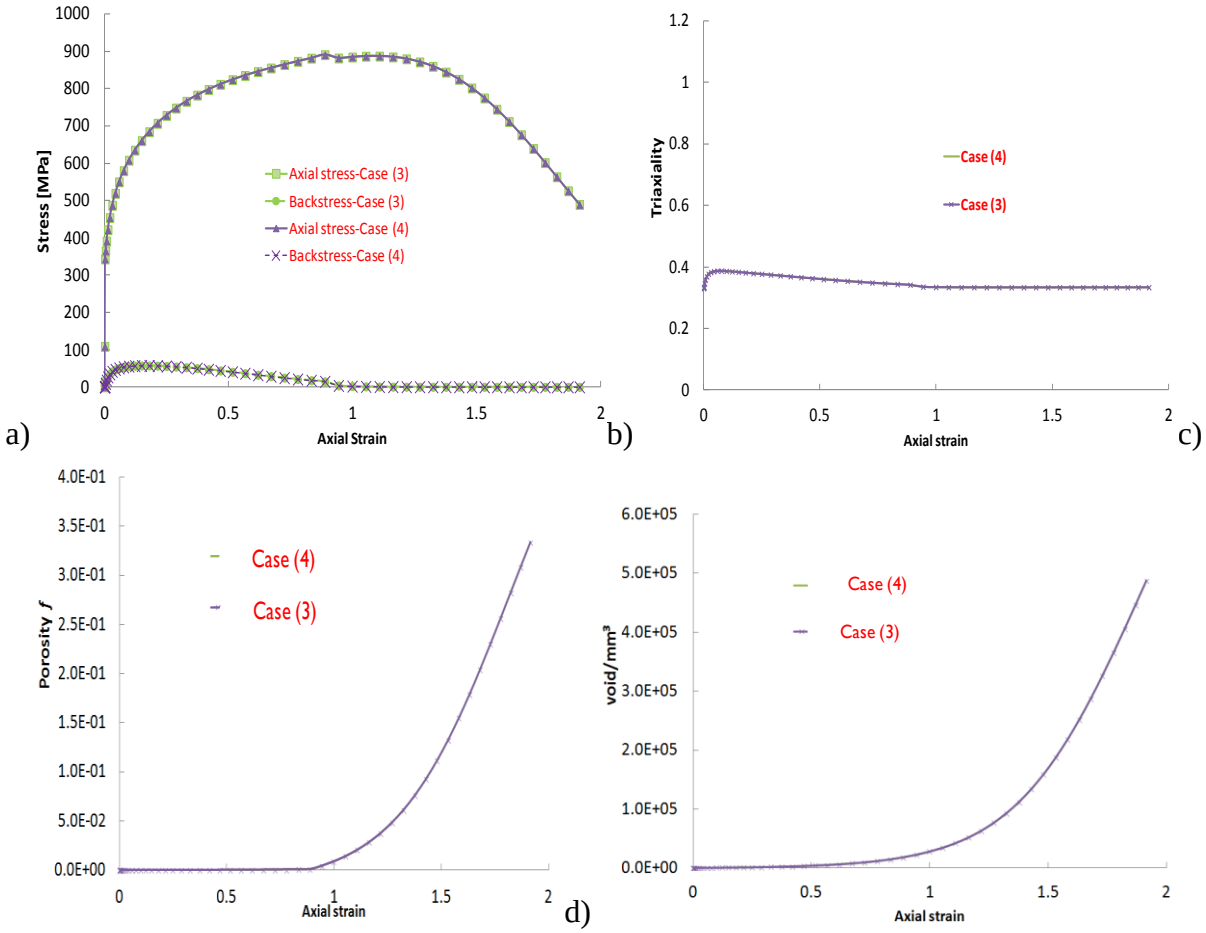

Figure VII.27: Backstress influence during the uniaxial tensile test; a) Tensile stress-strain curves, b) Triaxiality, c) total porosity *f*-strain curves, d) void density-strain curves for the DPI steel.

- Simple shear test

A pure shear test imposes certain stress components to be equal to zero: $\sigma_1 = \sigma_2 = \sigma_3 = 0$; $\sigma_{31} = \sigma_{23} = 0$. Only the shear stress component is different from zero, in the present simulation $\sigma_{12} \neq 0$. With these conditions Table VII.2 becomes Table VII.4 .

Table VII.4: Triaxiality cases for pure shear test.

Triaxiality cases	T_n
Case (1) (Classic)	0
Case (2)	$T_2 = \frac{\overline{\sigma}_m(\underline{\sigma} - \underline{X})}{\sqrt{3}\sigma_{12}}$
Case (3)	$T_3 = \frac{\overline{\sigma}_m(\underline{\sigma} - \underline{X})}{\overline{\sigma}_{eqv}(\underline{\sigma} - \underline{X})}$
Case (4) (chosen in GTNBF model)	$T_4 = \frac{0}{\overline{\sigma}_{eqv}(\underline{\sigma} - \underline{X})}$

The triaxiality evolutions, which are not sketched here, are all equal to zero due to the definition of the mean stress (including no shear direction). Also, the kinematic hardening has no influence regarding the cases (3).

The same conclusion as for the uniaxial tensile test can be written when analyzing the stress-strain curves in Figure VII.28a. The simple shear test shows that the damage is not predicted (see Figure VII.28b-c). Consequently, the total porosity f is constant and equal to f_0. The density of voids (fig VII.28c) is increasing due to the contribution of the equivalent shifted stress in the Landron nucleation law (see Eq IV.33). The equivalent void radius evolution (not in Figure VII.28) is equal to zero due to its dependency on the triaxiality factor. The shifted equivalent stress in the simple shear can be approximated at $\overline{\sigma}_{eqv}(\underline{\sigma} - \underline{X}) \approx \sigma_{eqv}(\underline{\sigma}) = \sqrt{3}\sigma_{12}$.

Again, the future work will be to take into account the damage due to shear loading.

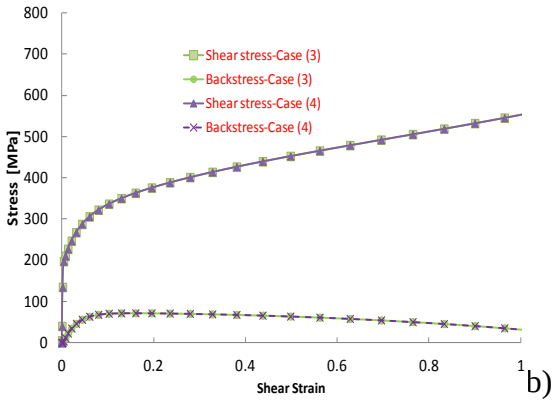

a)

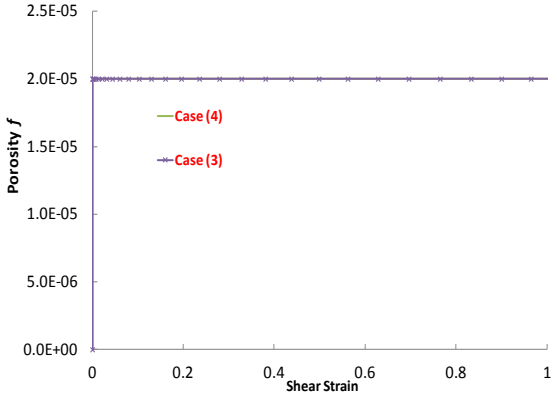

b)

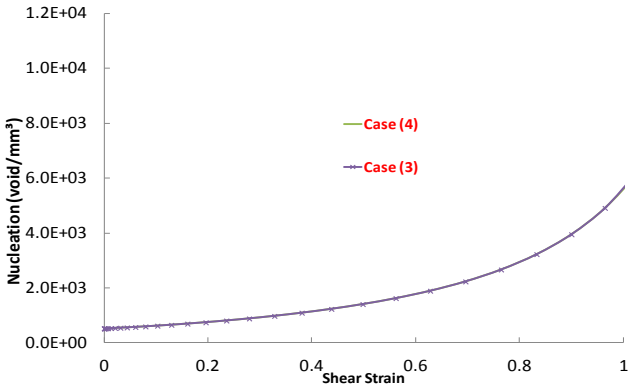

c)

Figure VII.28: Backstress influence during the simple shear test; a) Tensile stress-strain curves, b) total porosity *f*-strain curves, c) void density-strain curves for the DPI steel.

VII.3.5.2 Equivalent stress response to backstress definition

In this part of the study, the four triaxiality definitions (see Table VII.2) have been applied on the simulated notched specimen already presented in chapter VI. As mentioned in the single element simulations, the graphic (Figure VII.29a) underlines that the backstress ($\underline{X}$) has no influence on the mean normal stress (mean value at the minimal cross-section). In opposite, the graphic (Figure VII.29b) underscores the importance of taking the anisotropic equivalent shifted stress (with respect to the Hill criterion). The difference with the traditional triaxiality (T_1) appears at the coalescence stage when the material softens and the backstress is applied.

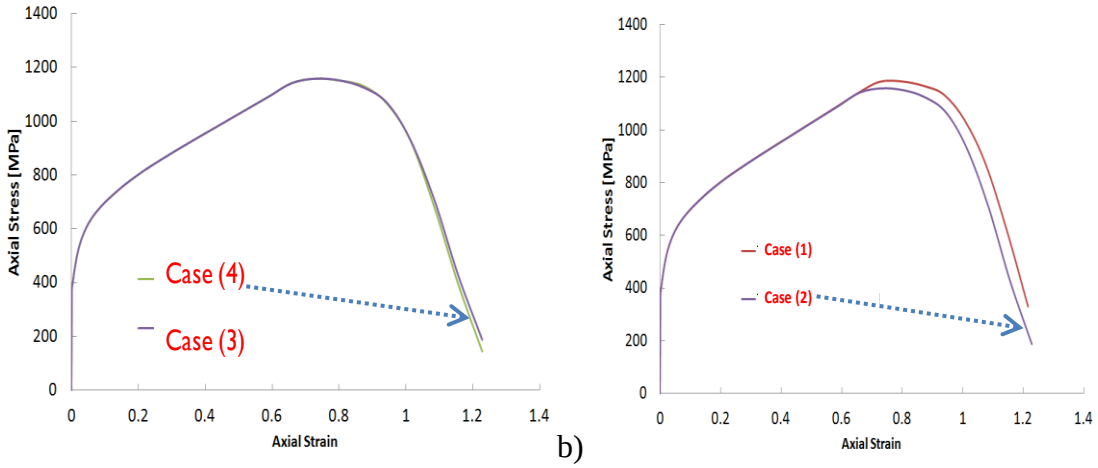

a) b)

Figure VII.29: Backstress influence during the cylindrical notched specimen loaded in tensile test; a) Axial stress-strain curves in cases 3 and 4, b) Tensile stress-strain curves in cases 1 and 2.

The backstress tensor has no influence on the sigma mean stress regarding the triaxiality curve evolution ($\overline{\sigma}_m(\underline{\sigma}-\underline{X}) \approx \sigma_m$ and case (1) =case (2)). In fact, Figure VII.30 expresses the idea that the mean stress and the mean shifted stress are equal. The impact of the backstress is very important in the anisotropic equivalent shifted stress (with respect to the Hill criterion).

One can observe that the anisotropic equivalent shifted stress has a higher triaxiality value. Both case 3 and case 4 are different from case 1. As a consequence of this introduction, it is to notice a strong peak of the triaxiality value at the beginning of the loading when the backstress is introduced in the equivalent stress, meaning $\bar{\sigma}_{eqv}(\underline{\sigma} - \underline{X}) \neq \sigma_{eqv}(\underline{\sigma})$.

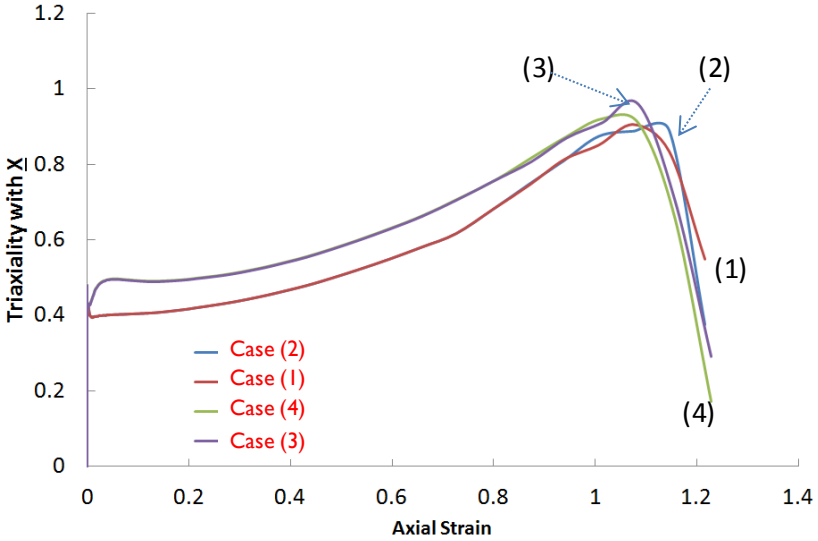

Figure VII.30: Backstress influence during the cylindrical notched specimen loaded in tensile test, triaxiality-axial strain curves for the DPI steel.

The impact on the damage variables (provided as their mean value at the minimum cross-section) is shown below. Indeed, the backstress tensor can be neglected on the mean stress definition regarding the porosity evolution.

The same conclusion can be taken on the porosity (Figure 31a) regarding the influence of the backstress but with a particularity concerning the anisotropic equivalent shifted stress. In fact, the impact of this tensor starts at around 0.65 of axial strain which is the same as the axial stress-strain evolution (fig VII.29).

As seen for the porosity, the stress, and the triaxiality variables, the backstress tensor has no influence on mean stress for the density of voids evolution (Fig VII.31b). The influence of this tensor significantly impacts the equivalent shifted stress. The gap between the two triaxiality definitions (case (3), case (4)) starts at about 0.5 of axial strain.

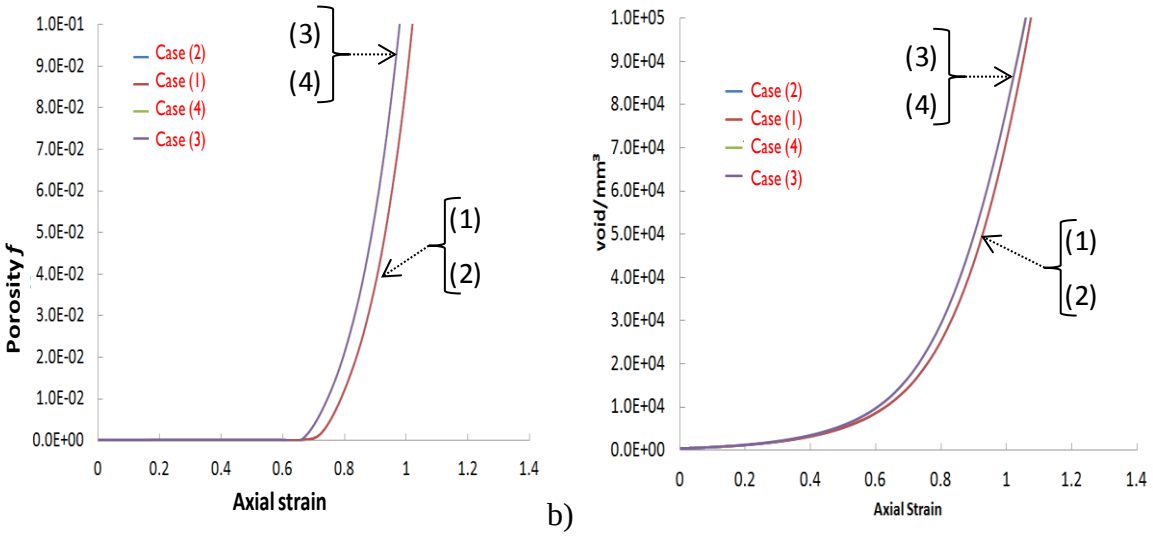

a) b)

Figure VII.31: Backstress influence during the cylindrical notched specimen loaded in tensile test, a) porosity *f* due to void coalescence-axial strain, b) density of voids-axial strain curves for the DPI steel.

In outline, a negligible influence of the backstress tensor on the mean stress through diverse simulations (tensile tests, simple shear test) has been observed. The mean stress can approximated as following: $\overline{\sigma}_m(\underline{\sigma}-\underline{X}) \approx \sigma_m$ in the GTNBF model. In the opposite analysis, a strong impact of this tensor variable on the equivalent stress has been noted and quantified $\overline{\sigma}_{eqv}(\underline{\sigma}-\underline{X}) \neq \sigma_{eqv}(\underline{\sigma})$. As a consequence, it modifies the evolution of the triaxiality especially at the beginning of the loading. The damage occurs earlier and affects only the end of the stress-strain curve. Finally, the porosity (*f*) and the density of voids (*N*) seem to the most sensitive variables sensitive to the definition of the equivalent stress.

VII.4 Conclusions

The potentialities of the GTNBF model have been established by conducting a parameter variation in the aim to evaluate their influence on the damage state variables.

First, the introduction of the anisotropy through Lankford coefficients in the GTNBF model has a strong effect on the porosity, and the void density. Globally, the stiffness of the voided DP steel is lost faster and yields to earlier fracture for stronger anisotropic material. The GTNBF model in Abaqus-Explicit demonstrates that the contribution of the anisotropic plastic affects at the porosity evolution due to void growth and the void nucleation.

Afterwards, the tensile test on the cylindrical notch specimen highlights the strong importance of taking into account the cavities evolution in the modeling. The stress extracted at the center of the specimen softens at around 50% of strain before fracture brutally occurs. A more detailed investigation on f_o and f_f parameters points out their significant influence on the damage modeling in the Landron voids nucleation evolution [LAN 2011]. It is characterized by a sharply drop of the axial stress value when the initial void volume fraction increases in the material. Also, the f_f sensitivity study underscores that this failure parameter modifies the fracture apparition. This event earlier occurs when the final void volume fraction f_f decreases.

Beside this sensitivity parameter study, a mesh influence has been carried out on a tensile notched specimen, where six different element sizes and an adapted mesh design have been compared. A strong heterogeneity of the distribution of the damage variables (porosity *f*, density of voids *N*) through the sample cross-section was observed. The element size had no influence on the axial strain and equivalent void radius distributions, except for a too coarse element size. The damage state variables such as the porosity and the density of voids seem to be more mesh sensitive. As stated earlier, in the current study, the element size choice has been restricted by the experimental conditions to densities which verify by far these numerical considerations.

The responses of the GTNBF model have been validated by using the "adapted mesh" designed to ensure an accurate extraction of average values over the same volumes/areas of observation as in the actual experiments. The predicted porosity evolution from Landron et al. [LAN 2011] is well validated up to a strain of 0.5. Furthermore, each of the two ingredients of the porosity evolution, number of voids and their mean radius are in good agreement with the experimental evolutions, thus confirming the importance of this physically inspired description. For larger strain levels, the apparition of the coalescence weakens the physical meaning of these quantities and of the hypothesis of spherical voids. Consequently, a simple phenomenological description is adopted to describe this phenomenon. In addition to the average values used for the confrontation to experiments, the numerical simulation illustrates the heterogeneity of most state variables, with the maximum values of, e.g., porosity and plastic strain, located near the center of the specimen. This heterogeneity, which increases during the loading, exhibited little mesh sensitivity prior to the development of coalescence.

Computing the mean stress tensor value or the mean of the shifted stress tensor demonstrates low value of the mean backstress and no impact on σ_m or $\overline{\sigma}_m(\underline{\sigma}-\underline{X})$. The conclusion is different when dealing with the equivalent stress tensor. For this case, taking into account the shifted value due to the backstress modifies the computation results.

As a consequence, the damage occurs earlier and affects only the end of the stress-strain curve for the studied tests. At the end of the loading, the porosity and the density of voids seem to be the most sensitive variables to the definition of the equivalent stress.

Next to these significant potentialities of the current ductile damage model, some limitations have been noticed. The first constraint concerns the lack of damage evolution in simple shear. Unfortunately, experimental evolution of the porosity *f* and the density of voids on such loading cases have not been realized during the PhD time framework. Consequently, the GTNBF model contains no contribution of these loading cases. Chapter IX will give more details regarding the possibilities to take into account these components. The second limitation is focused on the great number of material parameters required by the model. Indeed, compared to existing GTN model present in Abaqus-Explicit, the user has to introduce and identify 21 material parameters for the GTNBF model when the GTN model only needs 14. The last restriction is the small element size required to accurately analyze the strong heterogeneity of the distribution of the damage variables and the localization of the fracture initiation. Therefore, this point requires generating refined meshes which increases the calculation duration.

Chapter VIII. **Applications**

Contents

VIII.1 Introduction

Products developed by steelmakers such as ArcelorMittal usually follow a so called product development process. The product characterization starts with an evaluation of the first idea, then the study of the opportunity, conception, industrialization, the commercial perspectives and finally the volume and the innovation. During this process, samples are ordered with a specific geometry. Two samples can be designed: the cold rolled flat sheet with a thickness from 1 to 2mm and the hot rolled flat sheet from 2 to 4mm thick.
According to ArcelorMittal proceeding [BOU 2011], the samples are analyzed to check the interest of the material (mechanical properties in three directions, chemical analysis, and microstructural observation). When the samples are validated for forming application (Forming Limit Diagram FLD), folding tests, uniaxial tensile on cut edge, hole expansion, cross tool ..., the fatigue and other tests are considered.
After this sheet metal-forming process brief overview, the present chapter is focused on comparing the experimental and simulated behavior of 1.5 mm cold rolled flat sheets in two industrial applications. The first part is dedicated to constrain the DPIII steel specimen in uniaxial tensile test (smooth, holed, notched sheets) and the second part compares the DPI and DPIII steels using the cross-die drawing test.

VIII.2 Tensile tests

VIII.2.1 Experiments and Finite element model

VIII.2.1.1 Experiments

The present mechanical experiments consist of:

- ✓ Tensile tests on smooth specimens at low deformation speed.
- ✓ Quasi-static tensile tests on notched specimens (2, 5, 20mm radius).
- ✓ Quasi-static tensile tests on holed specimens (5mm radius).

All tensile tests have been performed on a 100 KN Zwick force machine at 8.10^{-3} 1/s deformation speed. The flat geometries made of DPIII steel used in this experimental campaign are illustrated in Figure VIII.1.
Figure VIII.1a sketches the smooth specimen based on the 1.5 and 2mm thick cold rolled sheet. Then, Figure VIII.1b illustrates the 1.5 mm thick flat sheet used to build the 2 and 20 mm notched radius specimens. Thus, Figure VIII.1c shows the 5 mm notched radius specimen. Eventually, the 5 mm holed radius specimen used in this study is drawn in Figure VIII.1d.

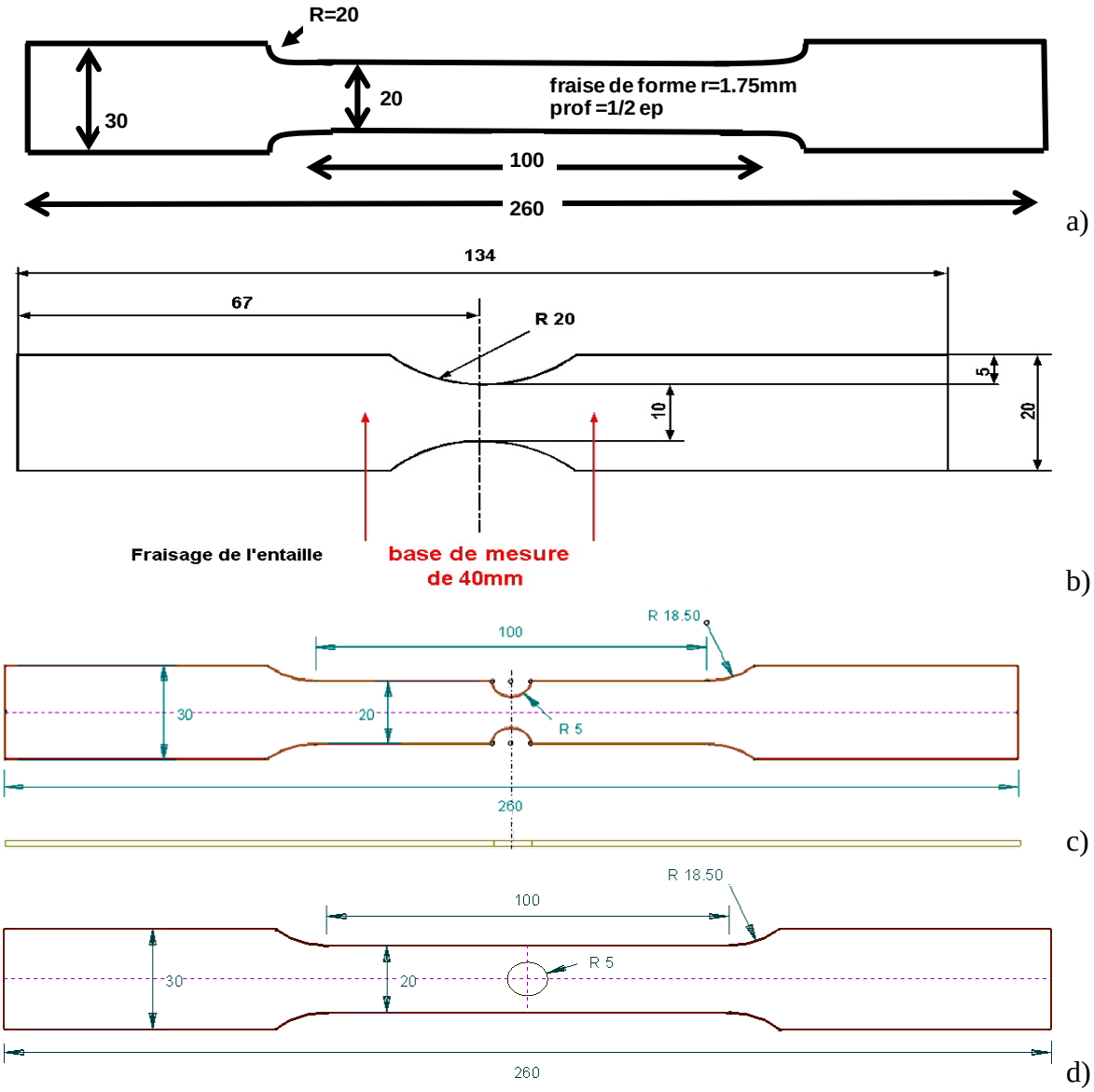

Figure VIII.1: a) Smooth, b) 20mm notch, c) 5 mm notch, d) 5 mm hole specimen sketches.

The specimen mounted in the tensile machine is often equipped with strain gauges or extensometer to measure the deformation components (see figure VIII.2). Unfortunately, these measurement methods contain some drawbacks. When using strain gauges, it appears that the gauges slide or are not well stuck on the surface and some data are usually missing. For the extensometer method, it seems that the use of this mechanical equipment facilitates the failure apparition.

In recent years a non destructive technique called digital image correlation (DIC) has been applied on sheet steel tests with many in-house and commercial software tools.

Briefly, it used proper image magnifications and decorated surface contrast patterns internally called by ArcelorMittal researchers "Mouchtis". According to Yang et al. [YAN 2012] large plastic strains and high strain gradients over gage dimensions as small as only a fraction of the original sheet thickness within the necking region in a thin sheet can be easily mapped out in great detail. The DIC provides a direct experimental estimation on upper and lower bounds of

post-necking effective plastic stress-strain curves and improves the accuracy and reliability of some analytical methods.

The bunch of mechanical tests realized in ArcelorMittal laboratory in Maizières-Les-Metz with Zwick machine was equipped with the optical system ARAMIS developed by GOM group. Figure VIII.2 presents the tensile machine with two cameras of 2448*2050 pixels resolution. It records the evolution of the "Mouchtis" painted on the surface of the specimen made with acrylic paint.

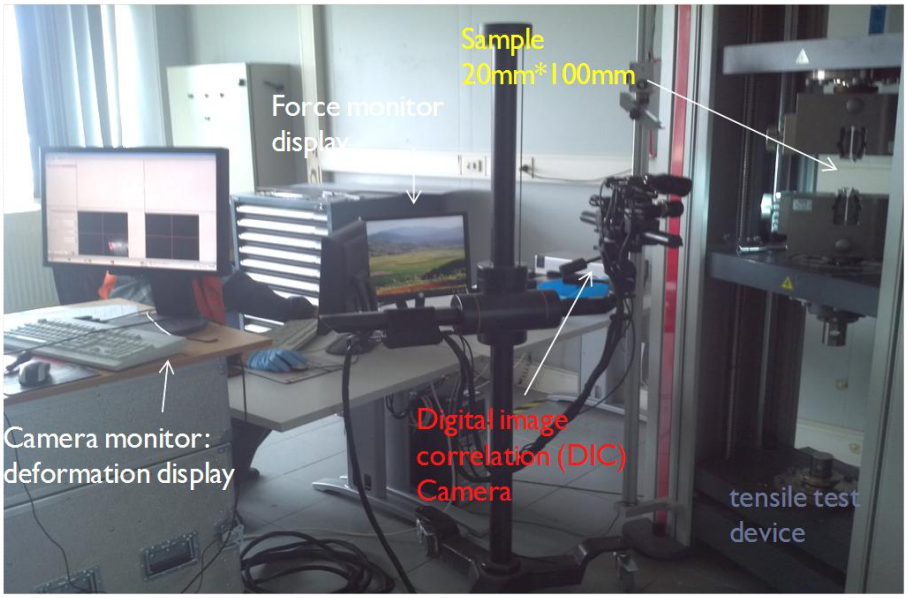

Figure VIII.2: Experimental tensile test setting using the DIC method in ArcelorMittal research Laboratory in Maizières-Les-Metz.

At each measurement step, pictures are taken. The most important image is captured at the very beginning when no force is applied. It defines the elements constituting the initial virtual meshing of the tested specimen. These configurations provide the reference picture before any loading. Figure VIII.3 shows all virtual meshing created with the system ARAMIS. Their dimensions are just about 0.35*0.35 mm².

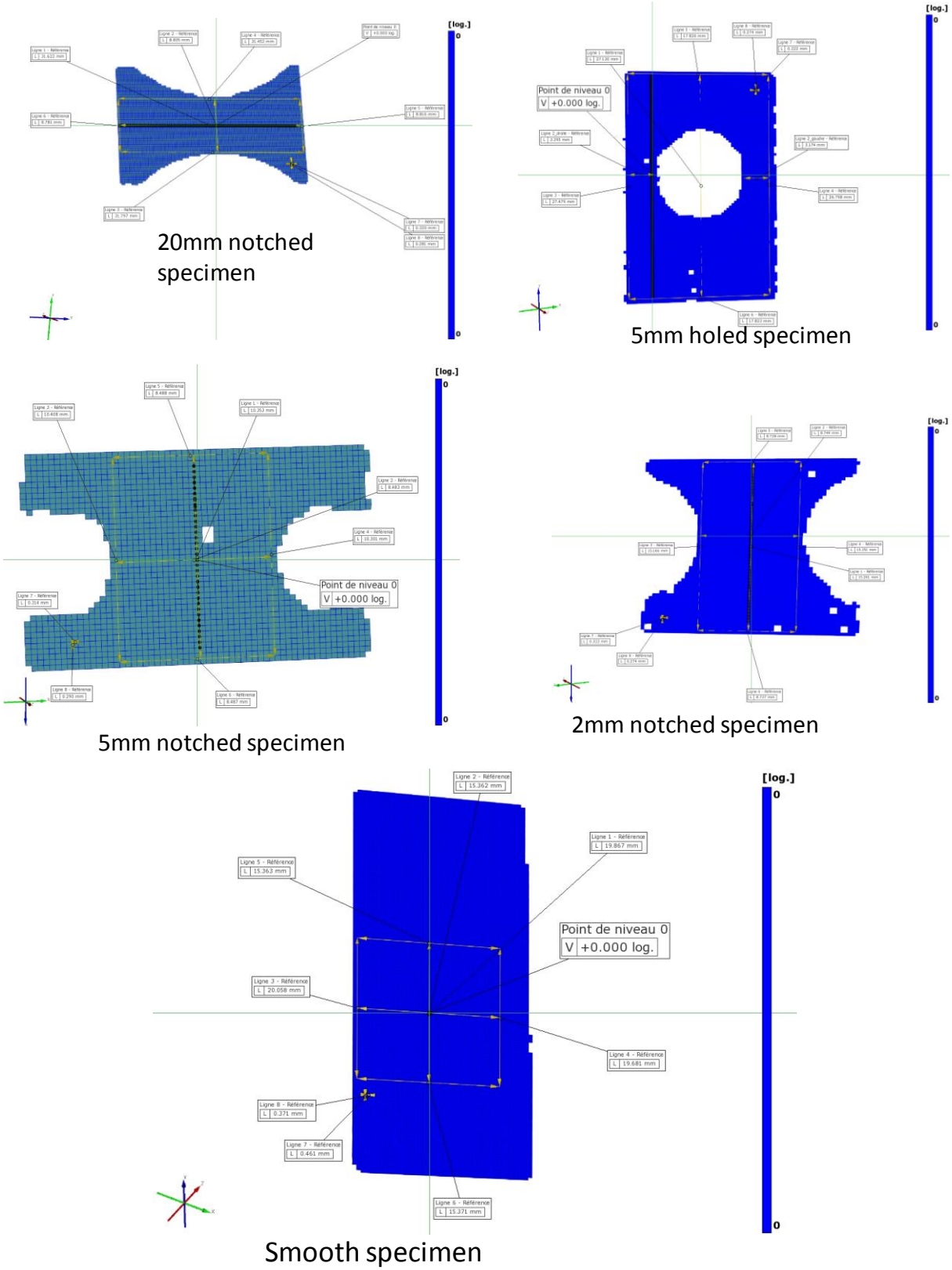

Figure VIII.3: Virtual meshing (DIC method) of the tested specimen built before the loading.

The coordinates are followed by correlating the pictures and recording them all along the loading until the fracture occurs. Unfortunately, the instantaneous strain at fracture is not recorded and only the picture is taken when the specimen is failed in two pieces. The data recorded before fracture is used to estimate the fracture force and strain. Thanks to this

setting, the local deformation can be more accurately estimated with a mechanical measurement method. The recording frequency is limited at 0.2 to 1 picture per second [LOR 2011] depending on the fracture type, location and propagation speed. For each specimen, three tests are provided: one to calibrate the tensile force device, another to estimate the recording frequency and the painting contrast "Mouchtis" with the cameras. Finally, the last one really serves to the tensile test.
The most expensive time cost is the analysis of the measurements. For each deformation step, engineers have to fit the virtual meshing with the chosen picture and calculate the local strain components.

VIII.2.1.2 Finite element simulations and post processing

Finite element simulations

Numerical simulations of the tensile specimens presented above were carried out using the GTNBF model implemented via a VUMAT in Abaqus-Explicit (see chapter VI). The half of each specimen has been meshed using 3D finite element with 8-node brick element (C3D8R). The modeling procedure has been already presented in chapter VII.2.2.
Figure VIII.4 shows the generated meshed geometries. They are constrained by the specific post-processing procedures developed in order to extract from the numerical simulations the physical quantities corresponding to those obtained from the experiments. Homogeneous velocity boundary conditions were applied on the top surface, along with usual symmetry boundary conditions in axial direction. The material properties introduced in the GTNBF model, corresponding to DPIII steel sheet have been presented in Table.4 of chapter V.

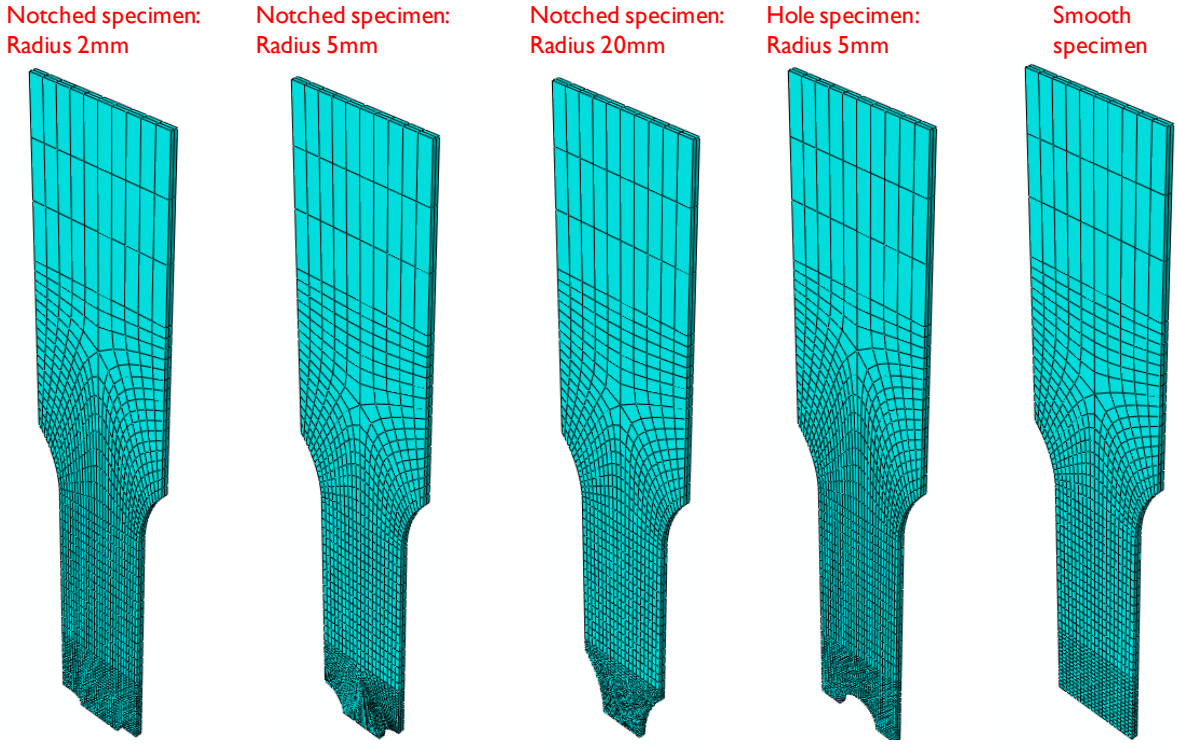

Figure VIII.4: Finite element meshes of the tensile tests on the notched, holed, and smooth samples

Post processing of FE values

Comparison between finite element and experimental tests has been done by extracting the force, the displacement and the local strain. The force history (*F*) has been extracted by adding the force values of the nodes located on top of the specimen. The displacement has been taken at the same node location as the experimental point. The elongation has been deduced near the surface reduction. Unfortunately, a so called cushioning effect has been found with all specimens. Where the thickness is unequally reduced along the width and the breadth are unequally reduced at one edge making difficult the surface calculation as seen in Figure VIII.5. This effect has also been described by Choung et al. [CHO 2008]. Consequently, mean values of the thickness and the breadth have been considered when this effect appears.

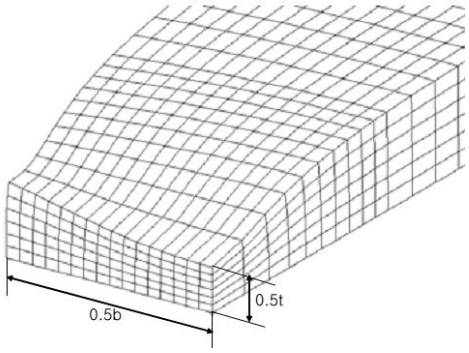

Figure VIII.5: Cushioning effect. t and b are respectively reduced thickness and breadth [CHO 2008].

Thanks to values (thickness and breadth), the axial stress and strain have been recalculated with respect to the expressions below Eqs VIII.1-2.

The average stress calculation uses the measurement of the minimal cross-section of the specimen and the measured force (F) given by the sensor during the tensile test:

$$\sigma_{axial} = \frac{F}{S} \tag{VIII.1}$$

The average axial strain is defined as an average value over the entire minimal cross-section:

$$\varepsilon_{axial} = \ln \frac{S_0}{S} \tag{VIII.2}$$

With S_0 and S (thickness*breadth) are the initial and the current section of the minimum cross-section.

The maximum and the last recorded effort before fracture extracted from the experiment are taken as a reference to determine the axial strain and the fracture location in the simulation. With this information in mind, the damage state variables evolutions (*f, N, R*) of each geometry will be compared.

VIII.2.2 Results and comparisons

The current section presents the experimental/simulation results from the tensile tests. The comparisons have been done with DPIII steel presented in Table V.4.

VIII.2.2.1 Smooth specimen

As explained in VIII.2.1.2, the axial stress is calculated by using the force measured with the tensile device. Afterwards, the surface at the minimal cross-section is defined in the experimental data by extracting the axial and width strain. Regarding the simulation, the surface at the minimal cross-section is extracted at each time increment. Figure VIII.6 shows the evolution of the force-displacement (a) while the left graphic corresponds to the axial stress-strain curves (b). Although a small gap between the experiment and the calculation is detected, the comparison is satisfying. Surprisingly, the usual stress softening is not drawn for the experimental curve whereas the GTNBF model clearly shows this behaviour. As a rule, the strain measurement with DIC method is often not very accurate when approaching the coalescence or failure stages. According to specialists concerned with this matter, results can be improved by using cameras with higher resolutions. The flip side of this enhancement is the huge among of data to analyze, increasing significantly the data time analysis.

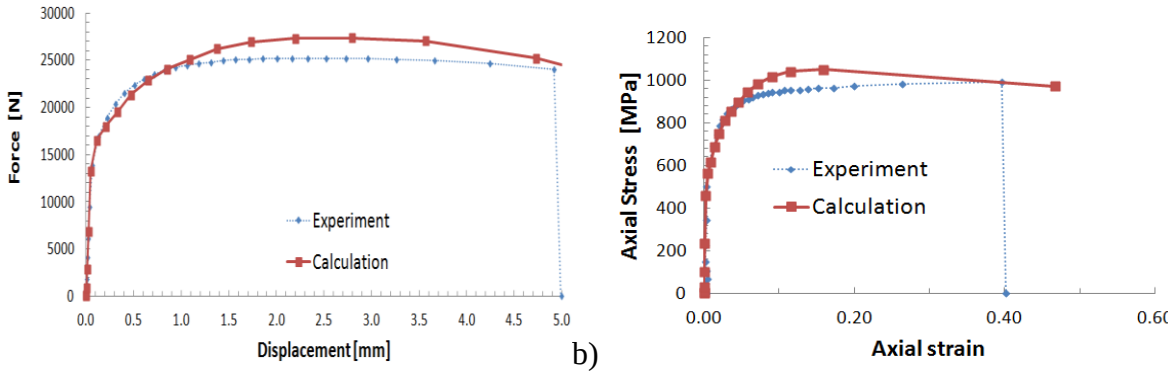

a) b)

Figure VIII.6: Tensile test on smooth specimen for DPIII steel, a) force-displacement curves, b) axial stress-strain curves.

The visualization of the strain isovalues (Figure VIII.7a-c) before the fracture point confirms that the previous stress and force gaps (Figure VIII.6) measured between the experiment and the simulation are caused by the lack of coating "Mouchtis" in the Virtual meshing surface (see Figure VIII.3).

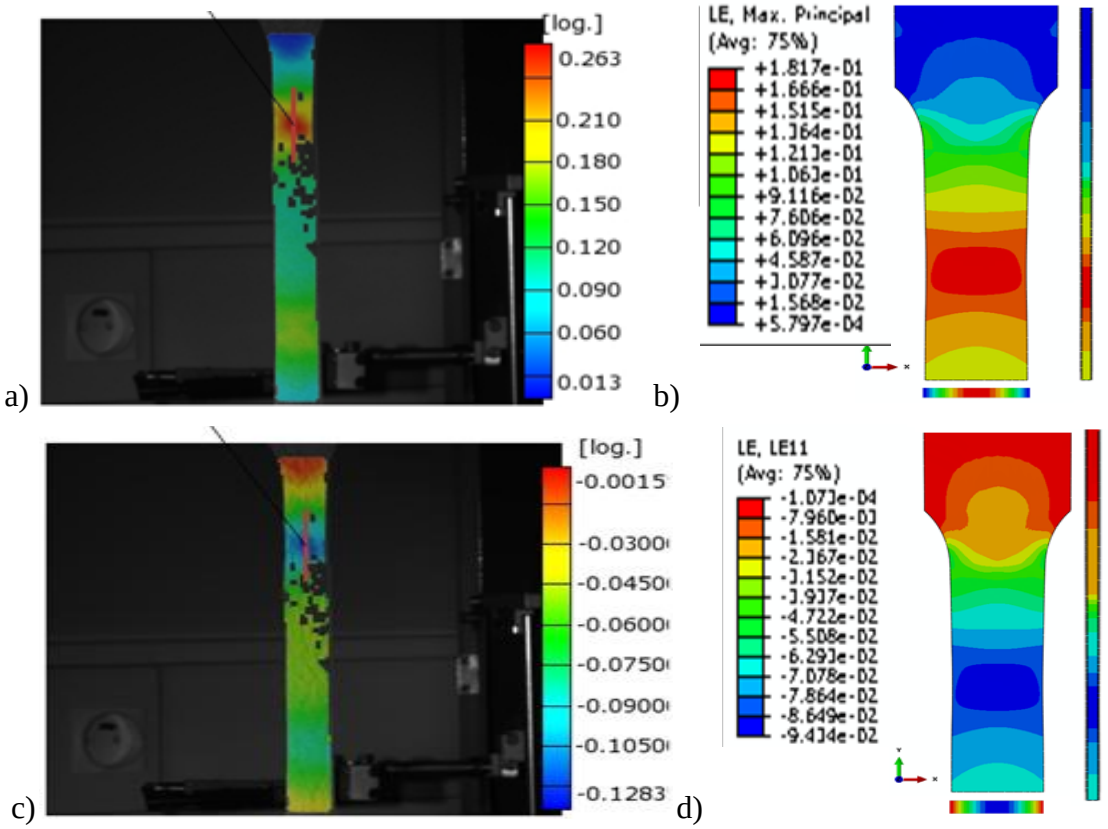

Figure VIII.7: Isovalues of the tensile test on smooth specimen for DPIII steel before the fracture point; major strain a) Experiment and b) simulation; minor strain c) experiment and d) simulation.

Despite the lack of coating, simulation and experiment show that the fracture appears at the same area. The crack (see below) is inclined to the loading direction at one-fourth distance from the top and not located at the middle of the specimen as usually expected for this kind of testing. The experimental test (Figure VIII.7a) shows a total fracture after 41% of deformation and the GTNBF model predicted the fracture initiation at 46% of axial strain as illustrated in Figure VIII.8b. The simulation reveals that the deformation seems to be homogenous near the central region of the necking and not uniform in the neutral area underlined by a cross failure form.

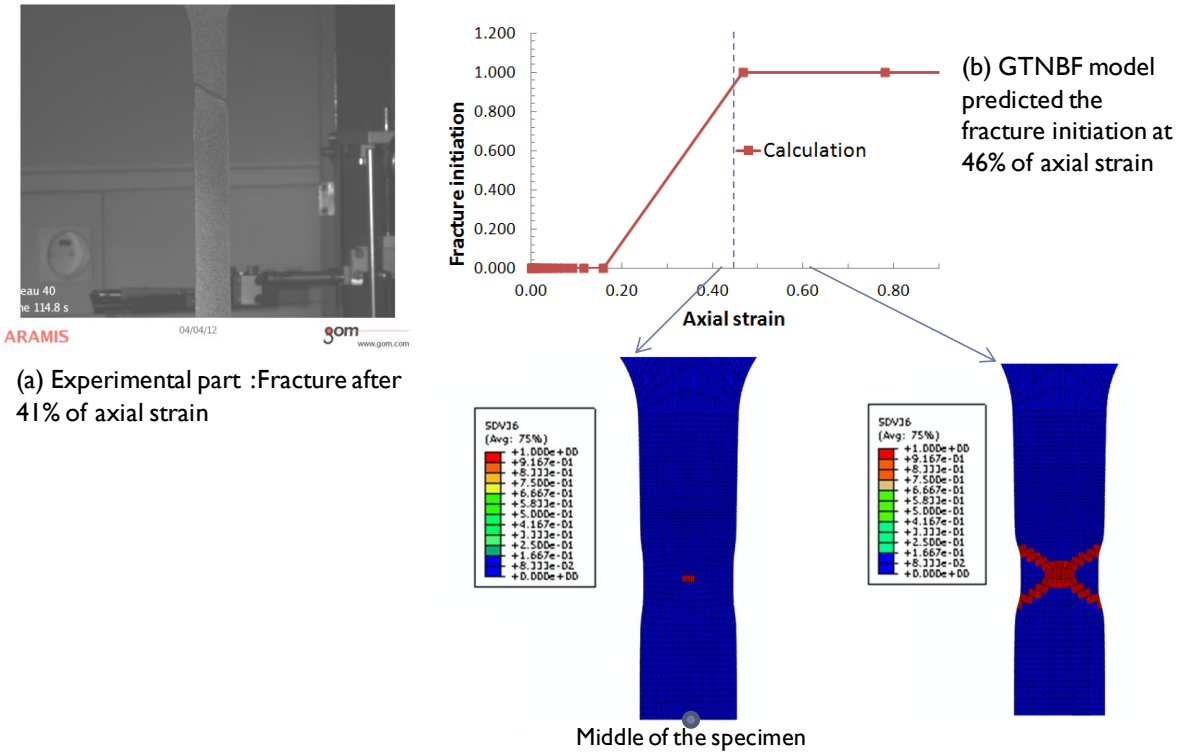

Figure VIII.8: Fracture visualization of the smooth specimen made of DPIII steel, a) Experiment, b) Simulation with distance inter-cavities criterion (λ_f), (blue is equal to zero and red is equal to 1).

Similar observations have been described by Niazi [NIA 2012] when developing an anisotropic damage model named as modified Lemaitre model.
During his PhD work, he performed a likewise tensile test on a DP600 where martensite bands oriented in 90° of the rolling direction on a flat sheet equipped with the same system ARAMIS to measure the deformation components. These results show that the crack is inclined to the loading direction (Figure VIII.9a) and the strain is dominantly concentrated in the central region of the neck, and not uniform along the cross-section, see Figure VIII.9b-c.

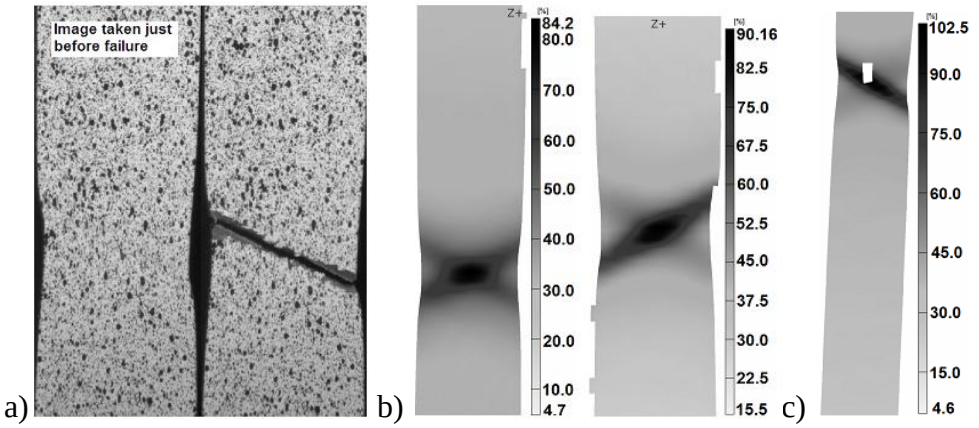

Figure VIII.9: a) Images captured from the ARAMIS system during failure of the DP600 tensile specimen TD (cut in 90° of the rolling direction); b) major strain distribution after the test was stopped, c) Just the moment before the fracture appears [NIA 2012].

The same author performed tests on the similar Dual-Phase steel where the martensite bands were oriented in 0° of the loading direction. A different failure mode is highlighted. The crack

is now perpendicular to the loading direction (Figure VIII.10a) and the strain is as well dominantly concentrated in the central region of the neck (Figure VIII.10b-c). Tensile tests on different DP600 microstructures proved that the crack initiation seems to depend on the martensite bands direction compared to loading direction. So the anisotropy of the material affects its damage field.

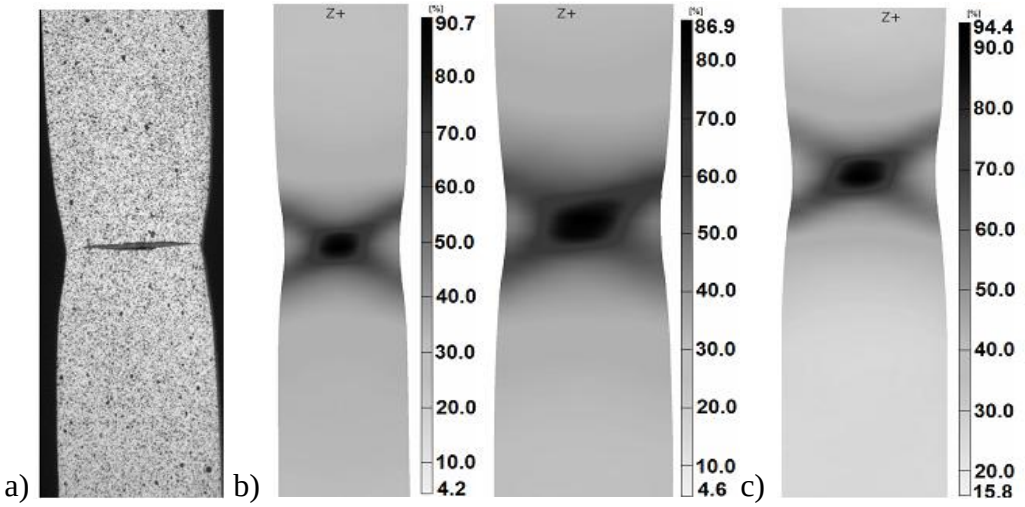

Figure VIII.10: a) Images captured from the ARAMIS system during failure of a DP600 tensile specimen RD (cut in 0° of the rolling direction); b) major strain distribution after the test was stopped, c) Just a moment away from the fracture apparition [NIA 2012].

For the DPIII steel, Figure VIII.11 shows the isovalues of axial stress-strain component, triaxiality factor (T_B), numerical density of voids per mm³ (N), mean void radius (R) and porosity (f). These isovalues are shown at the moment when the maximum plastic strain is close to 0.46 in the minimal cross-section. The damage variables and the axial stress are maximum at the center of the necking section due to the high concentration of the plastic deformation and the triaxiality.

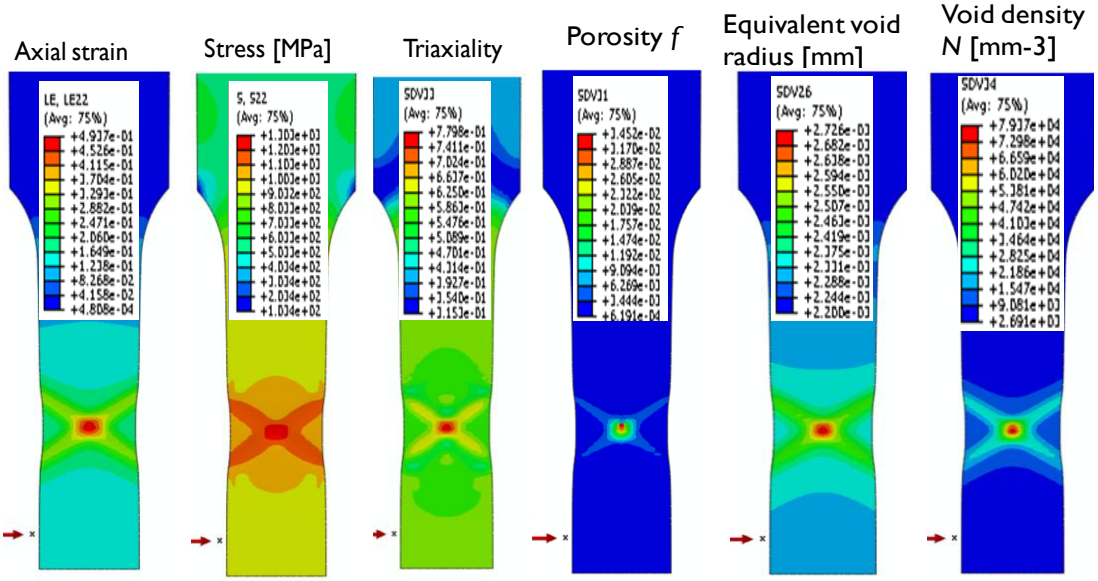

Figure VIII.11: Simulation results isovalues when maximum plastic strain is near 0.46: axial strain, axial stress, triaxiality, porosity, mean void radius and numerical void density.

Figure VIII.12 provides for indication the evolution of the damage state variables evolutions (*f*, *N*, *R*) recorded at the maximum plastic strain.

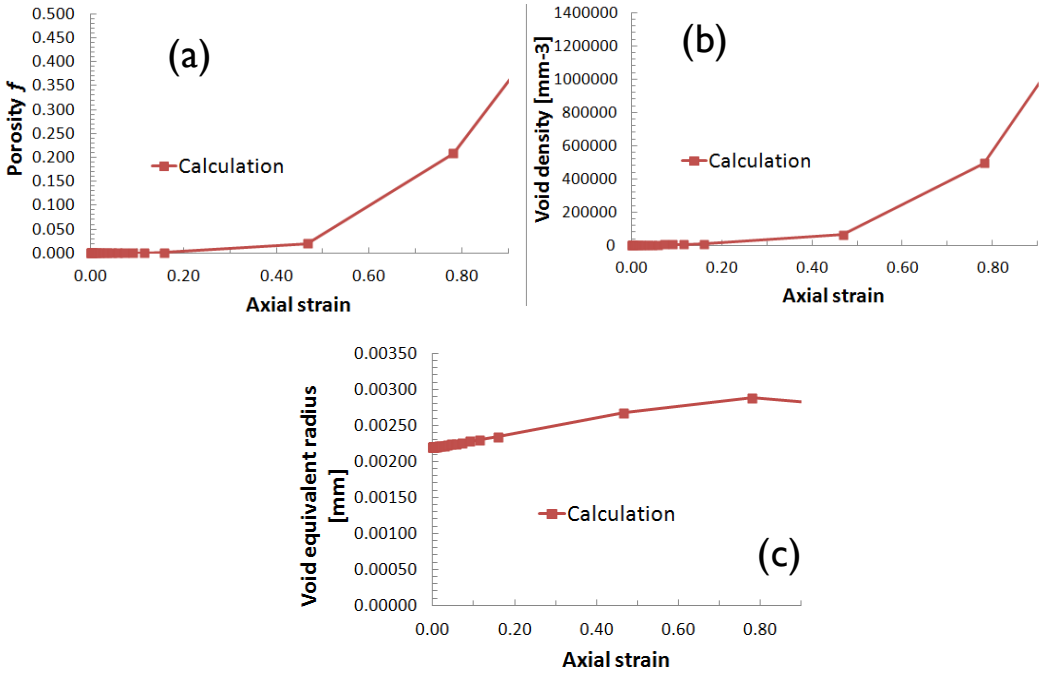

Figure VIII.12: Tensile test simulation results with GTNBF model for DPIII steel; a) total porosity -axial strain curve, b) void density-axial strain curve, c) void mean radius-axial strain curve.

VIII.2.2.2 Notched specimens

VIII.2.2.2.1 Comparison experimental/simulation

Given that the notch radius dimension in cylindrical specimens has a strong influence on the triaxiality evolution as numerically seen in chapter VII (section 2.3) and confirmed by the experiments of Landron et al. [LAN 2011], three notched flat sheets have been tested and compared to the simulations: 2-5 and 20mm radius. It will be verified if the influence remains true for flat specimens.

<u>2mm notched radius</u>

Figure VIII.13 underlines the evolution of the force in function of the displacement (Left) and the local axial stress-strain curves (Right) for the experiment and the simulation tensile test. Both comparisons are in good agreement during the loading.

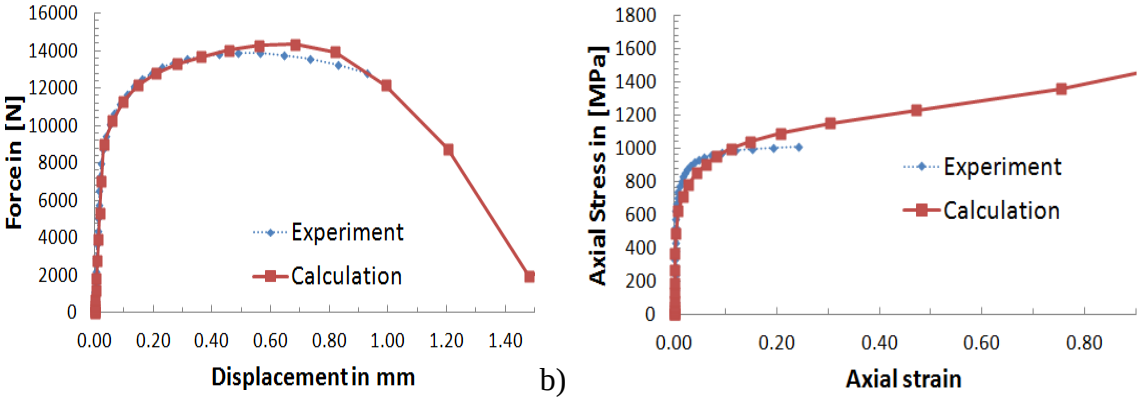

Figure VIII.13: Tensile test on 2mm notched specimen for DPIII steel, a) force-displacement curves, b) Axial stress-strain curves.

Following the quantitative analysis, comparison between the DIC-measured and FE computed surface strain field has been performed. Figure VIII.12 illustrates the experimented and simulated isovalues of major (a) and minor (b) strain shortly before the material failed (0.47 of axial strain). At first, the maximum axial strain contours in both cases are similar and concentrated at the notch root. Besides, the transversal deformation representing the minor strain is experimentally and numerically in good agreement. A minor strain value is found at around -0.27.

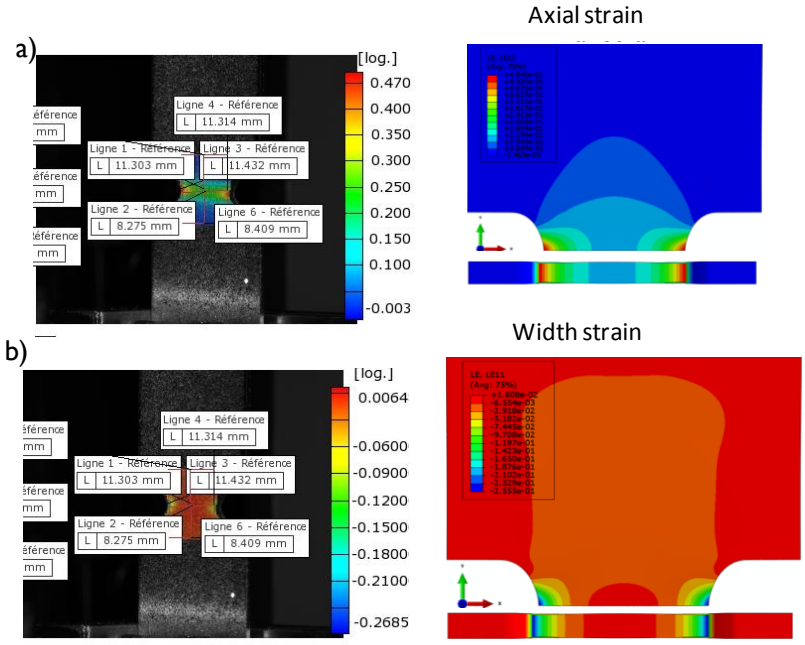

Figure VIII.14: Experimented and simulated isovalues of the tensile test on 2mm notched specimen for DPIII steel before the fracture point; a) major strain b) minor strain.

When the fracture physically occurs, the "Mouchti" gives no more contrast field and the camera is not able to record the strain. On the face of it, the exact position of the fracture initiation cannot be experimentally detected. Fortunately, the numerical counterpart tensile test is capable to accurately localize and follow the weak zone thanks to the additional fracture criterion integrated in the GTNBF model. This criterion already presented in chapter

IV section 3.3 is based on integrating the physical measurement of the mean distance between two cavities (λ) provided by Landron [LAN 2012] (see eq.IV.38).

The analysis of this criterion is summarized in Figure VIII.15 where the evolution of the fracture initiation criterion is shown during the loading. The picture illustrates that the fracture initiates at the notch root where the maximum plastic strain (0.47 of strain, bottom left) has been previously extracted (Figure VII.16a) and assumedly ends at the middle of the surface (0.94 of strain, bottom right). Bearing in mind this fracture kinetic, it can be assumed that the fracture propagates brutally inside the material.

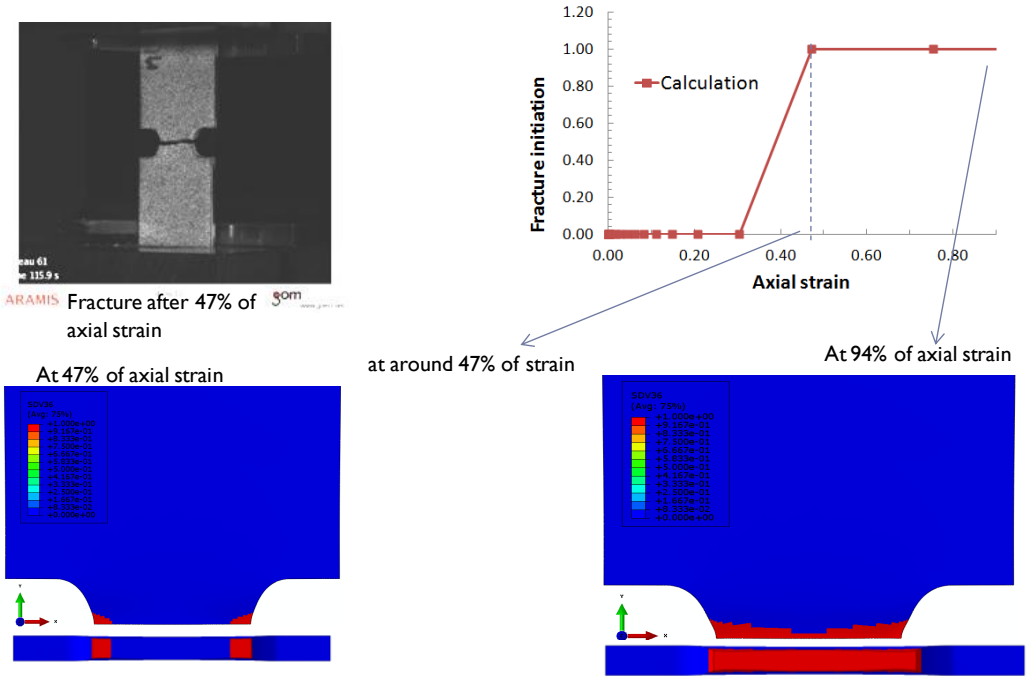

Figure VIII.15: Fracture initiation localization on the 2mm notched radius specimen simulates in tensile direction with DPIII material (blue is equal to zero and red is equal to 1).

Figure VIII.16 gives the isovalues overview of numerical density of voids per mm³ (*N*), mean void radius (*R*) and porosity (*f*). These isovalues are shown at the moment when the maximum plastic strain is close to 0.47 in the minimal cross-section. The damage variables and the axial stress are maximum at the notch root of the necking section due to the high concentration of the plastic deformation and triaxiality.

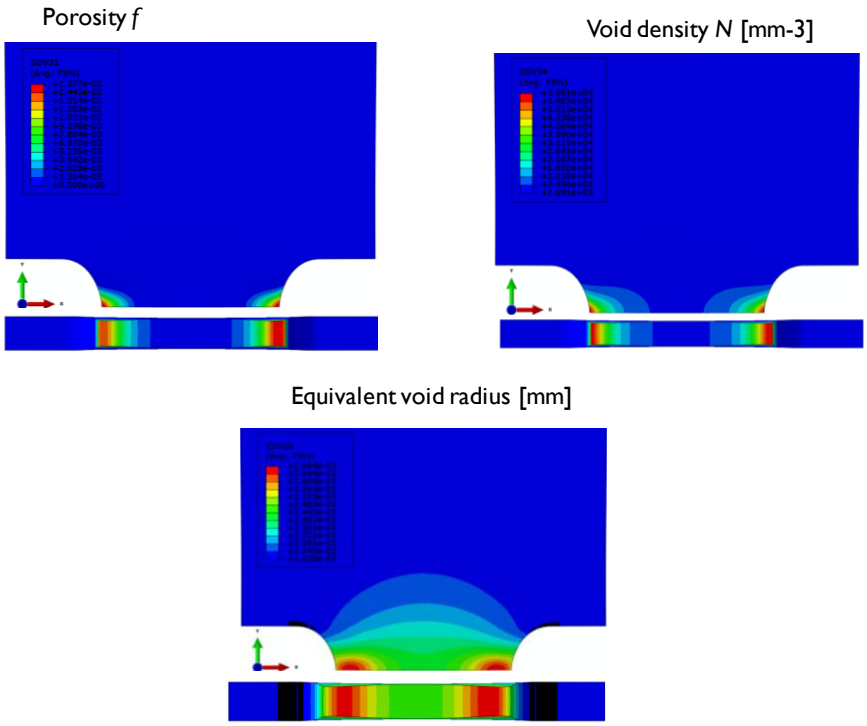

Figure VIII.16: Simulation results isovalues when maximum plastic strain is near 0.47: porosity (max value at 1.6%), mean void radius (max value at 2.68 µm) and numerical void density (max value at 59610 voids/mm³).

5mm notched radius

Following the same analysis procedure as for the 2mm notched radius tensile specimen, simulations are performed of the experiments on the specimens with a 5mm notched tensile specimen.

Figure VIII.17 presents the quantitative results in term of force-displacement (a) and stress-strain (b) evolutions. Figure VIII.17a depicts the simulated force-displacement curve (red line) along with the corresponding experimental data (blue line). A 1kN force gap is observed between the simulation and the experiment when the curves reach their maximums. The differences between the finite element calculation and the experimental force evolutions have different causes. Some possibilities are described hereafter. The first one assumes that the force sensor has not been recalibrated after each test. Indeed, it often appears that the zero force is not really obtained after clamping the specimen in the device. It results that the tensile test starts at a value below the zero force. In addition to these experimental remarks, the simulation does not take into account the residual device stress after the specimen clamping. Considering that, the force evolution starts at exactly zero for the simulation. The second cause less clear to demonstrate is based on the displacement measurement. An error on the coordinate point taken for extracting the experimental and simulated axial displacement has perhaps been introduced. The third assumption is attributed to the DIC algorithm and differences in the location of the reported displacement. This hypothesis has been shortly described by Luo et al. [LUO 2012]. The last cause is that the displacement is not constant along the width of the specimen at that position [MAR 2012], [DUN 2010]. If so, it explains that the displacements measured with the DIC method are over estimated. However, Figure

VIII.17b underlines that the evolution of the local axial stress-strain curve for the experiment is in good agreement with the simulation which validates the good measurement of the strain with the virtual extensometer (DIC method).

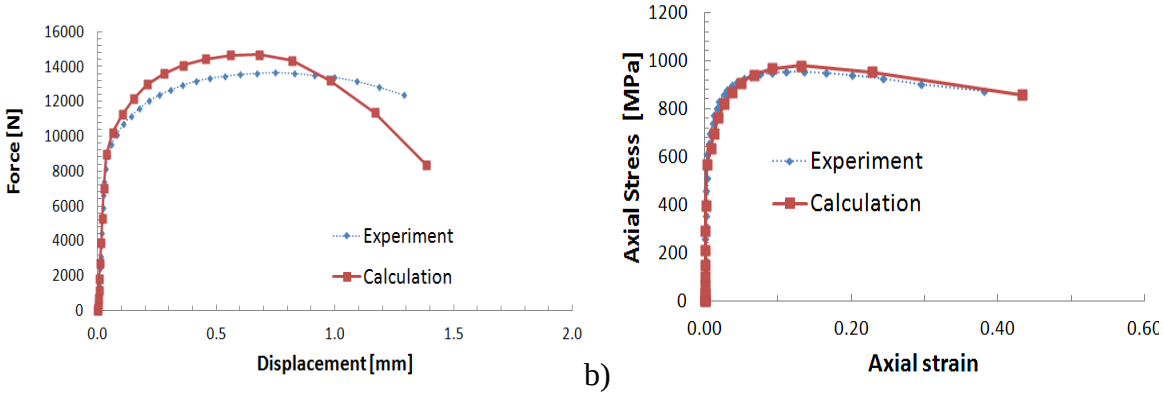

a) b)

Figure VIII.17: Tensile test on 5mm notched specimen for DPIII steel, a) force-displacement curves, b) Axial stress-strain curves.

Figure VIII.18 illustrates the experimented and simulated isovalues of major (a) and minor (b) strain shortly before the material failed (0.42 of axial strain). At first, the maximum axial strain contours in both cases are similar and homogenously distributed at the cross-section. Besides, the width deformation representing the minor strain is experimentally and numerically in good agreement. A minor strain value is found at around -0.23 and concentrated at the notch root. These comparisons validate the stress-strain curve extrapolation for large strains seen in Figure VIII17b. In opposite to the 2mm notched radius specimen, the maximum plastic strain location is not clearly identified with the simple observation of the strain contours.

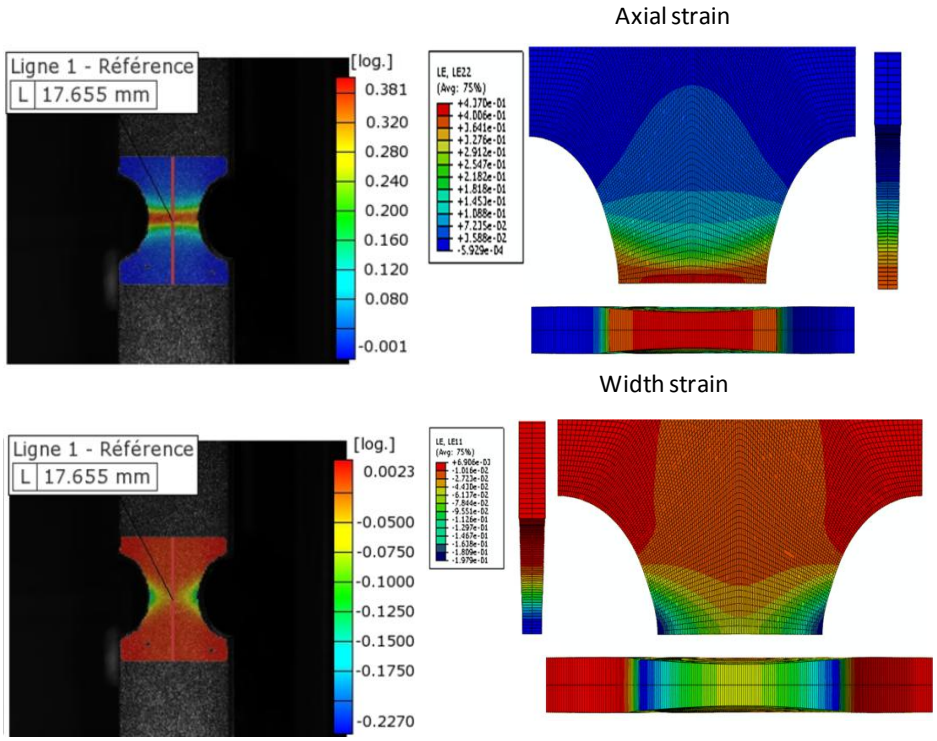

Figure VIII.18: Experimented and simulated isovalues of the tensile test on 5mm notched specimen for DPIII steel before the fracture point; a) Major strain b) Minor strain.

The axial strain contour plots at the fracture initiation for the 5mm notched tensile test have revealed a homogenous strain distribution. However, the analysis of the mean distance between two cavities (λ) evolution has pointed out the exact fracture initiation location as seen in Figure VIII.19 (Top right). The picture depicts that the fracture initiates at the middle-surface of the minimal cross-section where the plastic strain is maximum (0.42 of strain, bottom left). The fracture progress is assumed to end up at the edge of the cross-section (0.72 of strain, bottom right). Comparison with the 2mm notched radius specimen shows a different fracture mechanism, underlining the importance of the notch radius size. A micrographic analysis observation has to be done to exactly localize the fracture initiation.

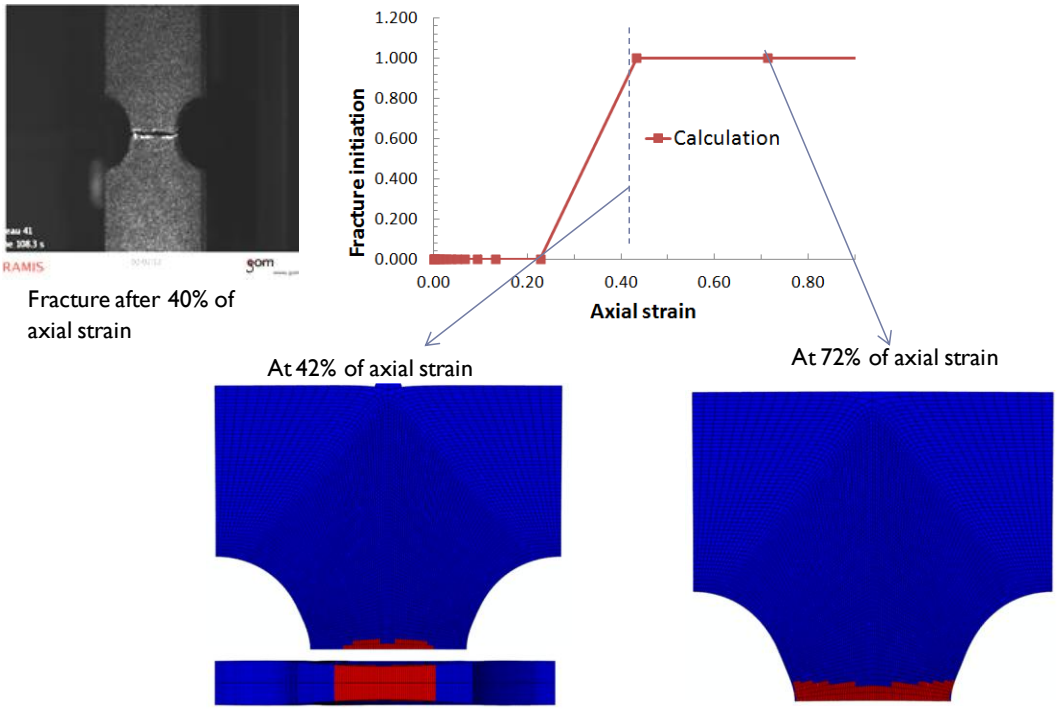

Figure VIII.19: Fracture initiation localization on the 5mm notched radius specimen simulates in tensile direction with DPIII material, (blue is equal to zero and red is equal to 1).

Figure VIII.20 gives the isovalues of numerical density of voids per mm³ (*N*), mean void radius (*R*) and porosity (*f*). These isovalues are shown at the moment when the maximum plastic strain is close to 0.42 in the minimal cross-section. The damage variables are maximum at the middle of the necking section due to the high concentration of the plastic deformation and the triaxiality.

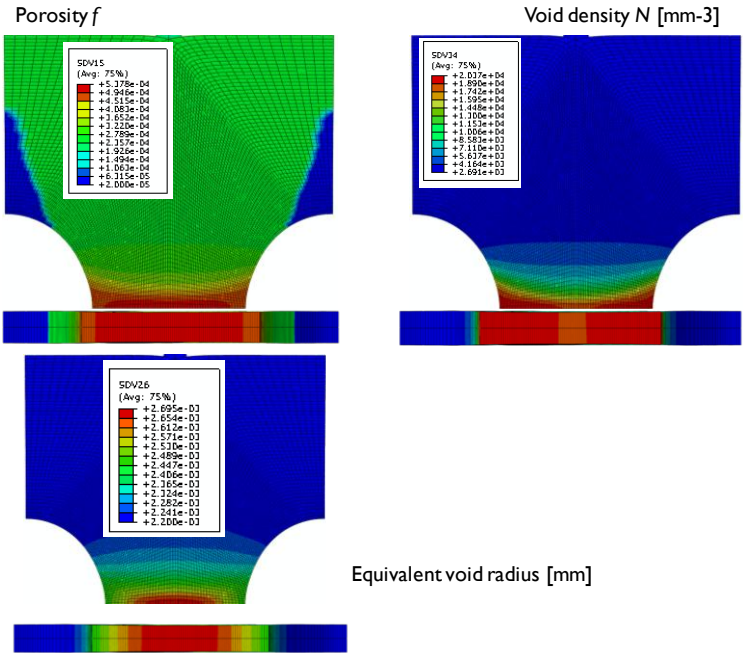

Figure VIII.20: Simulation results isovalues when maximum equivalent plastic strain is near 0.42: porosity (max at 0.5%), mean void radius (max at 2.68 µm) and numerical void density (max at 20370 voids/mm³).

20mm notched radius

The same analysis as for the previous notched specimens has been conducted with the largest notched radius. Figure VIII.21 presents the quantitative results in term of force-displacement (a) and stress-strain (b) evolutions. Figure VIII.19a depicts the simulated force-displacement curve (red line) along with the corresponding experimental data (blue line).
The force displacement curves are not well correlated after 0.4mm of displacement between the experiment and the simulation. After analyzing the entire experimental data to find the best fitting point (see Figure VIII21a) some DIC algorithm problems and differences in the location of the reported displacement have been found. The error on the exact displacement could be due to the inaccurate correlation points taken during the uniaxial tensile loading. In opposite, the axial stress- strain curves between the experiment and the calculation are very closed. The stress evolution stops brutally at around 0.48 of axial strain, defining the fracture of the specimen with no stress softening.

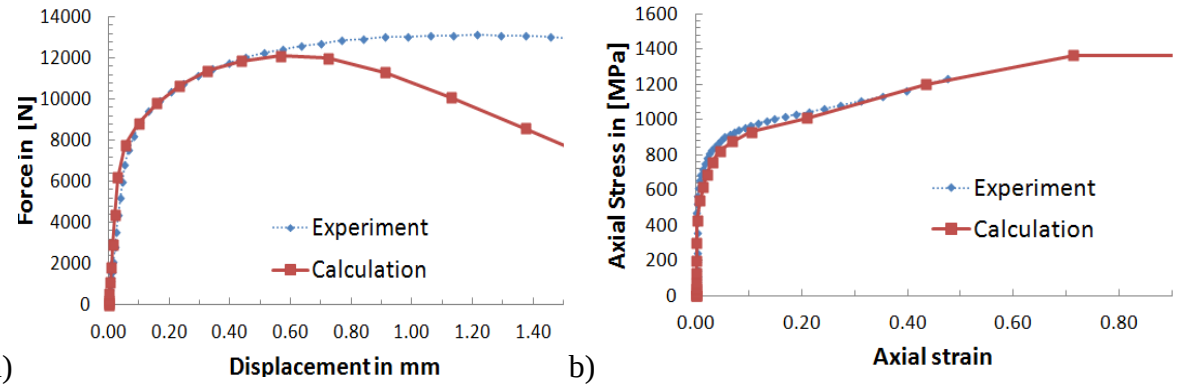

a) b)

Figure VIII.21: Tensile test on 20mm notched specimen for DPIII steel, a) force-displacement

curves, b) axial stress-strain curves.

Figure VIII.22 illustrates the experimental and simulated isovalues of major (a) and minor (b) strain shortly before the material failed (0.48 of axial strain). The maximum axial strain contours in both cases are similar and concentrated at the minimal cross-section. Besides, the radial deformation representing the minor strain is experimentally and analytically in good agreement. A minor strain value is found at around -0.16 with a larger homogenous distribution around the cross-section. These comparisons validate the stress-strain curve extrapolation for large strains seen in Figure VIII21b. Likewise to the 2mm notched radius specimen, the maximum plastic strain location is clearly identified at the middle-surface of the necking (see Figure 22a).

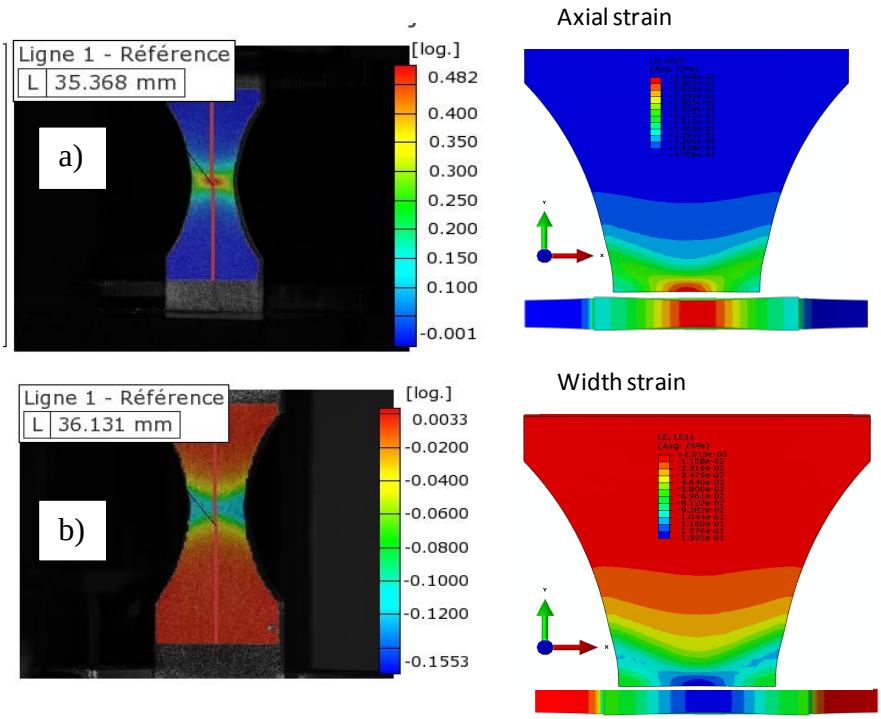

Figure VIII.22: Experimented and simulated isovalues of the tensile test on 20mm notched specimen for DPIII steel before the fracture point; a) major strain b) minor strain.

The finite element analysis of the mean distance between two cavities (λ) evolution confirms that the fracture initiates the same way as the 2mm notched radius at the middle-surface of the cross-section where the plastic strain is maximum (0.44 of strain, bottom left). Surprisingly, the fracture progress is not ending brutally at the edge of the cross-section (0.72 of strain, bottom right in Figure VIII.23) but slowly going up. Comparison between the 2mm and 5mm notched radius specimens shows a different fracture mechanism.

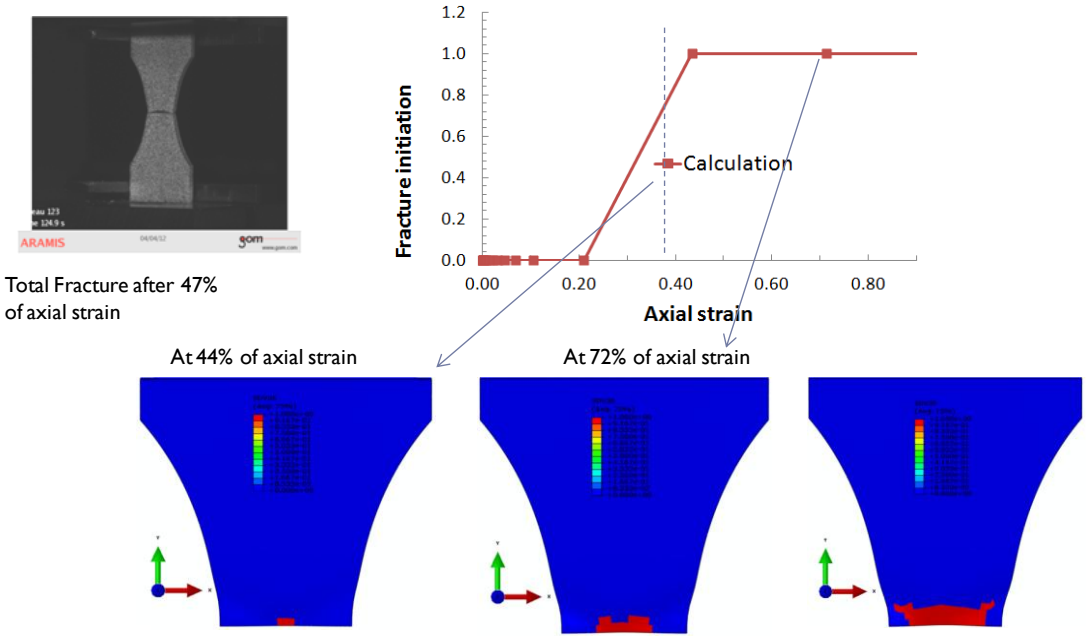

Figure VIII.23: Fracture initiation localization on the 20mm notched radius specimen simulates in tensile direction with DPIII material (blue is equal to zero and red is equal to 1).

Figure VIII.24 gives the isovalues of numerical density of voids per mm³ (*N*), mean void radius (*R*) and porosity (*f*). These isovalues are shown at the moment when the maximum plastic strain is close to 0.44 in the minimal cross-section. The damage variables are maximum in the middle of the necking section due to the high concentration of the plastic deformation and triaxiality but zero around the root notch.

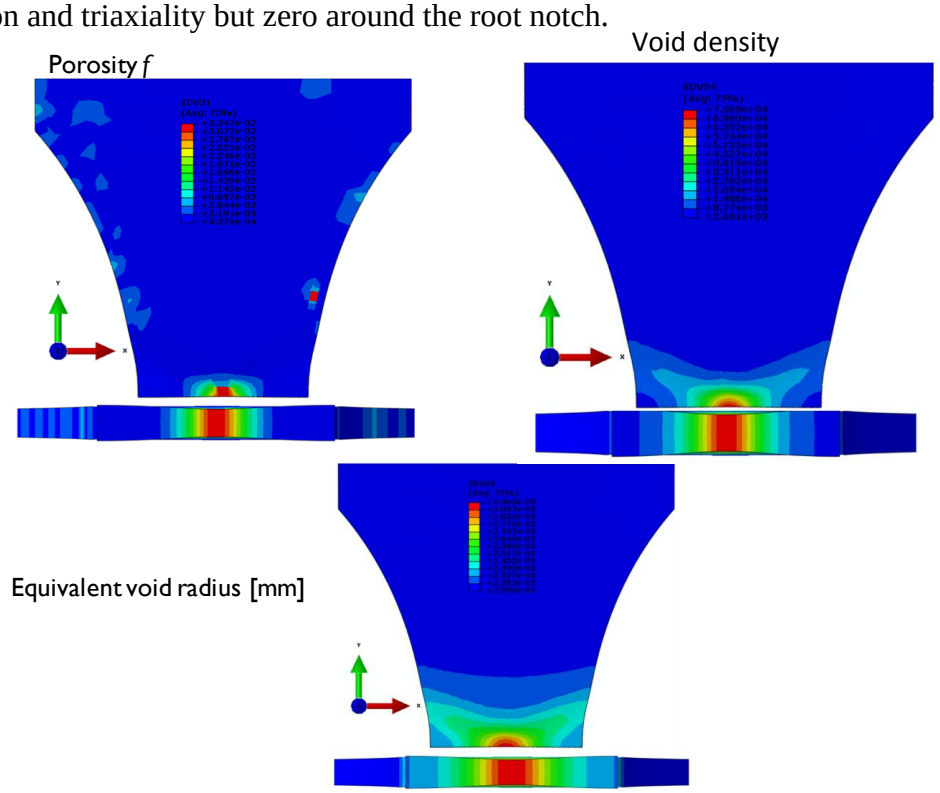

Figure VIII.24: Simulation results isovalues when maximum plastic strain is near 0.44: porosity (max at 3.3%), equivalent mean void radius (max at 3 µm) and numerical void density (max at 75000 voids/mm³).

VIII.2.2.2.3 Conclusion and discussions

The current part collects and compares the force, the triaxiality and damage evolutions for the three studied flat notched specimens. Here, the aim is to highlight the influence of the notch radius dimension.

Before giving more details, it is important to underline that this kind of study has been done for the notched cylindrical specimens in chapter VII when estimating the potentialities and limitations of the GTNBF model (see VII.3). In this section discussions will take place to verify if the notch radius dimension also more affects the triaxiality factor than the damage variables as in chapter VII when using a flat sheet. The introduction of the damage variables in the GTNBF model lead to the stress softening causing high localizations of the strain, density of voids per mm³ (*N)*, mean void radius (*R*) and porosity (*f*) fields. Numerous studies on tensile notch specimens have been published with mesh adaptation to the damage phenomenon [BOR 2005], [ROD 2000], [SVE 2000], [ROD 2001], [AND 2004], [ASK 2000]. Unfortunately, the current damage model has no such a remeshing tool, therefore a homogenized element size definition equal to 0.25*0.25 mm² has been created around the cross-section to minimize the mesh influence. This element size has been set inferior to the virtual mesh required by the system ARAMIS (see section VIII.2.1.1). It insures a good agreement between the experiment and simulated strain evolutions. In front of that, the force and the displacement resulting from the experiment have been compared to the simulated counterparts with an average success. Nevertheless, it has to be pointed out that the simulated flat notch sheet loaded in tensile direction does not take into account the stiffness of the global tensile device. In our point of view, this hypothesis explains in half part why a slight softening has been observed in the experimental force-displacement evolution.

Figure VIII.25 depicts the force-displacement (a) and the triaxiality-displacement curves of the three notch radius (2, 5, 20 mm).

The force-displacement curves show that the notch radius dimension has a real impact on the mechanical material behaviour. It also highlighted by a strong concentration of the triaxiality and plastic deformation at the fracture area. Analyzing the triaxiality-displacement curves, it can be underlined that the notch radius size reduction increases the triaxiality factor at the beginning of the loading.

The second idea resulting from this comparison is that the 2 and 5 mm notch radius are quite identical in term of force-displacement and triaxiality at 0 displacements. The third idea expresses the fact that if the notch radius is increased above 20 mm, the force-displacement curves will tend to decrease until reaching the smooth specimen behaviour. In the same way, the triaxiality value will approach 1/3 which is the theoretical calculation for a specimen without notch.

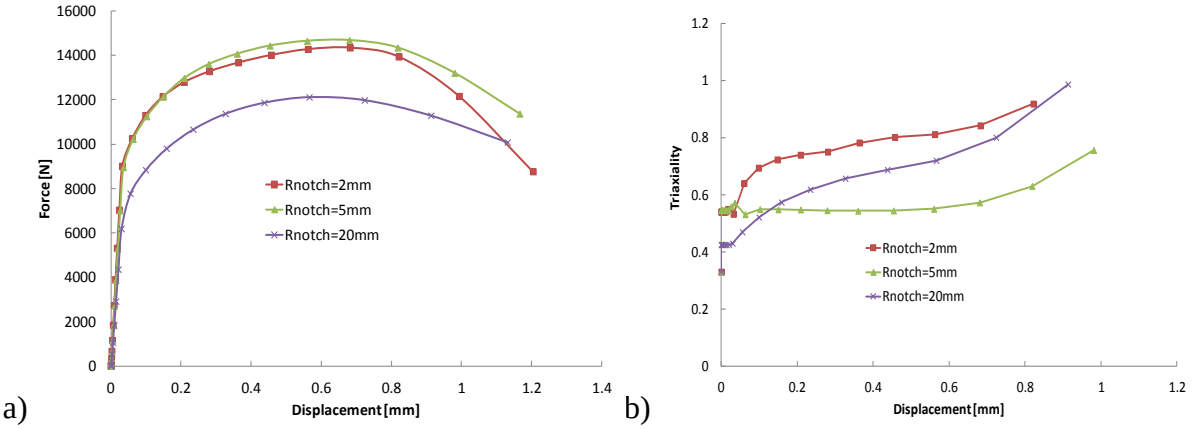

a) b)

Figure VIII.25: Influence of the notch radius size during the tensile test for DPIII steel, a) force-displacement curves at the top of the specimen, b) triaxiality-displacement curves.

The notch radius influence on damage variables is presented in Figure VIII.26. The decrease of the notch radius is favorable to a rapid void growth (see Figure VIII.26a) and new void nucleation (see Figure VIII.26b). Apart from this, the mean void radius remains quasi unchanged (see Figure VIII.26c).

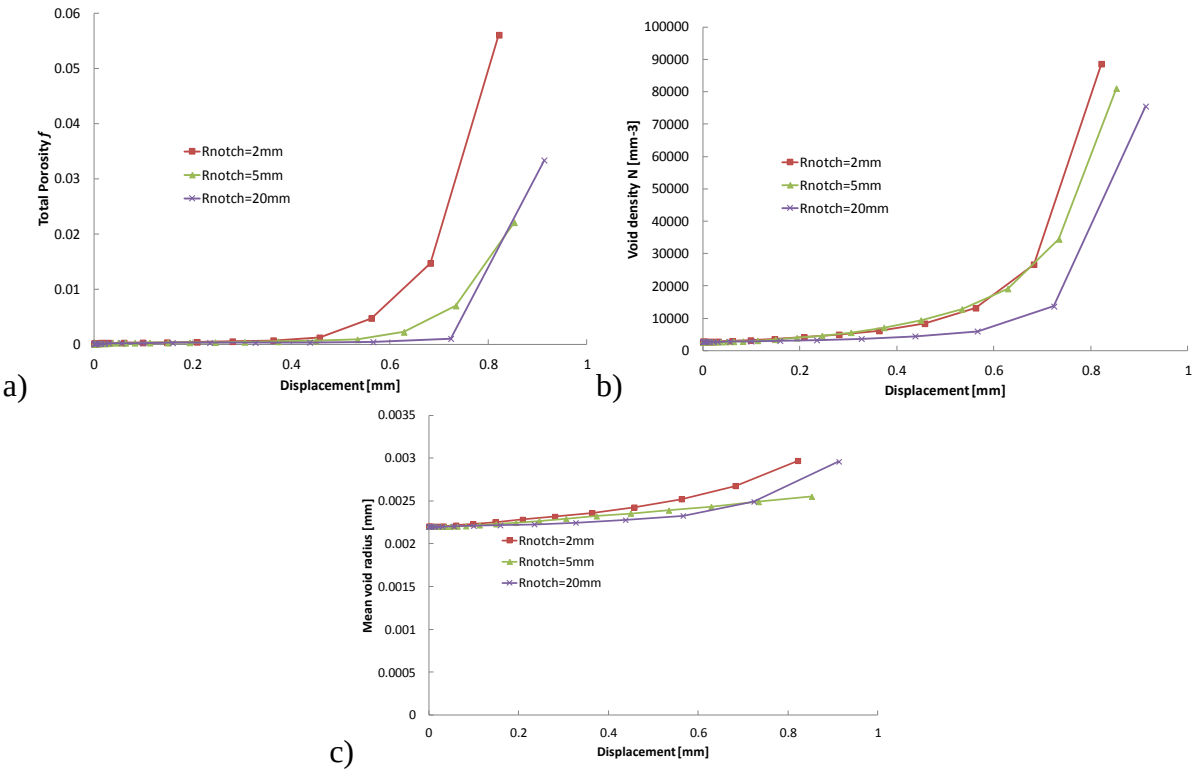

a) b) c)

Figure VIII.26: Notch radius design influence during a tensile test simulation with GTNBF model for DPIII steel; a) total porosity *f* -Displacement curves, b) void density-Axial Displacement curves, c) Mean void radius-Displacement strain curves (element located at the center of the minimal cross-section.

The last discussion concerns the impact of the notch radius on the fracture initiation. The fracture initiation is detected when one element reach the critical inter-cavities distance (λ). At this moment, the element changes from blue (for zero) to red (for unit) color. Comparison of the final axial strain resulting from the experimental and simulated tensile tests shows a good agreement. Only a gap of 7% strain at fracture has been detected which is relative weak when

adding some technical issues (tensile device stiffness not taken into account and lack of stochastic pattern applied to the surface using a color spray for some samples). At a first overview, Figure VIII.27 reveals a light notch radius influence on the axial strain value taken a moment before the material fails. However, a different conclusion is made when inspecting more carefully the fracture initiation areas thanks to the physical-based critical inter-cavities distance λ_f integrated for the first time in a ductile damage model.

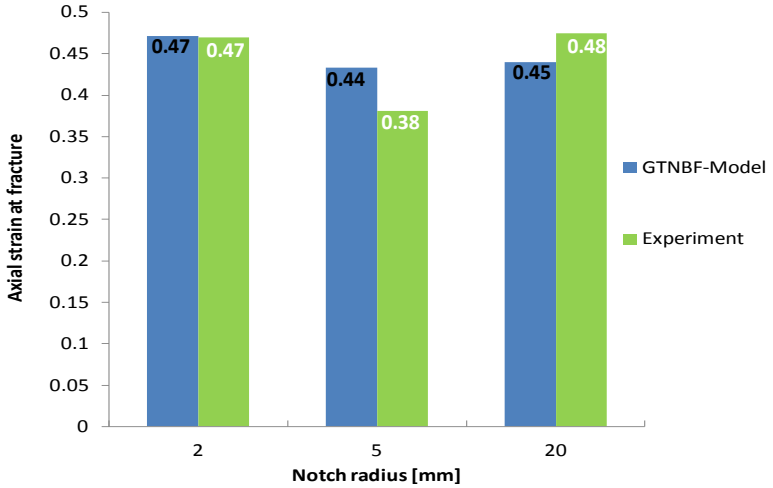

Figure VIII.27: Axial strain fracture comparison between the experiment and the GTNBF model during the flat sheet tensile test designed with various radii (for DPIII steel).

Figure VIII.28 illustrates the fracture initiation moment detected when the mean inter-cavities distance reaches the critical value λ_f (measured at 20µm for all DP steel by Landron [LAN 2011]) in the material for three notch radius sizes. The fracture initiation materialized by red color appears not at the same area for various notch radiuses. Indeed, the sample with the notch radius at 2 mm (left of the figure) fractures at the bottom of the notch radius near the cross-section, thus the 5 mm radius (center of the figure) fails at the middle of the cross-section and eventually the biggest notch radius (right of the figure) fails at the same zone but with a weaker intensity. The failure zones describe likewise the maximum value of the plastic deformation and the triaxiality factor.

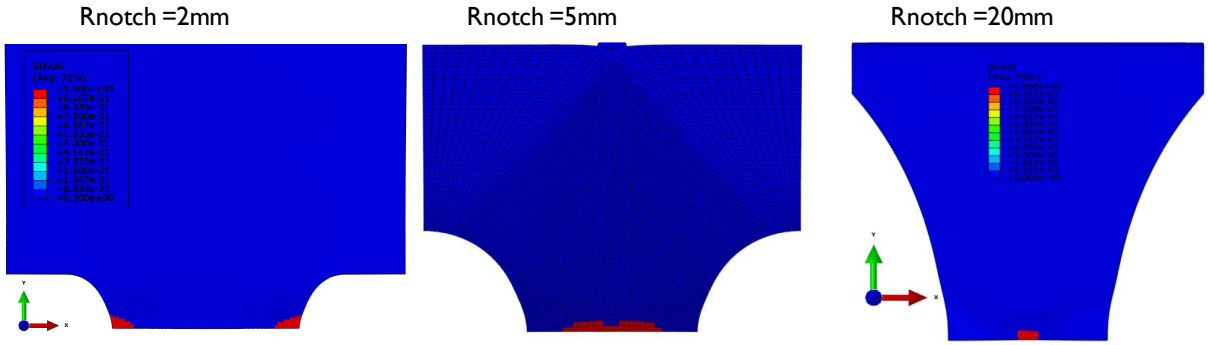

Figure VIII.28: Critical inter-cavities distance λ_f comparison during the flat sheet tensile test designed with various radius (for DPIII steel), (blue is equal to zero and red is equal to 1).

In summary, the tensile tests on various notched radius flat sheets has underlined a strong influence of the radius design on triaxiality factor and damage variables especially the localization of the fracture initiation through the critical inter-cavities distance criterion (λ_f) introduced in the GTNBF model.

VIII.2.2.3 Holed Specimen

The ultimate results concern the tensile test on the 5 mm radius holed flat sheet. Figure VIII.29 presents the force-displacement curves (a) and the axial stress-strain curves comparisons between the experiment (blue color) and the simulation (red color). The force-displacement curves show a mixed agreement. The curves are similar in elastic zone until reaching 0.2 mm of displacement. Thus, the curves begin to diverge when entering completely in the plastic stage. The calculation curve slows down earlier whereas the experimental one continues to rise. The usual softening on the coalescence beginning and the fracture stages are clearly visible in the calculated curve, while the experiment stopped brutally with a light curve inclination. Again, it is assumed that the experimental curve expresses a strong influence of the tensile test device stiffness which is not taken into account in the simulation settings. In the flip side of this analysis, the axial stress-strain curves are in a good agreement and underscores the quality of the virtual deformation technique measure with the system ARAMIS.
Here, the stress evolution in both cases depicts no softening before the material completely fails.

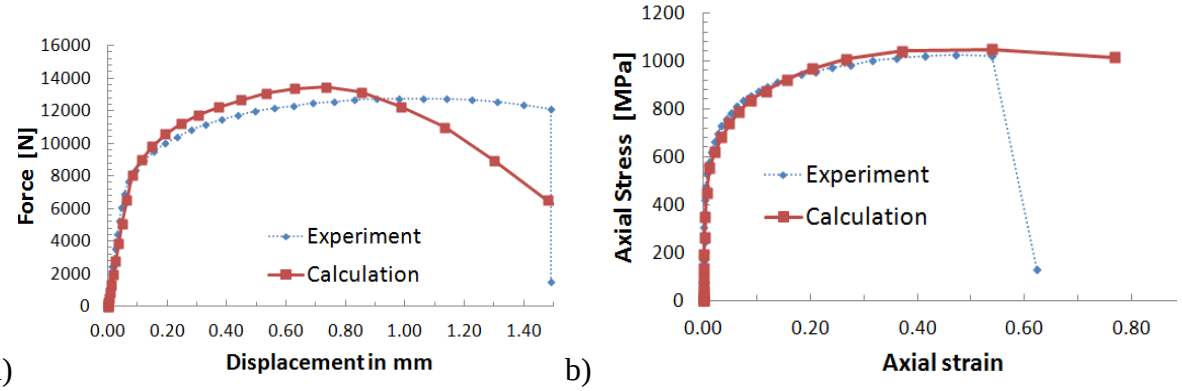

a) b)

Figure VIII.29: Tensile test on 5mm holed specimen for DPIII steel, a) force-displacement curves, b) Axial stress-strain curves.

The axial strain evolution coupled with the width strain isovalues (see Figure VIII.30) shows a good agreement between experiments and simulations and the final axial strain value recorded before the fracture occurred is at 0.595.
In front of that, the maximum axial value is concentrated at the edges of the hole exactly in the necking-section (center of the specimen). The simulated test shows perfectly the same strain distribution.

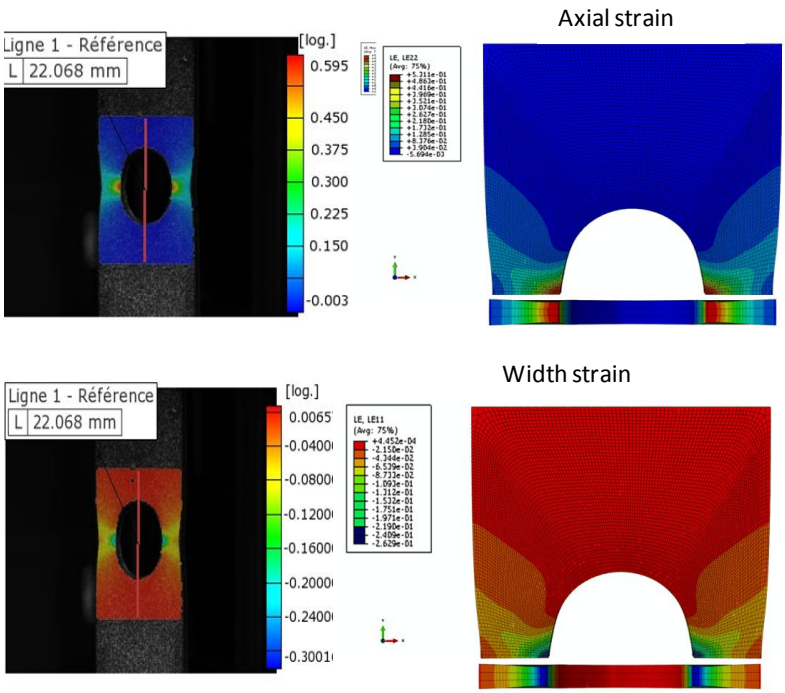

Figure VIII.30: Experimented and simulated isovalues of the tensile test on 5 mm holed specimen for DPIII steel before the fracture point; a) axial strain (max at 0.54) b) width strain (min at -0.26).

The axial strain concentrated at the edges of the hole corresponds to the final fracture localization. The picture of the specimen after the failure of the DPIII steel (top left) expresses a fracture perpendicular to the tensile direction. The same description can be easily seen when following the critical inter-cavities distance criterion (λ_f) implemented in the GTNBF model. A detailed observation of this variable confirms a fracture initiation at the edges of the hole and slowly progressing at the outside of the hole. The axial strain value extracted at 0.54 with the current GTNBF model is in similar range than the experiment and the axial strain value at 0.8 confirms the slow fracture progression.

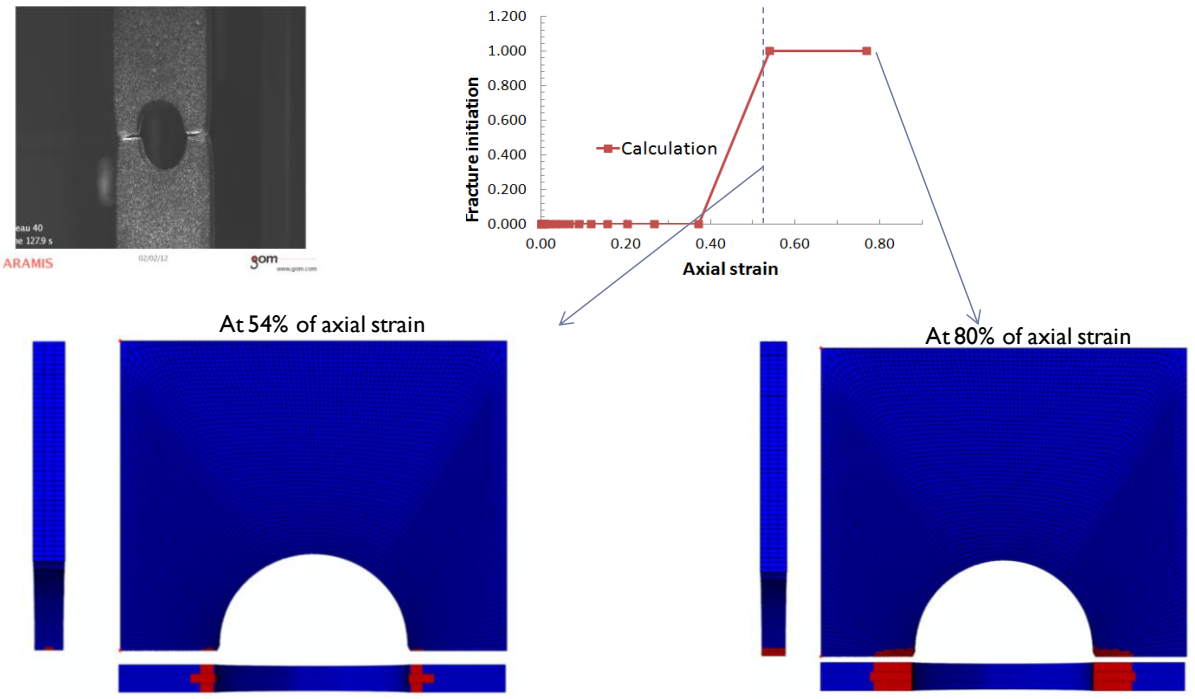

Figure VIII.31: Fracture initiation localization in the 5 mm holed radius specimen loaded in vertical direction with DPIII material (blue is equal to zero and red is equal to 1).

Figure VIII.32 collects the damage isovalues when the fracture occurs. The porosity *f*, the void density and the mean void radius show a strong concentration at the same location as the fracture initiation presented in Figure VIII.31.

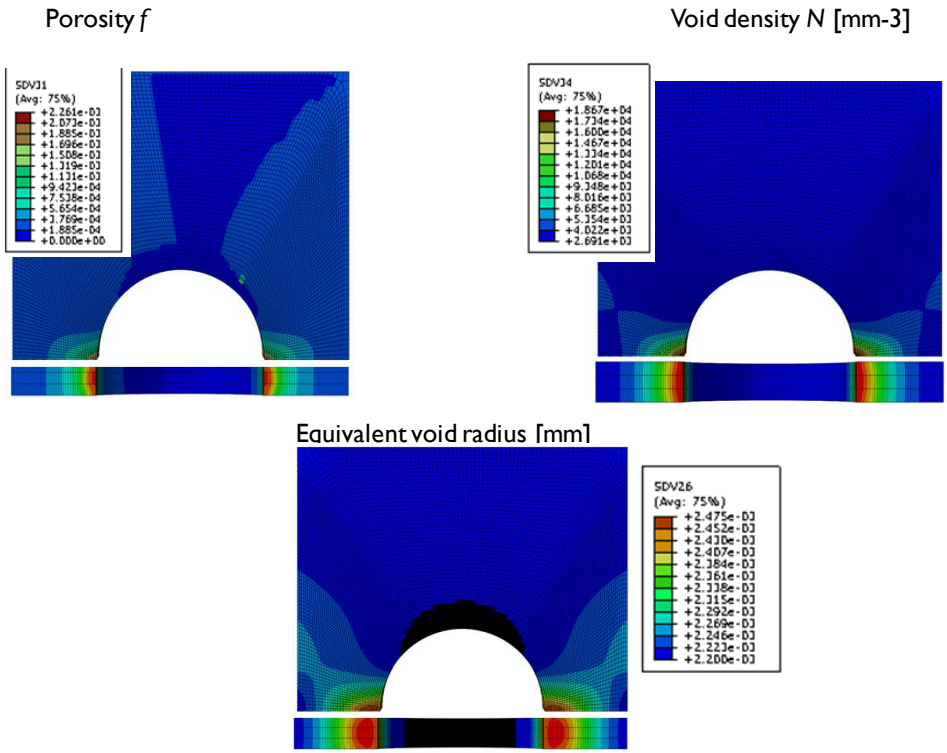

Figure VIII.32: Simulation results isovalues when maximum plastic strain is near 0.54: porosity (max at 0.023%), equivalent mean void radius (max at 2.47 µm) and numerical void density (max at 18670 voids/mm³).

VIII.2.2.4 GTN and GTNBF models comparison

After analyzing the experimental tensile and the simulation results on various flat sheet geometries, the current section is focused on comparing the well known GTN to the GTNBF models predictions. Figure VIII.33 illustrates the force-elongation evolution of the five studied specimens (smooth, notch and hole). The GTN and GTNBF models are compared to the experiment for curves. As a rule, the GTN model is drawn in red line, the GTNBF model in blue and finally the experiment in green. It appears that the optimal comparison with the experiment is made with the GTNBF model. The smooth (a) and the 2 mm notch radius (b) specimen simulate with the original advanced Gurson model fractured earlier than the GTNBF model and the experiment. With other specimens, it appears clearly that the GTN model does not predict accurately the damage stage and the fracture point. For these latter cases, the force-displacement GTN-model curves are far beyond the experiment.

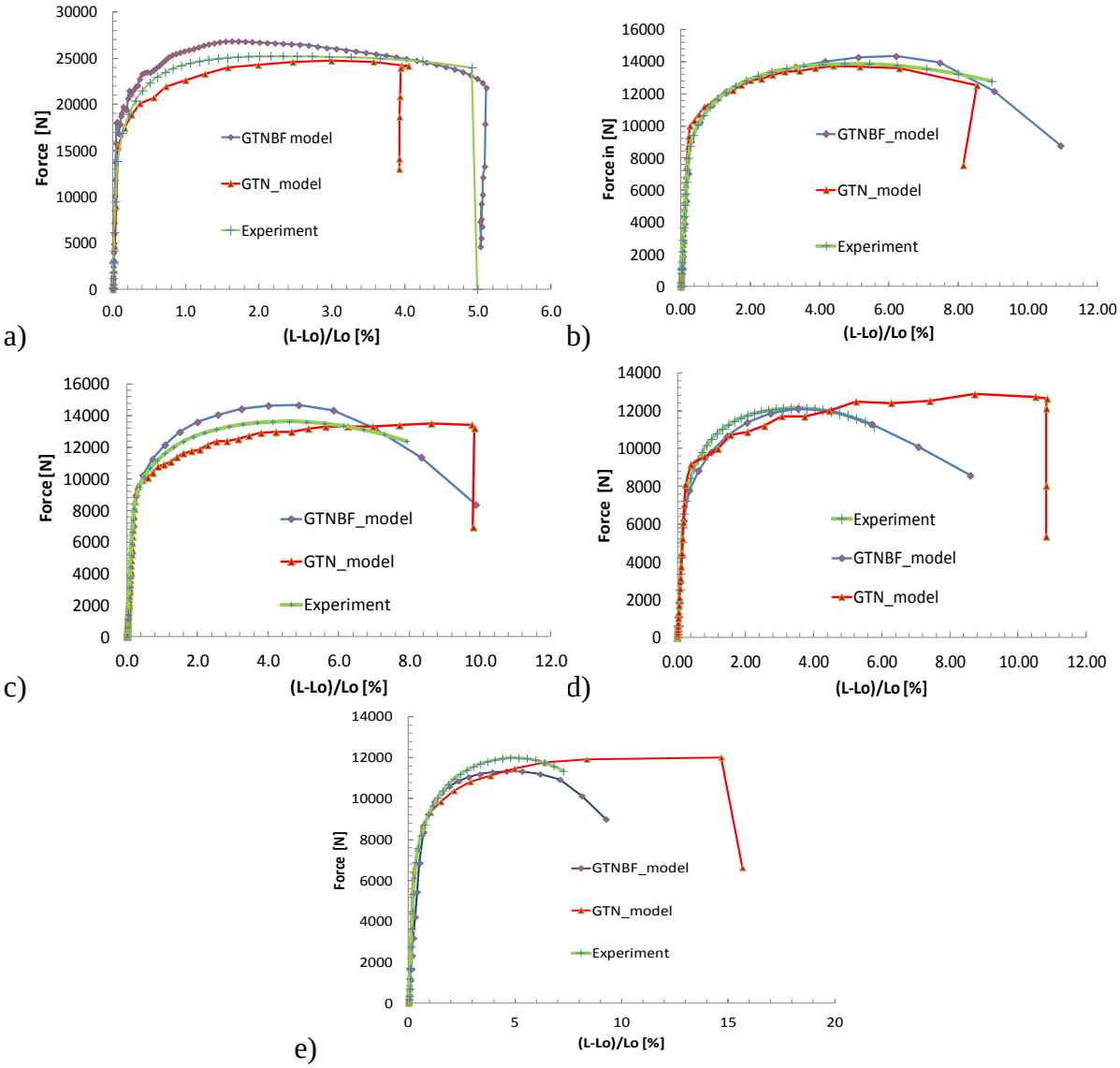

Figure VIII.33: GTN and GTNBF models comparisons with a) smooth, b) 2 mm notch radius, c) 5 mm notch radius, d) 20 mm notch radius, e) 5 mm hole radius specimens (DPIII steel).

The fracture initiation localization has been inspected between the simulated and the experimental tensile test specimens. It seems that the GTN and the GTNBF models predict the same fracture initial location. However, differences are significant when comparing the final axial strain values located at the minimal cross-section. Indeed, Figure VIII.34 presents the axial strain when the distance inter-cavities (λ) reaches 1 for all specimens used in this chapter. More specifically, the green color symbolizes the experimental point; red the GTN model and blue is the GTNBF model. The last axial strain values for the GTN model have been extracted when the void volume fraction reach the critical value set at 0.0316 (see chapter V for the identification) for the DPIII steel.
The analysis of the graphic shows a better prediction of the fracture initiation with the GTNBF model. As seen, the final axial strains are in good agreement with the experimental results when the advanced GTN is used for all type of flat sheets.

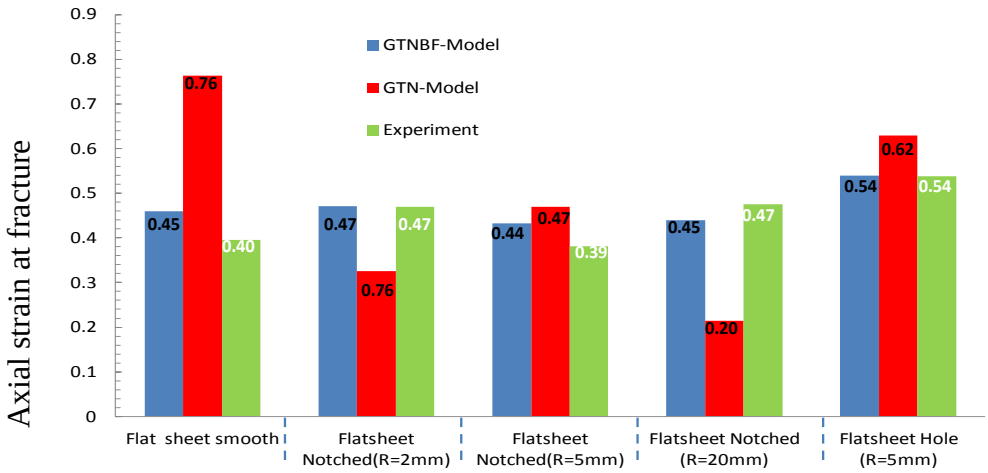

Figure VIII.34: Axial strain fracture comparison between the experiment, the GTN model and the GTNBF model during the flat sheet tensile test designed with various geometries (for DPIII steel).

VIII.2.3 Conclusions

The tensile experiment tests with digital image correlation (DIC) have shown in overall good results in term of deformations. Unfortunately, some difficulties have been encountered during the measurement regarding the force and displacement values. The force measured by the tensile device was sometime not well recorded due to some electrical instability. A post analysis treatment was needed to delete the force induced by the sample setting in the tensile device. On top of that, the "Mouchti" has shown sometimes bad tenacity especially after the maximum force was reached. Eventually, the displacement was not very good measured due to the lack of significant number of images taken with the camera after the maximum force, and in front of that some specimens were not well aligned with the tensile device. It is to underscore that the specimen dimension equal to 260*20*1.5 mm^3 makes particularly difficult its installation without tilting.
Also, the comparison force-displacement was not 100% successful due to the influence of the tensile test device stiffness which is not taken into account in the simulation settings.

However, the extraction of the axial stress (with help of the force measured by the tensile device) and the deformations (axial, radial, thickness directions, for the surface calculation at the minimal cross-section) have given a good correlation between the simulation and the experiment.
The simulation using the GTNBF model predicts better than the GTN model the material behavior. Mainly, it is due to the introduction of all damage stages (void growth, nucleation and coalescence) physically based on an accurate tomography measurements [LAN 2011]. The damage model through the VUMAT shows with good accuracy the fracture initiation area correlated with the last image taken by the cameras after fracture.
With these considerations, a better comparison could be done by reducing the grid points for the digital image correlation, make sure to calibrate the tensile device after each test and taking more images to catch the failure progress as done by Niazi [NIA 2012].
Finally, the GTNBF model has revealed a strong influence of the notch design during the tensile loading of the flat sheet specimen. Indeed, thanks to the inter-cavities distance criterion λ_f various fracture initiation locations have been detected.

VIII.3 Cross-Die Drawing test

VIII.3.1 Experimental and finite element model

The main idea of choosing the cross-die drawing test is to assess the drawing ability of the flat sheet in complex strain path and validate behavior laws such as GTN and GTNBF models with numerical simulations. According to Riel et al.[RIE 2009] the cross-die forming process covers a wide range of triaxialities and it is very useful for determining the formability coupled with a FLC (Forming Limit Curve) or known as a Keeler-Goodwin diagramm [GOD 1968]. Also, apart from the wide range of triaxialities, some regions of the blank undergo severe strain path changes. In addition to this major advantages, the test accurately simulated the sheet metal forming processes describing different forming modes better than a traditional deep drawing tests such as cylindrical or square cup drawing. This test simultaneously estimates the formability prediction and the material ranking.

VIII.3.1.1 Experiments

The current test has originally been designed to find the formability limits for aluminum during a joint venture research called '*Brite-Euram Light weight vehicle* project 'in 1995 [BRI 1995]. The final test geometry illustrated in Figure VIII.35b is designed to obtain all possible strain distributions in one overview to assess overall drawing performance. The final form presents both convex and concave drawn in a single punch action (see Figure VIII.35a).

a) 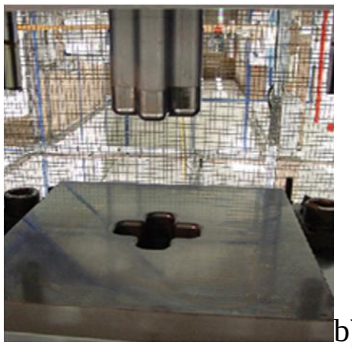 b)  c) 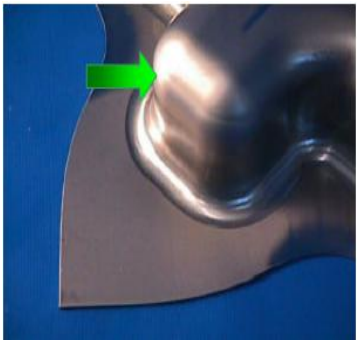

Figure VIII.35: a) The tools used for the cross-die test, b) The final configuration of the deformed specimen, c) necking in the product [ATE 2004].

Procedure

The cross-die deep drawing experiments have been performed on an industrial press following the ArcelorMittal standard procedure for deep drawing as seen in Figure VIII.36. The blank is a 300x300 mm² flat sheet made of DPI and DPIII steels (see Table .V.4 in chapter V). A lubrication called Quaker 6130 is applied on both sides of the blank to obtain a friction coefficient value of 0.13. The constant speed punch is around 30mm/s to attempt a critical punch displacement found at 26 mm and the blank holder force is measured at 333kN.

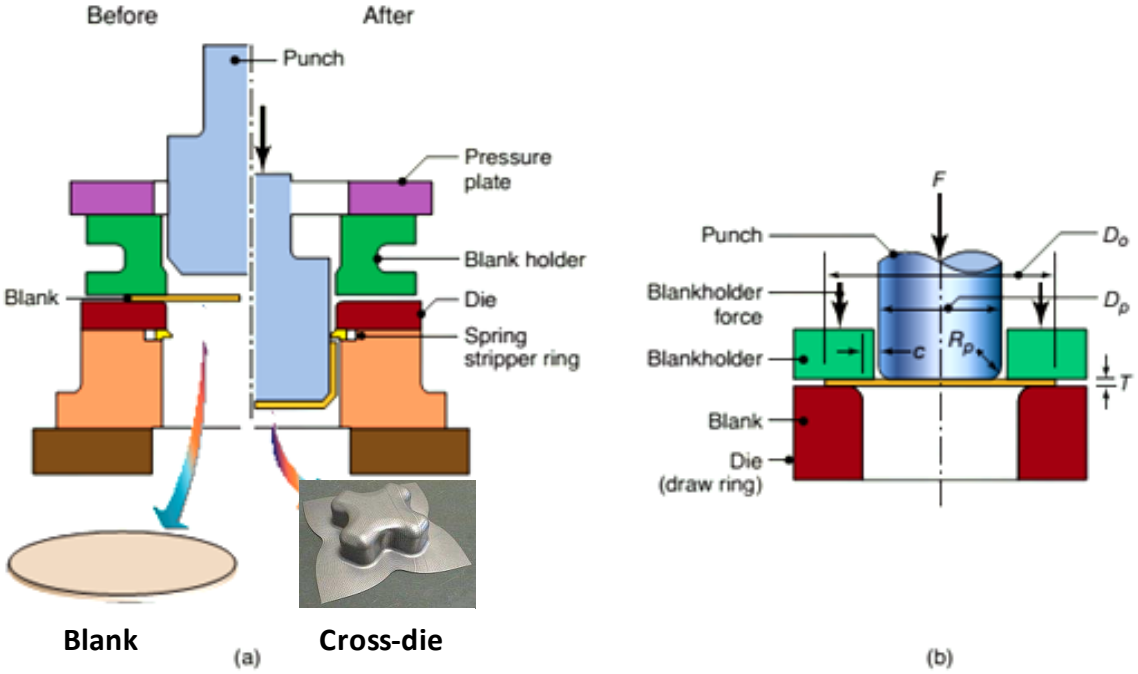

Figure VIII.36: Schematic illustration of the deep drawing process on a circular sheet-metal blank, a) The stripper ring facilitates the removal of the formed cup from the punch, b) Variables in deep drawing of a cylindrical cup [KAL 2008].

The strain distribution was measured in the experiment that reached the critical height but did not localize. The strain was virtually obtained by gridding the blank with a 2.5 mm square dot marked onto the surface of the blank using electrochemical-etching technique. Figure VIII.37 shows the gridded blank (a) and the strain diagram (b). The strain distribution is presented in a two-dimensional coordinate system, with the major strain plotted on the Y-axis and the minor

strain plotted on the X-axis. The magenta dots represent the isovalues of the deformed cross-die at 26mm punch displacement.

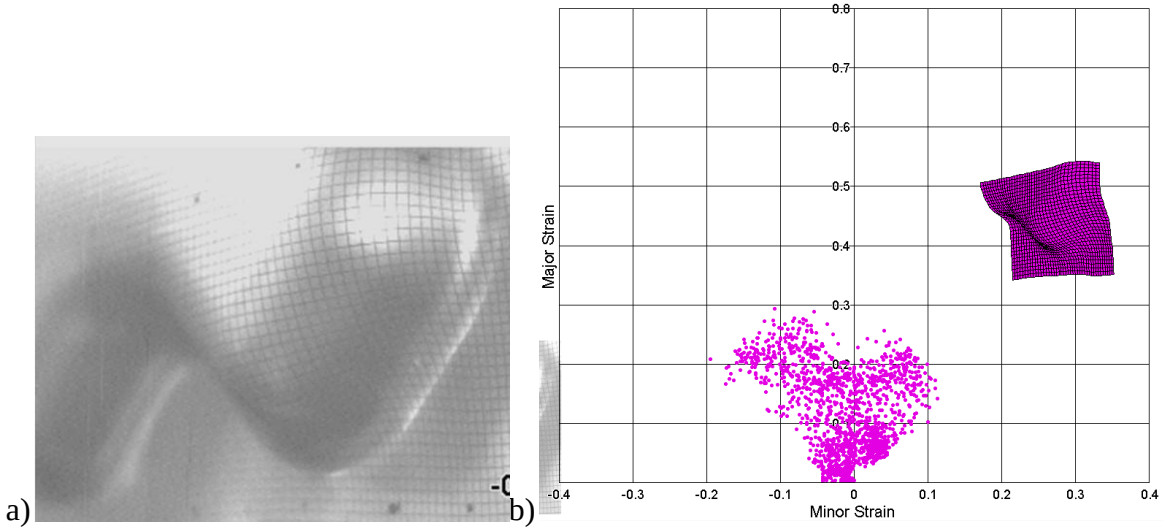

Figure VIII.37: a) The 2.5 mm square grid marked onto the blank surface, b) Representing major and the minor strain distribution of the blank part at 26mm punch displacement (for DPIII steel).

VIII.3.1.2 Finite element model

The cross-die test simulation was computed with Abaqus-Explicit using the proposed GTNBF damage model and the well known GTN model. One quarter of the blank has been meshed. The blank mesh consists of 10000 homogeneous elements and 5 elements have been taken in the thickness direction. The blank holder force is 83.25 KN representing one fourth of the total force. Although this test is used to characterize the material, other effects such as tool deformation and friction (through lubrication) play an important role as well [LIN 2008] [HOL 2010]. These effects are ignored in the current modeling and the tools are taken rigid. Therefore, the contacts between tools and blank are modeled with a penalty contact algorithm and the constant Coulomb friction coefficient is set at 0.13.

The setting of the cross-die in Abaqus-Explicit finite element code is presented in Figure VIII.38. The tools are in green color and the blank is in blue. The orange triangles describe the symmetric conditions. The material properties of DPI and DPIII steels were already presented in Table V.3.

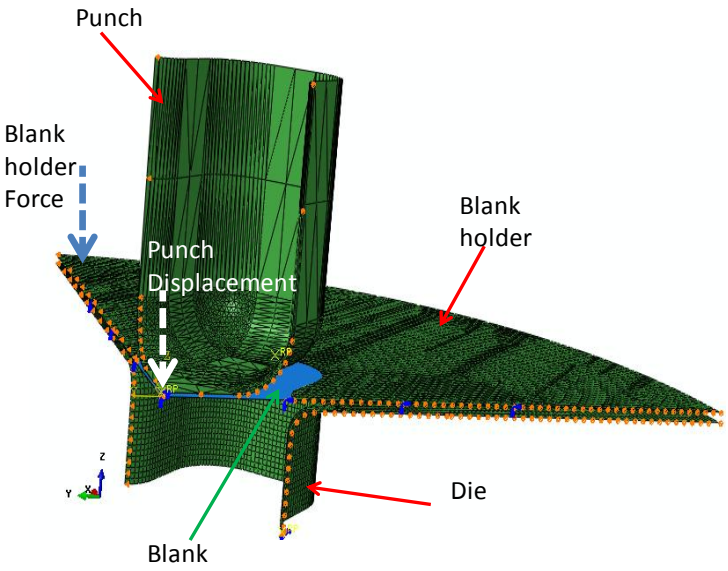

Figure VIII.38: Schematic One-fourth cross-die process set-up with the commercial finite element code (Abaqus-Explicit).

VIII.3.2 Results and comparisons

Simulation results of the cross-die drawing test with two damage models (GTN and GTNBF) were compared to the experimental measurements i.e. the punch force-displacement curves, the strain distributions and the fracture initiation localization.

VIII.3.2.1 Punch Force-Displacement curves

Figure VIII.39 and Figure VIII.40 respectively illustrate the punch Force-displacement curves for DPI and DPIII steels. The force is plotted on the Y-axis and the displacement on the X-axis. In details, the dash curve belongs to the experimental punch force evolution while the solid curves are the simulated counterparts. The red solid curve represents the force-displacement simulated with the GTN model whereas the blue solid curve is the result with the GTNBF model.
As a rule for both DP steels, all curves can be divided in three stages. The first stage the contact pressure of the punch tool on the blank at 0 displacements. The force brutally surges from 0 KN to around 60 kN. The second stage is characterized by force stagnation at around 60 KN between 0 and 5 mm of displacement. The third stage is the true linear force punch evolution followed by a sudden stop when the tool reaches the required height.

Simulation and experiment comparison in Figure VIII.39 for DPI steel translates that the simulations reach their maximum force earlier than the experiment. The punch height found for the simulations is 30 mm where it is 35 mm for the experiment. This difference is often due to the experimental setting which requires more displacement to achieve the pressure contact and reduce clearance between the punch and the blank. The second important remark

concerns a better agreement with the experiment for the cross-die drawing test with the GTNBF model. Indeed, it is astonishing to see the test simulated with the GTN model far below the experiment after 15 mm of punch displacement. It probably suggests that the isotropic hardening and the damage parameters are not well enough identified to model the current test. Besides, it is known from the previous application on flat sheet loaded in tensile direction that the classic GTN model is not the perfect ductile damage model candidate to reproduce an accurate material behaviour of the DP steel. It has been proved in section VII.3.4 in chapter VII that the GTN model with no kinematic hardening law and a phenomenological damage model are less accurate than the GTNBF model.

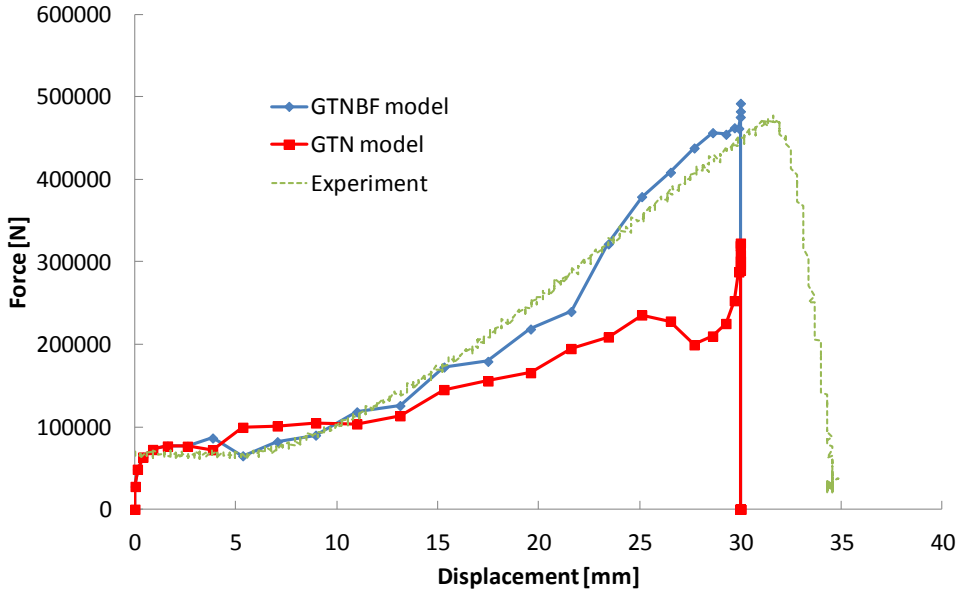

Figure VIII.39: Punch force-displacement curves for DPI steel; GTN model in solid red, GTNBF model in blue solid, and Experiment in dash green.

Herewith, Figure VIII.40 presents the comparison for the DPIII steel. The experimental force history strongly differs from the DPI steel (Figure VIII.39). For DPIII steel, the simulations reach at the same displacement their maximum force. On top of that, a fracture initiation has been experimentally detected near the corner of the blank when reaches its final form at around 20 mm of the punch displacement. This rupture happens in the same location as seen in Figure VIII.35c from Atzema et al. tested product [ATE 2004]. A necking has been also observed in both simulations. The simulations and the experiment are not perfectly superimposed but their agreement is sufficient to validate the modeling application.

Focusing on simulations, one can observe that both damage models start the contact between the punch and the blank later and smoothly at around 3 mm compared to 0 displacements for the DPI steel. It seems that the material parameters significantly influence the contact pressure. Here, the punch is considered rigid like the blank holder and the die. Only the blank is taken as deformable body. In reality the tools are not rigid and the contacts are not perfectly set tight along the punch displacement. In recent publication Atzema et al. [ATE 2004] demonstrates in a similar test that the tools stiffness have a large influence on formability. The dominant deformation is bending of the blank holder. A localized blank holder contact with the blank due to bending of the tool results into a fully non - linear forming simulation with non constant blank holder force. The blank older should be a function of the displacement in

the simulation with rigid tools. Apart from this observation, the graphic depicts that both finite element model evolve linearly and similarly until 15 mm of displacement. After this point, the damage models differently rise. The GTNBF model reach a maximum force around 50% higher than the maximum value for the GTN model before sharply dropping down.

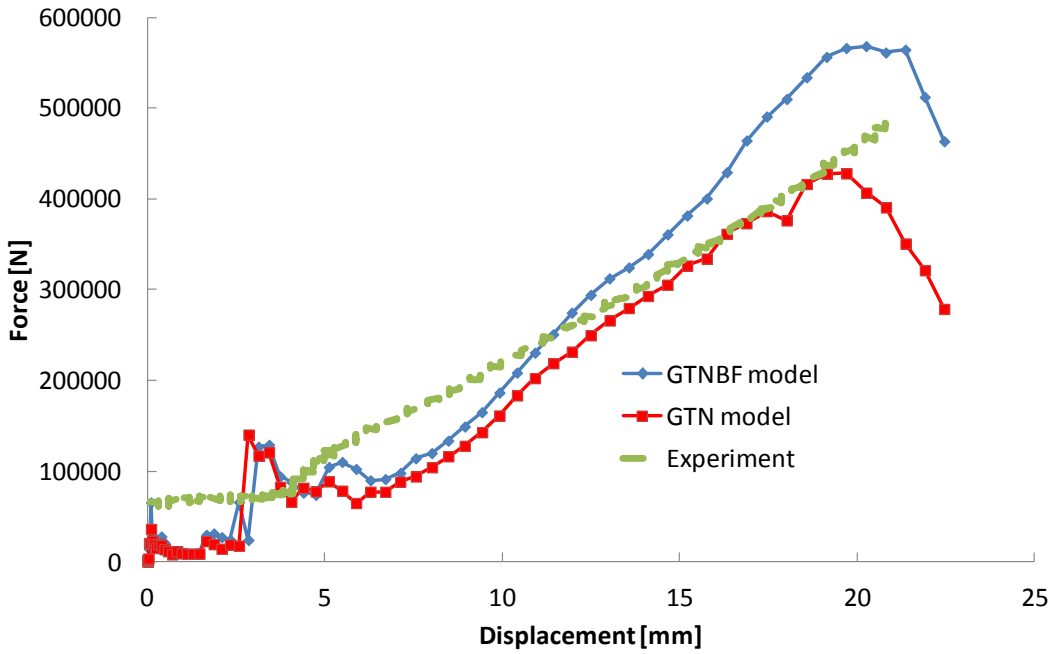

Figure VIII.40: Punch force displacement curves for DPIII steel; GTN model in solid red, GTNBF model in blue solid, and Experiment in dash green.

VIII.3.2.2 Friction coefficient influence

In this study, the friction coefficient has been taken at 0.13 for the lubrication applied between the punch and the blank. Niazi [NIA 2012] and Hol [HOL 2010-2011] have observed that among the uncertainties causing the deviation of the experimental and the simulated force displacement curves, friction is one of the most important factor. Besides, Hol et al. [HOL 2011] added that the friction evolution during the cross-die test is extremely difficult to understand and depends on the contact area and pressure. According to the same author the friction coefficient is not constant but varies during the loading. Wang et al. [WAN 2011] investigation shows that the profile of the draw die radius has a significant effect on the wear distribution, and that a lower contact pressure distribution can be achieved by using a combination of circular and high elliptical curved geometries.

Unfortunately, the friction evolution data was not available during the experimental drawing process. However, the effect of changing the constant friction parameter has been conducted with the simulation model. In other words, the same cross-die simulation has been computed with a weaker friction coefficient between the punch and blank contact. This value has been taken at 0.001 representing a quasi frictionless contact model. It physically models the use of a complex lubrication mixture based on Teflon.

The simulations conducted with the GTNBF model using a quasi frictionless value have been compared with the experimental value (0.13) and previous simulations in Figure VIII.41. The graphics compare results both for DPI (a) and DPIII (b) steels. The friction effects are significant on both materials. It appears that a weaker friction coefficient imposes a lower generalized force slope. A specific curve analysis of each DP steel reveals different influence.
Figure VIII.41a unveils a 30% maximum force drop when a quasi frictionless value is introduced in simulation for the DPI steel. In opposite, Figure VIII.41b expresses a mixed influence for the DPIII steel. Indeed, in the simulation with a weaker friction value, the force is reduced all along the drawing process and delays the fracture initiation. When the fracture initiates at around 20 mm of punch displacement for the experimental friction value, the simulation with a weaker friction value (0.001) a later fracture at about 30 mm without force softening.
With these analyses in mind, the idea of the pressure contact and area dependency initiated by the friction development from Hol et al. [HOL 2010-2011] is confirmed.

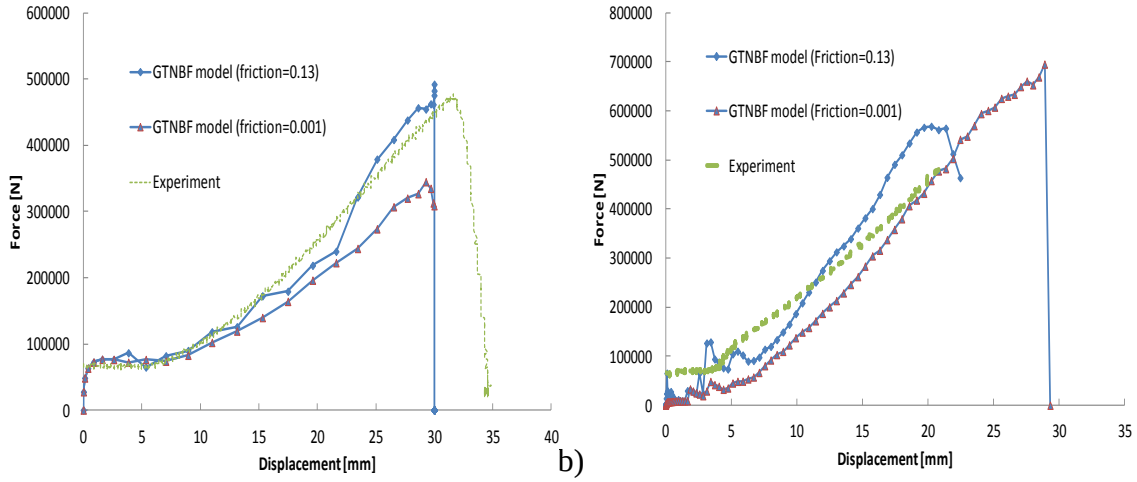

a) b)

Figure VIII.41: Friction coefficient influence on punch force displacement curves; a) DPI steel, b) DPIII steel.

VIII.3.2.3 Strain distributions

As already mentioned, the strain distribution has been experimentally measured on inner surface of the blank when the punch reaches the critical displacement of 26mm. Parallel to this experimental campaign, a determination of the forming limit diagrams has been conducted according to Nakajima method [NAK 1971] with DPI and DPIII steels. Numerous publications such as those from Goodwin [GOD 1968] Bao et al. [BAO 2004], Wierzbicki et al. [WIE 2005], Uthaisangsuk et al. [UTH 2008], Ramazani et al. [RAM 2010] and others [LEM 2003] [XUE 2007] [LIN 2008] [LI 2010] [PAN 2010] [LOU 2012] [LUO 2010] [PAN 2011] have revealed some notable contributions on improving the forming limit curves determination and predictions for Dual-phase steels by using Nakazyma or Marciniak [MAR 1992] tests. In all those enhancements, efforts have been essentially put to optimize tool geometries, blank holder pressure, lubrication, material and eventually the strain measurement.

VIII.3.2.3.1 FLC diagrams determination through Nakazima procedure

According to GOM (Gesellschaft für Optische Messtechnik) specialized in optical measuring techniques, the Nakajima tests, which determine the FLC diagrams, is based on the principle of deforming sheet metal blanks of different geometries using a hemispherical punch until fracture occurs (Figure VIII.42a). By varying the specimen width (Figure VIII.42b), different deep draw and stretch forming conditions occur on the sheet metal surface (from a regular biaxial deformation to a simple tensile load). The maximum deformations (prior to breakage) of the different specimen shapes are determined and define the forming limit curve of the corresponding material. The strains contributions are measured by using the optical system ARAMIS (same as the flat sheet tensile tests) thanks to a stochastic pattern applied to the surface using a color spray see Figure VIII.42c. The system ARAMIS calculates the characteristic values (theoretical maximum of major and minor strain) by the computation of an ideal shape of the curve from the captured measuring values.

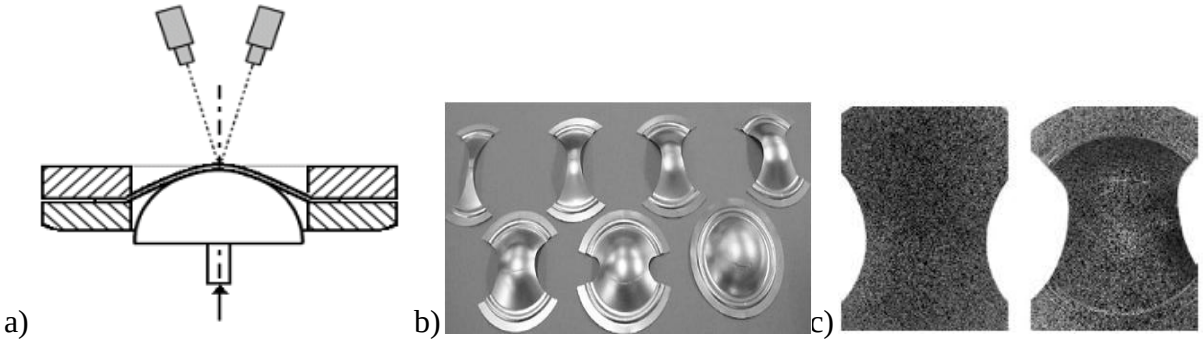

Figure VIII.42: a) Schematic process set-up, b) different specimen geometries, from the entire blank to strongly waisted blanks c) undeformed and deformed Nakajima specimens with stochastic pattern used for FLC diagrams measurement [GOM 2009].

VIII.3.2.3.2 Results

Figure VIII.43 and Figure VIII.45 provide the FLC diagrams respectively for DPI and DPIII steels. In details, the green solid curve connecting 8 points (averaged major and minor strain) represents the measuring results of 8 different sheet metal geometries. For each geometry, the deformations at material failure were evaluated for 3 specimens each with 3 sections and averaged in the diagram. The cloudy gray dot represents the experimental isovalues of the deformed cross-die at 26mm punch displacement. Eventually, the red triangle and the blue square dash points respectively for GTN and GTNBF models described the evolution of the simulated major and minor strain where the maximum plastic strain is reached.

In the FLC diagram for DPI steel, all points are under the forming limit curve (green line). It means that the blank reaches its final form without failure at 26 mm of punch displacement.

This conclusion is also confirmed by the simulated cross-die drawing test using the GTN and the GTNBF models.

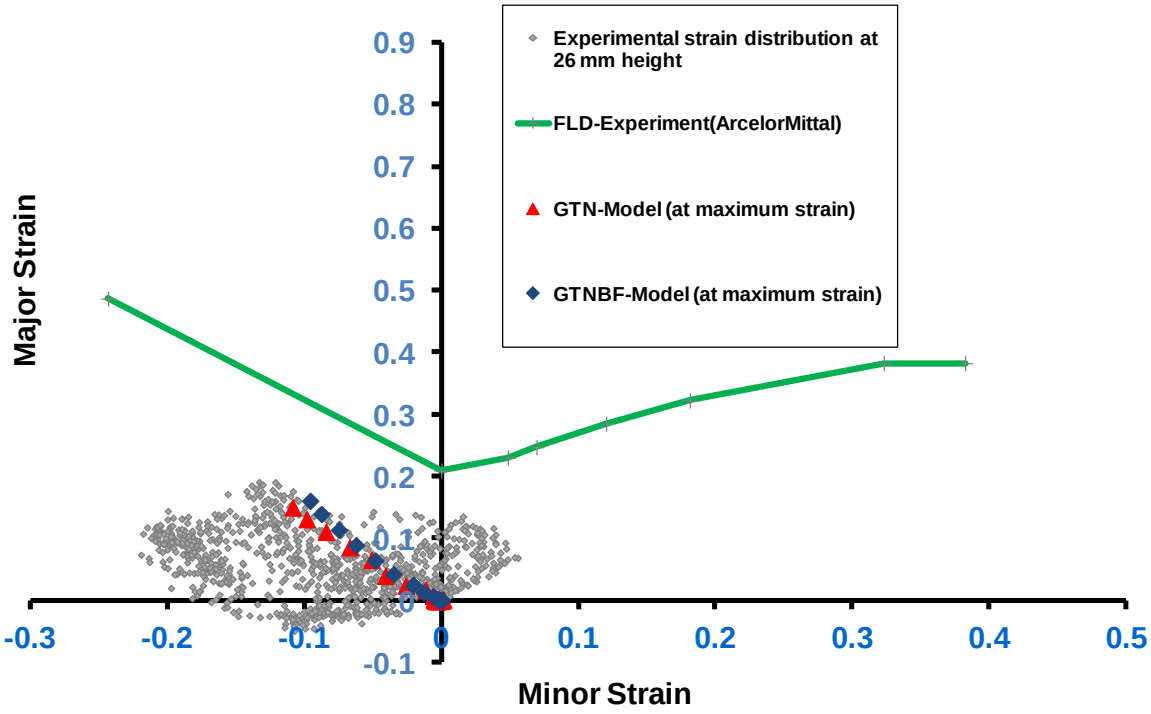

Figure VIII.43: Experimental FLC, experimental cross-die strain distribution and simulated evolution of the major and the minor strain at 26mm punch displacement for DPI steel.

The maximum major strain is located at the same position for both damage models as seen in Figure VIII.44.

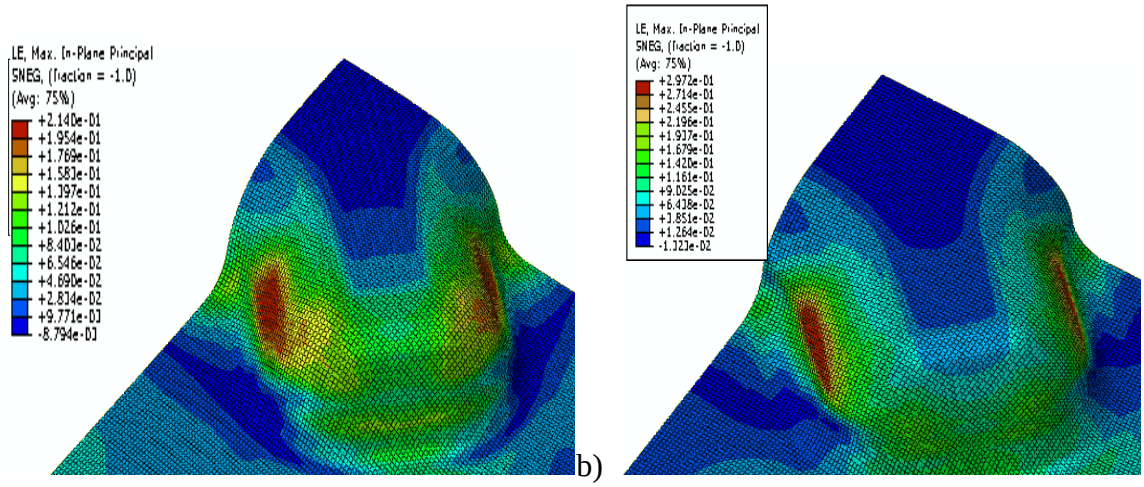

a) b)

Figure VIII.44: Cross-die maximum major strain isovalues when the punch displacement is closed to 26 mm; a) GTN model, b) GTNBF model for DPI steel.

The FLC diagram for the DPIII steel reveals different results which are completely opposite to the DPI steel. At first, a third of the experimental gray dots are near or far beyond the experimental FLC (green line). These results highlight that the final form of the blank contains failure. The conclusion is in perfect agreement with the blank surface visual

inspection. Indeed, some final products have been found with a necking around the corner of the cross-die as seen above in Figure VIII.35c (section VIII.3.1.1).
The finite element predictions with GTN and GTNBF models converge to the same results. However, the GTN model plastic strain is less accurate by predicting a fracture initiation later at higher major strain and stopping its strain evolution just at the experimental FLC before decreasing. On the contrary, the GTNBF model shows a straightforward answer by detecting the failure earlier at another location on the blank (see hereafter section VIII.3.2.4).

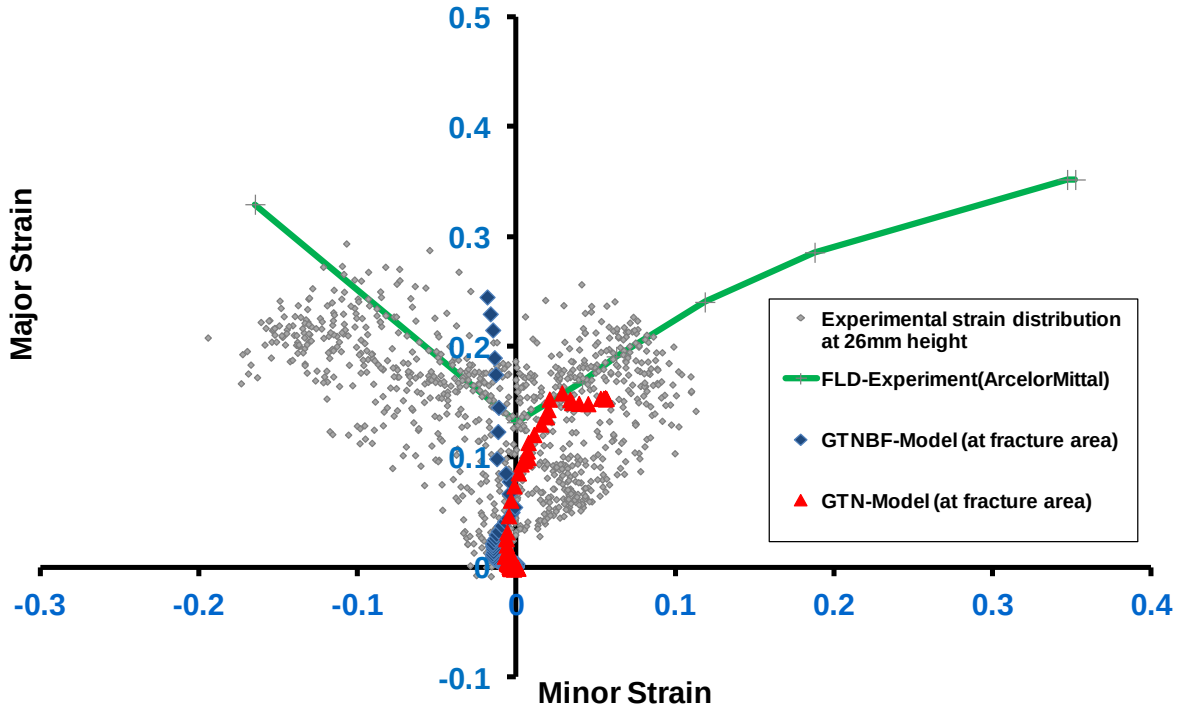

Figure VIII.45: Experimental FLC, experimental cross-die strain distribution and simulated evolution of the major- minor strain at 26mm punch displacement for DPIII steel.

The maximum major strain is differently distributed as seen in Figure VIII.44. With GTN model, the maximum strain is located at the bottom of the cross whereas the GTNBF model shows its maximum value at the corner.

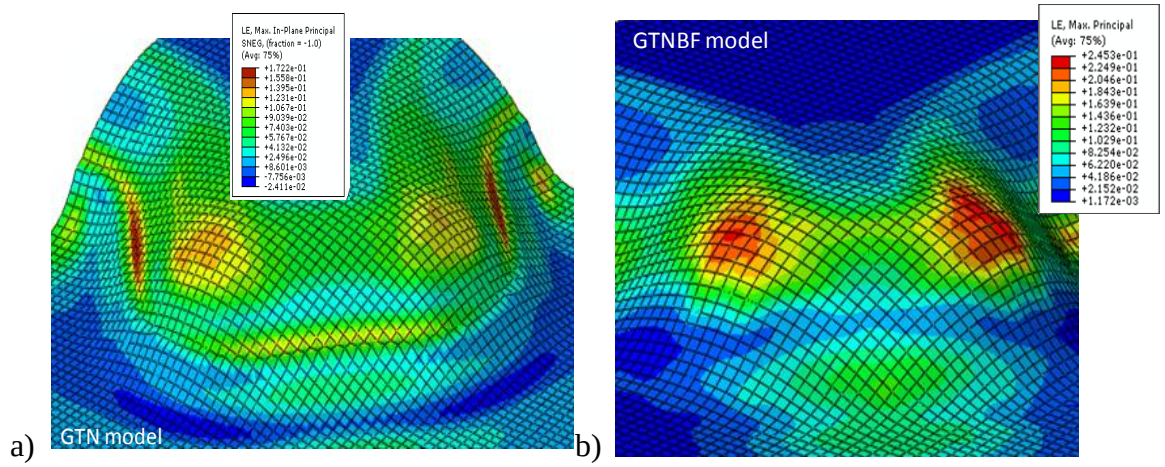

Figure VIII.46: Cross-die maximum strain isovalues closed to fracture a) GTN model, b) GTNBF model for DPIII steel.

VIII.3.2.4 Fracture initiation

The present section gives more information with respect to the fracture initiation appearing during the cross-die drawing operation for the DPIII steel. The DPIII FLC diagram presented above detects for both damage models (GTN and GTNBF) a fracture on the surface of the blank thanks to the extraction of the major and minor train values. Unfortunately, this diagram is not sufficient alone to accurately localize the fracture initiation area and must be coupled with optical observations.

It is already known that the necking occurs at the end of the process (at 26 mm of punch displacement) around the corner of the inner surface of the blank as seen in Figure VIII.35c. Though, the leading goal is to compare the experimental necking localization with those obtained by the simulations.

Figure VIII.47 illustrates the porosity *f* evolution of the blank during the simulated cross-die drawing process. The porosity variable extracted from the simulations is plotted on the Y-axis and the punch displacement is on the X-axis. The red solid curve represents the phenomenological GTN damage model implemented in Abaqus-explicit software. Thus, the blue solid curve is the porosity evolution given by the physically-based GTNBF damage model. Bearing in mind that in GTN model case, the ultimate value of the void volume fraction (VVF) when the material fails has been defined from the literature survey and experimentally determined with the measurement of the critical cavities distance (λ_f) for the GTNBF model case, the graphic also gives an appreciation of the fracture area (left; the GTN model and right; the GTNBF model).

At first, the curve comparison depict that those damage models give different results. The cross-die drawing test simulated with the GTN model shows a fracture initiation occurring at around 19.5 mm of punch displacement whereas the same simulation with the GTNBF model failed later at around 22 mm (red elements on both pictures characterizes the fracture of the material). The second opposition lies on the fracture localization. Indeed, the fracture seems to initiate at the bottom edge of the final product with a GTN model while the failure is located around the corner with the GTNBF model. Comparing the final experimental product to the simulated one, it seems clear that the simulation with the GTNBF model is closer to the experimental observations.

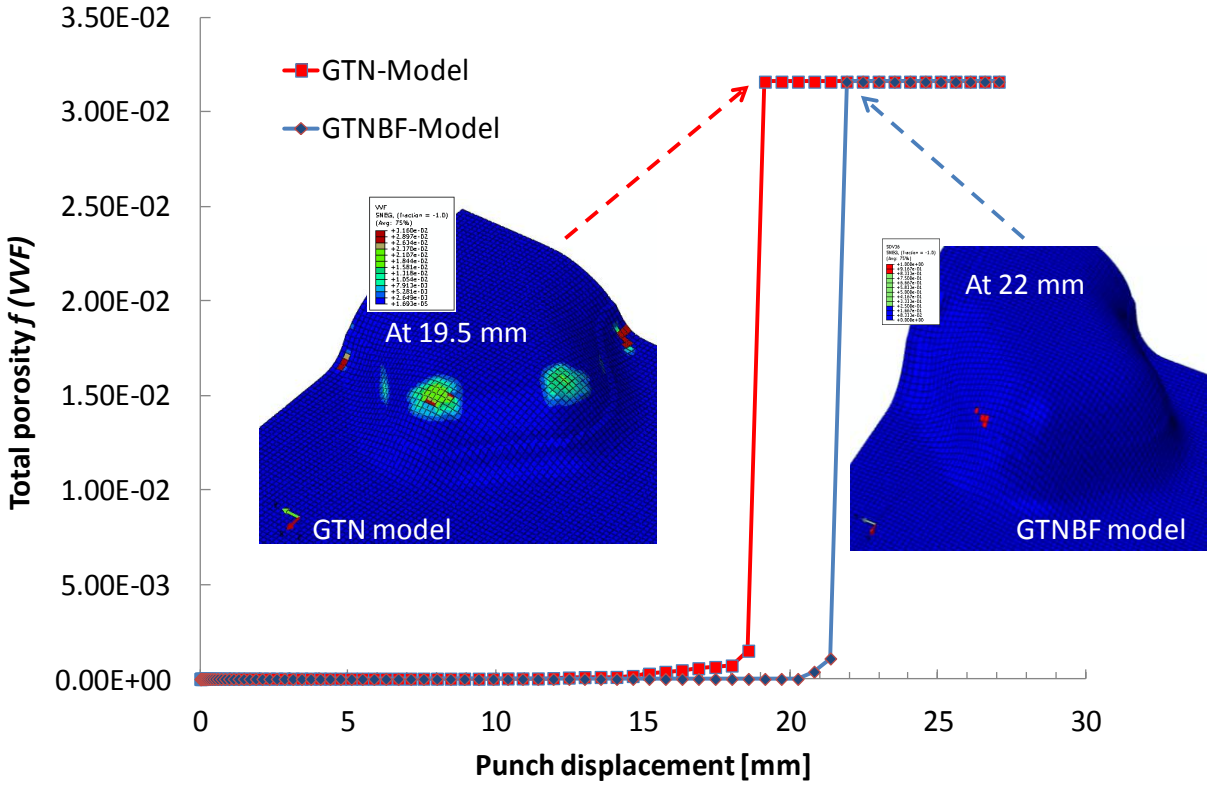

Figure VIII.47: Visualizations of the porosity *f* evolution in function of punch displacement at the fracture zone for the cross-die drawing test simulated with GTN (red curve) and GTNBF (blue curve) models for DPIII steel. The red elements characterize the fracture of the material.

VIII.4 Conclusions

This chapter has been dedicated to forming applications of the GTNBF model. Two tests often used by industrials have been chosen. The first one is the widely used uniaxial tensile test and the second one corresponds to the cross-die drawing test. Both have been equipped with the optical system ARAMIS for strain distribution measurement. The cross-die drawing test has been preferred to the hole expansion or cylindrical cut drawing tests because it provides a large range of triaxialities, an easy formability determination and the ranking of the materials.

The literature survey on flat sheet forming validation usually proposes a simulation-experiment correlation by using force-displacement curves evolution coupled with strain distributions. Few , damage-displacement evolutions are proposed when the DP steel is modeled with modified Lemaitre [NIA 2012], advanced GTN or more recently fracture [WIE 2005], [Mohr 2010] predictions. Rarely proposed, the present applications simulated by GTNBF model have been focused on correlating simulation and experiment results by comparing different geometries, loadings and DP steel grades. It also has used a hybrid experimental-numerical determination of the loading history proposed by Mohr [MOH 2012] as seen hereafter. This procedure consists of analyzing the force-displacement given by the tensile device, stress-strain of the material (through the optical system ARAMIS), the FLC diagram, and the damage evolution.

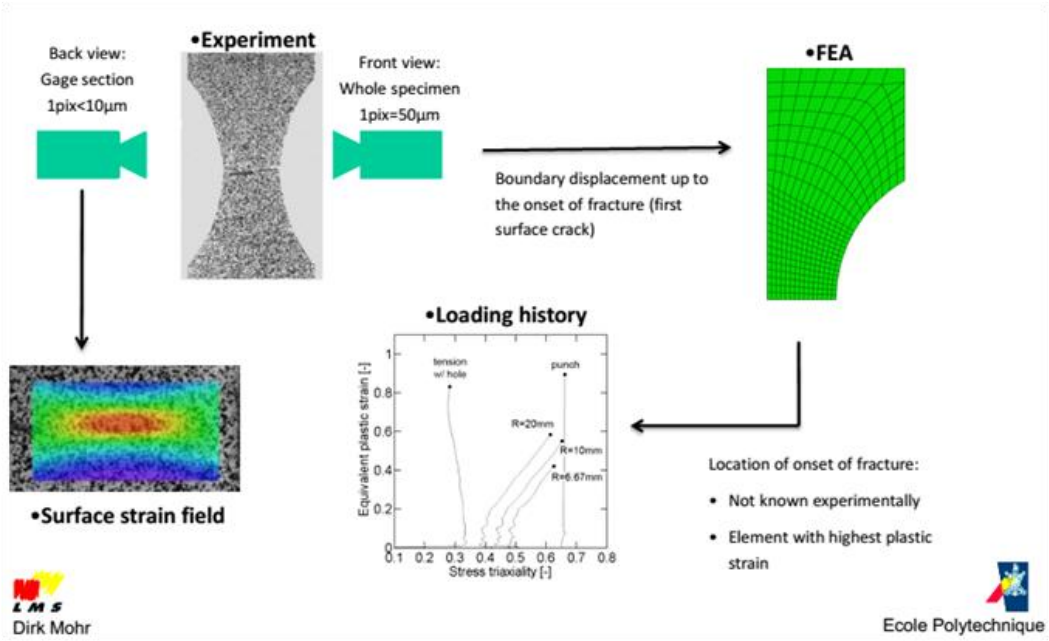

Figure VIII.48: Hybrid experimental-numerical determination of the loading history [MOH 2012].

In Figure VIII.43 and Figure VIII.45 loading paths to fracture initiation based on an accurate physically-based experimental damage evolution for DP steel is recovered. The fracture modeling proposed is based on inter-cavities distance (λ) measured by Landron [LAN 2011]. This criterion is simple to implement and to use as a post-processing tool. It takes into account all porosity evolution stages (growth, nucleation, and coalescence of voids). Unfortunately, this fracture criterion has a significant drawback. Indeed, the model has been validated for voids remaining spherical during the loading. The author is aware that significant advanced Gurson model extensions have been developed (see chapter III). For instance, the works of Nahshon et al. [NAH 2008], Nielsen et al. [NIE 2010], Bai et al. [BAI 2008], Bao et al. [BAO 2004], and Wierzbicki et al. [WIE 2005] have contributed to improve the porosity evolution by adding a shear component coupled with forming limit curves for flat sheets. As a consequence, further experimental damage investigations with DP steel have taken place to integrate the porosity shear component in the GTNBF model. Despite the lack of damage information data in shear direction, the applications on tensile tests and cross-die drawing tests have been a promising success. In details, the tensile tests have revealed with all geometries that the strain distribution is homogeneous near the central region of the necking and heterogeneous in the neutral area of the fracture. As a complement of information, Niazi [NIA 2012] noted that the crack initiation has a strong dependency on the martensite orientation. Other comparisons with various notch radius designs underscored an influence on the triaxiality, the void growth and void density. An important step has been reached during the study. Indeed, the crack localization changes with the notch size. The fracture initiates at the bottom edge of the notch (with small radius) and migrates to the center of the necking when increasing the notch radius. In the aim to evaluate the GTNBF model potentialities, comparisons with the GTN model available in the commercial FE code Abaqus-Explicit have been realized. The GTNBF model matched better the experimental force-displacement curves

than the GTN model. As already presented in chapter III, the original Gurson extension integrates a phenomenological damage prediction, with no kinematic hardening law and an approximated void volume fraction evolution. Therefore, the GTN model has failed to give an accurate strain deformation value at the fracture zone.

The second application using cross-die drawing test has been covered with success. Two DP steels have been compared using experiments and simulations. In addition, the GTN and GTNBF model responses have been analyzed. At first the forming test has been better modeled by using the GTNBF model. In fact, the comparison with the experiments has depicted a better force-displacement curve fitting with the current model and the fracture initiation was better predicted than the proposed Abaqus-Explicit model. Finally, the FLC diagram underlines the ranking of the DP steel. The DPI steel is more deformable, and softens very smoothly with a high level of plastic deformation. No crack has been revealed with this material at the end of the cross-die process. On the opposite, the DPIII steel has shown behaviour. The material is less deformable and reaches at higher stress compared to the DPI steel. The cross-die test performed with DPIII steel did not reach the process end, and some cracks have been observed with the experiment or the simulation. The crack localization provided with the GTNBF model has matched with the experiment.

Chapter IX. **Conclusions and Perspectives**

Contents

IX.1 Conclusions

Damage contributions in GTNBF model

The document has been focused on tracing the different mathematical models available to predict the DP steel mechanical behaviour. It can be separated in three parts; plasticity, damage and fracture modeling.
Due to its micromechanical roots and to the explicit use of the void volume fraction as a state variable, the modified GTNB model developed by Ben Bettaieb [BEN 2011] has been chosen in the current research to introduce results from recent experimental X-ray tomography measurements. The new extension of the damage called GTNBF model is physically based on in-situ high resolution X-ray tomography technique (Landron et al.) [LAN 2011].

- The first contribution of this model is a new kinetic law of void nucleation predicting the evolution of the void density N . This model based on Bouaziz and Maire works [BOU 2008] [MAI 2008] integrates the backstress tensor and the triaxiality factor. The question of the form of the triaxiality factor has been investigated by proposing other definitions.
- The second enhancement concerns the improvement of the growth model. The experimental contribution of Landron et al. [LAN 2011a] validates at different triaxiality states the Huang correction in the classical Rice & Tracey model [RIC 1969]. After modifying the classical model, Landron introduced it in the previous Bouaziz's kinetic law used in the GTNBF model. The final evolution of the mean void radius *R* implemented in GTNBF model is defined by the Rice and Tracey model [RIC 1969] modified by Bouaziz [BOU 2008], Maire [MAI 2008], and Huang [HUA 1991] to take into account nucleation and different void sizes.
- The third enhancement is the coalescence stage. The apparition of the coalescence has been precisely observed and quantified by Landron. The modeling of this phenomenon used the original GTN model form for the coalescence but difference appears when determining the value of the critical and the ultimate porosity values. The critical void volume fraction value f_c has been provided by measuring the mean distance between two cavities (λ) provided by Landron [LAN 2012]. In this new approach, the f_c value is accurate and available for different DP steels.

GTNBF model implementation in Abaqus-explicit

The first step was the design of a FORTRAN link called VUMAT which connects the GTNB model (built in Lagamine implicit FE code built by Ben Bettaieb) to Abaqus-Explicit software. Beside this important step, the implementation of GTNBF model has taken place. Within the law integration scheme, the Jacobian matrix $\underline{J}$ and its invert have been computed by taking into account the f^* function of the porosity f . This small modification in term of

quantity has a strong impact on the whole modeling. Indeed, the apparition of f^* has allowed to complete the ductile damage stages by including the physically-based nucleation, growth, and coalescence laws. Of course, the numerical work added the implementation of the new nucleation law from Landron [LAN 2011] and introduced a secondary physical fracture initiation criterion based on the distance between two cavities.

GTNBF model validations

As already predicted by many damage models, GTNBF model confirms that the triaxiality evolves when the notch dimension decreases and the fracture appears sooner when the notch radius is smaller. The responses of the GTNBF model have been validated by using an adapted mesh, designed to ensure an accurate extraction of average values over the same volumes/areas of observation as in the actual experiments. The predicted porosity evolution from Landron et al. [LAN 2011] is well validated up to a strain of 0.5. Furthermore, each of the two ingredients of the porosity evolution. The number of voids and their mean radius are in good agreement with the experimental evolutions, thus confirming the importance of this physically inspired description. For larger strain levels, the apparition of the coalescence weakens the physical meaning of these quantities and of the hypothesis of spherical voids. Consequently, a simple phenomenological description is adopted to describe the phenomenon. In addition to the average values used for the confrontation to experiments, the numerical simulation illustrated the heterogeneity of most variables, e.g., porosity and plastic strain whose maximum values, are located near the center of the specimen. This heterogeneity, which increases during the loading, exhibited little mesh sensitivity prior to the development of coalescence. Finally, a negligible influence of the back stress tensor on the mean stress through diverse simulations (tensile test, simple shear test) has been observed. In the opposite, a strong impact of this tensor variable on the equivalent stress has been noted and quantified. As a consequence, the damage occurs earlier and affects only the end of the stress-strain curve. At the end of the loading, the porosity (f) and the density of voids (N) seem to be the most sensitive variables to the definition of the equivalent stress.
Next to these significant potentialities of the current ductile damage model, some limitations have been noticed. The first constraint concerns the lack of damage evolution in simple shear. Unfortunately, experimental evolutions of the porosity and the density of voids have not been performed during the PhD time framework. Consequently, the GTNBF model contains no contribution about this loading case. The second limitation is centered on the great number of material parameters to enter the model before running the simulation. Indeed, compared to existing GTN model present in Abaqus-Explicit, the user has to introduce and identify 21 material parameters for the GTNBF model when the GTN model only needs 14. The last restriction is the small element size required to accurately analyze the strong heterogeneity of the distribution of the damage variables and the localization of the fracture initiation. Therefore, this constraint imposes to generate refined meshes which induce long time calculation.

Industrial applications

For all geometries, the uniaxial tensile tests have revealed that the strain distribution is homogeneous near the central region of the necking. Other comparisons with various notch radius designs underscored an influence of the triaxiality on the void growth and void density. Indeed, the crack localization changes with the notch size. The fracture initiates at the bottom edge of the notch (with small radius) and migrates to the center of the necking when increasing the notch radius. In the aim to evaluate the GTNBF model potentialities, comparison with the GTN model available in the commercial FE code Abaqus-Explicit has been performed. The GTNBF model results matched better the experimental curves than the GTN ones. The second application, the simulation of the cross-die drawing test has been covered with success. Two DP steels have been compared using the experiments and the simulations. In addition, the GTN and GTNBF models responses have been analyzed. The forming test has been better modeled by using the GTNBF model. In fact, the comparison with the experiments has depicted a better curves fitting with the current model and the fracture initiation was better predicted than the proposed Abaqus-Explicit model. Finally, the FLC diagram underlines the ranking of the DP steels. The DPI steel is more deformable, and softens very smoothly with a high level of plastic deformation. No crack happened with this material at the end of the cross-die process. On the contrary, the DPIII steel has shown a crack event. The material is less deformable and evolves at higher stress compared to the DPI steel. The cross-die test launched with DPIII steel did not reach the end the process, and some cracks have been observed both with the experiment and the simulation. The crack localization provided with the GTNBF model has matched the experiment.

In summary, the physically based ductile damage model incorporates with success the effect of the kinematic hardening on nucleation, along with an improved evolution of the mean radius of the voids, inferred from X-ray diffraction tomography observations in dual-phase steels. The model is extended to include the coalescence stage coupled with a fracture criterion thanks to recent observations of fracture strains and microstructure of void populations in DP steels. The model has been validated with good agreement in tensile direction loading on various sample geometries in flat sheet steels as well as industrial application such as cross-die drawing process.

IX.2 Perspectives

Unfortunately, limited by the PhD time framework, some improvements have not been taken into account to completely fulfill the industrial needs. During the present study it has been questions of void shape influence. The model assumes that the voids are and remain spherical during the growth stage. This assumption is true at low triaxiality factor but void growth observations at higher stress triaxiality [LAN 2011] [WEC 2008] have revealed that the voids are elongated, flattened or elliptic and look like needle when the fracture occurred. The stress triaxiality influence on ductile damage studied by McClintock [MCC 1968], Marini et al. [MAR 1985], Pardoen and Delannay [PAR 1998]... shows that an increasing triaxiality induces a significant increase of the void growth rate. The GTNBF model can be modified with a yield function taking into account the void shape effect by using the Gologanu, Leblond and Devaux model (GLD model) [GOL 1993]. Another possibility is to keep the GTNBF model assumption until the beginning of the coalescence stage. At this point, the GTN coalescence model based on critical porosity and acceleration factor can be replaced by a Thomason [THO 1990] or Pardoen [PAR 1998] coalescence models taking into account the void shape during the tensile plastic localization in the intervoid ligaments.

The constitutive equations of the GTNBF model have pointed out that the porosity rate contribution is not well reflected during the simple shear test validation. It is well known that the GTN model does not describe the damage evolution in pure shear loading. However, quantitative data and observations [CRO 2002] for instance underlined that tangential residual stress appears at the interface of inclusion introducing local decohesion (ferrite/martensite). A further numerical work is to include the porosity shear rate $\dot{f}_s$ by modifying the GTNBF nucleation law [CRO 2002] or using the Lode angle parameter [LOD 1926] (see section IX.2.2). However, these extensions require accurate damage parameters obtained by a simple mechanical shear test or coupled with X-ray tomography measurement to count the number of cavities developed during the experiment.

The current damage model predicts well the tensile loading. Literature review on sheet-forming process has shown that a springback effect occurs when the flat sheet is removed from the tools. However, current kinematic hardening in GTNBF model was not optimized for springback prediction. A solution to accurately model the springback is to improve the hardening model by adding two backstress tensors (see section IX.2.1).
The damage parameters from GTNBF model have been identified with respect to direct porosity measurements obtained by X-ray diffraction tomography located inside a studied spatial volume at the center of the specimen, of dimensions 0.3 x 0.3 x 0.3 mm³. Landron [LAN 2011] underlines that the damage parameters are sensitive to the tomography resolution. During the measurement, Landron has kept constant this spatial volume during the specimen axial deformation to facilitate the void counting. However, a question is still pending. Do these damage parameters remain constant if the spatial volume moves during the tensile test?

The following section presents with details two various research works started to enlarge the GTNBF model. Those future contributions are based on knowledge gained during this current research. The plasticity behaviour with two backstress tensor has been initiated by ArcelorMittal research while the shear damage contribution has been launched in University of Liège by Guzman et al. [GUZ 2013].

IX.2.1 Improvement of the hardening model

In a recent experimental study Lemoine et al. [LEM 2011] suggested that a perfect agreement on stress-strain curve for cyclic tests on DPIII steel can be reached when using two backstress tensors as shown in Figure IX.1. The flow curves from the experimental test have been compared with a hardening model of Lemaitre-Chaboche [LEM 1992] comparable to Amstrong-Frederick model. In the graph LC 1*X* means the results of Lemaitre-Chaboche with one backstress and LC 2*X* the same law but with two backstress.

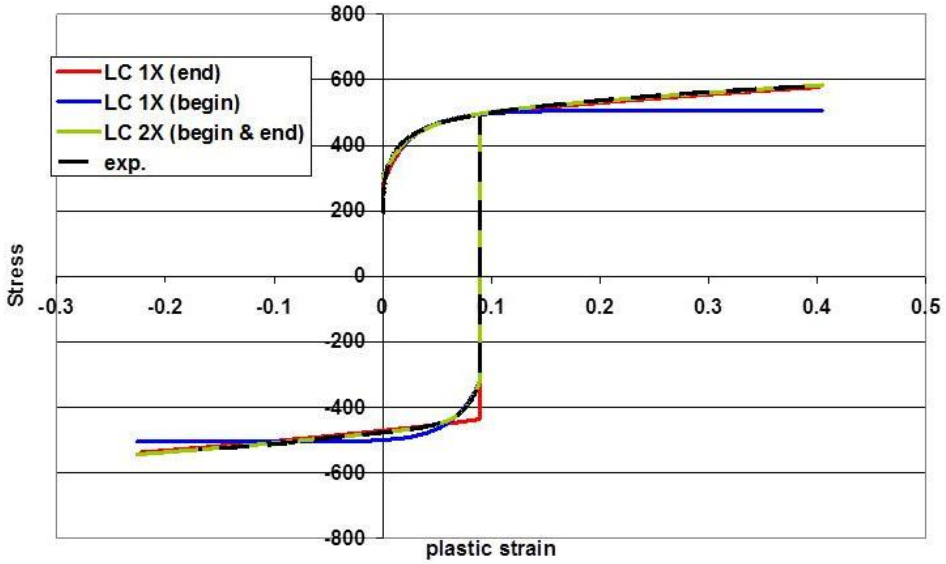

Figure IX.1: For a DPIII, to represent correctly the reverse path, the Lemaitre-Chaboche model (LC) needs two back stress tensors (*X*) [LEM 2011].

The practical path will be to modify the kinematic hardening law (Armstrong-Frederick) [ARM 1966] from one backstress tensor to two backstress tensors for the GTNBF model.
The kinematic hardening law can take the following form:

$$\begin{aligned} \underline{X} &= \left(1-q_1 f^*\right)\left(\underline{X_1}^* + \underline{X_2}^*\right) \\ \underline{\dot{X}_1}^* &= C_{1x}\left(S_{1sat}\,\underline{\dot{\varepsilon}}^p - \underline{X_1}^*\,\varepsilon_{eqv}^p\right) \\ \underline{\dot{X}_2}^* &= C_{2x}\left(S_{2sat}\,\underline{\dot{\varepsilon}}^p - \underline{X_2}^*\,\varepsilon_{eqv}^p\right) \end{aligned} \qquad \text{(IX.1)}$$

Where C_{1x}, C_{2x} and S_{1sat}, S_{2sat} are material parameters and ε^{p}_{eqv} is the equivalent plastic strain.
The implementation of this modified hardening law has to be made with special care. Indeed, the components and the derivatives involved in the computation of the Jacobian matrix (*J*) have to be recalculated with the modified kinematic hardening law described above. This part of the work will cost time to verify each derivative in the FORTRAN program before launching a finite element simulation.

IX.2.2 Improvement of the porosity evolution for vanishing triaxiality

Porosity shear contribution through Lode Angle.

The GTNBF model has shown good enhancement relative to the damage contributions. However, a major drawback has been identified. The numerical investigation of the present ductile damage prediction has underlined that the model does not behave well under shear dominated mechanisms. The main reasons are;

- The porosity evolution does not include the damage due to shear.
- The shape of the void remains spherical along the loading when they rotates and flatters in shear.
- The void nucleation model has been only validated for tensile state.

Many contributors have given some solutions to overcome this inconveniency by modifying the original Gurson model [GUR 1977]. The most used Gurson shear extensions were proposed by Xue [XUE 2008], Nahshon and Hutchinson [NAH 2008] and Nielsen and Tvergaard [NIE 2010]. The researchers introduced the damage shear mechanisms through the cavities law evolution written as:

$$\dot{f} = \dot{f}_g + \dot{f}_n + \dot{f}_s \tag{IX.2}$$

$\dot{f}_g, \dot{f}_n, \dot{f}_s$ are respectively, the porosity evolution due to growth, nucleation and shear.

Since a decade, $\dot{f}_s$ has been introduced thanks to the Lode angle parameter [LOD 1926]. It has been proven that this parameter is an interesting mean to characterize on the strain paths and the porosity evolution [ZHA 2001].

The porosity due to shear contribution introduced by Xue [XUE 2008] is expressed by:

$$\dot{f}_s = q_4 f^{q_5} g_0 \tag{IX.3}$$

Where q_4 and q_5 are material parameters. f is the porosity, $\underline{\dot{\varepsilon}}^{p}$ is the macroscopic plastic strain rate, and g_0 is a function introducing the shear contribution through the Lode angle parameter. If g_0 is equal to 0, only the nucleation and the growth contribution are considered.

The function g_0 is defined by:

$$g_0 = 1 - \frac{6|\theta|}{\pi} = 1 - \frac{2}{\pi}\arccos\xi \tag{IX.4}$$

θ is the Lode angle and ξ is the third invariant.

$$\xi = \frac{27 j_3}{2q^3} \quad ; \; j_3 = \det(s) \text{ is the third invariant}$$
$$\theta = \tan^{-1}\left[\frac{1}{\sqrt{3}}\left[2\left(\frac{s_2 - s_3}{s_1 - s_3}\right) - 1\right]\right] \quad s \text{ is the deviatoric stress tensor} \tag{IX.5}$$

The porosity due to shear contribution introduced by Nahshon and Hutchinson [NAH 2008] is expressed by:

$$\dot{f}_s = k_w \frac{f w_0(\sigma)}{q} s : \underline{\dot{\varepsilon}}^p \tag{IX.6}$$

Where $w_0(\sigma)$ is a function linking ξ and k_w. k_w is a material parameter characterizing the shear damage intensity.

$$w_0(\sigma) = w(\xi) = 1 - \xi^2 \tag{IX.7}$$

The porosity due to shear contribution introduced by Nielsen and Tvergaard [NIE 2010] is the same expression as above but the function $w_0(\sigma)$ is modified to make the shear contribution adapted for wear or strong triaxiality.

$$w_0(\sigma) = w(\xi)\Omega(T) \quad \text{with} \quad \Omega(T) = \begin{cases} 1 & T < T_1 \\ \dfrac{T - T_1}{T_1 - T_2} & T_1 \le T \le T_2 \\ 0 & T > T_2 \end{cases} \tag{IX.8}$$

Where Ω depends on triaxiality factor (T).

The first work of Guzman started in 2012 and still in progress [GUZ 2013] has been to choose and experimentally test different Lode angle definitions before integrating one of the previously presented porosity shear modeling into the GTNBF model.

Porosity shear contribution through void nucleation.

Another approach to take into account the porosity shear rate $\dot{f}_s$ from Equation (IX.2) is to modify the GTN nucleation law from Chu & Needleman [CHU 1980] by introducing the volume fraction of porosity created by decohesion of second phase particles [CRO 2002]. $\dot{f}_s$ depends on tangential plastic deformation $\dot{\bar{\varepsilon}}^p_{eqv}$ reached inside the material.

$$\dot{f}_s = \frac{f_s}{s_s\sqrt{2\pi}} \exp\left[-0.5*\left(\frac{\bar{\varepsilon}^p_{eqv} - \varepsilon_s}{s_s} \right)^2 \right] \dot{\bar{\varepsilon}}^p_{eqv} \qquad \text{(IX.9)}$$

Where

f_s : Potential nucleated microvoid void fraction in relation, for instance, with the inclusion volume fraction.

ε_s : Mean effective plastic strain of the matrix at maximum local decohesion

S_s : Gaussian standard deviation of the normal distribution of inclusions.

$\bar{\varepsilon}^p_{eqv}$: Equivalent effective plastic strain in the matrix.

$\dot{\bar{\varepsilon}}^p_{eqv}$: Rate of equivalent effective plastic strain in the matrix.

This phenomenological approach introduces the void nucleation evolution for shear state direction but the void growth evolution $\dot{f}_g$ is kept at zero at pure shear due to the trace of the plastic strain rate $\dot{\underline{\varepsilon}}^p$ (see equation below).

$$\dot{f}_g = (1-f)\,tr\left(\dot{\underline{\varepsilon}}^p\right) \qquad \text{(IX.10)}$$

Appendix

Contents

Appendix (A) Extensions to GTN model

(A).1 Hardening functions

Reference	hardening	relation	Notice
Leblond et al. [LEB 1995]	isotropic	$F_p = \frac{\sigma_{eq}^2}{\Sigma_1^{\,2}} + 2qf\,\cosh\left(\frac{3\sigma_m}{2\Sigma_2}\right) - 1 - qf^2 = 0$	The hardening is considered by the introduction of Σ_1 and Σ_2 Yield stress
Pardoen et al. [PAR 2006]	isotropic	$F_p = \frac{C}{\sigma_y^{\,2}}\left\|\underline{\sigma}_d + \eta\sigma_h^g\,\underline{X}\right\|^2 + 2q(g+1)(g+f)$ $\cosh\left(\kappa\frac{\sigma_h^g}{\sigma_y}\right) - (g+1)^2 - q^2(g+f)^2 = 0$	The GLD model is extended heuristically to hardening by considering the dependence of q on the hardening coefficient n
	kinematic	$F_p = \frac{\left\|\underline{\sigma}_d - \underline{\alpha}_d\right\|^2}{\sigma_Y^{\,2}} + 2f\,\cosh\left(\frac{1}{2}\frac{(\sigma_{kk} - a_{kk})}{\sigma_y}\right) - 1 - (q_1 f)^2$	The equivalent stress takes into account the backstress $\underline{\alpha}$
	mixed	$F_p = \frac{\left\|\underline{\sigma}_d - \underline{\alpha}_d\right\|^2}{\sigma_F^{\,2}} + 2f\,\cosh\left(\frac{q_2}{2}\frac{tr(\underline{\sigma} - \underline{\alpha})}{\sigma_F}\right) - 1 - (q_1 f)^2$ $\sigma_F = (\rho\sigma_0 + (1-\rho)\Sigma_M)$	The yield stress takes into account the initial yield stress σ_0 and the stress issue form the isotropic hardening Σ_M
Brunet et al. [BRU 2005]	kinematic	$F_p = C\frac{\sigma_{eq}^{\,2}}{\sigma_Y^{\,2}} + 2q_1 f\,\cosh\left(\kappa\frac{\sigma_H}{\sigma_Y}\right) - (1 + q_3 f^2) = 0$	The kinematic hardening is considered in the expression of σ_{eq} and of σ_H
Ragab et al. [RAG 2002]	kinematic	$\frac{(\underline{\sigma}_d - \underline{\alpha}_d) : \underline{\underline{H}} : (\underline{\sigma}_d - \underline{\alpha}_d)}{\sigma_0^{\,2}} + 2qf\,\cosh\left(\frac{tr(\underline{\sigma} - \underline{\alpha})}{2\sigma_0}\right) - (1 + q^2 f^2) = 0$	The kinematic hardening is coupled with Hill yield function

(A).2 Plastic anisotropy

Reference	Plastic criterion	Relation
Ragab et al. [RAG 2002]	Hill 48	$F_p = (\frac{\underline{\sigma}_{eqa}}{\sigma_Y})^2 + 2qf\cosh\left(\frac{tr\underline{\sigma}}{2\sigma_Y}\right) - (1+q^2f^2) = 0 \quad ; \quad \underline{\sigma}_{eqa} = \left\{\frac{1}{2(1+\bar{r})}\left[\left\|2\sigma_3 - \sigma_1 - \sigma_2\right\|^m + (1+2\bar{r})\left\|\sigma_1 - \sigma_2\right\|^m\right]\right\}^{1/m}$
Brunet et al. [BRU 2001]	Hill	$F_p = C\frac{\sigma_{eq}^{\ 2}}{\sigma_Y^{\ 2}} + 2q_1 f\cosh\left(\kappa\frac{\sigma_H}{\sigma_Y}\right) - (1+q_3f^2) = 0$ $\sigma_{eq}^{\ 2} = (\underline{\sigma}_d - \underline{\alpha}_d) : \underline{\underline{M}} : (\underline{\sigma}_d - \underline{\alpha}_d) \quad ; \quad \sigma_H = (1-2\alpha_2)(\sigma_{xx} - \alpha_{xx}) + \alpha_1(\sigma_{yy} - \alpha_{yy})$
Benzerga et al. [BEN 2001]	Hill	$F_p = \frac{\sigma_{eqa}^2}{\sigma_Y^2} + 2q_1 f\cosh\left(\theta\frac{q_2\sigma_m}{\sigma_Y}\right) - 1 - q_3f^2 = 0 \quad ; \quad \sigma_{eqa} = \sqrt{\underline{\sigma}_d : \underline{\underline{H}} : \underline{\sigma}_d}$ $\theta = \frac{\sqrt{3}}{2\,h_m} \quad ; \quad h_m = \left[\frac{1}{4}\frac{h_1+h_2+4h_3}{h_1h_2+h_2h_3+h_1h_3} + \frac{1}{2h_6}\right]$
Ragab & Saleh [RAG 2002]	Hill	$F_p = (\frac{\underline{\sigma}_{eqa}}{\sigma_Y})^2 + 2qf\cosh\left(\frac{tr\underline{\sigma}}{2\sigma_Y}\right) - (1+q^2f^2) = 0 \quad ; \quad \underline{\sigma}_{eqa} = \frac{1}{1+\bar{r}}\left[\bar{r}\left(\sigma_1-\sigma_2\right)^2 + \left(\sigma_2-\sigma_3\right)^2 + \left(\sigma_1-\sigma_3\right)^2\right]$
Monchiet et al. [MON 2006]	Hill	$F_p = \left(\frac{\sigma_{eqa}}{\sigma_0}\right)^2 + 2q(g+1)(g+f)\cosh\left(\kappa\frac{\sigma_h^*}{p\sigma_0}\right) - (g+1)^2 - (g+f)^2 = 0$ $\sigma_{eqa} = F(\sigma_{11}-\sigma_{22})^2 + G(\sigma_{22}-\sigma_{33})^2 + H(\sigma_{11}-\sigma_{33})^2 + 2L\sigma_{23}^2 + 2M\sigma_{13}^2 + 2N\sigma_{12}^2$
Son & Kim [SON 2003]	Barlat & Lian	$F_p = \left(\frac{\sigma_{eqa}}{\sigma_Y}\right)^2 + 2qf\cosh\left(\kappa\frac{\sigma_m}{\sigma_Y}\right) - (1+q^2f^2) = 0 \quad ; \quad \sigma_{eqa} = \left[\frac{2-c}{2}\left\{\left\|k_1+k_2\right\|^M + \left\|k_1-k_2\right\|^M + \frac{c}{2-c}\left\|2k_2\right\|^M\right\}\right]^{1/M}$

(A).3 Visco-plasticity

Reference	Visco-plastic	Relation
Klöker & Tvergaard [KLO 2003]	potential for spherical voids	$\sigma_Y = \sigma_0 \left(1+\frac{E}{\sigma_0}\varepsilon^p\right)^n \left(1+\frac{\dot{\varepsilon}^p}{\dot{\varepsilon}_0}\right)^{1/m}$ $F_p = C\left(\frac{\sigma_{eq}+\eta\sigma_m}{\sigma_Y}\right)^2 + 2q_1 f\ p_m\left(q_2\kappa\frac{\sigma_m}{\sigma_Y}\right) - \left[q_1\left(g+\frac{(1-m)}{(1+m)}f\right)\right]^2 = 0$ $p_m(x) = h_m(x) + \frac{(1-m)}{(1+m)}\frac{1}{h_m(x)} \quad ; \quad h_m(x) = \left[1+mx^{(1+m)}\right]^{1/m}$

(A).4 Void nucleation

Reference	Void nucleation	Relation
Helbert et al. [HEL 1998]	α/β titanium alloys	$dN_a / N_a = D\, d\varepsilon_{eq}^{p}$ Where D is a function of the triaxiality factor. In α/β titanium alloys, $D = E\exp(FT)$ seems to be well adapted to describe experimental results. account for the change in N_a with $(\varepsilon_{eq}^{p} - \varepsilon_{eq}^{pa})$, the following relationship is obtained: $N = N_0 \exp\left[D(\varepsilon_{eq}^{p} - \varepsilon_{eq}^{pcr}) \right]$ N_0 corresponds to the nucleation of voids in the analyzed surface element (0.5x0.5 mm^2) when ε_{eq}^{p} reaches ε_{eq}^{pcr}. N_0 is experimentally identified and remains constant and equals to *4* voids/mm^2. The parameters E and F are defined in a table for the different titanium alloys
Bouaziz et al. [BOU 2008] and Ben Bettaieb et al [BEN 2012]	for the case of dual-phase steels	This new law is empirically identified in the basis of some experimental results (tensile tests) and allows to connect the void density N (expressed in mm^{-3}) in term of the ratio $\varepsilon_{eq}/\varepsilon_N$ $N = A\frac{\varepsilon_{eq}}{\varepsilon_N}\exp\left(\frac{\varepsilon_{eq}}{\varepsilon_N}\right)$ Where A is a constant equal to *5000* mm^{-3} and ε_N a critical deformation representative of the nucleation phase. The same authors have clearly demonstrated that ε_N depends on the triaxiality factor by the following relation: $\varepsilon_N = \varepsilon_{N0}\exp(-T)$ Where ε_{N0} is the critical deformation at nucleation in the case of pure shearing (taken equal to 0.8). Growth: $\frac{dR}{d\varepsilon_{eq}} = 0.283\exp\left(\frac{3}{2}\frac{\sigma_m}{\sigma_{eq}}\right)R - \frac{1}{N}\frac{dN}{d\varepsilon_{eq}}(R - R_0)$

Landron et al. [LAN 2011] and Fansi et al. [FAN 2013]	dual-phase steels	Strong dependency between the density of voids, the backstress, and the triaxiality: $\frac{dN}{d\varepsilon^p_{eqv}} = \frac{B\,\bar{\sigma}(\sigma)}{\sigma_c}\left(1+T\frac{\bar{\sigma}(\sigma)}{\bar{\sigma}(\sigma)-X}\right)\frac{N}{N_0}$

(A).5 Void growth

Reference	Void growth	Relation
Ragab [RAG 2002]	effect of matrix hardening	$\frac{df_g}{d\varepsilon_1} = \frac{3f(1-f)q_1q_2\sinh\beta}{3\left(\frac{\sigma_1-\sigma_m}{\sigma_Y}\right)+fq_1q_2\sinh\beta}$ Where ε_1 and σ_1 are respectively the major principal strain and stress. β is equal to $3q_2\sigma_m/2\sigma_{eq}$.
Parteder et al. [PAR 2002]	for uniaxial compression	$\frac{df_g}{d\varepsilon} = \frac{3f(1-f)q_2^2}{4+q_1q_2^2\,f}$ Where ε is the component of the plastic strain along the compressive axis.
Zhang et al. [ZHA 2001]	influence of the Lode parameter μ_σ on the void growth law	The Lode parameter μ_σ is defined by the following relation: $\mu_\sigma = \frac{2\sigma_2-\sigma_1-\sigma_3}{\sigma_1-\sigma_3}$

(A).6 Void coalescence

Reference	Void coalescence	Relation
Brown & Embury [BRO 1973]	necking of the ligament	The updated distance between the centers of neighboring voids is deduced from the local strain ε_1 and the initial intervoid length l_{c0} : $l_c = l_{c0}\exp(\varepsilon_1)$ $l_c = 2\sqrt{R_1^2 + R_3^2}$
Thomason criterion [THO 1990]	non-hardening rigid plastic solid, which contains a regular three-dimensional distribution of spherical microvoids	$\frac{3}{2}(1-\chi^2)\left[\alpha\left(\frac{1-\chi}{\chi\exp(S)}\right)^2 + \beta\sqrt{\frac{1}{\chi}}\right] = \frac{\sigma_{\max\ princ}}{\sigma_Y}$ Where $\sigma_{\max\ princ}$ is the value of maximal principal stress, χ is relative void spacing (void diameter divided by void spacing) and S is the void aspect ratio. In the initial version of the Thomason model, parameters α and β are equal respectively to *0.1* and *1.2*.
Pardoen & Hutchinson [PAR 2000]	full coalescence and hardening case	$F_{coalescence} = \frac{\|\underline{\sigma}_d\|}{\sigma_Y} + \frac{3}{2}\frac{\|\sigma_m\|}{\sigma_Y} - \frac{3}{2}(1-\chi^2)\left[\alpha\left(\frac{1-\chi}{\chi W}\right)^2 + \beta\sqrt{\frac{1}{\chi}}\right] = 0$ Where W denotes the void shape factor, α and β are two material parameters.

(A).7 Shear failure

Reference	Shear failure	Relation
K. Nahshon, J.W. Hutchinson [NAH 2007]	incorporates damage growth under low triaxiality straining for shear-dominated states (for Aluminum)	$\dot{f} = (1-f)\varepsilon_{kk}^{p} + k_{\omega} f \omega(\sigma) \frac{s_{ij}\varepsilon_{ij}^{p}}{\sigma_e}$ $\omega(\sigma) = 1 - \left(\frac{27 j_3}{2\sigma_e^3} \right)^2$ The numerical constant, k_{ω}, sets the magnitude of the damage growth rate in pure shear states
[Xue 2007]	for simple shear and for small void volume fractions	For the 3D case damage D_{rot} is written $D_{rot} = \frac{3}{2}\left(\frac{6}{\pi}\right)^{(1/3)} f^{(1/3)} \varepsilon_{eqv}^2$ The incremental void shear damage: $dD_{rot} = q_3 f^{q_4} \varepsilon_{eqv} d\varepsilon_{eqv}$ where q3= 3.39 and q4= 1/2 for 2D or q3= 3.72 and q4= 1/3 for 3D

(A).8 Evolution of a cavity around an inclusion

(A).8.1 Tensile test of a HSLA sample

Evolution of the necking area during the in-situ tensile test: a) just before the necking, b) at the necking start, c) just before fracture, d) after fracture [ACH 2012].

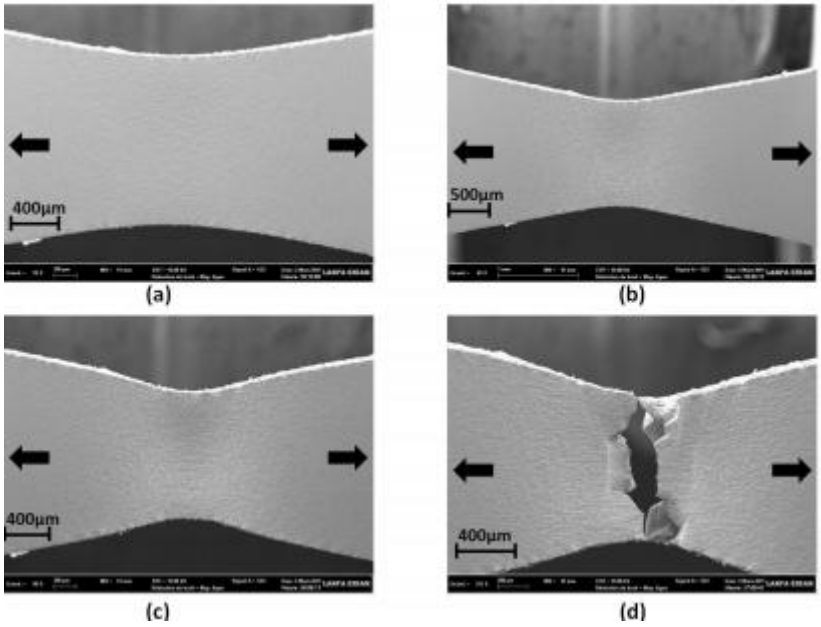

Force-displacement curve during the in-situ tensile test of a HSLA sample.

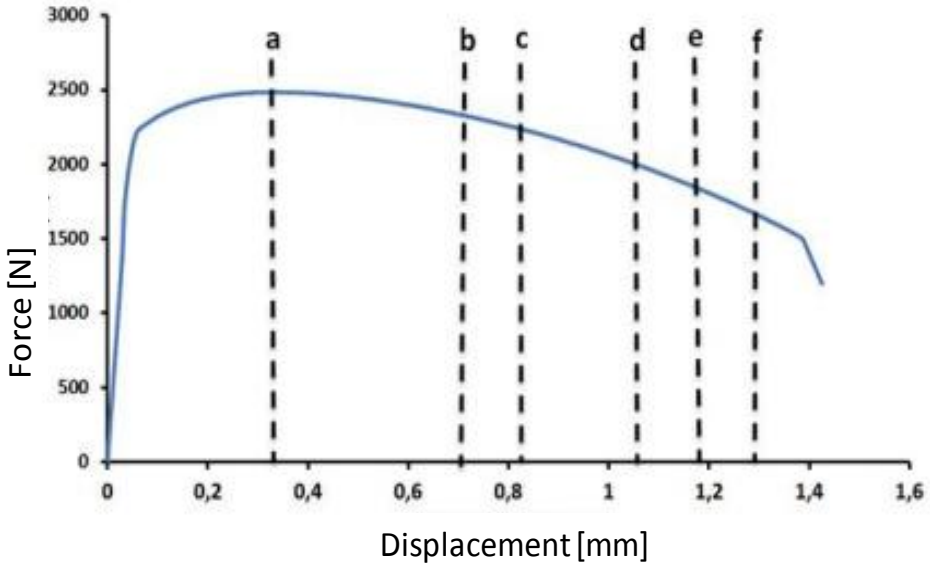

Cavity evolution around a MgO-Al2O3 particle corresponding to the force-displacement curve (above).

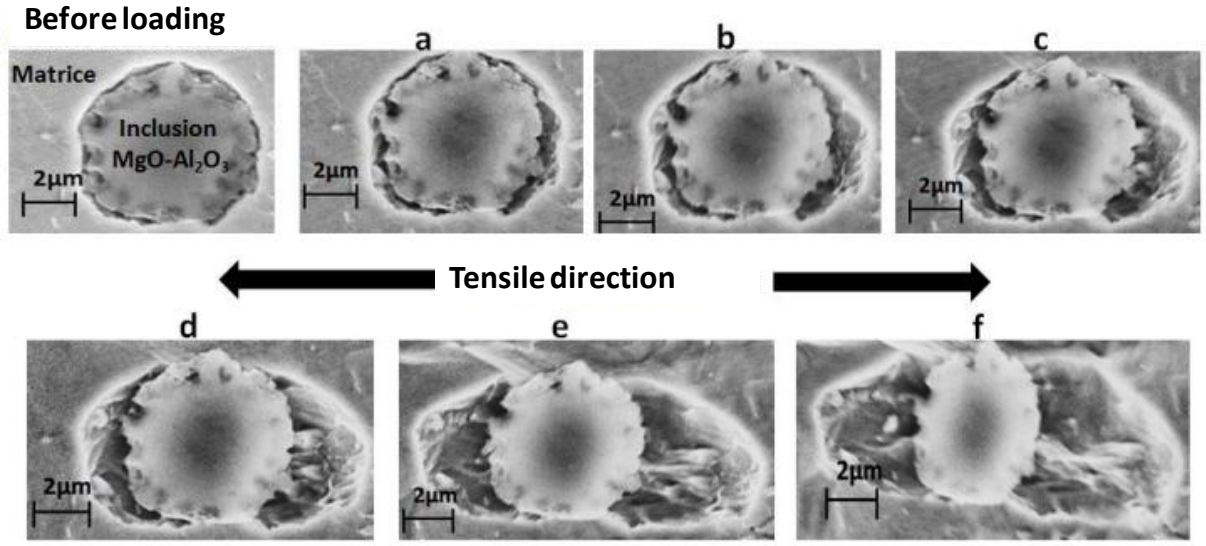

Schematic of the ductile damage mechanisms in tensile test.

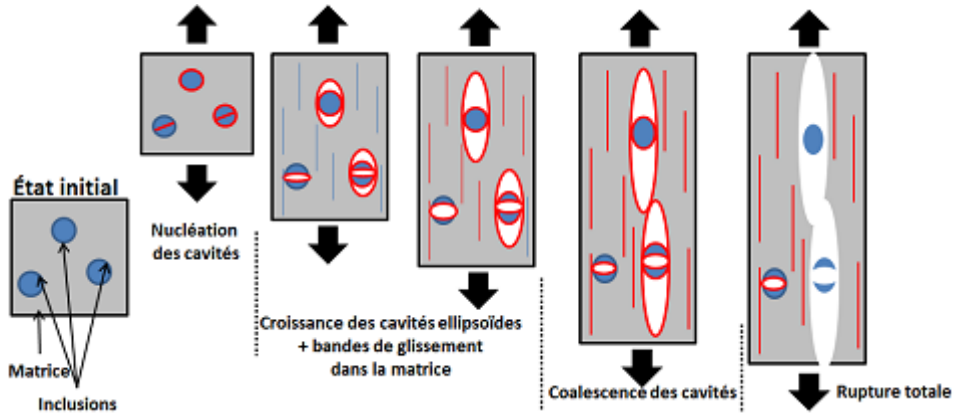

(A).8.2 Shear test of a HSLA sample

Evolution of a micro-crack during the in-situ shear test: a) shear area, b) micro-crack initiation c) after fracture [ACH 2012].

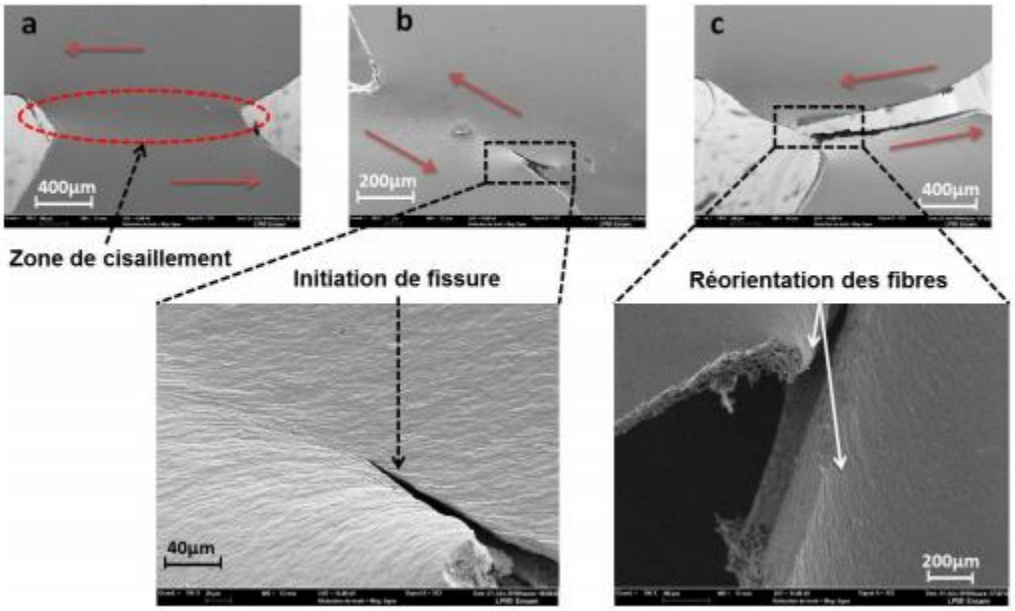

Evolution of the nucleation and coalescence mechanisms during an in-situ shear test: a) Location of the studied inclusion, b) Decohesion mechanism in (line 1), c) Decohesion mechanism and Fracture of the inclusion in (line 1), d) Fragmentation mechanism in (line 2).

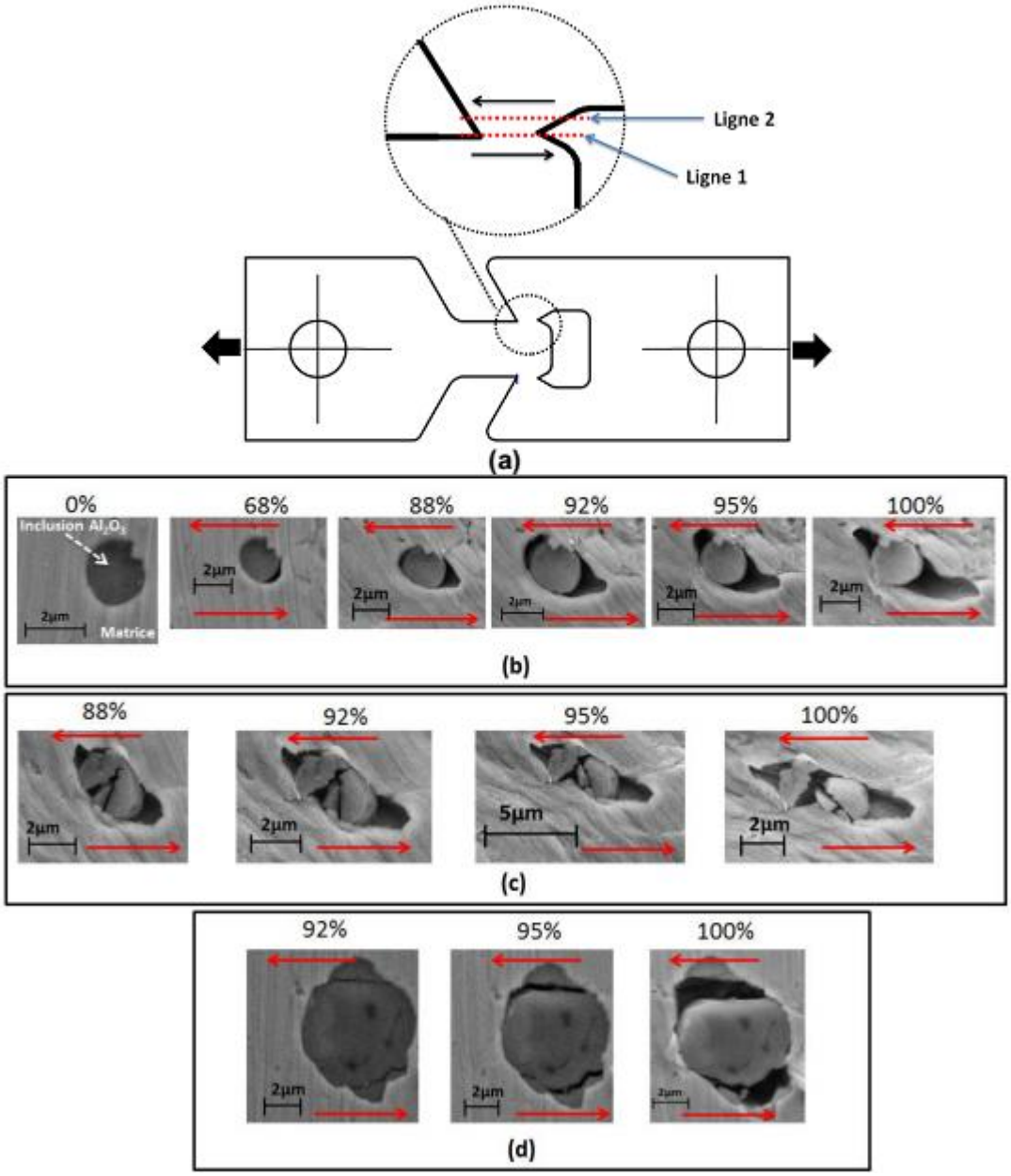

Schematic of the ductile damage mechanisms during shear test.

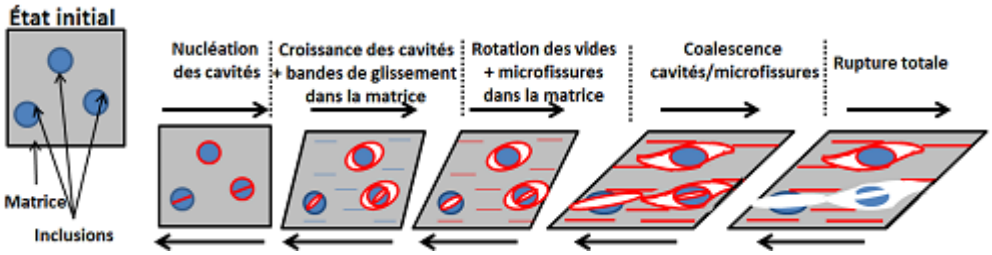

Appendix (B) Calculations of anisotropy data and Jacobian

(B).1 Hill and Pseudo invert Hill matrix

HILL MATRIX ($\underline{\underline{H}}$)

$$\underline{\underline{H}} = \begin{bmatrix} G+H & -H & -G & 0 & 0 & 0 \\ -H & H+F & -F & 0 & 0 & 0 \\ -G & -F & F+G & 0 & 0 & 0 \\ 0 & 0 & 0 & 2N & 0 & 0 \\ 0 & 0 & 0 & 0 & 2L & 0 \\ 0 & 0 & 0 & 0 & 0 & 2M \end{bmatrix}$$

$$F = \frac{2r_0}{r_{90}\left(1+r_0\right)};\ G = \frac{2}{\left(1+r_0\right)};\ H = \frac{2r_0}{\left(1+r_0\right)};\ L = M = N = \left(F+G\right)\left(r_{45}+0.5\right)$$

PSEUDO INVERT HILL MATRIX

$$\underline{\underline{H}}^{-1} = \begin{bmatrix} [B_{11}] & 0 \\ 0 & [B_{22}] \end{bmatrix}\ ;\ [B_{22}] = \begin{bmatrix} 2/N & 0 & 0 \\ 0 & 2/L & 0 \\ 0 & 0 & 2/M \end{bmatrix}$$

$$[B_{11}] = \frac{1}{9(HG+HF+GF)} \begin{bmatrix} H+G+4F & H-2F-2G & G-2H-2F \\ H-2F-2G & H+4G+F & F-2H-2G \\ G-2H-2F & F-2H-2G & F+G+4H \end{bmatrix}$$

(B).2 Calculation of coefficient κ

The coefficient κ introduced into the cosh of the yield function [BEN 2001].

$$\kappa = \sqrt{\left(1.6\left(\frac{h_1+h_2+h_3}{h_1h_2+h_2h_3+h_1h_3}\right)+0.8\left(\frac{1}{h_4}+\frac{1}{h_5}+\frac{1}{h_6}\right)\right)}$$

$$h_1 = -\frac{2}{3}\left(\frac{r_0\, r_{90}-2\,r_0-2}{1+r_0}\right) \quad ; \quad h_2 = h_1\left(1-\frac{3(r_0\, r_{90}-1)}{r_0\, r_{90}-2\,r_0-2}\right)$$

$$h_3 = h_1\left(1-\frac{3r_0\,(r_{90}-1)}{r_0\, r_{90}-2\,r_{90}-2}\right) \quad ; \quad h_4 = h_1\left(-0.5\left(\frac{3(r_{90}+1)}{r_0\, r_{90}-2\,r_{90}-2}\right)\right)$$

$$h_5 = h_1\left(-0.5\left(\frac{3r_0\,(r_{90}+1)}{r_0\, r_{90}-2\,r_0-2}\right)\right) \quad ; \quad h_6 = h_1\left(-0.5\left(\frac{(2r_{45}+1)(r_{90}+1)}{r_0\, r_{90}-2\,r_0-2}\right)\right)$$

(B).3 Jacobian matrix and derivates for the modified GTNBF model

The components involved in the computation of the Jacobian matrix $\underline{\underline{J}}$ (modifications in red color). Same Jacobian matrix and derivates as Ben Bettaieb [BEN 2011]

$$J_{1i} = \frac{\partial \Gamma_1}{\partial Y_i} = \frac{\partial F_p}{\partial Y_i} = \frac{\partial F_p}{\partial \tilde{p}}\frac{\partial \tilde{p}}{\partial Y_i} + \frac{\partial F_p}{\partial \tilde{q}}\frac{\partial \tilde{q}}{\partial Y_i}$$

$$J_{2i} = \frac{\partial \Gamma_2}{\partial Y_i} = \left(\frac{\partial F_p}{\partial \tilde{q}}\right)\frac{\partial \Delta\varepsilon_p}{\partial Y_i} + \Delta\varepsilon_p\left(\frac{\partial^2 F_p}{\partial \tilde{p}\partial \tilde{q}}\frac{\partial \tilde{p}}{\partial Y_i} + \frac{\partial^2 F_p}{\partial \tilde{q}^2}\frac{\partial \tilde{q}}{\partial Y_i}\right)$$

$$+\left(\frac{\partial F_p}{\partial \tilde{p}}\right)\frac{\partial \Delta\varepsilon_p}{\partial Y_i} + \Delta\varepsilon_p\left(\frac{\partial^2 F_p}{\partial \tilde{p}^2}\frac{\partial \tilde{p}}{\partial Y_i} + \frac{\partial^2 F_p}{\partial \tilde{p}\partial \tilde{q}}\frac{\partial \tilde{q}}{\partial Y_i}\right)$$

$$J_{R1(j)i} = \frac{\partial \Gamma_{R1(j)}}{\partial Y_i} = \frac{\partial n_j}{\partial Y_i} - \frac{\partial\left(\frac{\left(\underline{\underline{H}} : \underline{\tilde{\sigma}}\right)_{R2(j)}}{2q}\right)}{\partial Y_i} \; ; \; j = 1,\cdots,5 \; ; \; R1 = \{3,4,5,6,7\} \; ; \; R2 = \{11,22,12,13,23\}$$

$$J_{8i} = \frac{\partial \Gamma_8}{\partial Y_i} = \frac{\partial\left(\left(1-f^*\right)\Delta\varepsilon_m^p\sigma_Y + \tilde{p}\Delta\varepsilon_p - \tilde{q}\Delta\varepsilon_p\right)}{\partial Y_i}$$

$$J_{91} = \frac{\partial \Gamma_9}{\partial Y_1} = \frac{f^*_t - 1}{\left(1+\Delta\varepsilon_p\right)^2}; J_{9j} = \frac{\partial \Gamma_9}{\partial Y_j} = 0 \ \ (j = 2,\cdots,8); J_{99} = 1$$

The partial derivatives (modifications in red color) required in the previous equations are:

$$\frac{\partial F_p}{\partial \tilde{p}} = \frac{-6 f^* q_1 q_2 \sinh\left(-\frac{q_2\tilde{p}}{\kappa\sigma_Y}\right)}{\kappa\sigma_Y}; \frac{\partial^2 F_p}{\partial \tilde{p}^2} = \frac{18 f^* q_1 q_2^2 \cosh\left(-\frac{q_2\tilde{p}}{\kappa\sigma_Y}\right)}{\kappa^2\sigma_Y^2}$$

$$\frac{\partial F_p}{\partial \tilde{q}} = \frac{2q_2}{\sigma_Y^2}; \frac{\partial^2 F_p}{\partial \tilde{q}^2} = \frac{2}{\sigma_Y^2}; \frac{\partial^2 F_p}{\partial \tilde{p}\partial \tilde{q}} = 0$$

- The derivatives (modifications in red color) required to compute the consistent tangent matrix are:

$$\frac{\partial F_p}{\partial \sigma_{ij}} = \frac{H_{ijkl}\tilde{\sigma}_{kl}}{\sigma_Y^2} + 2q_1 f^* \frac{\partial \alpha}{\partial \sigma_{ij}}\sinh(\alpha)$$

$$\frac{\partial F_p}{\partial \Delta\varepsilon_{ij}^p} = \left(-\frac{H_{mnkl}\tilde{\sigma}_{kl}}{\sigma_Y^2} + 2q_1 f^* \frac{\partial \alpha}{\partial X_{mn}}\sinh(\alpha)\right)\frac{\partial X_{mn}}{\partial \Delta\varepsilon_{ij}^p}$$

$$\frac{\partial F_p}{\partial f} = -\frac{\tilde{\sigma}_{ij}H_{ijkl}\frac{\partial X_{kl}}{\partial f}}{\sigma_Y^2} + 2q_1\cosh(\alpha) + 2q_1 f^*\frac{\partial \alpha}{\partial f}\sinh(\alpha) - 2q_3 f^*$$

$$\frac{\partial F_p}{\partial \sigma_Y} = -\frac{2\tilde{q}}{\sigma_Y^3} + 2q_1 f^* \frac{\partial \alpha}{\partial \sigma_Y}\sinh(\alpha)$$

$$\frac{\partial^2 F_p}{\partial \sigma_{ij}\partial \sigma_{kl}} = \frac{H_{ijkl}}{\sigma_Y^2} + 2q_1 f^* \frac{\partial \alpha}{\partial \sigma_{ij}}\frac{\partial \alpha}{\partial \sigma_{kl}}\cosh(\alpha)$$

$$\frac{\partial^2 F_p}{\partial \sigma_{ij}\partial \Delta\varepsilon_{kl}^p} = 2q_1 f^* \frac{\partial \alpha}{\partial \sigma_{ij}}\frac{\partial \alpha}{\partial \Delta\varepsilon_{kl}^p}\cosh(\alpha) - \frac{H_{ijmn}\frac{\partial X_{mn}}{\partial \Delta\varepsilon_{kl}^p}}{\sigma_Y^2}$$

$$\frac{\partial^2 F_p}{\partial \sigma_{ij}\partial f} = -\frac{H_{ijkl}\frac{\partial X_{kl}}{\partial f}}{\sigma_Y^2} + 2q_1\frac{\partial \alpha}{\partial \sigma_{ij}}\sinh(\alpha) + 2q_1 f^*\frac{\partial \alpha}{\partial \sigma_{ij}}\frac{\partial \alpha}{\partial f}\cosh(\alpha)$$

$$\frac{\partial^2 F_p}{\partial \sigma_{ij}\partial \sigma_Y} = -\frac{H_{ijkl}X_{kl}}{\sigma_Y^3} + 2q_1 f^*\left(\frac{\partial^2 \alpha}{\partial \sigma_{ij}\partial \sigma_Y}\sinh(\alpha) + \frac{\partial \alpha}{\partial \sigma_{ij}}\frac{\partial \alpha}{\partial \sigma_Y}\cosh(\alpha)\right)$$

$$\frac{\partial h_1}{\partial f} = -\Delta\varepsilon_p; \frac{\partial h_1}{\partial \sigma_Y} = 0$$

$$\frac{\partial h_2}{\partial f}=\frac{h\tilde{\sigma}_{ij}\Delta\varepsilon_{ij}^{p}}{\left(1-f^{*}\right)^{2}\sigma_Y};\frac{\partial h_2}{\partial \sigma_Y}=-\frac{h\tilde{\sigma}_{ij}\Delta\varepsilon_{ij}^{p}}{\left(1-f^{*}\right)\sigma_Y^{2}}$$

$$\frac{\partial h_1}{\partial \sigma_{ij}}=0;\frac{\partial h_1}{\partial \Delta\varepsilon_{ij}^{p}}=\left(1-f^{*}\right)\delta_{ij}$$

$$\frac{\partial h_2}{\partial \sigma_{ij}}=\frac{h\Delta\varepsilon_{ij}^{p}}{\left(1-f^{*}\right)\sigma_Y};\frac{\partial h_2}{\partial \Delta\varepsilon_{ij}^{p}}=\frac{h\tilde{\sigma}_{ij}}{\left(1-f^{*}\right)\sigma_Y}-\frac{h\Delta\varepsilon_{kl}^{p}\dfrac{\partial X_{kl}}{\partial\Delta\varepsilon_{ij}^{p}}}{\left(1-f^{*}\right)\sigma_Y}$$

Where:

$$\alpha=\frac{q_2\tilde{p}}{\kappa\sigma_Y};\frac{\partial\alpha}{\partial X_{ij}}=-\frac{q_2\delta_{ij}}{\kappa\sigma_Y};\frac{\partial\alpha}{\partial\sigma_{ij}}=\frac{q_2\delta_{ij}}{\kappa\sigma_Y};\frac{\partial\alpha}{\partial f}=-\frac{q_2\left(\dfrac{\partial X_{ij}}{\partial f}\delta_{ij}\right)}{\kappa\sigma_Y};\frac{\partial\alpha}{\partial\sigma_Y}=-\frac{q_2\tilde{\sigma}_{ij}\delta_{ij}}{\kappa\sigma_Y}$$

Where δ_{ij} is the Kronecker symbol (modifications in red color).

$$\frac{\partial\alpha}{\partial\Delta\varepsilon_{ij}^{p}}=\frac{\partial\alpha}{\partial X_{kl}}\frac{\partial X_{kl}}{\partial\Delta\varepsilon_{ij}^{p}};\frac{\partial X_{ij}}{\partial\Delta\varepsilon_{kl}^{p}}=\left(1-f^{*}\right)\left(\frac{C_S\delta_{ij}\delta_{kl}\left(1+C\Delta\varepsilon_q\right)-CT_{ij}\left(X_{kl}^{*t}+C_S\Delta\varepsilon_{kl}^{p}\right)}{\left(1+C\Delta\varepsilon_q\right)^{2}}\right)$$

$$T_{ij}=\frac{\partial\Delta\varepsilon_q}{\partial\Delta\varepsilon_{ij}^{p}}=\frac{2H_{ijkl}^{-1}\partial\Delta\varepsilon_{kl}^{p}}{\partial\Delta\varepsilon_q};\frac{\partial^2\alpha}{\partial\sigma_{ij}\partial\sigma_Y}=-\frac{q_2\delta_{ij}}{\kappa\sigma_Y^{2}};\frac{\partial X_{ij}}{\partial f}=-\left(\frac{X_{ij}^{*t}+C_S\Delta\varepsilon_{ij}^{p}}{1+C\Delta\varepsilon_q}\right)$$

Appendix (C) Void nucleation: 3D views

3Dviews of the specimens at various steps of deformation [LAN 2011a].

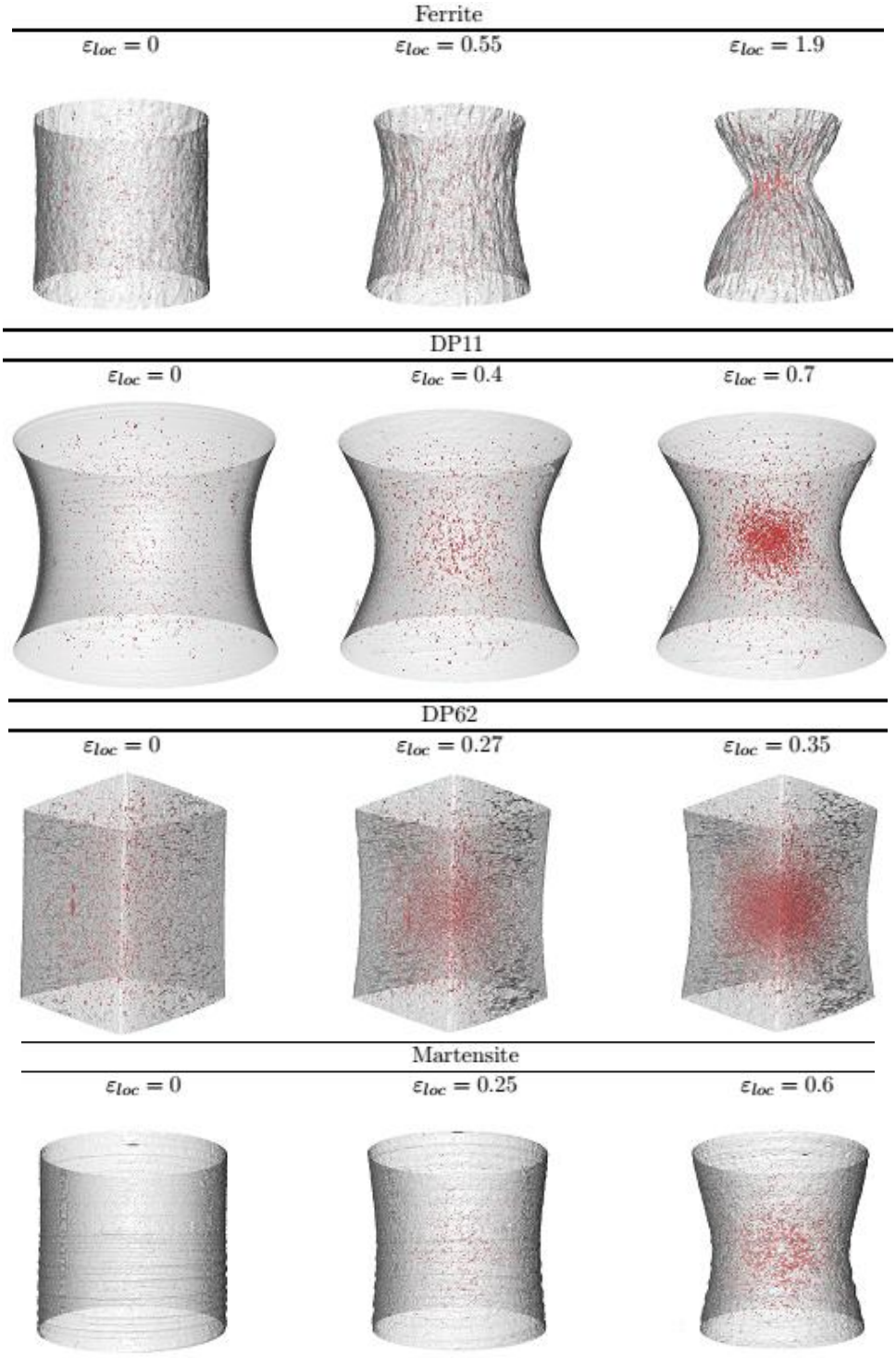

Appendix (D) Further results on tensile test samples

(D).1 Heterogeneity visualisation after tensile test with GTNB model

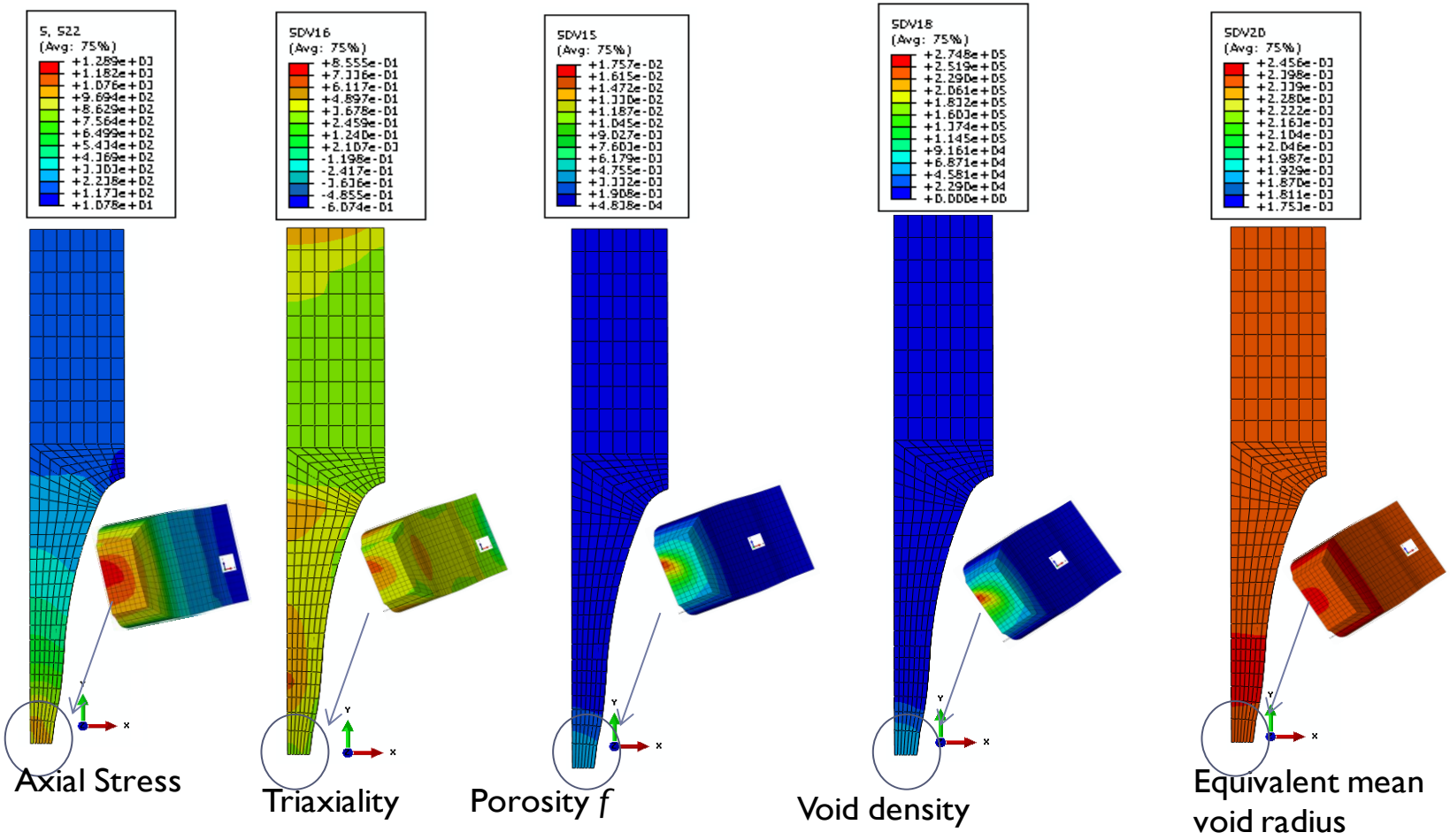

Heterogeneity on the triaxiality

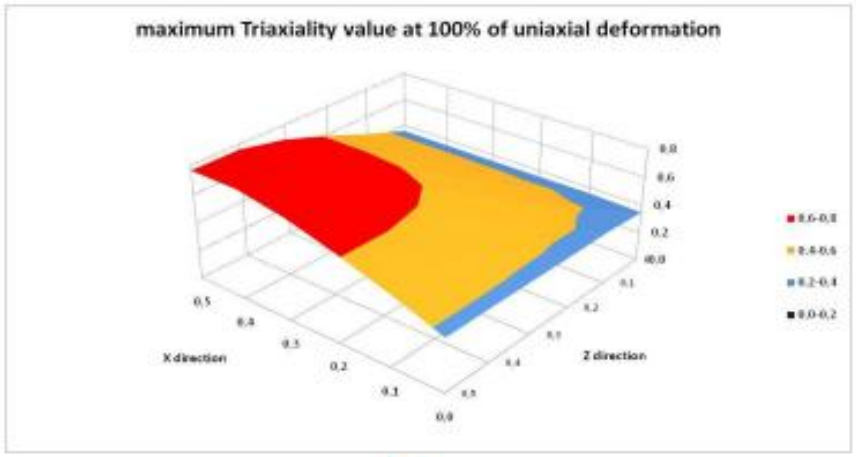

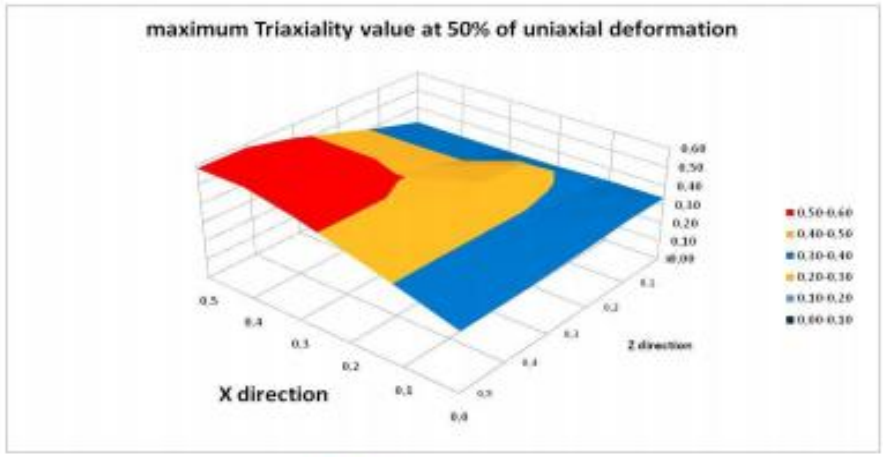

Strong heterogeneity on Triaxiality

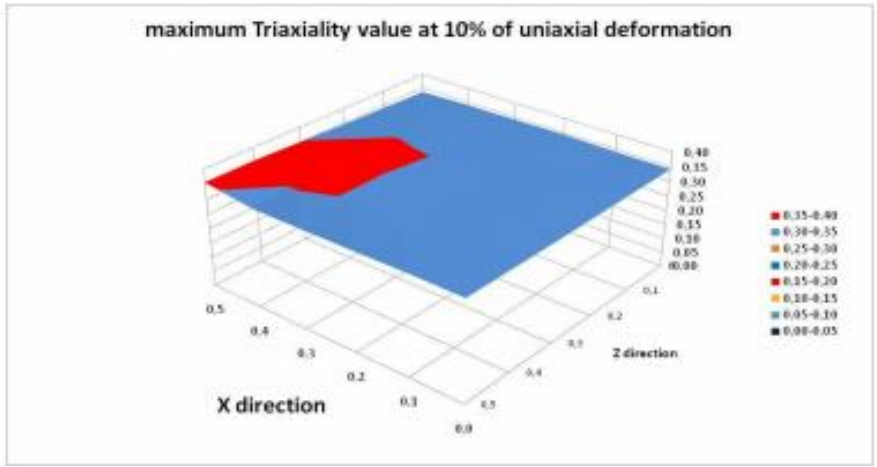

4

Heterogeneity on void volume fraction

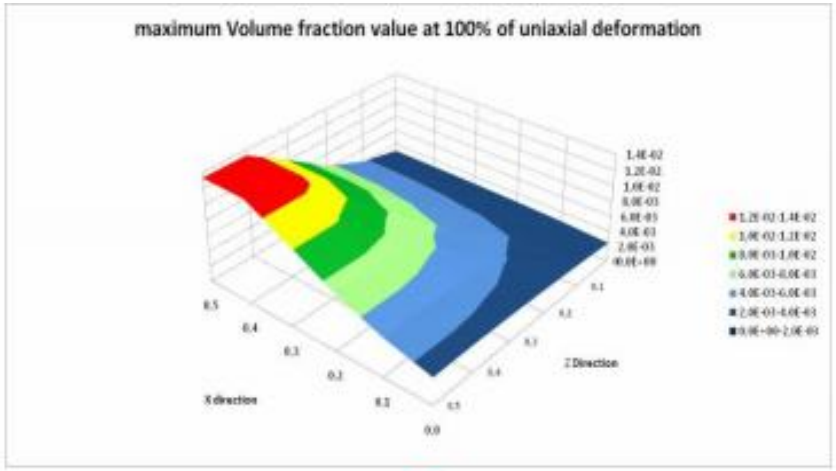

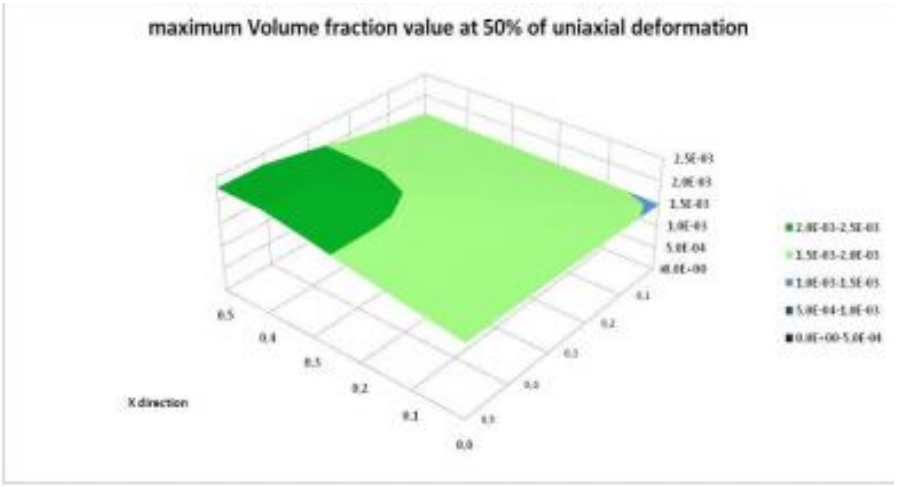

Strong heterogeneity on Volume fraction of porosity

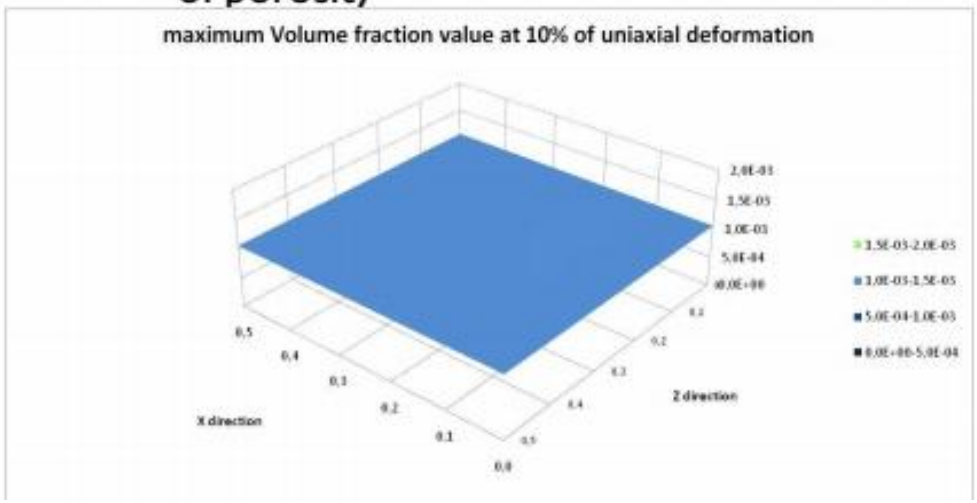

(D).2 Tensile test isovalues on flat notched specimen

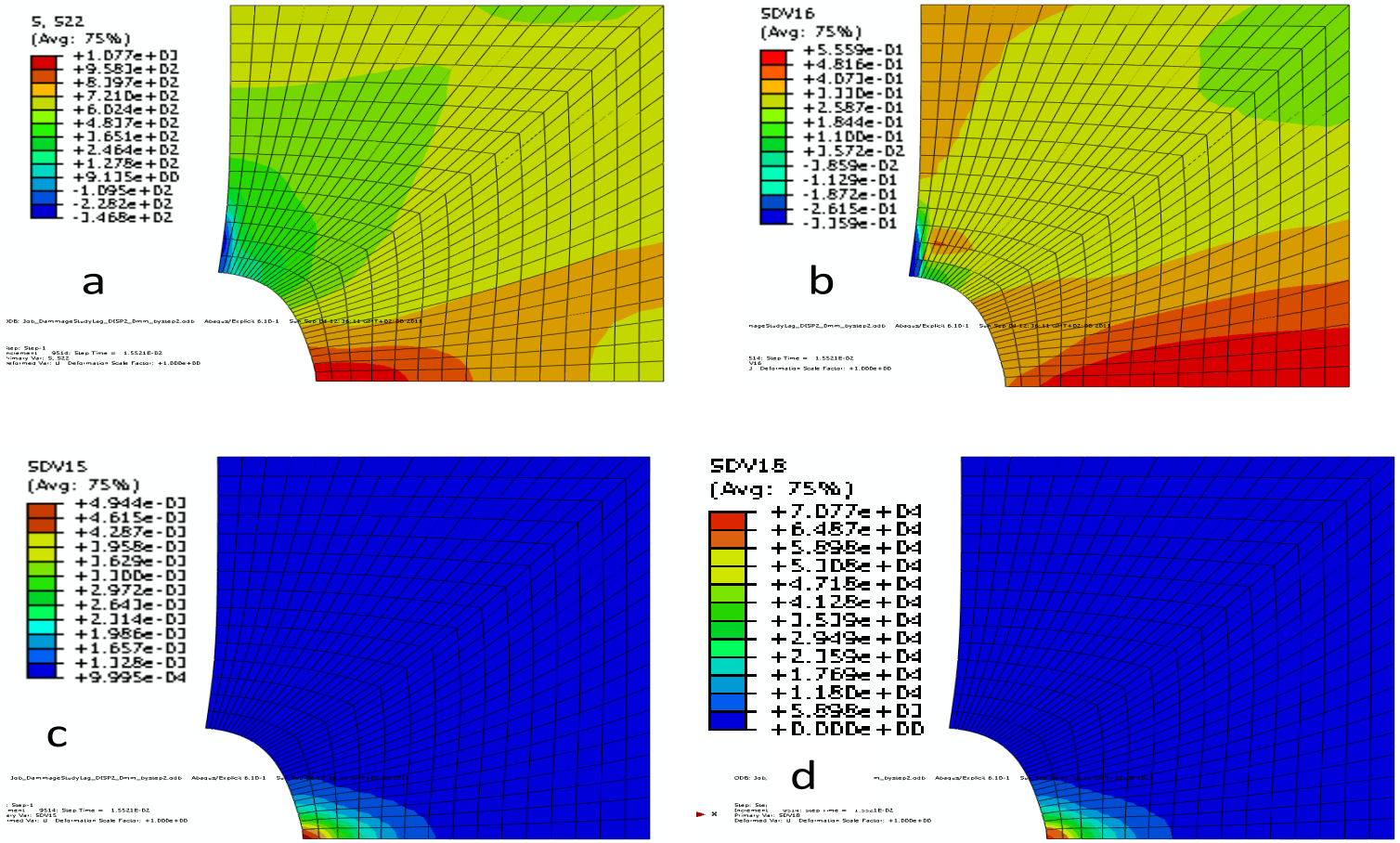

a) Isovalues of the stress (22); b) the triaxiality; c) the porosity; d) the void density at maximum plastic strain close to unity (Abaqus -Explicit).

(D).3 Tensile test isovalues on cylindrical notched specimen

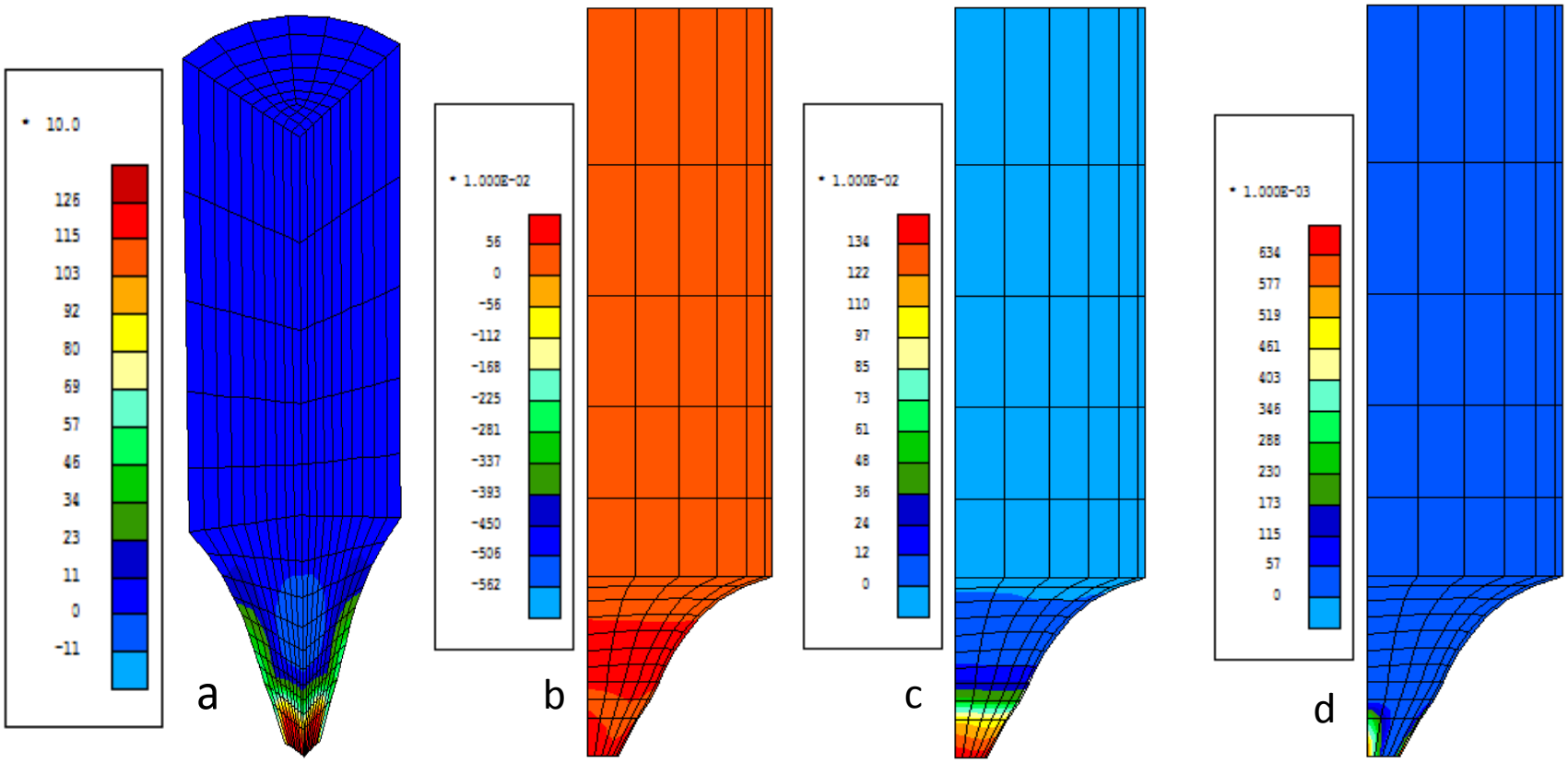

a) Isovalues of the stress (22); b) the triaxiality; c) The equivalent plastic strain porosity; d) the porosity *f* at maximum plastic strain close to unity (Lagamine).

Nomenclature

Roman

A, B	Material constant
b	Length
C_c	Critical value
$\underline{\underline{C}}^e$	Elastic stiffness tensor
C_x, S_{sat}	Material parameters for Armstrong-Frederick law
D	Damage parameter
D_{eq}	Equivalent cavity diameter
E	Elastic Young's modulus
F	Force
F_p	Yield function or surface
$F_p^{Gurs}(*)$	Gurson yield function
$F_p^{GTN}(*)$	Gurson-Tvergaard-Needleman yield function
f	Void volume fraction or porosity
$\dot{f}$	Total porosity evolution rate
f_0	Initial void volume fraction
f_c	Void volume fraction or porosity due to coalescence
$\dot{f}_{coal}$	Void volume fraction or Porosity evolution due to coalescence rate
f_f	Porosity at final failure
$f^*(f)$	Coalescence function
f^*	Effective porosity for the coalescence model
f_g	Void volume fraction due to growth stage
$\dot{f}_g$	Porosity evolution rate due to growth
f_n	Void volume fraction due to nucleation stage
f_N	Potential nucleated void fraction
f_u	Ultimate porosity value at the occurrence of ductile rupture
$\underline{\underline{H}}$	Fourth order quadratic Hill matrix
$\underline{\underline{H}}^{-1}$	Pseudo-inverse of Hill's anisotropy matrix
$\overline{H_k}$	Proportionality factor related to the plastic modulus
J_3	Third invariant of the stress deviator

k_s	Stress concentration factor
l	Length
L	Center to center average inter-cavities distance
$\underline{\underline{M}}$	Effective stress operator
$\underline{n}$	Normal tensor
N	Number of voids per unit volume
N_0	Initial number of voids per unit volume
q_1, q_2 and q_3	Damage parameters for GTN model
r_0, r_{45}, r_{90}	Lankford coefficients
R_0	Mean void radius
R_0^i	Initial void Size nucleating at the beginning of the deformation
R	Mean void radius
r_{ini}	current radii of the minimum cross-section
r_{notch}	Notch radius
$r_{section}$	Minimal cross-section radius
$r_{rolling\ direction}$	Normal anisotropy
S_0, S	Initial and the current surfaces of the necking section
S_N	Standard deviation
t	Thickness
T	Triaxiality
T_B	Triaxiality with back stress
V_f	Volume of voids
V_v	Void volume
V_m	Matrix volume
$\underline{X}$	Back stress tensor
X	Back stress scalar
$\underline{X}'$	Deviatoric back-stress tensor
$\dot{\underline{X}}$	Back stress tensor rate

Greek

α_H	Huang material constant
ε_{N0}	Critical strain for pure shear loading for nucleation model
ε^{el}	Elastic strain
$\dot{\varepsilon}^p_{eqv}$	Equivalent plastic strain rate

ε_{eqv}^{p}	Equivalent plastic strain
ε_N	Mean equivalent plastic strain for nucleation model
ε_{axial}	The average axial strain
ε_t	Thickness strain
ε_w	width strain
$\underline{\underline{\varepsilon}}$	Total macroscopic strain tensor
$\underline{\underline{\varepsilon}}^{e}$	Elastic strain tensor
$\underline{\underline{\varepsilon}}^{p}$	Plastic strain tensor
$\dot{\underline{\underline{\varepsilon}}}^{p}$	Plastic strain rate tensor
ε_f	Strain at fracture in coalescence model
κ	Benzerga plastic anisotropy
ε_0, K, n	Swift material parameters
$\dot{\lambda}$	Plastic multiplier
λ	Mean distance between two cavities
λ_f	Ultimate average inter-cavities distance.
v	Poisson coefficient
σ_{axial}	The average stress calculation
σ_c	The critical shear stress
$\overline{\sigma}(*),\ \sigma_{eqv}$	Equivalent stress
$\overline{\underline{\underline{\sigma}}}_{=***}$	Shifted stress tensor
$\overline{\sigma}(*), \overline{\sigma}_{eqv\,=***}$	Anisotropic equivalent shifted stress
σ_y	Yield stress scalar
σ_m	Mean normal stress
$\overline{\sigma}_{m\,=***}$	Macroscopic mean shifted stress
$\underline{\underline{\sigma}}$	Cauchy stress tensor
$\underline{\underline{\sigma}}'$	Deviatoric stress tensor
$\sigma_I, \sigma_{II}, \sigma_{III}$	Principal stress
$\sigma_I^{\max}$	Maximal principal stress
σ_C	Argon critical stress
$\underline{\underline{\sigma}}^{effec}$	Effective stress tensor
$\tau_{\max}$	Maximum shear in fracture model or Tresca yield surface
τ_F	Critical shear value in fracture model

Abbreviations

2D	Two-Dimension
3D	Three-Dimension
AHSS	Advanced High Strength Steels
BH	Bake Hardenable
CP	Complex Phase
CR	Cold Rolling
DIC	Digital Image Correlation
DP	Dual Phase
FB	Ferritic Bainitic
FE code	Finite Element code
FFLD	Fracture Forming Limit Diagram
FLC	Forming Limit curve
FLD	Forming Limit Diagram
FORTRAN	FORmula TRANslating
GLD	Gologanu-Leblond-Devaux model
GTN	Gurson-Tvergaad-Needleman model
GTNB	Gurson-Tvergaard-Needleman-Ben Bettaieb
GTNBF	Gurson-Tvergaard-Needleman-Ben Bettaieb-Fansi
Gur3DANI	Gurson 3D ANIsotropy
HF	Hot Formed
HR	Hot Rolling
HSLA	High-Strength Low-Alloy
IBM	International Business Machines corporation
IF	Interstitial Free
INSA	Institut National des Sciences Appliquées
Mild	Mild steel
MS or MART	Martensitic
PhD	Doctor of Philosophy
SEM	Scanning Electron Microscope
SF	Stretch-Flangeable
TEM	Transmission Electron Microscope
TRIP	Transformation Induced Plasticity
TWIP	Twinnin-Induced Plasticity
UMAT	User MATerial
UTS	Ultimate tensile strength
VUMAT	Velocity User MATerial
Y.S	Yield Strength

References

[ABA 2011] Abaqus Theory and verification manuals, version 6.10, HKS INC. 2011.

[ABB 2003] F.M. Al-Abbasi, J.A. Nemes, Micromechanical modeling of dual phase steels Original Research Article International Journal of Mechanical Sciences, 45, 2003, 1449-1465.

[ABB 2010] F. Abbassi, O. Pantelé, S. Mistou, A. Zghal R. Rakotomalala, Roger Effect of Ductile Damage Evolution in Sheet Metal Forming: Experimental and Numerical Investigations, Key Engineering Materials, vol. 446, 157-169. ISSN, 2010, 1662-9795.

[ABE 2003] M. Abendroth, M. Kuna, Determination of deformation and failure properties of ductile materials by means of the small punch test and neural networks, Computational Materials Science 28, 2003, 633–644.

[ADA 1992] J. C. Adams, W. S. Brainerd, J. T. Martin, Brian T. Smith, J. L. Wagener, Fortran 90 Handbook, Complete ANSI / ISO Reference, Inter text Publications McGraw-Hill Book Company, 1992.

[ACH 2012] M. Achouri, Caractérisation expérimentale et contribution à la modélisation numérique de l'endommagement en cisaillement des aciers HLE. Applications au procédé de poinçonnage, PhD Thesis, Arts et Métiers ParisTech, 2012.

[AHM 2011] E. A. A. Ahmed, Laser Welding of Advanced High Strength Steels PhD thesis, Univeristy of Aachen, 2011.

[ALL 2008] S. Allain, O. Bouaziz, Mater. Sci. Eng. 496A, 2008, 329–336.

[ALL 2012] S. Allain, Comportement mécanique des aciers: des mécanismes fondamentaux à la déformation macroscopique, thesis to obtain the academic accreditation to supervise research, HDR, Lorraine University, 2012, In French.

[ARA 1987] N. Aravas, On the Numerical Integration of a Class of Pressure Dependent Plasticity Models. Int. J. Numer. Meth. Eng. 24, 1987, 1395–1416.

[ARC 2012] ArcelorMittal http://www.arcelormittal.com/[Web resources], 2012.

[ARG 1975] A. Argon, J. Im, Separation of second phase particles in spheroidized 1045 steel, Cu-0.6pct Cr alloy, and maraging steel in plastic straining, Metallurgical and Materials Transactions A, Vol. 6, 1975, 839–851.

[ARM 1966] P.J Armstrong, C.O. Frederick, A mathematical representation of the multiaxial Bauschinger effect. G.E.G.B report RD/B/N 731, 1966.

[ARN 1997] S. Arndt, B. Svendsen, D. Klingbeil, Modellierung der Eigenspannungen und der Rißspitze mit einem Schagi-gungsmodell, Technische Mechanik. 17,1997.

[ASK 2000] H. Askes, L.J. Sluys, Remeshing strategies for adaptive ale analysis of strain localization, Eur. J. Mech. A: Solids 19, 2000, 447-467.

[ATE 2008] E. H. Atzema, C. H. L. J. ten Horn, and H. Vegter. Influence of tooling layout on sheet forming process analysis. In Proceeding of European congress on computational methods in applied sciences and engineering, Jyvaskyla, Finland, 2004.

[AVR 2009] G. Avramovic-Cingara, Y. Ososkova, Jain MK, Wilkinson DS, Effect of martensite distribution on damage behavior inDP600 dual phase steels, Mater Sci Eng 516, 1– 2, 2009, 7–16.

[BAI 2008] Bai, Y., Wierzbicki, T., A new model of metal plasticity and fracture with pressure and Lode dependence. Int. J. Plasticity 24, 2008, 1071–1096.

[BAG 1999] A. Bag, K.K. Ray, and E.S. Dwarakadasa. Influence of martensite content and morphology on tensile and impact properties of high-martensite dual-phase steels. Metallurgical and Materials transactions A, 30, 1999, 1193–1202.

[BAL 2011] V.H. Baltazar Hernandez, S.S. Nayak, Y. Zhou, Tempering of Martensite in Dual-Phase Steels and Its Effects on Softening Behavior, The Minerals, Metals & Materials Society and ASM International, Metallurgical and Materials Transactions A, DOI: 10.1007/s11661-011-0739-3, 2011.

[BAN 2005] D. Banabic, H. Aretz, D.S. Comsa, L. Paraianu, An improved analytical description of orthotropy in metallic sheets, Int. J. Plasticity, 2005,21:493–512.

[BAO 2004] Bao, Y.B., Wierzbicki, T., A comparative study on various ductile cracks formation criteria. Journal of Engineering Materials and Technology - Transactions of the ASME 126, 2004, 314-324.

[BAR 2004] F. Barlat, O. Cazacu, M. Zyczkowski, D. Banabic, J.W. Yoon, Yield surface plasticity and anisotropy, Continuum scale simulation of engineering materials: fundamentals microstructure-process applications. Berlin: Wiley-VCH., 2004, 145–85.

[BAR 2012] A. Bareggi, E. Maire, O. Bouaziz, M. Di Michiel, Damage in dual phase steels and its constituents studied by X-ray tomography, Int J Fract, 2012, 174:217–227.

[BEL 2007] K.A. Bello, S.B. Hassan, M. Abdulwahab, U. Shehu, Effect of ferrite-martensite microstructural evolution on hardness and impact toughness behaviour of high martensite dual phase steel Australian journal of basic and applied sciences 1, 2007, N. 4, P. 407-414.

[BEN 2000] A. A. Benzerga. Rupture ductile des tôles anisotropes. PhD thesis, Ecole Nationale Supérieure des Mines de Paris, 2000.

[BEN 2001] A. A. Benzerga, J. Besson, Plastic potentials for anisotropic porous solids, Eur. J. Mech. A - Solids, 20 ,2001, 397-434.

[BEN 2008] M. Ben Bettaieb, A.M. Habraken, Literature review: state of the art of rupture criteria, MS²F-Argenco, Belgium, intern report, 2008.

[BEN 2010] M. Ben Bettaieb, X. Lemoine, O. Bouaziz, A-M. Habraken, L. Duchêne, Numerical modelling of damage evolution of DP steels on the basis of X-ray tomography measurements, Mechanics of Materials, 2010, 139-156.

[BEN 2010a] M. Ben Bettaieb, X. Lemoine, L. Duchêne, A-M. Habraken, Simulation of the bending process of hardening metallic sheets using damage model. Part II: Numerical investigations", Materials Science and Engineering A, 528, 2010, Pages 442-448.

[BEN 2011] M. Ben Bettaieb, X. Lemoine, O. Bouaziz, A-M. Habraken, L. Duchêne, Numerical modelling of damage evolution of DP steels on the basis of X-ray tomography measurements, Mechanics of Materials 43, 2011, 139-156.

[BEN 2011a] M. Ben Bettaieb, X. Lemoine, O. Bouaziz, L. Duchêne, A-M. Habraken. "A finite element analysis of the bending and the bendability of metallic sheets", International Journal of Material Forming, published online DOI: 10.1007/s12289-010-0993-8, 2011.

[BEN 2012] M. Ben Bettaieb, X. Lemoine, L. Duchêne, A-M. Habraken, On the numerical integration of an advanced Gurson model, International Journal for Numerical Methods in Engineering. 85, 8, 2012, 1049-1072.

[BER 1981] F. Beremin, Cavity formation from inclusions in ductile fracture of A508 steel, Metallurgical and Materials Transactions A, Vol. 12, 1981. 723–731.

[BES 2005] B. Tanguy and J. Besson, Simulation of the ductile to brittle Charpy transition curve after irradiation: effect of the hardening behavior". In: G. Augusti, G. I. Schuller, and M. Ciampoli, Eds., Proceedings of 9th inter-national conference on structural safety and reliability, 2005. 587 – 590, Rome.

[BOI 2010] R. Boistel, M. Langer, E. Pagot, P. Cloetens, F. Peyrin, X-ray in-line phase microtomography for biomedical applications, Microscopy: Science, Technology, Applications and Education A. Méndez-Vilas and J. Díaz , Eds., FORMATEX 2010.

[BOR 2005] H. Borouchaki, P. Laug, A. Cherouat, K. Saanouni, Adaptive remeshing in large plastic strain with damage, Int. J. Numer. Methods Eng. 63, 2005, 1-36.

[BOU 2008] O. Bouaziz, E. Maire, M. Giton, J. Lamarre, Y. Salingue, M. Dimichiele, A model for initiation and growth of damage in dual phase steels identified by X-ray micro-tomography, Rev. Met. 2, 2008, pages 102–107.

[BOU 2011] I. Boul, D. Rèche, D. Cornette, Data files of AHSS steels characterized according AHSS handbook, Ref. 2011 15932 RDMA, 2011, report DUPAU-343, 1-52.

[BRI 1945] P. W Bridgman, Effects of hydrostatic pressure on the plastic properties of the metals, Rev.Mod.Phy. 17, 1945, 3-17.

[BRI 1995] Brite Euram Light Weight Vehicle project, 1995.

[BRO 1972] P. Brozzo, B. De Luca, R. Rendina, 1972, Eine neue Methode zur Vorherzsage der Umformbarkeit von Metallfeinblechen. Proc. 7thBiennal Congress IDDRG, 1972 9-13.

[BRO 1973] L. M Brown, J. D Embury, The initiation and growth of voids at second phase particles, Proceedings 3rd International Conference on Strength of Metals and Alloys, 1973, 164–169.

[BRO 1995] W. Brocks, G. Bernauer, Determination of the Gurson parameters by numerical simulations, in: 2nd Griffith Conference Sheffield, September 13–15, 1995.

[BRO 2004] F. Bron and J. Besson, A yield function for anisotropic materials application to aluminium alloys, Int. J. Plasticity, 2004, 20:356-364.

[BRU 2001] M. Brunet, F. Morestin, H. Walter, Numerical analysis of failure in sheet metal forming with experimental validation, Euromech 417, 2001.

[BRU 2005] M. Brunet, F. Morestin, H. Walter-Leberre, Failure analysis of anisotropic sheet-metals using a non-local plastic damage model. Journal of Materials Processing Technology, Volume 170, Issues 1-2, 2005, 457-470.

[BUF 1999] J.Y. Buffiere, E. Maire, P. Cloetens, G. Lormand, R. Fougeres, Acta Metall. 47 , 1999, 1613–1625.

[BUI 2011] http://boronextrication.com/2010/10/2011-buick-lucerne-body-structure/

[CAI 1985] Xue-Ling Cai, J. Feng, and W.S. Owen. The dependence of some tensile and fatigue properties of a dual-phase steel on its microstructure. Metallurgical and Materials transactions A, 16, 1985, 1405–1415.

[CAL 2009] M. Calcagnotto, D. Ponge, Y. Adachi, D. Raabe, Effect of Grain Refinement on Strength and Ductility in Dual-Phase Steels, Proceedings of the 2nd International Symposium on Steel Science , ISSS 2009 Oct. 21-24, 2009, Kyoto, Japan: The Iron and Steel Institute of Japan.

[CAL 2010] M. Calcagnotto, D. Ponge, E. Demir, D. Raabe, Orientation gradients and geometrically necessary dislocations in ultrafine grained dual-phase steels studied by 2D and 3D EBSD, Materials Science and Engineering A527, 2010, 2738–2746.

[CAZ 2006] O. Cazacu, B. Plunkett, F. Barlat, Orthotropic yield criterion for hexagonal closed pack metals, Int. J. Plasticity, 2006, 22:1171-1194.

[CHA 1983] J.L. Chaboche, J.L., G. Rousselier, On the plastic and viscoplastic constitutive equations. J.Press. vess. technol. 105, 1983, 105-164.

[CHA 1986] JL. Chaboche, Time-independent constitutive theories for cyclic plasticity. International Journal of plasticity 1986, 2:149–88.

[CHA 2008] Chaboche JL. A review of some plasticity and viscoplasticity constitutive theories. Int J Plast 2008, 24:1642–93.

[CHO 2008] J.M Choung, S.R Cho, Study on true stress correction from tensile tests, Journal of Mechanical Science and Technology 22, 2008, 1039~1051.

[CHO 2013] S.-H. Choi, E.-Y. Kim, W. Woo, S.H. Han, J.H. Kwak, The effect of crystallographic orientation on the micromechanical deformation and failure behaviors of DP980 steel during uniaxial tension, International Journal of Plasticity , 2013.

[CHU 1980] C.C Chu, A. Needleman, Void Nucleation Effects In Biaxially Stretched Sheets. Journal Of Engineering Materials And Technology-Transactions of the ASME, Volume 102, Issue 3, 1980, 249-256.

[CHU 2009] K. H. Chung, W. Lee, J. H. Kim, C. Kim, S. H. Park, D. Kwon, K. Chung, Characterization of mechanical properties by indentation tests and FE analysis – validation by application to a weld zone of DP590 steel, International Journal of Solids and Structures 46, 2009, 344–363.

[CHU 2010] K. Chung et al., Formability of TWIP, twinning induced plasticity automotive sheets, International Journal of Plasticity, 2010.

[CHU 2012] K. Chung, T. Park, Consistency condition of isotropic–kinematic hardening of anisotropic yield functions with full isotropic hardening under monotonously proportional loading, International Journal of Plasticity, 2012, http://dx.doi.org/10.1016/j.ijplas.2012.10.012.

[COC 1968] M.G Cockroft, D.J. Latham, Ductility and the workability of metals. Journal of the Institute of Metals, Volume 96, 1968, 33-39.

[COR 1983] J. P. Cordebois, Critères d'instabilité plastiques et endommagement ductile en grandes déformations, PhD Thesis, University Pierre et Marie Curie, 1983, France.

[COR 2006] S. Cooreman, C. Bouffioux, D. Lecompte, D. Debruyne, H. Sol, J. Vantomme, Elasto-Kunststoff Parameteridentifikation durch inverse Methoden: Sensitivitätsmatrix Berechnung, Proceedings of the SEM Annual Conference and Exposition 2006, St-Louis, Missouri, 4 - 7. Juni 2006.

[COR 2009] S. Cooreman, D. Lecompte, H. Sola, J. Vantomme, D. Debruyne, Elasto-plastic material parameter identification by inverse methods: Calculation of the sensitivity matrix, International Journal of Solids and Structures, (44), Issue 13, 2007, 4329–4341.

[CRO 2002] P. Croix, Endommagement et rupture des métaux anisotropes pour la dynamique et les crash de véhicules, Thèse de doctorat, Université de Valenciennes et du Hainaut Cambrésis, 2002.

[DAR 2003] M. Darrieulat and F. Montheillet, A texture based continuum approach for predicting the plastic behaviour of rolled sheet, Int. J. Plasticity, 2003, 19:517-546.

[DEB 2009] D. Debruyne, S. Cooreman, P. Lava S. Coppieters, Identification of the plastic material behaviour through inverse modelling and DIC: influence of the specimen's geometry, Proceedings of the SEM Annual Conference June 1-4, 2009, Albuquerque New Mexico USA, 2009 Society for Experimental Mechanics Inc.

[DUN 2011] M. Dunand, D. Mohr, On the predictive capabilities of the shear modified Gurson and the modified Mohr–Coulomb fracture models over a wide range of stress triaxialities and Lode angles, Journal of the Mechanics and Physics of Solids, Volume 59, Issue 7, July 2011, Pages 1374-1394.

[DUN 2012] M. Dunand, Hybrid-experimental-Numerical determination of the loading path to fracture in TRIP780 sheets subjected to multi-axial loading, Master thesis/MIT 2010.

[ERD 2002] M. Erdogan. The effect of new ferrite content on the tensile fracture behaviour of dual phase steels. Journal of material science, 37:3623–3630, 2002.

[ESH 1957] J. D. Eshelby, The Determination of the Elastic Field of an Ellipsoidal Inclusion, and Related Problems, Proceedings of the Royal Society of Lon-don. Series A, Mathematical and Physical Sciences, Vol. 241, 1957, 376–396.

[FAN 2012] J. Fansi, PhD thesis progress report-1st year: Development, implementation and validation of a tridimensional formability criterion fitted for high strength steel, ArcelorMittal Research Maizières, Project: DUDPI11, 2012.

[FAN 2012a] J. Fansi, M. Ben Bettaieb, T. Balan, X. Lemoine, A.-M. Habraken, Key Eng. Mater. , 2012, 77–80.

[FAN 2012b] J. Fansi, A.-M. Habraken, T. Balan, X. Lemoine, C. Landron, E. Maire, O. Bouaziz, M. Ben Bettaieb, Proceedings of the 11th Biennial Conference on Engineering Systems Design and Analysis, Transactions of the ASME, 2012.

[FAN 2013] J.Fansi, T. Balan, X. Lemoine, E. Maire, C. Landron, O. Bouaziz, M. Ben Bettaieb, A. M. Habraken, Numerical investigation and experimental validation

of physically based advanced GTN model for DP steels, Materials Science and Engineering: A, Volume 569, 1 May 2013, 1-12.

[FIC 2010] E. Fictorie, A. H. van den Boogaard, and E. H. Atzema. Influence of punch radius in a Nakazima test for mild steel and aluminum. International Journal of Material Forming, 3(1), 2010, 1179-1182.

[FOR 1956] The Fortran Automatic Coding System for the IBM 704 EDPM (Programmer's Reference Manual ed., New York, New York: International Business Machines Corporation, cover OCLC: 223331944, 1956.

[GEO 2003] J.L Geoffroy, Notion of 'unloading tangent modulus' used to a better prediction of Spring Back, ArcelorMittal, IDDRG2003, 2003.

[GOD 1968] Goodwin, G.M., 1968. Application of strain analysis to sheet metal forming in the press shop. SAE paper 680093.

[GOM 2009] Rev. A (en) 22012009 www.gom.com.

[GOL 1993] M. Gologanu, J. Leblond, J. Devaux, Approximate models for ductile metals containing non-spherical voids –case of axisymmetric prolate ellipsoidal cavities, J. Mech. Phys. Solids 41 (11), 1993, 1723-1754.

[GOO 1979] S. H. Goods, L. M. Brown, Overview No. 1: The nucleation of cavities, by plastic deformation, Acta Metallurgica, Vol. 27, 1979, 1–15.

[GOU 1993] M. Gologanu, J. B. Leblond, J. Devaux, Approximate models for ductile metals containing non-spherical voids - Case of axisymmetric prolate ellipsoidal cavities, Journal of the Mechanics and Physics of Solids, 41, Issue 11, 1993, 1723-1754.

[GRU 2012] G. Gruben, O.S. Hopperstad, T. Børvik, Evaluation of uncoupled ductile fracture criteria for the dual-phase steel Docol 600DL Original Research Article, International Journal of Mechanical Sciences, Volume 62, Issue 1, September 2012, 133-146.

[GUR 1977] A. L. Gurson, "Continuum theory of ductile rupture by void nucleation and growth: Part I: Yield criteria and flow rules for porous ductile media," Journal of Engineering Materials and Technology, vol. 99, no. 1, 1977, 2–15.

[GUZ 2013] C.F. Guzmán, A.M. Habraken, Towards fracture prediction in single point incremental forming, Key Engineering Materials Vols. 554-557 2013, 2355-2362.

[HAB 2004] A.M, Habraken, Modeling the plastic anisotropy of metals. Archives of computational method in Engineering 2004 vol II, ISS1, 3-96.

[HAB 2012] A.M, Habraken, Nonlinear finite elements, course #3, Grasmech University of Liège, 2012.

[HAL 1953] E.O. Hall, The brittle fracture of metals, Journal of the Mechanics and Physics of solids, 1, 1953, 227-233.

[HAR 2007] F.J. Harewood, P.E. McHugh, Comparison of the implicit and explicit finite element methods using crystal plasticity, Computational Materials Science 39 , 2007, 481–494.

[HEL 1996] A.L, Helbert, X. Feaugas, M. Clavel, The influence of the back stress (X) and the hardening rate (dX/depeq) on void nucleation in titanium alloys, 1996, J. Phys-Paris 6, 101–111.

[HEL 1998] A. L. Helbert, X. Feaugas, M. Clavel, Effect of microstructural parameters and backstress on damage mecanisms in alpha/beta titanium alloys, Acta Metallurgica. 46, 1998, 939–951.

[HEL 1999] A.L, Helbert, X. Feaugas, M. Clavel, The influence of internal stresses on the fracture toughness of a/b titanium alloys, Metall.Mater. Trans. A 30, 1999, 2853–2863.

[HIB 2010] Hibbitt, Karlsson & Sorensen, Abaqus User's Manual, Version 6.10, 2010.

[HIL 1948] R. Hill, A theory of the yielding and plastic flow of anisotropic metals, In Proc, Royal Soc. Of London, 1948, A193:281-297.

[HIL 1979] R. Hill, Theoretical plasticity of textured aggregates, Math. Proc. Camb. Phil. Soc., 85(1), 1979, 179–191.

[HOC 1975] J.E. Hockett, O.D. Sherby, Large strain deformation of polycrystalline metals at low homologous temperatures. Journal of the Mechanics and Physics of Solids, 23, 1975, 87-98.

[HOL 1945] L.H. Hollomon, Tensile deformation. Trans. Met. Soc. AIME, 162, 1945, 268- 290.

[HOL 2010] J. Hol, M. V. cid Alfaro, M. B. de Rooij, and T. Meinders. Multiscale friction modeling for sheet metal forming. In Proceedings of 4th International Conference on Tribology in Manufacturing Processes (ICTMP), volume 2, pages 573-582, CEMEF, MINES ParisTech, 2010.

[HOL 2011] J. Hol, M. V. Cid Alfaro, T. Meinders, and J. Hu´etink. Advanced friction modeling in sheet metal forming. Key Engineering Materials, 473:715-722, 2011.

[HOS 1979] W.F. Hosford, On yield loci of anisotropic cubic metals, In: Proc. of the 7th north American metalworking conference, Dearborn, MI: SME, 1979, 191-7

[HOS 2005] W.F Hosford, Mechanical behaviour of materials, Cambridge, University of Michigan, 2005.

[HOU 2008] D. Houcque, Applications of MATLAB: Ordinary Differential Equations (ODE), Northwestern University, 2008.

[HU 2007] W. Hu, A novel quadratic yield model to describe the feature of multi-yield-surface of rolled sheet metals, Int. J. Plast. 23, 2007, 2004-2028.

[HUA 1989] Huang-Chuan Chen, Gwo-Hwa Cheng Effect of martensite strength on the tensile strength of dual phase steels Materials science 24, 1989, P. 1991-1994.

[HUA 1991] Y. Huang, Accurate dilatation rates for spherical voids in triaxial stress fields, Transactions of the ASME. 58, 1991, 1084–1086.

[HUG 2003] P.E McHugh, P.J Connolly, Micromechanical modelling of ductile crack growth in the binder phase of WC–Co Original Research Article, Computational Materials Science, Volume 27, Issue 4, June 2003, 423-436.

[KAC 1958] L. Kachanov, Time of Rupture Process Under Creep Conditions, Izv. Akad. Nauk SSR otd Tech. Nauk 8, 1958, 26-31.

[KAD 2011] J. Kadkhodapour, A. Butz, S. Ziaei-Rad, S. Schmauder, A micro mechanical study on failure initiation of dual phase steels under tension using single crystal plasticity model, International Journal of Plasticity, 27, 2011, 1103-1125.

[KAL 2001] S. Kalpakjian and S. R. Schmid, Manufacturing Processes for Engineering Materials, Addison Wesley Publishing Co., 2001.

[KAL 2008] S. Kalpakjian, S. Schmid, Manufacturing Processes for Engineering Materials, 5th ed., Pearson Education ISBN No. 0-13-227271-7, 2008.

[KAN 1995] N. Kanetake, M. Nomura, and T. Choh. "Continuous observation of microstructural degradation during tensile loading of particle reinforced aluminium matrix composites". Materials Science and Technology, Vol. 11 , 1995, 1246–1252.

[KAR 1993] A.P. Karafillis, M.C. Boyce, A general anisotropic yield criterion using bounds and a transformation weighting tensor, J. Mech. Phys. Solids, 1993, 41:1859–86.

[KAW 2003] Kawasaki steel 2003, http://www.jfe-21st-cf.or.jp/chapter_1/

[KEE 2009] S. Keeler, S., The Science of Forming: Defining to AHSS (Articles): Advanced High-Strength Steels." Metal Forming, 2009, 32-33.

[KIM 2006] J. Kim, W. Lee, D. Kim, J. Kong, C. Kim, M.L. Wenner, K. Chung, Effect of hardening laws and Yield function types on spring-back simulations of Dual-Phase steel automotive sheets, Metals and Materials International, 12, 2006, 293-305.

[KIM 2011] J. H. Kim, J. Sung, K. Piao, R.H. Wagoner, the shear fracture of dual-phase steel Original Research Article International Journal of Plasticity, Volume 27, Issue 10, October 2011, Pages 1658-1676.

[KLO 2003] H. Klöcker, V. Tvergaard, Growth and coalescence of non-spherical voids in metals deformed at elevated temperature. International journal of mechanical sciences, Volume 25, 2003, 1283–308.

[KOB 1979] Oh, S.I., Chen, C.C., Kobayashi, S., Ductile fracture in axisymmetric extrusion and drawing. Journal of Engineering for Industry, Volume 101, 1979, 36-44

[KRE 2010] B. Krebs, A. Hazotte, L. Germain, M. Gouné, Quantitative analysis of banded structures in Dual-Phase steels, Image Anal Stereol., 29, 2010, 85-90.

[KUR 2000] M. Kuroda and V. Tvergaard, Effect of strain path change on limits to ductility of anisotropic metal sheets, Int. J. Mech. Scien., 2000, 42, 867–887.

[JOH 1983] G.R. Johnson, W.H. Cook, A constitutive model and data for metals subjected to large strains, high temperatures, in Proceedings of the seventh International Symposium on Ballistic, The Netherlands, The Hague, 1983, 541-547.

[JOH 1985] G.R. Johnson, W.H. Cook, Fracture characteristics of three metals subjected to various strains, strain rates, temperatures and pressures, Engineering Fracture Mechanics Vol. 21, No. 1, 1985, 31-48.

[LAN 1950] W. T. Lankford, S. C. Snyder, J. A. Bausher, New criteria for predicting the press performance of deep drawing sheets. Trans. ASM, 42, 1197–1205, 1950.

[LAN 2010] C. Landron, O. Bouaziz, E. Maire, J. Adrien, Characterization and modeling of void nucleation by interface decohesion in dual phase steels, Scripta Materialia., 63, 2010, 973-976.

[LAN 2011] C. Landron, Ductile damage characterization in Dual-Phase steels using X-ray tomography, PhD thesis/INSA-Lyon, N° d'ordre: 2011-ISAL-0147, 2011.

[LAN 2011a] C. Landron, E. Maire, J. Adrien, O. Bouaziz, L. Lecarme, A. Bareggi, Validation of void growth models using X-ray microtomography characterization of damage in dual phase steels, Acta Materialia, 59, 2011 7564-7573.

[LAN 2012] C. Landron, E. Maire, J. Adrien, O. Bouaziz, M. Di Michiel, P. Cloetens, H. Suhonen, Resolution effect on the study of ductile damage using synchrotron X-ray tomography, Nuclear instruments & Methods in physics research section B, 284, 2012, 15-18.

[LEB 1995] J. B. Leblond, G. Perrin, J. Devaux, An improved Gurson-type model for hardenable ductile metals, European Journal of Mechanics A / Solids 14, 1995 499-527.

[LEM 1988] J. Lemaitre, J.L Chaboche, Mécanique des Matériaux Solides, Dunod, 1988, (second édition), In French.

[LEM 1992] J. Lemaitre, A course on damage mechanics, Berlin: Springer– Verlag (1992).

[LER 1981] G. Leroy, J. D. Embury, G. Edwards, M. F. Ashby, Acta Met.vol.29, p. 1509-1522, 1981.

[LEM 2003] Lemoine, X., Kamoulakos, A., 2003. Calibrating and using the EWK rupture model application on arcelor high strength steel, EuroPAM, 2003, Mainz, Germany.

[LEM 2008] X. Lemoine, A. Aoufi, Bauschinger effect correspondence of experimental tests, In: Int J Mater Form Suppl, pp. 241–244, 2008.

[LEM 2011] X. Lemoine, L. Durrenbergera, H. Zhuc, R. Kergen, Mixed hardening models: parameters identification on AHSS steels, IDDRG, Bilbao (Spain), 6-8 June 2011.

[LI 2010] Y. Li, M. Luo, J. Gerlach, T. Wierzbicki, Prediction of shear-induced fracture in sheet metal forming Original Research Article Journal of Materials Processing Technology, Volume 210, Issue 14, 1 November 2010,1858-1869.

[LIE 2009] M. Liewald, C. Held, R. Schleich, Characterisation of Sheet Metal Formability - A Review and New Approaches, Metal Forming, DOI:10.2374/SRI09SP005, 2009.

[LIN 1996] Y. Ling, Uniaxial true stress-strain after necking, AMP Journal of Technology, Harrisburg (Pennsylvania), 5, 1996, 37-48.

[LIN 2008] Lingbeek, R., Meinders, T., and Rietman, A., Tool and blank interaction in the cross-die forming process. Int. Journal of Material Forming ,2008.

[LOD 1926] W. Lode, "Versuche über den Einfluß der mittleren Hauptspannung auf das Fließen der Metalle Eisen, Kupfer und Nickel," Zeitschrift für Physik, vol. 36, no. 11–12, pp. 913–939, Nov. 1926.

[LOR 2011] J. Lorthios, Endommagement des aciers TWIP pour application automobile, PhD thesis/MINES-Paris, 51-52, 2011.

[LOV 2000] A.M. Lovatt, H.R. Shercliff, P.J. Withers, Material Selection and Processing, CD-ROM and supporting booklets, Technology Enhancement Programme ,part of Gatsby Technical Education Project ,2000 London.

[LUD 1909] P. Ludwik, Elemente der technologischen Mechanik, Berlin: Springer, 1909, in German.

[LUO 2010] M. Luo, T. Wierzbicki, Numerical failure analysis of a stretch-bending test on dual-phase steel sheets using a phenomenological fracture model Original Research Article International Journal of Solids and Structures, Volume 47, Issues 22–23, November 2010, Pages 3084-3102.

[LOU 2012] Y. Lou, H. Huh, S. Lim, K. Pack, New ductile fracture criterion for prediction of fracture forming limit diagrams of sheet metals, International Journal of Solids and Structures 49, 2012 3605-3615.

[MAI 2006] E. Maire, N. Gimenez, V. Sauvant-Moynot, H. Sauterau, X-ray tomography and three-dimensional image analysis of epoxy-glass syntactic foams, Philosophical Transactions. 364, p. 69-88, 2006

[MAI 2008] E. Maire, O. Bouaziz, M. Di Michiel, C Verdu, Initiation and growth of damage in a dual-phase steel observed by X-ray microtomography, Acta Mater 56, ,2008 4954–4964.

[MAI 2012] Maiorca M, Hanssen E, Kazmierczak E, Maco B, Kudryashev M, Hall R, Quiney H, Tilley L., Improving the quality of electron tomography image volumes using pre-reconstruction filtering, J Struct Biol. 2012 Oct;180,1:132-42.

[MAL 1846] M.A. Malberg, On the crystaline fracture of wrought-iron, and the causes of the same, Journal of the Franklin Institute, 42, 1846, 119-124.

[MAR 1982] A.R. Marder. Deformation characteristics of dual-phase steels. Metallurgical and Materials transactions A, 13:85–92, 1982.

[MAR 1985] B. Marini, F. Mudry, and A. Pineau, Ductile rupture of A508 steel under non radial loading". Engineering Fracture Mechanics, Vol. 22, pp. 375 – 386, 1985.

[MAR 2000] C.F. Martin, C. Josserond, L. Salvo, J.J. Blandin, P.Cloetens, E. Boller, Scripta Mater. 42, 2000, 375–381.

[MAR 2012] S. Marcadet, effect of non-linear loading paths on sheet metal fracture: large strain In-plane compression followed by uniaxial tension, Master thesis/MIT 2012.

[MAT 2012] D.K. Matlock, J.G. Speer, E. De Moor, Recent AHSS Developments for Automotive applications: Processing, Microstructures, and Properties, I Advanced High-Strength steels for Automotive light weighting, USCAR offices, Southfield. www.worldautosteel.org,2012.

[MAZ 2007] M. Mazinani and W.J. Poole. Effect of martensite plasticity on the deformation behavior of a low-carbon dual-phase steel. Metallurgical and Materials transactions A, 38:328–339, 2007.

[MAS 2010] T. Massé, Study and optimization of high carbon steel flat wires, PhD/Thesis, l'École nationale supérieure des mines de Paris, 2010.

[MCC 1968] F.A. McClintock, A criterion for ductile fracture by growth of holes. Trans. ASME. Journal of Applied Mechanics, Volume 35, 1968, 363–371.

[MEA 1985] M. Mear, J. W. Hutchinson, Influence of yield surface curvature on flow localization in dilatant plasticity, Mechanics of Materials, 4, 1985 395–407.

[MEI 1999] Meinders, T. and Boogaard van den, A.H. and Huetink, J., A mixed elastoplastic / rigid plastic material model. In: Numisheet conference, 1999.

[MIE 1996] C. Miehe, Numerical computation of algorithmic, consistent tangent moduli in large-strain computational inelasticity, Comput. Method. App. M., 134, 1996, 223-240.

[MIS 1928] R. Von Mises, Mechanik der plastischen Formänderung von Kristallen, Z. Angew Math. Mech., 1928, 8:161-185, In German.

[MIS 2011] A. Mishra, C. Leguen, S. Thuillier, E. Mairie, Investigation of ductile damage in DP980 steel sheets using Mechanical tests and X-ray Micro-Tomography, The 14Th International ESAFORM Conference on material forming, P 1464-1469 ,2011, Beslfast.

[MOH 2007] Mohr, D., Henn, S., 2007. Calibration of stress-triaxiality dependent crack formation criteria: a new hybrid experimental–numerical method. Exp. Mech. 47, 2007, 805–820.

[MOH 2008] Mohr, D., Oswald, M., A new experimental technique for the multi-axial testing of advanced high strength steels. Exp. Mech, 2008, 48, 65–77.

[MOH 2009] Mohr, D., Ebnoether, F., Plasticity and fracture of martensitic boron steel under plane stress conditions. Int. J. Solids Struct. 46, 20, 2009, 3535–3547.

[MOH 2010] D. Mohr, M. Dunand, K. Kim, Evaluation of associated and non-associated quadratic plasticity models for advanced high strength steel sheets under multi-axial loading, International Journal of Plasticity 26 ,2010, 939–956.

[MOH 2012] Mohr, D., Experimental methods for characterizing plasticity and fracture, Presentation Summer School, 2012, Dortmund.

[MON 2006] V. Monchiet, C. Gruescu, E. Charkaluk., D. Kondo, Approximate yield criteria for anisotropic metals with prolate or oblate voids. Comptes Rendus Mecanique, Volume 334, Issue 7, 2006, 431-439.

[MOR 2000] L.P. Moreira, G. Ferron, G. Ferran, Experimental and numerical analysis of the cup drawing test for orthotropic metal sheets, J. Mater. Process. Technol. 108, 2000, 78–86.

[MRO 1967] Z. Mroz, On the description of anisotropic work hardening. Journal of Mechanics and Physics of Solids 1967; 15:163–75.

[MUR 2011] O. Muransky, C.J. Halmelin, M.C. Smith, P.J Bendeich, L. Edwards, The effect of plasticity theory on predicted residual stress fields in numerical weld analyses, Computational Materials Science 54 ,2012, 125–134.

[NAH 2008] K. Nahshon, J.W. Hutchinson, Modification of the Gurson Model for shear failure, European Journal of Mechanics A/Solids 27 ,2008, 1–17.

[NAK 1971] Nakazima, K., Kikuma, T. & Hasuka, Study on the formability of steel sheets, Technology Report, 1971, 284: 678-680.

[NAK 2007] T. Nakamura, Y. Gu, Identification of elastic–plastic anisotropic parameters using instrumented indentation and inverse analysis, Mechanics of Materials 39 , 2007, 340–356.

[NAS 2012] A. Nasser, A. Yadav, P. Pathak, T. Altan, Determination of the flow stress of five AHSS sheet materials ,DP 600, DP 780, DP780-CR, DP 780-HY and TRIP 780 using the uniaxial tensile and the biaxial Viscous Pressure Bulge ,VPB tests, Journal of Materials Processing Technology210 ,2010, 429–436.

[NEE 1987] A. Needleman, V. Tvergaard, An analysis of ductile rupture modes at a crack tip, Journal of the Mechanics and Physics of Solids, Vol. 35, 1987, 151– 183.

[NEG 2003] P. Nègre, D. Steglich, W. Brocks, M. Koçak, Numerical simulation of crack extension in aluminium welds, Computational Materials Science, 28, Issues 3-4 ,2003, 723-731.

[NIA 2012] M.S Niazi, Plasticity induced anisotropic damage modeling for forming processes, PhD Thesis/University of Twente, 2012.

[NIE 2008] K. L. Nielsen, 3D modelling of plug failure in resistance spot welded shear-lab specimens ,(DP600-steel), International Journal of Fracture, 2008, Volume 153, Issue 2, 125-139.

[NIE 2010] K. L. Nielsen and V. Tvergaard, "Ductile shear failure or plug failure of spot welds modeled by modified Gurson model," Engineering Fracture Mechanics, vol. 77, no. 7, pp. 1031–1047, May 2010.

[NIA 2012] M.S Niazi, Plasticity induced anisotropic damage modeling for forming processes, PhD Thesis/University of Twente, 2012.

[OLI 2005] M.C. Oliveira, J.L. Alves, B.M. Chaparro, L.F. Menezes, Study on the Influence of the Work Hardening Models Constitutive Parameters Identification in the Springback Prediction, CP778 volume A, American Institute of Physics, Numisheet 2005.

[OUS 2012] A. Ou-Sair, Comparaison des modeles d'endommagement et de rupture sur la prediction de tests de formabilité, Master thesis: Uninversite de Lorraine-Metz 2012.

[PAD 2008] R. Padmanabhan, A.J. Baptista, M.C. Oliveira, L.F. Menezes, Effect of anisotropy on the deep-drawing of mild steel and dual-phase steel tailor-welded blanks, Journal of Materials Processing Technology 184 , 2007, 288–293.

[PAN 2010] S. K. Panda, D. R. Kumar, Experimental and numerical studies on the forming behavior of tailor welded steel sheets in biaxial stretch forming, Materials and Design 31 , 2010, 1365-1383.

[PAN 2011] S. Panich V. Uthaisangsuk, J. Juntaratin, S. Suranuntchai, Determination of Forming Limit Stress Diagram for Formability Prediction of SPCE 270 Steel Sheet, Journal of Metals, Materials and Minerals, Vol.21 No.1 pp.19-27, 2011

[PAR 2012] I. N. Paralikas, Cold roll forming process energy efficiency optimization, PhD thesis, University of Patras, 2012.

[PAR 1998] T. Pardoen, I. Doghri, and F. Delannay, Experimental and numerical com-parison of void growth models and void coalescence criteria for the prediction of ductile fracture in copper bars, Acta Materialia, Vol. 46, 1998 541–552.

[PAR 2000] T. Pardoen, J.W. Hutchinson, An extended model for void growth and coalescence, Journal of the Mechanics and Physics of Solids, Volume 48, Issue 12, 2000, 2467-2512.

[PAR 2002] E. Parteder, H. Riedel, D.Z. Sun, Simulation of hot forming processes of refractory metals using porous metal plasticity models. International Journal of Refractory Metals and Hard Materials, Volume 20, Issue 4, 2002, 287-293.

[PAR 2006] T. Pardoen, Numerical simulation of low stress triaxiality ductile fracture, Comput. Struct. 84, 2006, 1641-1650.

[PER 2010] N. Peranio, Y.J. Li, F. Roters, D. Raabe, Microstructure and texture evolution in dual-phase steels: Competition between recovery, recrystallization, and phase transformation, Materials Science and Engineering A527, 2010, 4161–4168.

[PIN 2012] A.Pineau, materiaux et mobilité, Saint-Germain en Laye, 2012.

[PRA 1956] W. Prager, A new method of analysing stresses and strains in work hardening plastic solids. Transactions of ASME, Journal of Applied Mechanics 1956; 23:493–6.

[PRA 1958] W. Prager, Problèmes de plasticité théorique. Dunod, 1958, in French.

[RAB 2009] M. Rabahallah et al., Parameter identification of advanced plastic strain rate potentials and impact on plastic anisotropy prediction, International Journal of Plasticity 25, 2009, 491–512.

[RAG 2002] A.R. Ragab, Ch. Saleh, N.N Zaafarani, Forming limit diagrams for kinematically hardened voided sheet metals. Journal of Materials Processing Technology, Volume 128, Issues 1-3, 2002, 302-312.

[RAM 1979] L.F. Ramos, D.K. Matlock, and G. Krauss. On the deformation of dual-phase steels, Metallurgical transactions A, 10:259–261, 1979.

[RAM 2010] A. Ramazani, M. Abbasi, U. Prahl, W. Bleck, Failure analysis of DP600 steel during the cross-die test, Computational Materials Science, 2012.

[RAM 2012] A. Ramazani, M. Abbasi, U. Prahl, W. Bleck, Failure analysis of DP600 steel during the cross-die test, Computational Materials Science, 2012.

[RAS 1976] M.S. Rashid. Gm 980x a high unique high strength sheet metal with superior formability, pages 938–949, Detroit, 1976. Society of Automotive Engineers.

[REC 2012] D. Reche, J. Besson, T. Sturel, X. Lemoine, A.F. Gourgues-Lorenzon, Analysis of the air-bending test using finite-element simulation: Application to steel sheets, International Journal of Mechanical Sciences 57 , 2012 43–53.

[RIC 1969] J. R. Rice, D. M. Tracey, On the ductile enlargement of voids in triaxial stress fields, Journal of the Mechanics and Physics of solids, 17, 1969, 201-217.

[RIE 2009] M. van Riel. Strain path dependency in sheet metal. PhD thesis, University of Twente, Enschede, The Netherlands, 2009.

[ROD 2000] A. Rodriguez-Ferran, A. Huerta, Error estimation and adaptivity for non-local damage models, Int. J. Solids Struct. 37, 2000, 7501-7528.

[ROD 2001] A. Rodriguez-Ferran, I. Erbos, A. Huerta, Adaptive analysis based on error estimation for nonlocal damage models, Rev. Eur. E´le ´m. Finis 10, 2001, 193-207.

[ROS 1965] W. Rostoker, J.R. Dvorak, Interpretation of metallographic structures, Academic press New York Book, 1965, 195-211.

[ROE 2006] J. Roesler, H. Harders, M. Baeker, Mechanical behaviour of engineering materials, Metals, Ceramics, Polymers, and Composites, Springer, , 2006.

[SAI 1881] M. Saint-Venant, A. De Clebsch, L'élasticité des corps solides, 1881, http://www.archive.org/details/thoriedellas01cleb, In French.

[SAN 2001] A. Sandu, Lecture Notes Introduction to Fortran95 and Numerical Computing A Jump-Start for Scientists and Engineers, Michigan Technological University 2001.

[SAR 1996] M. Sarwar, R. Priestner, Influence of ferrite-martensite microstructural morphology on tensile properties of dualphase steel Materials Science 31 , 1996, p. 2091-2095.

[SCH 2008] F. Scheyvaerts, Multiscale modelling of ductlie fracture in heterogeneous metallic alloys, PhD thesis, Universite catholique de Louvain, Belgium, 2008.

[SCH 2010] M. Schellekens, Microstructural modeling of Dual-Phase steel, Master thesis/Technische Universiteit Eindhoven, 2010.

[SHA 2009] K. P. Shah, Annealing of hypoeutectoid carbon-steel. "Heat treatment of steel" in The Handbook of Mechanical Maintenance. Retrieved from http://practicalmaintenance.net/?p=1329.

[SMI 1957] B.O Smith, A.P.H Jenning, A.G Grimshaw, A portable lamination detector for steel sheet, The British Iron and Steel Research Association, Battersea Park Road, 1957, London.

[SOD 2012] S. Sodjit, V. Uthaisangsuk, Microstructure based prediction of strain hardening behavior of dual phase steels, Materials&Design, 41, 2012, 370-379.

[SON 2003] H.S. Son, Y.S. Kim, Prediction of forming limits for anisotropic sheets containing prolate ellipsoidal voids. International Journal of Mechanical Sciences, Volume 45, 2003, 1625–1643.

[STE 1988] D.L. Steinbrunner, D.K. Matlock, G. Krauss, Metall. Trans. 19A, 1988, 579–589.

[SUH 1997] Dongwoo Suh, Dongil Kwon, Sungak Lee, and Nack J. Kim. Orientation dependence of microfracture behavior in a dual-phase high-strength low-alloy steel. Metallurgical and Materials transactions A, 28:504–509, 1997.

[SUN 2009] X. Sun, K.S. Choi, W.N. Liu, M.A. Khaleel, Predicting failure modes and ductility of dual phase steels using plastic strain localization Original Research Article International Journal of Plasticity, Volume 25, Issue 10, October 2009, Pages 1888-1909.

[SUN 2013] L. Sun, R.H. Wagoner, Proportional and Non-Proportional Hardening Behavior of Dual-Phase Steels, International Journal of Plasticity, 2013, doi: http://dx.doi.org/10.1016/j.ijplas.2013.01.018.

[SVE 2000] T. Svedberg, K. Runesson, An adaptive finite element algorithm for gradient theory of plasticity with coupling to damage, Int. J. Solids Struct. 37, 2000, 7481-7499.

[SWI 1952] H.W. Swift, Plastic instability under plain stress. Journal of the Mechanics and Physics of Solids, 1, 1952, 1-18.

[TAH 2009] A. Taherizadeh et al., Finite element simulation of springback for a channel draw process with drawbead using different hardening models, International Journal of Mechanical Sciences 51, 2009, 314–325.

[TAM 2011] C. M. Tamarelli, The Evolving Use of Advanced High-Strength Steels for Automotive Applications, report ; Materials Science and Engineering, a business unit of AISI, www.autosteel.org University of Michigan, 2011.

[TAS 2009] C.C. Tasan, J.P.M. Hoefnagels, M.G.D. Geers, A brittle-fracture methodology for three-dimensional visualization of ductile deformation micromechanisms, Scripta Materialia, 61:20-23, 2009.

[TAS 2010] C.C. Tasan, J.P.M. Hoefnagels, and M.G.D. Geers. Microstructural banding effects clarified through micrographic digital image correlation. Scripta Materialia, 62:835–838, 2010.

[THO 1985] P. Thomason. "A three-dimensional model for ductile fracture by the growth and coalescence of microvoids". Acta Metallurgica, Vol. 33, No. 6, 1985, 1087– 1095.

[THO 1987] A. Thompson. "Modeling of local strains in ductile fracture". Metallurgical and Materials Transactions A, Vol. 18, pp. 1877–1886, 1987.

[THO 1990] P. F Thomason, Ductile fracture of metals, Oxford: Pergamon Press, 1990.

[TRE 1868] H. Tresca, Mémoire sur l'écoulement des solides, 1868, Vol. 18, 733-799, In French.

[TUG 2001] P. Tugcu, K.W. Neale, P.D. Wu, S.R. MacEwen, Effect of planar anisotropy on wrinkle formation tendencies in curved sheets, Int. J. Mech. Scien., , 2001, 43, 2883–2897.

[TSI 2006] P. Tsipouridis, Mechanical properties of Dual-Phase steels, PhD thesis/Technische Universität München, 2006.

[TVE 1982] V. Tvergaard, On localization in ductile materials containing spherical voids, Int. J. Fract. 18, 1982, 237–252.

[TVE 1984] V. Tvergaard, A. Needleman, Analysis of the Cup-cone Fracture in a Round Tensile Bar, Acta Metall. 32 , 1984, 157-169.

[TVE 1987] Tvergaard V, Ductile shear failure at the surface of a bent specimen. Mech. Mater., 1987, 53-69.

[UTH 2008] V. Uthaisangsuk, U. Prahl, and W. Bleck. Micromechanical modelling of damage behaviour of multiphase steels. Computational Materials Science, 43:27–35, 2008.

[UTH 2009] V. Uthaisangsuk, U. Prahl•, W. Bleck, Characterization of formability behaviour of multiphase steels by micromechanical modelling, Int J Fract , 2009, 157:55–69.

[UTH 2009a] V. Uthaisangsuk, U. Prahl, and W. Bleck. Failure modeling of multiphase steels using representative volume elements based on real microstructures. Procedia Engineering, 1:171–176, 2009.

[UTH 2011] V. Uthaisangsuk, U. Prahl, W. Bleck, Modelling of damage and failure in multiphase high strength DP and TRIP steels Original Research Article Engineering Fracture Mechanics, Volume 78, Issue 3, February 2011, Pages 469-486.

[VAJ 2012] N. Vajragupta, V. Uthaisangsuk, B. Schmaling, S. Münstermann, A. Hartmaier, W. Bleck, A micromechanical damage simulation of dual phase steels using XFEM, Computational Materials Science 54, 2012, 271–279.

[VLA 2010] I.N. Vladimirov et al., Anisotropic finite elastoplasticity with nonlinear kinematic and isotropic hardening and application to sheet metal forming, International Journal of Plasticity 26, 2010, 659–687.

[VOC 1948] E.J. Voce, Inst. Met., 74, 1948, 537, 562, 760.

[WAG 2006] R.H. Wagoner, Advanced High Strength Steel Workshop, Department of Materials Science and Engineering, The Ohio State University, Columbus, Ohio-USA, report: October 22-23, 2006.

[WAN 2011] X.Z. Wang, S.H. Masood, Investigation of die radius arc profile on wear behaviour in sheet metal processing of advanced high strength steels, Materials and Design 32, 2011, 1118-1128.

[WEC 2007] A. Weck, Atomic The role of coalescence on ductile fracture, PhD thesis, McMaster University, Canada, 2007.

[WIE 2005] Wierzbicki, T., Xue, L., On the effect of the third invariant of the stress deviator on ductile fracture. Technical report. Impact and Crash. 2005.

[WIE 2005a] T. Wierzbicki, Y. Bao, Y.W. Lee, Y. Bai, Calibration and evaluation of seven fracture models. International Journal of Mechanical Sciences, Volume 47, Issues 4-5, 2005, 719-743.

[WIE 2005b] T. Wierzbicki, L. Xue, On the effect of the third invariant of the stress deviator on ductile fracture. Impact and Crashworthiness Lab Report, Volume 136, 2005.

[WIE 2006] T.Wierzbicki Fracture of Advanced High Strength Steels, AHSS, to be conducted at the Impact and Crashworthiness, Part I: Technical Proposal, Report MIT 2006.

[WIS 2011] Wisselink, H.H. and Niazi, M.S. and Huetink, J. , 2011, Validation of advanced material models using the cross-die test. In: IDDRG Conference 2011: Towards sustainable sheet forming processes, 5-8 June 2011, Bilbao, Spain.

[Xue 2007] L. Xue, L., Damage accumulation and fracture initiation in uncracked ductile solids subject to triaxial loading. International Journal of Solids and Structures, Volume 44, Issue 16, 2007, 5163-5181.

[XUE 2008] L. Xue, Constitutive modeling of void shearing effect in ductile fracture of porous materials, Engineering Fracture Mechanics, vol. 75, pp. 3343-3366, 2008.

[XUE 2012] F. Xue, F. Li, B. Chen, J. Fan, R. Wang, A ductile–brittle fracture model for material ductile damage in plastic deformation based on microvoid growth, Computational Materials Science, 65: 182-192, 2012.

[YAN 2012] S.-Y. Yang, W. Tong, A Finite Element Analysis of a Tapered Flat Sheet Tensile Specimen, Experimental Mechanics, 2009, 49:317-330

[YOS 1968] F. Yoshida, Constitutive modeling of large-strain cyclic plasticity for anisotropic metals, www.lem3.fr/summerschool/00-Files/FY-lecture2.pdf, 2012 Dortmund.

[YOU 2005] S. Youssef, E. Maire, R. Gaertner - Finite element modelling of the actual structure of cellular materials determined by X ray tomography, Acta Materialia, , 53,p.719-730, February 2005.

[ZEN 2005] C. Zengtao, J. Worswick Michael, A. Keith Pilkey et J. Lloyd David, Damage percolation during stretch flange forming of aluminum alloy sheet, Journal of the Mechanics and Physics of Solids, vol. 53, 2692–2717, 2005.

[ZHA 1995] Z. Zhang, «Explicit consistent tangent moduli with a return mapping algorithm

for pressure-dependent elastoplasticity models, » Computer Methods in Applied Mechanics and Engineering, vol. 121, 29-44, 1995.

[ZHA 1994] Z.L. Zhang, E. Niemi, Studies on the ductility predictions by different local failure criteria Original Research Article, Engineering Fracture Mechanics, Volume 48, Issue 4, July 1994, Pages 529-540.

[ZHA 2001] K.S. Zhang, J.B. Bai, D. François, Numerical analysis of the influence of the Lode parameter on void growth. International Journal of Solids and Structures, Volume 38, Issues 32-33, 2001, 5847-5856.

[ZHI 2009] C. Zhiying, D. Xianghuai, The GTN damage model based on Hill'48 anisotropic yield criterion and its application in sheet metal forming, Computational Materials Science 44 , 2009, 1013–1021.

[ZHU 1992] Y.Y Zhu, S. Cescotto, A.M. Habraken, A fully coupled elastoplastic damage modelling and fracture criteria in metalforming processes, Journal of Materials Processing Technology, 1992, Volume 32, Issues 1-2, Pages 197-204.

[ZHU 1995] YY Zhu, S. Cescotto, A fully coupled elasto-visco-plastic damage theory for anisotropic materials. Int J Solids Struct, 1995, 1607–1641.

[ZIE 1959] H. Ziegler, A modification of Prager's hardening rule. Quart. Appl. Math. 17, 1959, 55–65.

[ZÜR 2005] K.H. Zürl, Modern English for the automotive industry-Englisch für Aus-und weiterbildung von Ingenieuren, 3.Auflage, Hanser, 2005.

PREDICTION PAR ELEMENTS FINIS DE LA RUPTURE DES ACIERS DUAL_PHASE EN UTILISANT UN MODELE DE GURSON AVANCE

RESUME : L'actuelle investigation numérique du Gurson-Tvergaard-Needleman (GTN) modèle avancé est une extension du travail de Ben Bettaieb et al. (2011). Le modèle a été implémenté à l'aide d'une sous routine (VUMAT) contenu dans le code commerciale d'éléments finis Abaqus/explicit. Le modèle d'endommagement améliore l'original en intégrant les trois mécanismes d'endommagement, la nucléation, la croissance, et la coalescence des cavités. Le modèle d'endommagement intègre les lois de nucléation et de croissance basés sur les phénomènes purement physiques. Ces nouvelles contributions incluant l'influence de l'écrouissage cinématique, ont été validées par les résultats de mesures expérimentales de tomographie à rayon X à haute résolution. Aussi, l'implémentation numérique de l'écrouissage cinématique dans le modèle modifié a contraint de proposer et de réarranger la définition de la triaxialité que l'on trouve habituellement dans la littérature. A coté de cela, un second critère d'initiation à la rupture basé sur l'ultime distance inter-cavités a été inclue afin de localiser et de quantifier avec plus de précision la distribution des déformations peu avant que le matériau ne casse complètement. L'actuel modèle d'endommagement a été appliqué dans des conditions industrielles pour prédire l'évolution de l'endommagement, l'état de contraintes, et l'initiation à la rupture pour différentes géométries de tôles et sur des essais d'emboutissage de tôles minces.

Mots clés : Endommagement, GTN modèle, Nucléation, Croissance, Coalescence, Aciers DP, Tomographie, Initiation à la rupture.

PREDITION OF DP STEEL FRACTURE BY FEM SIMULATIONS USING AN ADVANCED GURSON MODEL

ABSTRACT: This numerical investigation of an advanced Gurson–Tvergaard–Needleman (GTN) model is an extension of the original work of Ben Bettaieb et al. (2011). The model has been implemented as a user-defined material model subroutine (VUMAT) in the Abaqus/explicit FE code. The current damage model extends the previous version by integrating the three damage mechanisms: nucleation, growth and coalescence of voids. Physically based void nucleation and growth laws are considered, including an effect of the kinematic hardening. These new contributions are based and validated on experimental results provided by high-resolution X-ray absorption tomography measurements. Also, the numerical implementation of the kinematic hardening in this damage extension has obliged to readapt the classical triaxiality definition. Besides, a secondary fracture initiation criterion based on the ultimate average inter-cavities distance has been integrated to localize and quantify with good accuracy the strain distribution just before the material fails apart. The current damage model is applied in industrial conditions to predict the damage evolution, the stress state and the fracture initiation in various tensile thin flat sheet geometries and the cross-die drawing tests.

Keywords : Damage, GTN model, Nucleation, Growth, Coalescence, DP steel, Tomography, Fracture initiation.